ANALYSIS OF CHEMICAL SIGNALS FROM COMPLEX OCEANIC GAS HYDRATE ECOSYSTEMS WITH INFRARED SPECTROSCOPY

A Thesis
Presented To
The Academic Faculty

By

Gary T. Dobbs

In Partial Fulfillment
Of the Requirements for the Degree
Doctor of Philosophy in Chemistry

Georgia Institute of Technology

December, 2007

ANALYSIS OF CHEMICAL SIGNALS FROM COMPLEX OCEANIC GAS HYDRATE ECOSYSTEMS WITH INFRARED SPECTROSCOPY

Approved by:

Dr. Boris Mizaikoff, Advisor
School of Chemistry and Biochemistry
Georgia Institute of Technology

Dr. Donald R. Webster
School of Civil & Environmental Engineering
Georgia Institute of Technology

Dr. Andrew Lyon
School of Chemistry and Biochemistry
Georgia Institute of Technology

Dr. Facundo M. Fernandez
School of Chemistry and Biochemistry
Georgia Institute of Technology

Dr. Joseph Montoya
School of Biology
Georgia Institute of Technology

Dr. Dennis W. Hess, Honorary
School of Chemical & Biomolecular Engineering
Georgia Institute of Technology

Date Approved: September 21, 2007

This thesis is dedicated to my family.

ACKNOWLEDGEMENTS

I wish to thank my advisor Dr. Boris Mizaikoff for giving me the opportunity to continue my education as a scientist and a person during my doctoral research at the Applied Sensors Laboratory, School of Chemistry and Biochemistry, Georgia Institute of Technology. His enthusiasm and encouragement of individual creativity and scientific exploration are deeply appreciated. I would also like to thank all past and present members of the ASL team for their friendship, encouragement, and scientific contributions. I particularly wish to thank; Dr. Christine Kranz for her assistance with AFM and SEM measurements, An Nguyen for the many hours he spent assisting with the spectral analysis of sediment samples, Dr. Nicola Menagazzo for his assistance in the lab and the many intellectual discussions over the years, and Dr. Manfred Karlowatz, Dr. Christy Charlton, Yuliya Luzinova, and Douglas Rudolph for their assistance and camaraderie.

I am grateful for the critical feedback and input provided by my thesis committee.

In addition, this work has been facilitated with the assistance of many collaborative partners, and I wish to thank all of those individuals who helped make this possible.

The Gulf of Mexico Gas Hydrate Research Consortium managed by the Center for Marine Resources and Environmental Technology at the University of Mississippi, Oxford, MS has provided an excellent platform for the interaction and exchange of ideas with many scientists and professionals. I would like to express my gratitude for the assistance of GOMGHRC members: Dr. Carol Lutken, Dr. Bob Woolsey, Ken Sleeper, and the CMRET technical team and staff of the University of Mississippi; Dr. Roger Sassen of Texas A & M University, College Station, Texas; Dr. Rudy Rogers from Mississippi State University, Starkville, MS; Dr. Chris Martens and Dr. Laura Lapham of the University of North Carolina, Chapel Hill, NC; Dr. Jeff Chanton at Florida State University, Tallahassee, FL; Dr. Mandy Joye of the University of Georgia, Athens, GA; and Dr. Jean Whelan and Dr. Richard Camilli, Woods Hole Oceanographic Institution, Woods Hole, MA.

I am appreciative of Dr. Abraham Katzir and Dr. Yosef Raichlin for providing silver halide fibers, including hand delivery in Germany.

I would also like to thank all past and present faculty, staff, and students I have interacted with and the opportunities accessed from the Signals in the Sea NSF IGERT program. Special thanks to; Dr. Mark Hay, Alex Chequer, Jason Landrum, Zachary Hallinan, and Sara Brogdon.

I also wish to thank those individuals I have had the opportunity to work with throughout the course of my doctoral studies: Dr. Nan Jokerst and Sang-Yeon Cho at Duke University, Durham, NC; James Bradshaw, Dr. Dennis W. Hess, Balamurali Balu, Dr. Oliver Brand, Albert Byun, and the CoS machine shop staff at Georgia Tech.

I am also grateful for funding provided by the Signals in the Sea NSF IGERT program, ExxonMobil, U.S. Department of Energy, Mineral Management Services, CMRET, MMRI, and Georgia Tech.

I wish to express my deepest gratitude to all the educators and athletics coaches who have contributed to my learning and growth as an individual over the past 23 years; including those from the Russellville Public School System, Russellville, AR; the University of Central Arkansas, Conway, AR; and the Georgia Institute of Technology, Atlanta, GA. I would like to particularly thank Dr. Jeffrey Draves, Dr. William Taylor, and Dr. Douglas Duckworth for their guidance and mentorship during undergraduate research studies.

Lastly, all of this would not have been possible without the unconditional love and support I have received from my family. I extend my greatest thanks to you all; Grammy, Papa, Grandma, Mom, Dad, Sheri (a.k.a. Dr. Beavis), Heather, Thomas James, and to the memories of Pappy, Uncle Gary (my namesake), Uncle Flint, Uncle June, Uncle Jack, and Suzie.

TABLE OF CONTENTS

ACKNOWLEDGEMENTS iv

LIST OF TABLES xiii

LIST OF FIGURES xvii

LIST OF ABBREVIATIONS xxix

SUMMARY xxxiv

CHAPTER 1: INTRODUCTION 1

Thesis Objective 1

Original Contributions of This Thesis 1

1.1 Motivation 2

1.2 Overview of Gas Hydrates in the Gulf of Mexico 3

1.3 Overview and Scientific Objectives of the GOMGHRC 5

1.4 Introduction to the Gas Hydrate Ecosystem at Mississippi Canyon 118 8

1.5 IR Spectroscopy and Oceanic Gas Hydrate Ecosystems 11

1.6 References 12

CHAPTER 2: BACKGROUND 17

2.1 Infrared Spectroscopy 17

2.1.1 Infrared-Attenuated Total Reflection (IR-ATR) Spectroscopy 19

2.1.2 IR-ATR Waveguides 21

2.1.3 Evanescent Field Sensing Strategies 22
2.1.3.1 Uncoated Waveguides 22
2.1.3.2 Surface-Modified Waveguides 22

2.2 General Characteristics and Methods for Detecting Oceanic Gas Hydrates 23

2.2.1 General Characteristics of Oceanic Gas Hydrates 23
2.2.1.1 Biogenic and Thermogenic Gas Hydrates 24
2.2.1.2 Gas Hydrate Morphologies 24
2.2.1.3 Gas Hydrate Structures 25

2.2.2 Detection, Indication, and Characterization of Oceanic Gas Hydrates 25
2.2.2.1 Visual Observation and Hydrate Sampling Methods 26
2.2.2.2 Seismo-Acoustic Detection of Gas Hydrates 27
2.2.2.3 Geochemical Indicators of Gas Hydrates 27

2.3 General Overview of Classical Characterization Methods for Marine Carbonates 28

2.4 References 29

CHAPTER 3: EXPERIMENTAL DESIGN AND APPARATUS 32

3.1 Experimental Setup for IR Spectroscopic Monitoring of Gas Hydrates 32

3.1.1 Initial Pressure Chamber Design 33

3.1.2 Construction Modifications to Main Body of Pressure Chamber 34

3.1.3 High Pressure Optical Viewport Design, Construction, and Specifications 34

3.1.4 Fiber-optic Integration for IR Spectroscopic Access 37

3.1.5 Imaging System for Hydrate Chamber 39

3.1.6 Cooling System for Hydrate Growth Chamber 40

3.1.7 Pressure and Temperature Monitoring System 42

3.1.8 Assembly of the Pressure Chamber 44

3.1.9 Optics Layout for Hydrate Measurements 47

3.1.10 Additional Features of the Hydrate Experimental Setup 48

3.1.11 Concluding Remarks on the Hydrate Monitoring Apparatus 50

3.2 Horizontal Attenuated Total Reflection Accessories and Optical Configuration 50

3.3 References 53

CHAPTER 4: FIBER-OPTIC MID-IR SPECTROSCOPY FOR MONITORING GAS HYDRATES 54

4.1 Motivation 54

4.1.1 Clathrate Hydrates of Natural Gases 55
4.1.1.1 Naturally Occurring Gas Hydrates 56
4.1.1.2 General Molecular Characteristics of Gas Hydrate Structures 56
4.1.1.3 General Characteristics of Methane, Ethane, and Propane Hydrates 58
4.1.1.4 Cluster Nucleation and Kinetic Growth Models for Gas Hydrates 60

4.1.2 IR Spectroscopy and Water 63
4.1.2.1 The IR Absorption of Liquid Water 64
4.1.2.2 Influences on the IR Absorption of Liquid Water 65

4.2 Laboratory Growth of Simple Gas Hydrates from Solution 67

4.2.1 Chemicals for Growth of Gas Hydrates from Solution 67

4.2.2 General Experimental Procedures for IR Monitoring of Gas Hydrates 67

4.2.3 Non-spectroscopic Indications of Hydrate Nucleation and Growth 68

4.2.4 Visualizing Hydrate Dissociation and Comparisons with Ice 70

4.2.5 Inspection of Gas Hydrates Extracted from the Pressure Chamber 72

4.3 Fiber-optic IR-ATR Spectroscopic Monitoring of Gas Hydrates 75

4.3.1 Results and Discussion 77
4.3.1.1 IR Spectral Mixing During the Phase Transitioning of Water 77
4.3.1.2 The O-H Stretches 79
4.3.1.3 The H-O-H Bend 82
4.3.1.4 The Libration Band 85
4.3.1.5 The 3rd Libration Overtone 88

4.3.2 Evaluation of all Water Features during a Hydrate Trial: Model with Propane Hydrate 91

4.3.3 Deriving the Quantification of Gas Hydrate from IR Spectra 94

4.3.4 Feasibility for Extending Hydrate Monitoring Strategies into Oceanic Sediment Matrices 100

4.3.5 Power Limitations for Extending Hydrate Monitoring Strategies into Oceanic Settings 104

4.4 Hybridized Reaction Kinetic-Thermodynamic Model for Gas Hydrate Formation 108

4.5 Conclusions 111

4.6 Outlook 115

4.7 References 117

CHAPTER 5: IR-ATR EVALUATION OF CARBONATE MINERALS IN SEAFLOOR SEDIMENTS 124

5.1 Motivation 124

5.1.1 Introduction to the Classification of Carbonate Minerals 125

5.1.2 Carbonate Mineralogy of Oceanic Gas Hydrate Ecosystems in the GoM 126
5.1.2.1 Authigenic Carbonate Production 126
5.1.2.2 Dolomitization 129
5.1.2.3 Biological Sources of Carbonates 129
5.1.2.4 Mg-Calcite 131

5.1.3 IR Spectroscopy and Carbonate Mineralogy 132
5.1.3.1 Classification of Carbonate Minerals with IR Spectroscopy 133
5.1.3.2 Quantification of Carbonate Minerals with Infrared Spectroscopy 136
5.1.3.3 IR Spectral Characteristics of Mg-Calcite 137

5.2 IR-ATR Spectral Database for Identifying Carbonate Minerals 139

5.2.1 Experimental 139
5.2.1.1 Materials 139
5.2.1.2 IR-ATR Instrumentation 140
5.2.1.3 IR-ATR Measurement Procedures 140

5.2.2 Results and Discussion 141

5.3 Seafloor Sediment Collections from the GoM 144

5.3.1 Box Core Sediment Collections from MC118 in June 2006 145

5.3.2 Gravity Core Sediment Collections from MC118 in October 2005 149

5.3.3 Sediments from Piston Core MD02-2570 150

5.4 IR-ATR Spectroscopic Screening of Sediment Samples 150

5.4.1 Experimental 151

5.4.2 Results and Discussion 151
5.4.2.1 Assessment of Sediment Compositions from Native Samples 151
5.4.2.2 IR-ATR Characterization of Dried Sediment Samples 156

5.5 Calcite-Dolomite Ratios from Sediment Collections 161

5.5.1 Experimental 162
5.5.1.1 Materials and Instrumentation 162
5.5.1.2 Sample Preparations and IR-ATR Measurement Procedures 163

5.5.2 Results and Discussion 165
5.5.2.1 Calibration for Determining Mass % of Calcite and Dolomite to Total Carbonate 165
5.5.2.2 Evaluating Calcite and Dolomite in MC118 Sediments (June 2006 Cruise) 170
5.5.2.3 MC118 Gravity Core Sediments (October 2005 Cruise) 177
5.5.2.4 Sediments from Piston Core MD02-2570 178
5.5.2.5 Advantages, Limitations, and Potential of Quantitative Evaluations 180

5.6 Conclusions 183

5.7 Outlook 185

5.8 References 186

CHAPTER 6: SPECTROSCOPIC DETECTION OF AUTHIGENIC CARBONATES IN MARINE SEDIMENTS CONTAINTING COCCOLITH CALCITE 192

6.1 Motivation 192

6.1.1 Coccolithophores and Coccoliths 194
6.1.1.1 Coccolithophores in the Gulf of Mexico 195
6.1.1.2 Coccolith Distributions in Gulf of Mexico Sediments 196
6.1.1.3 General Characteristics of Coccolith Shields 198
6.1.1.4 Coccoliths versus Foraminifera Tests 199

6.2 Correlating Spectral Profiles of Authigenic Carbonate Nodules with Select Sediments 199

6.2.1 Experimental 200
6.2.1.1 IR-ATR Instrumentation 200
6.2.1.2 Sample Preparations and IR-ATR Measurement Procedures 201

6.2.2 Results and Discussion 202

6.3 Coccoliths Observed in MC118 Samples 205

6.3.1 Experimental 205

6.3.2 Results and Discussion 206
6.3.2.1 Taxonomic Characterization of Coccoliths in MC118 Samples 206
6.3.2.2 Coccolith Density in MC118 Sediments 207

6.4 IR-ATR Spectroscopic Evaluation of Coccoliths from Coccolithophore Cultures 209

6.4.1 Experimental 209
6.4.1.1 Coccolithophore Cultures 209
6.4.1.2 Sample Preparation 211
6.4.1.3 IR-ATR Instrumentation and Spectroscopic Measurement Procedures 211

6.4.2 Results and Discussion 212

6.5 Traceability of Coccolith IR Absorption Signatures in Sediments with and without Authigenic Carbonates 216

6.5.1 Molecular Characteristics of Coccoliths and Relationship to IR Absorption Features 216

6.5.2 Disruption to ν_3 Carbonate Signatures of Sediments Laden with Coccolith Calcite due to Authigenic Carbonate Formation 219

6.5.3 Consideration of ν_2 Carbonate Signatures of Coccolith Laden Sediments and the Impact of Authigenic Carbonate Formation 222

6.6 Concluding Remarks from IR-ATR Spectral Analyses of Sediment Collections and Nodule Samples 223

6.7 Outlook 228

6.8 References 231

CHAPTER 7: TOWARDS A 2ND GENERATION OF SUBMERSIBLE MIR CHEMICAL SENSORS 235

7.1 Spectrometers in the Deep-Sea 235

7.1.1 Submersible FT-IR Spectrometers 237
7.1.1.1 Concept of 'Sphere-IR': A 2nd Generation Deep-Sea FT-IR Spectrometer 237
7.1.1.2 Advantages and Disadvantages of 'Sphere-IR' Concept 240

7.2 Sensor Head Design Considerations 240

7.3 Characterizing 'Active' Sensing Regions along Trapezoidal ATR Waveguide Surfaces 241

7.3.1 Experimental 242
7.3.1.1 Instrumentation 242
7.3.1.2 Materials 243
7.3.1.3 Ray Tracing Simulation Environment 243

7.3.2 Measurement and Simulation Procedures 244
7.3.2.1 Experimental Data Acquisition 244
7.3.2.2 Simulated Data Acquisition 245
7.3.2.3 Experimental Data Analysis 246
7.3.2.4 Spectral Ray Tracing Data Analysis 249

7.3.3 Results and Discussion 251
7.3.3.1 Experimental Results 251
7.3.3.2 Ray Tracing Results 258
7.3.3.3 Error Considerations 265

7.4 Conclusions 266

7.5 Outlook 267

7.6 References 268

CHAPTER 8: CONCLUSIONS AND OUTLOOK 272

8.1 IR Spectroscopic Monitoring of Gas Hydrates 272

8.2 Characterizing Deep-Sea Carbonates with IR Spectroscopy 273

8.3 Outlook for Improving the Application of IR Spectroscopy for Hydrate Monitoring and Carbonate Analysis 275

8.4 Can IR Spectroscopy Currently Contribute to Deep-Sea Research and the Scientific Goals of the GOMGHRC? 275

APPENDIX A: 278

A-1 Carbon Isotope Analysis of Sediment and Nodule Samples 278

A-1.1 Sample Preparation and Sample Analysis 278

A-1.2 Results 279

A-2 IR-ATR Spectral Database for Anhydrous Normal Carbonate Minerals 280

A-3 Sediment Collections from GOMGHRC Cruise to MC118 during June 2006 286

A-4 IR-ATR Analysis of Calcite-Dolomite Standard and Blind Samples 287

A-5 IR-ATR Analysis of Calcite-Dolomite Composition Relative to the Total Carbonate Mass in Marine Sediment Samples from the GoM 290

A-6 Spectral Ray Tracing Simulation Settings for SPRAY Software 294

LIST OF TABLES

Table 4-1: Cage characteristics for the three known clathrate hydrate structures of natural gases. Table adapted from Sloan.[2] 57

Table 5-1: Dana classification of carbonate minerals addressed with IR-ATR spectroscopy in this thesis. 125

Table 5-2: Source locations and qualitative contamination assessments for carbonate specimens examined for IR-ATR spectral database. The qualitative purity assessment follows from highest to lowest as: No Identifiable Contamination > Very Minor Contamination > Slight Contamination. 140

Table 5-3: Absorption frequencies in wavenumbers (cm^{-1}) for the ν_1 carbonate feature for aragonite group minerals. 142

Table 5-4: Absorption frequencies in wavenumbers (cm^{-1}) for the major ν_2 carbonate feature for all examined carbonate minerals. (* no reported value, or mineral not evaluated in the respective study). 142

Table 5-5: Absorption frequencies in wavenumbers (cm^{-1}) for the minor ν_2 carbonate feature for all examined carbonate minerals. (* no reported value, or mineral not evaluated in the respective study). 142

Table 5-6: Absorption frequencies in wavenumbers for the ν_4 carbonate features for all examined carbonate minerals. (* no reported value, or mineral not evaluated in the respective study). 143

Table 5-7: Predicted fundamental ν_4 band positions for various ranges of Mg^{2+} mole fractions as generated from data obtained from IR-ATR spectra of calcite, dolomite, and magnesite in the ATR spectral database. (* the predicted peak location for $X_{Mg} = 0.00$ of 711.93 is less than the experimental value for calcite, expected $X_{Mg} = 0.00$, at 712.4). 144

Table 5-8: USBL coordinate locations and field notes for box core samples (BC#) collected from MC118 in June 2006. All coordinates are referenced to Zone 16 in Universal Transverse Mercator (UTM) meters of the North American Datum of 1927 (NAD27) based on the Clarke ellipsoid of 1866. 149

Table 5-9: Composition information for calcite-dolomite calibration standards and blind samples. Mass % values represent both the absolute and relative mass compositions for each species with respect to the total sample and total carbonate content. (D = dolomite and C = calcite). 164

Table 5-10: Data table for IR-ATR analysis of standard samples. Prop. PAs were calculated from the average of triplicate analyses. The standard deviation (SD) of Prop. PAs are provided in addition to the % Error calculated using the linear calibration fit equation with the SD. The SD and % Error are the same for both Prop. PA calculation methods. Linear calibration fit parameters are provided. In addition, an approximation of the dynamic range for each Prop. PA calculation strategy is presented. The reported dynamic range is only valid for samples where the sum of the mass from (calcite+dolomite) = 100% of the sample mass. The % calcite and dolomite in each sample standard were calculated from mass values. (D = dolomite PA and C = calcite PA). 167

Table 5-11: Data table for IR-ATR analysis of blind samples. The average PA for calcite and dolomite, Prop. PA ratio calculated as either D/(C+D) or C/(C+D), and calculated mass % for calcite and dolomite are included. An excellent agreement is obtained by the comparison of sample mass % (determined from mass composition) with the mass % determination by IR analysis. The largest error in % determination was less than 1.4% of the respective mass composition. (BS2* was prepared from secondary calcite and dolomite stocks). 169

Table 5-12: Analytical results from evaluating ν_4 carbonate absorption features to determine the relative mass % of calcite and dolomite in the total carbonate content for sediments from push-core A of BC7 sediments. The negative values result from matrix interference indicating that calcite is the only carbonate species contributing to the IR-ATR spectrum (i.e., C = 100% of the carbonate composition). Similar values were obtained for BC2, BC4, BC6, BC8, and BC11 sediment samples. Visual inspections confirmed that calcite was the only carbonate species detected within IR-ATR spectra. 174

Table 6-1: Coccolithophore species accounting for ≥ 50% of the population in at least one sample as reported by Pariente.[7] Percent values in parenthesis reflect the maximum observed relative abundance from all samples with respect to each individual species. Despite the single sample reference, these four species were prevalent throughout most sampling locations. Table adapted from Pariente.[7] 196

Table 6-2: The overall relative % observation of coccolith taxa contributing > 0.5% from all surficial sediment samples collected throughout the Gulf of Mexico as reported by Pierce and Hart. Table adapted from Pierce and Hart.[1] (* Updated taxonomic classificatiion as *Calcidiscus leptoporus*).[2, 3] 197

Table 7-1: Spectral regions used for evaluation of IR-ATR absorbance spectra of PSCB residues. 247

Table 7-2: Experimental characterization of through-coupled radiation with and w/out the HATR accessory present in the instrument sample compartment. (* R_2 values are the ADC counts contributed to the overall signal throughput for the respective diaphragm settings. ** P is the percentage of total radiation throughput with respect to values of R_2. *** D is the calculated average radiation density as ADC counts per cm^2 for the area exposed between successive diaphragm settings). 255

Table 7-3. Ellipse minor axis diameters used for calculating the projected 'active' sensing regions depicted in **Figure 7-10**. (* CA represents cone angle. ** LSR represents the light source radius in cm). 264

Table A-1.1: Carbon isotope data for carbonate analysis of selected sediment and nodule samples from gas hydrate ecosystems in the GoM. Additional considerations to this data are provided in **Chapter 5** and **Chapter 6**. 279

Table A-3.1: List of sediments collected from the MC118 gas hydrate site during a GOMGHRC cruise in June 2006. 286

Table A-4.1: IR-ATR analytical results from the evaluation of carbonate standards with 90% dolomite and 10% calcite. 287

Table A-4.2: IR-ATR analytical results from the evaluation of carbonate standards with 70% dolomite and 30% calcite. 287

Table A-4.3: IR-ATR analytical results from the evaluation of carbonate standards with 50% dolomite and 50% calcite. 287

Table A-4.4: IR-ATR analytical results from the evaluation of carbonate standards with 30% dolomite and 70% calcite. 288

Table A-4.5: IR-ATR analytical results from the evaluation of carbonate standards with 10% dolomite and 90% calcite. 288

Table A-4.6: IR-ATR analytical results from the evaluation of blind carbonate samples. 289

Table A-5.1: IR-ATR analysis of calcite and dolomite in BC1 sediments. 290

Table A-5.2: IR-ATR analysis of calcite and dolomite in BC2 sediments. 290

Table A-5.3: IR-ATR analysis of calcite and dolomite in BC4 sediments. 290

Table A-5.4: IR-ATR analysis of calcite and dolomite in BC5 sediments. 291

Table A-5.5: IR-ATR analysis of calcite and dolomite in BC6 sediments. 291

Table A-5.6: IR-ATR analysis of calcite and dolomite in BC7 sediments. 291

Table A-5.7: IR-ATR analysis of calcite and dolomite in BC8 sediments. 291

Table A-5.8: IR-ATR analysis of calcite and dolomite in BC9 sediments. 291

Table A-5.9: IR-ATR analysis of calcite and dolomite in BC11 sediments. 292

Table A-5.10: IR-ATR analysis of calcite and dolomite in BC12 sediments. 292

Table A-5.11: IR-ATR analysis of calcite and dolomite in MC118 gravity core 21 sediments. 292

Table A-5.12: IR-ATR analysis of calcite and dolomite in MC118 gravity core 26 sediments. 292

Table A-5.13: IR-ATR analysis of calcite and dolomite in MC118 gravity core 38 sediments. 292

Table A-5.14: IR-ATR analysis of calcite and dolomite in MD02-2570 piston core sediments. 293

Table A-6.1: SPRAY values for dielectric function models for optical materials. 294

Table A-6.2: SPRAY values for dielectric properties of simulated absorbers. 294

Table A-6.3: SPRAY values for simulated object interfaces. 294

Table A-6.4: SPRAY parameters for simulated objects. 294

LIST OF FIGURES

Figure 1-1: Distribution of gas hydrates (thermogenic and biogenic) and high flux gas seeps without gas hydrate in the northern slope region of the Gulf of Mexico. (Map courtesy of Dr. Roger Sassen, Geochemical & Environmental Research Group (GERG), Texas A&M University). 4

Figure 1-2: Schematic overview of the anticipated GOMGHRC seafloor observatory comprising various geophysical, microbial, and biogeochemical sensor arrays for long-term monitoring of the Mississippi Canyon 118 hydrate site. (Figure courtesy of the GOMGHRC, by Paul Mitchell, Technical Design Specialist for CMRET and the Mississippi Mineral Resources Institute (MMRI)). 6

Figure 1-3: Survey of the hydrate system located in the south central area of MC118. This location is characterized by diverse topographical features with active hydrocarbon vent areas highlighted with red circles (smaller diameter). sII hydrate outcrops have been found at the NW vent (i) with recent findings of massive hydrate mounds around the SW vent (ii).13 (Swath batyhmetry shaded relief map provided courtesy of the GOMGHRC, and produced by Alessandro Bosman (University of Rome, La Sapienza) and Leonardo Macelloni (CMRET) from acoustic data collected by C&C Technologies (Lafayette, LA) with the Hugin 3000 AUV). 9

Figure 1-4: A massive, sediment draped gas hydrate outcrop around the SW vent (ii). 10

Figure 1-5: Large authigenic carbonate ledges and mounds resulting from chemosynthetic activity at the hydrate site with crabs scavenging the area for food. 10

Figure 1-6: Hydrocarbon gas bubbles emerging from the seafloor characterized by hydrate, carbonate, and mollusk shell accumulations. 11

Figure 1-7: Fracture filling gas hydrate stained orange with biodegraded crude oil in an authigenic carbonate mound. Hydrate grows in the crevices of large authigenic carbonate mounds are the result of copious gas venting. Abundant aragonite shell litter is scattered and cemented into the large carbonate mass. 11

Figure 2-1: The evanescent field arising from light propagating through an optically dense waveguide via total internal reflection. 20

Figure 3-1: Construction drawings for the initial status of the main body for the pressure chamber. (Drawings adapted from N.A. Pennington).[2] 33

Figure 3-2: Construction drawings for modifications to the pressure chamber main body: (1) fiber-optic coupling ports, (2) liquid drain, and (3) internal cooling coil ports. 34

Figure 3-3: Conceptual drawings of the high pressure optical viewport with sapphire window. (a.) Cross-sectional view with labeled components, and (b.) CAD 3-D rendering of the viewport. 35

Figure 3-4: Construction drawings for the custom-designed high pressure optical viewport components. 36

Figure 3-5: (a.) Construction drawings for the detachable viewport face plate, and (b.) optical image displaying the viewport and detachable face plate assembly attached to the main body of the pressure chamber. A cell thermostating copper coil is additionally indicated for later reference. 37

Figure 3-6: (a.) Mirrored and dimensionless representation of the custom PTFE fiber-optic coupling ferrules, and (b.) the dimensioned tool path utilized for CNC fabrication. 38

Figure 3-7: (a.) Labeled optical image of the PTFE ferrule and Swagelok fiber-optic coupling system with a 700 μm dia. test section of solid-core AgX fiber. (b. and c.) Additional images displaying assembly of the high pressure fiber feedthrough. 39

Figure 3-8: Optical image displaying labeled components of the hydrate imaging system. 40

Figure 3-9: Optical image of the internal cooling coil inside the sample chamber as visualized through the optical viewport and captured by the hydrate imaging system. 41

Figure 3-10: Optical images referencing each type of access port on the main body of the pressure chamber for (a.) the rear and sides of the chamber and (b.) the underside of the main body. Zip ties were used to secure silicone rubber tubing onto the inlet and outlet extensions of the internal cooling coil. 44

Figure 3-11: Optical image depicting the setup utilized for all IR fiber-optic spectroscopic measurements for monitoring gas hydrate growth and dissociation. The AgX fiber probes a cross-section of the pressure chamber via evanescent field absorption spectroscopy. The dashed (yellow) line indicates the radiation path. 48

Figure 3-12: Most current configuration of the experimental gas hydrate setup. Two PCs were used during hydrate measurement trials. One PC was utilized for controlling the FT-IR spectrometer and collecting IR spectra. A second PC was used for controlling and collecting data from the imaging and pressure and temperature logging systems. 49

Figure 3-13: Scaled CAD 3-D rendering of a 72 × 10 × 6 mm ZnSe waveguide showing radiation focused onto the in-coupling facet and transmitted by total internal reflection until exiting the waveguide. ‘Active’ sensing regions are generated at each area of internal reflection where sample molecules interact with the evanescent field at the waveguide surface. **Chapter 7** provides a combined experimental and simulation approach for characterizing sensing regions along planar waveguide surfaces. (Figure adapted from Dobbs and Mizaikoff).[9] 51

Figure 3-14: (a.) Optical image of HATR accessories placed inside the sample compartments of a Bruker Equinox 55 FT-IR spectrometer with trough-top plate assembly mounted onto the optics base unit and sample deposited onto a ZnSe crystal. (b.) Optical image displaying HATR components inside a Bruker IFS 66/S FT-IR spectrometer. (c.) Schematic diagram depicting sample placement onto a HATR waveguide with the radiation path traced through the optics base unit and HATR crystal. 52

Figure 4-1: Liquid water (Lw)-hydrate (H)-vapor (V) phase boundaries for simple methane, ethane, and propane hydrates in deionized water as reviewed by Sloan.[2] In this work, gas hydrates were grown between ~0 °C and ~4 °C. Dashed lines represent ceiling operational pressures for hydrate trials with respect to each guest gas. 59

Figure 4-2: The cluster nucleation hypothesis proposed by Christiansen and Sloan.[28] Upon entering hydrate conditions with no gas in solution (1), gas is readily solvated by liquid water coupled with the formation of higher-order liquid water structures including labile hydrate cages (2), labile clusters agglomerate through sharing of hydrate-like faces and increase solution entropy (3), agglomeration continues until a critical cluster size initiates primary nucleation followed by rapid hydrate growth (4). Figure adapted from Christiansen and Sloan.[2, 28] 61

Figure 4-3: The reaction kinetic (RK) model for gas hydrates grown from liquid water as proposed by Lekvam and Ruoff with graphical representations following the cluster nucleation hypothesis.[2, 26-28] ($k_1 \leftrightarrow k_{-1}$) dissolution of gas by water in hydrate conditions with formation of oligomeric precursors (N), ($k_2 \leftrightarrow k_{-2}$) uncatalyzed formation of hydrate from N precursors, ($\rightarrow k_{-3}$) primary nucleation of gas hydrate, which results in autocatalysis of the growth mechanisms indicated with ($k_4 \leftrightarrow k_{-4}$) and ($k_5 \leftrightarrow k_{-5}$). 62

Figure 4-4: The IR spectrum of liquid water as collected with a silver halide fiber-optic waveguide in this work. Conventional vibrational mode assignments are provided, indicating the four major absorption features of water. Minor atmospheric CO_2 (~2350 cm^{-1}) and PTFE features (from fiber feedthroughs at ~1150 cm^{-1})are observed as negative absorption bands relative to a reference spectrum of air at room temperature. The detector cut-off occurs at ~680 cm^{-1}. This spectrum is an average of 250 sample scans collected at 0.5 cm^{-1} resolution. (Lib. = Libration). 65

Figure 4-5: Representative IR transmittance profile from a reference spectrum (average of 250 sample scans at 0.5 cm^{-1} resolution) for a PTFE mounted AgX fiber. All reference spectra for hydrate monitoring trials were collected with an empty chamber at room temperature and atmospheric pressure. 68

Figure 4-6: Pressure and temperature traces from an ethane hydrate trial (with SDS) indicating a rapid drop in pressure and increase in temperature at hydrate nucleation. Pressure fluctuations reflect intermittent introduction of ethane into the sample chamber. Temperature spikes likely result from localized hydrate growth in close proximity to the submersed temperature probe as opposed to bulk solution temperature changes. 69

Figure 4-7: Image captures displaying the sample chamber contents from (a.) pre-hydrate nucleation, (b.) catastrophic hydrate nucleation with spindling growths, and (c. – f.) primary growth of ethane hydrate over a period of 2 mins. In images (a. – c.), the liquid water level is above the viewport, appears at the mid-line in capture (d.), and drops below the viewing region in capture (e.). 70

Figure 4-8: White surfactant foam formed inside the hydrate chamber from outgassing ethane during hydrate dissociation. Arrows accentuate growing ethane bubbles in sequential images collected at 2 min intervals. 70

Figure 4-9: Image series displaying visual cues inside the pressure chamber throughout an ice trial with SDS solution. Chamber contents with liquid water (a.) prior to nucleation. The initial minutes of ice growth following nucleation (b.) with continued growth (c.) until completion (d.) while maintaining a clear viewing of the internal cooling coil. Melting of ice (e. – h.) with few bubble formations until finally returning to initial conditions (i.) with no surfactant foaming. 71

Figure 4-10: Image series depicting the sample chamber contents throughout a methane hydrate trial with SDS. Viewing of liquid water (a.) followed by hydrate nucleation (b.) and growth (c. – e). Final viewing of methane hydrate (f.) prior to initial stages of pressure induced dissociation (g.). Continuing dissociation (h.) with formation of surfactant foam until returning to initial conditions with methane bubbles attached to the sapphire viewport. 72

Figure 4-11: Optical images of an extracted portion of ethane hydrate from the pressure cell. 73

Figure 4-12: IR transmission-absorption results from the interrogation of outgassing constituents from extracted gas hydrate structures for (a. and b.) methane hydrate, (c. and d.) ethane hydrate, and (e. and f.) propane hydrate. All graphs on the left side represent selected transmission-absorption spectra from each experiment. All graphs on the right side illustrate absorption intensity for the expulsion of guest gases versus time for each measurement series (≥ 36 mins) as the peak area respective to C-H stretching features for each hydrocarbon species. Peak integration criteria are provided in the respective graphs (b.), (d.), and (f.). 74

Figure 4-13: Series of image captures at 1 s time intervals demonstrating the combustion of propane expulsion from gas hydrate. In capture (a.), a white foam of propane filled surfactant bubbles is observed; obstructing the view of hydrate mass contained within the 250 mL glass jar. 75

Figure 4-14: Fiber-optic IR-ATR spectra for (a.) liquid water and methane hydrate with labeled absorption features for water and indication to spectral changes during the formation of gas hydrate and (b.) methane (sI), ethane (sI), and propane (sII) hydrates illustrating the similarity in spectral shifts observed for each clathrate hydrate structure. 76

Figure 4-15: (a.) Peak integration results from spectroscopic monitoring of propane gas hydrate formation and dissociation in DI water by evaluating the population dynamics of the highly H-bonded O-H stretch feature. (b.) Fiber-optic IR-ATR spectra displaying comparable shifts in H-bonded populations during propane hydrate growth in a trial with surfactant solution (380 ppm SDS). (IR spectra were collected at 360 s intervals (a.) with an average of 250 sample scans at 0.5 cm^{-1} resolution (a. and b.). 81

Figure 4-16: (a.) Peak integration analysis from spectroscopic monitoring of ethane hydrate formation and dissociation in 380 ppm SDS solution. (b.) IR-ATR spectra from a separate ethane hydrate trial (grown from a 380 ppm SDS solution) depicting spectral changes in the H-O-H bend throughout the liquid-to-hydrate phase transition. ((a.) IR spectra were an average of 1000 sample scans at 0.5 cm^{-1} resolution collected in 15 min intervals, and (b.) IR spectra are an average of 250 sample scans at 0.5 cm^{-1} resolution). 84

Figure 4-17: Spectroscopic results from a methane hydrate trial with SDS solution (380 ppm) for (a.) evaluation of the libration peak maximum and (b.) peak area of the libration region from 925 – 700 cm^{-1}. Representative fiber-optic IR-ATR spectra from an ethane hydrate trial (380 ppm SDS) display the shifting absorption behavior of the libration mode throughout formation of gas hydrate. ((a.) and (b.) were from analyses of IR spectra collected at 15 min intervals with an average of 1000 sample scans and 0.5 cm^{-1} resolution; (c.) IR spectra are an average of 250 sample scans at 0.5 cm^{-1} resolution). 87

Figure 4-18: (a.) Analysis of the peak maximum for the 3rd libration overtone from IR spectra during the formation and dissociation of propane hydrate in SDS solution (380 ppm). Fiber-optic IR-ATR spectra from a methane hydrate trial (DI water) exhibit shifts in the overtone absorption feature throughout formation of gas hydrate. ((a.) is from the analysis of IR spectra collected at 6 min intervals with an average of 250 sample scans at 0.5 cm^{-1} resolution; IR spectra in (b.) were collected with an average of 250 sample scans at 0.5 cm^{-1} resolution). 89

Figure 4-19: (a.) System temperature log recorded during a propane hydrate trial without SDS. (b.) Shifting peak maximum for the 3rd libration overtone in response to the corresponding temperature trace in (a.). (c.) Temperature dependent response of the 3rd libration overtone peak maximum for two propane hydrate trials; with 380 ppm SDS solution and DI water only (w/out SDS). Error bars are ± 1 standard deviation. (All spectral data were an average of 250 sample scans at 0.5 cm^{-1} resolution collected at 6 min intervals). 91

Figure 4-20: Analysis of fiber-optic evanescent field spectra with respect to each of the four absorption features of water for a propane hydrate trial grown from DI water. The data gap is the result of instrument down-time for servicing of the air dryer (see **Section 4.3.1.2**). 92

Figure 4-21: Plot of calculated %Hydrate within V_l during a methane hydrate trial (no SDS) following spectroscopic analysis of $3\nu_L$. This hydrate trial was carried out pressures comparable to oceanic environments in the GoM with documented hydrate occurrences.[1] IR-ATR spectra were an average of 250 sample scans with 0.5 cm^{-1} resolution collected at 6 min intervals. (Lines are present to assist visualization). 99

Figure 4-22: (a.) IR-ATR spectrum of hydrated sediments from the BC12 location at MC118, (b.) IR-ATR spectrum of dried sediments from the BC7 location at MC118, and (c.) selected IR-ATR spectra of hydrated sediments from different sampling locations at MC118. (All spectra were the average of 100 sample scans collected at 1 cm^{-1} resolution). 102

Figure 4-23: Spectroscopic analysis of the 3rd libration overtone for a propane hydrate trial (discussed in **Section 4.3.2**) with (a.) spectra collected at 6 min intervals and (b.) the same trial with reduction of data points by a factor of 100 (1 point per 600 min time interval). 105

Figure 4-24: Temporal analysis of the $3\nu_L$ peak position with respect to measurement-to-measurement changes in the peak maximum during a propane hydrate series with (a.) 6 min intervals between measurements and (b.) the same data reduced to one measurement point for 600 min intervals. (Lines are present to assist visualization). 106

Figure 4-25: Predicted measurement-to-measurement changes in the %Hydrate within V_l during a propane hydrate series with (a.) 6 min intervals between measurements and (b.) the same data reduced to one measurement point for a 600 min. Plot generated from the transformation of the 3rd libration overtone peak position data displayed in **Figure 4-24**. (Lines are present to assist visualization). 107

Figure 4-26: Proposed Reaction Kinetic-Thermodynamic Model expanded from the cluster nucleation hypothesis of Christiansen and Sloan and the RK model of Lekvam and Ruoff.[2, 26-28] 109

Figure 5-1: IR-ATR spectrum of witherite ($BaCO_3$) mined from Illinois, USA with carbonate vibrational mode assignments. The spectrum is an average of 100 sample scans collected at a spectral resolution of 1 cm^{-1}. This representative spectrum was collected for the IR-ATR spectral database described in **Section 5.2**. (Abbreviations are assym = asymmetric, sym. = symmetric, and oop = out-of-plane). 134

Figure 5-2: GPS trace of the June 2006 GOMGHRC cruise to MC118 aboard the R/V Pelican. The inset provides an accentuated view of grid profiles from the collection of geophysical lines for mapping acoustic reflections throughout the sediments. 145

Figure 5-3: Box core unit equipped with USBL navigational component (blue frame with black cylinder) utilized to collect seafloor sediments during the June 2006 GOMGHRC cruise to MC118 on the R/V Pelican. 146

Figure 5-4: Screen capture of navigational feedback for the ship and box core unit locations following a successful sampling event. The sample location is indicated by the bull's-eye with triangular center. The rings surrounding the bull's-eye are 100, 200, and 300 m in diameter. Screen shots were recorded for each target location containing the date, time, and coordinates for each sample location. 147

Figure 5-5: Representative image of a push-cored sub-sample with a 5.1 cm id. clear PVC pipe capped with rubber stoppers. Four distinct color changes within the sediments can be visualized in the pipe section next to the graduated ruler. The light brown layer in this image corresponds to the top sediment layer at the sediment-seawater interface. 148

Figure 5-6: IR-ATR spectrum of hydrated BC12 sediments. General absorption characteristics are labeled for point of reference. This spectrum contains substantial absorption features from water, carbonates, quartz, and clays. Additional minor C-H stretch features above 2800 cm^{-1} resulting from the presence of crude oil are also observed. Sample: BC12B Bot. 152

Figure 5-7: IR-ATR spectra from four box core locations at MC118. Variations in the spectral profiles for water, crude oil, and carbonates are readily apparent. Samples: BC7A Bot, BC9A Bot, BC5B Bot, and BC12A Bot. 153

Figure 5-8: Pockets of highly concentrated biodegraded crude oil (brown stains circled in red) in push-cored BC9 sediments from MC118 collected in June 2006. Although the crude appears to be a low mass percentage of the overall sediment composition, enough oil is present to generate absorption features in IR-ATR spectra when within evanescent field sensing regions. For scale, the diameter of this push-core tube is approx. 7.6 cm. 154

Figure 5-9: Accentuated view of ν_3 carbonate profiles in the IR-ATR spectra of native box core sediments collected from MC118. The spectral signature from each sample exhibits unique absorption characteristics. Samples: BC7A Bot, BC9A Bot, BC5B Bot, and BC12A Bot. 155

Figure 5-10: Representative IR-ATR spectrum of dried BC7 sediments collected from MC118. General absorption characteristics are labeled for reference. This spectrum displays improved spectral access to sediment components following the reduction of water interferences by drying. Sample: BC7A Bot. 156

Figure 5-11: Labeled view of the fingerprint region for an IR-ATR spectrum of dried BC7 sediments. Quartz and clay exhibit similar absorption features resulting from Si-O moieties. Improved spectral access to fundamental carbonate absorption bands is clearly observed. Sample: BC7A Bot. 157

Figure 5-12: Selected views of ν_4 carbonate absorption features for IR-ATR spectra obtained from (a.) BC1C Bot, (b.) BC7A Bot, (c.) BC9A Bot, (d.) BC12A Bot, (e.) MC118 Core 26, and (f.) 27+m sediments from core MD02-2570. The ν_4 absorption characteristic to calcite was observed in all samples. Dolomite is clearly present in BC1C Bot, BC12A Bot, and Core 26 sediments from MC118, as well as in 27+m sediments from MD02-2570. Mg-calcite was only observed in BC12 sediments, as indicated in (d.). 159

Figure 5-13: IR-ATR spectra highlighting the ν_4 carbonate region for calibration standards used to establish the correlation of peak areas to the mass % of each component. Spectra were uniformly shifted to a zero baseline at 740 cm^{-1}. As expected, the intensity of calcite and dolomite absorption features varied according to the relative mass fraction present in each sample. (D = dolomite and C = calcite). 165

Figure 5-14: Calibration functions for determining the mass % of calcite and dolomite contributions to the total carbonate content using Prop. PA ratios for ν_4 absorptions (a.) D/(C+D) and (b.) C/(C+D). Error bars represent the mass % error calculated from three times the SD of triplicate measurements. In addition, the mass % determinations of calcite and dolomite from IR analysis for four blind samples (BS#) are plotted along with actual mass % values calculated from the recorded mass composition. (BS2* was prepared from secondary calcite and dolomite stocks). 168

Figure 5-15: Condensed summary of IR-ATR spectral analyses of MC118 sediments collected in June 2006 (BC#) and October 2005 (C#). Each sampling location and significant findings are provided. Variability with respect to hydrocarbon detection and carbonate mineral diversity around the MC118 system is readily visualized and accentuated around the SW hydrate mound and the NW ridgeline. Dolomite mass % (red text with % D) are averages relative to the total carbonate mass, not sample mass. δ13C values (V-PDB scale as brown text with ‰) are also provided as discussed in **Appendix A-1** and **Chapter 6**. (Swath batyhmetry color-shaded relief map provided courtesy of the GOMGHRC, and produced by Alessandro Bosman (University of Rome, La Sapienza) and Leonardo Macelloni (CMRET) from acoustic data collected by C&C Technologies (Lafayette, LA) with the Hugin 3000 AUV). 171

Figure 5-16: Selected viewings of an IR-ATR spectrum for BC7A Bot sediments. (a.) IR-ATR spectrum displaying calcite-only carbonate absorption features and tailing of the clay absorption feature centered at ~750 cm^{-1} readily apparent. (b.) Accentuated view of the dolomite integration region imposed on the same IR-ATR spectrum from (a.). The red (solid) line illustrates a small gap below the baseline imposed during peak integration analysis resulting in the calculation of negative mass % values for dolomite in the total carbonate composition in sediment samples. Thus, C = 100% and D = 0% when this occurs during sediment analysis with the prescribed evaluation strategy. 172

Figure 5-17: Representative IR-ATR spectra for sediments from gravity cores 21, 26, and 38. Strong dolomite signatures are observed near 730 cm^{-1} in core 21 and core 26 sediments. While not clearly evident, a minor hump may indicate the presence of dolomite in core 38. 177

Figure 5-18: Semi-quantitative assessments from IR-ATR spectra for the mass % of dolomite and calcite in the total carbonate fraction of piston core sediments collected from MD02-2570. For each sediment depth, the calcite and dolomite mass % are plotted with the sum equal to 100% of the carbonate fraction. Error bars for 6, 18, and 21 mbsf samples are twice the SD from triplicate evaluation. Lines are present to assist visualization. 179

Figure 6-1: SEM images of coccoliths from MC118 gravity core 38 sediments. A small sediment portion was smeared onto a glass microscope slide and allowed to dry before collection of images with a Nova Nanolab 200 (FEI Company, Hillsboro, OR). Coccolith shield morphologies are characteristic of the coccolithophore species *Emiliania huxleyi* (*E. huxleyi*).[1-4] 194

Figure 6-2: Authigenic carbonate nodules collected from (a.) BC3* and (b.) BC5 MC118 samples. (* nodules provided courtesy of Dr. Roger Sassen, GERG, Texas A&M University). 200

Figure 6-3: An IR-ATR spectrum for an authigenic carbonate nodule recovered from BC5 sediments. Notice very strong carbonate absorption features in addition to minor spectral abosrptions from clay and quartz minerals. Of particular importance is the broad ν_3 carbonate absorption profile around 1500 cm^{-1}. 202

Figure 6-4: IR-ATR spectra of 7 nodule samples from MC118 demonstrating the diversity of carbonate mineral compositions observed for (a.) High Aragonite nodule samples, (b.) Medium Dolomite nodule samples, and (c.) a High Mg-calcite nodule sample. Spectra were uniformly shifted to and absorbance of 0.0 at 740 cm^{-1} to aid visualization. (* Sample provided courtesy of Dr. Roger Sassen, GERG, Texas A & M University). 203

Figure 6-5: Observed ν_3 carbonate absorption features from IR-ATR spectra of (a.) authigenic carbonate nodules from three general composition classifications (average $\delta^{13}C$ of -28.98‰ for 4 examined nodule specimens), (b.) sediments in close proximity to recovered nodules from BC5B Bot sample ($\delta^{13}C$ of -18.7‰), and (c.) sediments from BC11A Bot sample displaying sharp, well-defined absorption characteristics with no significant context clues indicative to authigenic carbonate formation at this sample collection (average $\delta^{13}C$ of 0.50‰ for BC7 and BC11 sediments). 204

Figure 6-6: SEM images exhibiting coccoliths with taxonomic identification of 4 primary taxa found in GoM sediments. Images (a.), (c.), and (d.) were collected from BC7 sediments, and image (b.) was collected during surface evaluation of an authigenic carbonate nodule collected from BC3. In images (b.) and (c.), well-preserved *E. huxleyi* coccoliths are also indicated without an identification tag. More coccoliths and coccolith fragments can be observed in each image. 207

Figure 6-7: SEM images with highlighted whole coccoliths and coccolith fragments from BC7 sediments; *E. huxleyi* (green), *G. oceanica* (blue), and an unidentified taxa (yellow). 208

Figure 6-8: Optical microscope image at x100 magnification (a.) and SEM image (b.) of coccoliths produced by *Pleurochrysis carterae*. The coccoliths are ellipsoidal shaped rings approx. 2 μm in length along the major axis. 210

Figure 6-9: IR-ATR spectra for each sample of coccolith condensates from cultured coccolithophores of *P. carterae*. 212

Figure 6-10: IR-ATR spectra displaying accentuated views of the ν_3 carbonate region for (a.) coccoliths from culture (CfC) for evaluated condensate samples and (b.) overlays of CfC and coccolith rich BC7A Bot sediments collected from MC118. Each carbonate profile exhibits an intense, narrow absorption feature centered at 1413 cm^{-1}. 213

Figure 6-11. OM image (x2.5) contrasting a bare portion of ZnSe crystal with a high surface density of coccolith/coccolithophore residue after IR-ATR measurements. 214

Figure 6-12: OM images of dried coccolith accumulations on ZnSe crystals following spectroscopic evaluation of (a.) CfC trial 1 at x50 magnification in dark-field lighting and (b.) CfC trial 2 at x50 magnification. Copious coccoliths are observed on the ZnSe waveguide surface in both images. 215

Figure 6-13: IR-ATR spectra focused on the ν_3 carbonate absorption features for calcite for coccoliths from culture (CfC) and hand ground non-biogenic calcite (calcite). The calcite spectrum was obtained from the IR-ATR spectral database described in **Section 5.2**. 217

Figure 6-14: The ν_2 carbonate absorption region displaying the IR absorption of hand ground inorganic calcite (calcite), coccoliths from culture (CfC), BC7A Bot sediments without authigenic carbonate interference, and BC1C Bot sediments with authigenic carbonate interference. 222

Figure 7-1: Conceptual scaled CAD rendering of the modeled 'Sphere-IR' unit indicating the design, construction, and incorporation of electronics sub-system components and initial modeling of primary optical components for the optics sub-system compartment. 238

Figure 7-2: Schematic for the electronics sub-system designed by Dr. Frank Vogt. The IRcube spectrometer components are treated as a single entity in this diagram. (Drawing not to scale). 239

Figure 7-3: (a.) Representative IR-ATR absorbance spectrum of PSCB with highlighted spectral features utilized for peak area evaluation. Spectral regions are provided in **Table 7-1**. Peak area values obtained for PSCB absorption features for (b.) internal reflection and (c.) non-reflection regions along the ZnSe waveguide surface. 247

Figure 7-4: Representative absorbance spectra from a simulated HATR reflection and non-reflection region. 250

Figure 7-5: (a.) Optical image of PSCB deposits along the HATR crystal surface mounted in a topless flow cell. (b.) Absorption intensity (as PAs) of PSCB vs. distance from the in-coupling facet along the measurement surface.* (c.) Surface map projecting the absorbance intensity of PSCB residues along the measurement surface of a HATR crystal and displaying discrete 'active' sensing regions along the crystal surface.** (* Lines are for assisting visual inspection. ** Plot generated from PAs for PSCB absorbance in the spectral region from 2986 – 2817 cm^{-1}). 252

Figure 7-6: Calculated signal densities across each incremental area exposed with stepped iris aperture diaphragm settings and the ATR bench placed in the sample chamber. Signal densities are plotted ± the aperture radius in cm with 0 representing the aperture center positioned on the central axis of radiation propagation. The Gaussian fit provides a close functional resemblance to the data plot assuming an axial-symmetric radiation profile. 256

Figure 7-7: Averages of normalized PAs for experimental and simulation data*,** with respect to the measurement location plotted versus distance from the in-coupling facet of the HATR crystal (error bars are ± 1 standard deviation).*** (* Simulation $Values_{CCA}$ represent normalized and averaged PAs for data obtained with combinations of a 0.1278 cm ± 0.042 cm light source radii with a constant cone angle (CCA) of 2°. ** Simulation $Values_{CLSR}$ represent normalized and averaged PAs for data obtained with combinations of a constant light source radius (CLSR) of 0.1278 cm with cone angles of 2° ± 1°. *** Lines are present for assisting visual inspection). 259

Figure 7-8: Simulated radiation density maps for visualizing internal reflection regions and the influence of increasing radiation cone angles from left to right (2º, 4°, 8°, and 16°). Simulations were generated with a source radius of 0.1278 cm. 260

Figure 7-9: (a.) Normalized peak areas for simulated deposits plotted versus distance from the HATR in-coupling facet with increasing cone angles and a source radius of 0.1278 cm.* (b.) Normalized peak areas for simulated deposits plotted versus distance from the HATR in-coupling facet with increasing source radii and a cone angle of 2°.* (* Lines are for assisting visual inspection). 261

Figure 7-10: Elliptical surface projections of (i) the estimated range of dimensions for 'active' sensing regions shaded green, (ii) the most probable range of dimensions for 'active' sensing regions shaded in red, (iii) always 'active' sensing regions shaded in orange, and (iv) always 'inactive' measurement regions shaded blue. The ellipse minor axis diameters used for calculating these projections are provided in **Table 7-3** where the minor axis diameter is approx. 41% of the major axis diameter. 264

Figure A-2.1: IR-ATR spectrum of calcite, $CaCO_3$. 281

Figure A-2.2: IR-ATR spectrum of magnesite*, $MgCO_3$ (* very minor dolomite contamination). 281

Figure A-2.3: IR-ATR spectrum of siderite, $FeCO_3$. 282

Figure A-2.4: IR-ATR spectrum of rhodochrosite, $MnCO_3$. 282

Figure A-2.5: IR-ATR spectrum of smithsonite: $ZnCO_3$. 283

Figure A-2.6: IR-ATR spectrum of aragonite: $CaCO_3$. 283

Figure A-2.7: IR-ATR spectrum of witherite, $BaCO_3$. 284

Figure A-2.8: IR-ATR spectrum of strontianite*, $SrCO_3$ (* very minor dolomite contamination). 284

Figure A-2.9: IR-ATR spectrum of cerussite, $PbCO_3$. 285

Figure A-2.10: IR-ATR spectrum of dolomite, $CaMg(CO_3)_2$. 285

LIST OF ABBREVIATIONS

.DXF	Drawing Interchange Format
°C	Degrees Celsius
3-D	Three-Dimensional
A/V	Audio-Visual
ACC	Amorphous Calcium Carbonate
AgX	Silver Halide
Approx.	Approximately
ASL	Applied Sensors Laboratory
ATR	Attenuated Total Reflection
AUV	Autonomous Underwater Vehicle
BC	Box Core
Bot	Bottom
BS	Blind Sample
CAD	Computer-Aided Design
CCA	Constant Cone Angle
CfC	Coccoliths from Culture
cm	Centimeter(s)
cm^{-1}	Wavenumber(s)
CLRS	Constant Light Source Radius
CMBSF	Centimeters-Below-Seafloor
CMRET	Center for Marine Resources and Environmental Technology
CNC	Computer Numerical Control
CTD	Conductivity, Temperature, and Depth
d_e	Effective Evanescent Field Penetration Depth

DI	Deionized
dia.	Diameter
d_p	Evanescent Field Penetration Depth where E = 1/e
DTGS	Deuterated Triglycerine Sulfate
E	Energy of Evanescent Field
FNPT	Female National Pipe Thread
FT-IR	Fourier Transform-Infrared
g	Gram(s)
GERG	Geochemical & Environmental Research Group
GoM	Gulf of Mexico
GOMGHRC	Gulf of Mexico Gas Hydrate Research Consortium
GPS	Global Positioning System
GTCoSMS	Georgia Tech College of Science Machine Shop
H-Bonded	Hydrogen Bonded
HATR	Horizontal Attenuated Total Reflection
Hex	Hexagonal
HPLC	High Performance Liquid Chromatography
hr	Hour(s)
id.	Inner Diameter
IR	Infrared
IR-ATR	Infrared-Attenuated Total Reflection
KOH	Potassium Hydroxide
kPa	Kilopascal
l.	Length
L	Liter(s)
Lib.	Libration

LN_2	Liquid Nitrogen
μm	Micrometer(s)
m	Meter(s)
m/v	Mass-to-Volume
max.	Maximum
MBSF	Meters-Below-Seafloor
MC118	Mississippi Canyon Block 118
MCT	Mercury-Cadmium-Telluride
mg	Milligram(s)
Mg-calcite	Magnesian Calcite
Mid	Middle
min	Minute(s)
min.	Minimum
MIR	Mid-Infrared
mL	Milliliter(s)
mm	Millimeter(s)
MMRI	Mississippi Mineral Resources Institute
MMS	Minerals Management Service
MNPT	Male National Pipe Thread
MPa	Megapascal
NAD27	North American Datum of 1927
n_D	Refractive Index
No.	Number
od.	Outer Diameter
OM	Optical Microscope
PA	Peak Area

PC	Personal Computer
ppb	Parts per Billion
ppm	Parts per Million
Prop.	Proportional
PS	Particle Size
PSCB	Poly(styrene-co-butadiene)
psi	Pounds per Square Inch
psig	Pounds per Square Inch Gauge
PTFE	Polytetrafluoroethylene
PVC	Polyvinylchloride
R	Resistance
R/V	Research Vessel
RK	Reaction Kinetic
RK-T	Reaction Kinetic-Thermodynamic
ROV	Remote Operated Vehicle
RSD	Relative Standard Deviation
s	Second(s)
sI	structure-I
sII	structure-II
SD	Standard Deviation
SEM	Scanning Electron Microscope
sH	structure-H
SI	International System of Units
SS	Stainless Steel
STF	Swagelok Tube Fitting
STP	Standard Temperature and Pressure

th.	Thickness
TRE	Total Residual Error
USB	Universal Serial Bus
USBL	Ultra-short Baseline
UTM	Universal Transverse Mercator
UV	Ultraviolet
v/v	Volume-to-Volume
VOC	Volatile Organic Compound(s)
w.	Width
ZnSe	Zinc Selenide

SUMMARY

Substantial amounts of methane are sequestered in naturally occurring ice-like formations known as gas hydrates. In particular, oceanic gas hydrates are globally distributed in complex heterogeneous ecosystems that typically occur at depths exceeding 300 m. Gas hydrates have received attention for their potential as an alternative energy resource, as marine geohazards, and their role in cycling of greenhouse gases. In addition, chemosynthetic communities often play a vital role in the cycling and sequestration of carbon emanating from cold hydrocarbon seeps surrounding hydrate sites. Research efforts are presently striving to better understand the significance and complexity of these ecosystems through the establishment of seafloor observatories capable of long-term monitoring with integrated sensor networks. In this thesis, infrared (IR) spectroscopy has been implemented for the investigation of molecular-specific signatures to monitor gas hydrate growth dynamics and evaluate carbonate minerals, which are intimately connected with complex chemosynthetic processes occurring in these harsh environments.

The first fundamental principles and data evaluation strategies for monitoring and quantifying gas hydrate growth dynamics utilizing mid-infrared (MIR) fiber-optic evanescent field spectroscopy have been established by exploiting the state-responsive IR absorption behavior of water. This has been achieved by peak area evaluation of the O-H stretch, H-O-H bend, and libration modes and assessing peak shifts in the 3rd libration overtone and libration bands during the formation and dissociation of simple clathrate hydrates of methane, ethane, and propane formed from aqueous solution. Hydrate growth and monitoring was facilitated with a customized pressure cell enabling operation up to ~5.9 MPa with spectroscopic, temperature, pressure, and video monitoring capabilities.

Furthermore, the initial feasibility for extending the developed IR spectroscopic hydrate monitoring strategies into oceanic gas hydrate ecosystems has been demonstrated through the

evaluation of potential spectroscopic interferences from sediment matrices in samples collected from two hydrate sites in the Gulf of Mexico (GoM). With exception of the libration band, the primary IR absorption features of water are readily accessed within hydrated sediment samples. Additional consideration for potential long-term hydrate monitoring applications revealed that the collection of approx. 2 IR spectra per day should enable direct insight into the temporal dynamics of hydrates within hydrate-bearing sediments, which further supports the development and application of deep-sea MIR chemical sensors for advancing the capabilities of exploration, characterization, and long-term monitoring of oceanic gas hydrate ecosystems.

It has previously been well established that chemosynthetic communities play a significant role in carbon cycling and sequestration within oceanic gas hydrate ecosystems. Specifically, enhanced sulfate reduction from the activity of chemosynthetic organisms shift pore water alkalinity to favor authigenic carbonate formation, which traps enormous amounts of carbon dioxide generated by various microbes and archaea from the anaerobic oxidation of methane and other hydrocarbons emanating from deep fault conduits surrounding many gas hydrate sites.

Complementary to investigating the dynamics of gas hydrate formation, IR attenuated total reflection (IR-ATR) spectroscopy was utilized for evaluating and characterizing the diversity of carbonate minerals within sediment and authigenic carbonate nodule samples collected from the Mississippi Canyon region in the GoM. Calcite was detected in all sediment and nodule samples. Dolomite and Mg-calcite were only detected in sediments indicative to authigenic carbonate formation. Authigenic nodules exhibited diverse carbonate compositions, which were grouped into three general classifications: (1) High Aragonite, (2) Medium Dolomite, and (3) Hign Mg-calcite.

In addition, it was discovered that unique changes in the ν_3 carbonate IR signature from seafloor sediments facilitate the detection of authigenic carbonate formation within very fine particle fractions containing an abundance of sedimented coccolith calcite, which is formed by single-celled algae that thrive within the photic zone in many of Earth's oceans and seas. The combined

spectroscopic evaluation of authigenic carbonate nodules and coccoliths formed by cultures of the coccolithophore *Pleurochrysis carterae* and carbon isotope analyses of sediment and nodule samples confirmed the origin of peculiar carbonate signatures within seafloor sediments arise from the regional distribution of coccoliths within GoM sediments. Thus, IR-ATR spectroscopy was utilized for characterizing the diversity and patchy distributions of authigenic carbonate minerals from samples collected around the Mississippi Canyon 118 (MC118) gas hydrate site. Overall, spectroscopic evidence enabled the characterization and assessment of carbonate origins within biological, biogeochemical, and geophysical frameworks extending from the photic zone to surficial seafloor sediments at a prominent gas hydrate system, providing attractive applications following the development of suitable MIR sensing platforms for on-ship and *in situ* measurements.

CHAPTER 1

INTRODUCTION

Thesis Objective: The objective for this thesis was the fundamental and practical development of mid-infrared (MIR) chemical sensor applications for evaluating and monitoring oceanic gas hydrate ecosystems with specific focus on gas hydrate growth dynamics and carbonate mineralogy.

Original Contributions of This Thesis:

- *In situ* monitoring of simple clathrate hydrates of methane, ethane, and propane grown from solution in a pressure chamber with infrared (IR) fiber-optic evanescent field spectroscopy.
- Verification of the feasibility for extending hydrate monitoring strategies utilizing IR spectroscopy into oceanic gas hydrate ecosystems.
- IR-attenuated total reflection (IR-ATR) characterization of carbonate mineral diversity surrounding the Mississippi Canyon Block 118 (MC118) hydrate site in the Gulf of Mexico (GoM) as proof-of-concept for future on-ship and *in situ* IR-ATR sediment studies.
- Established the traceability of IR signatures for coccolith shields produced by single-celled photosynthetic algae (coccolithophores) within seafloor sediments.
- IR-ATR spectroscopic detection of authigenic carbonates within shallow seafloor sediments from spectral differences in the ν_3 carbonate signature of coccolith-rich sediments from the GoM.

- Development of complimentary experimental and simulation strategies for characterizing and predicting 'active' IR sensing regions along planar attenuated total reflection (ATR) waveguide surfaces.

1.1 Motivation

Globally, a substantial amount of methane is sequestered in naturally occurring ice-like structures known as gas hydrates, which are estimated to contain approximately (approx.) 10×10^{18} g of methane carbon.[1, 2] The most prominent environmental factors influencing the natural occurrence of gas hydrates, including pressure, temperature, source gas composition, and water ionic strength, are generally well understood after many years of extensive research.[1] Although naturally occurring gas hydrates have been discovered at many locations on Earth, they are limited to specific geographic settings providing thermodynamically favorable conditions for hydrate stability.[1-8] In oceanic environments, gas hydrates are generally restricted to sediments below approx. 300 m of water depth.[1, 9] The abundance of greenhouse gasses sequestered within gas hydrate and authigenic carbonate minerals (carbonate formed in-place) corroborates the importance of oceanic hydrate ecosystems to the global carbon cycle and the regulation of global climate.[2, 4, 5, 7, 10-14]

In oceanic hydrate ecosystems, the potential migration of greenhouse gasses into the atmosphere from hydrocarbon seeps and microbial activity is buffered by the formation of metastable gas hydrates and authigenic carbonate minerals with cycling and sequestration of methane and carbon dioxide strongly influenced by thriving chemosynthetic communities.[10, 11, 14-27] However, a growing body of experimental and theoretical evidence supports the presence of atmospheric methane that has escaped gas hydrate sequestration following release of hydrate masses into the water column and/or catastrophic dissociation from thermal or pressure disturbances that overwhelm natural compensatory processes (i.e., dissolution or microbial oxidation).[28-36] Although a broad knowledge base regarding oceanic hydrate systems is accumulating, limited

evidence is currently available to fully assess methane flux into the atmosphere. This is confounded by the dynamics subsurface venting and hydrate dissociation whereby the frequency and magnitude of outgassing events and the buffering capacity of degradation/sequestration pathways remain to be intermittently observed and somewhat obscure processes.[1, 2, 4, 18, 20, 26, 34, 37] To address the complexity and scope of this problem, enhanced characterization and quantification of biodiversity, bioactivity, viability, stability, and temporal dynamics of hydrate ecosystems are necessary; however, this remains a challenging task due to the occasional and limited access to the harsh, isolated environments where these events occur.

In 1998, the Gulf of Mexico Gas Hydrate Research Consortium (GOMGHRC) was formed as a joint effort between academic, government, and industry partners to further understand the intricate relationships and temporal dynamics of oceanic gas hydrate ecosystems by establishing a seafloor observatory with integrated sensing networks capable of sustainable, long-term monitoring campaigns. The GOMGHRC has additionally fostered the development of novel sensor technologies, which has facilitated studies in this thesis focusing on the development and application of MIR chemical sensors for evaluating and monitoring oceanic gas hydrate ecosystems.

1.2 Overview of Gas Hydrates in the Gulf of Mexico

The first documented recovery of gas hydrates from the Gulf of Mexico (GoM) dates to 1983.[38] In the years following this initial discovery, extensive studies have revealed abundant, complex gas hydrate ecosystems scattered throughout the GoM.[13, 16, 37, 39-42] A map of the Gulf region (**Figure 1-1)** displays many documented occurrences of gas hydrates (thermogenic and biogenic) in addition to gas seeps commonly associated with chemosynthetic communities in the absence of gas hydrate.

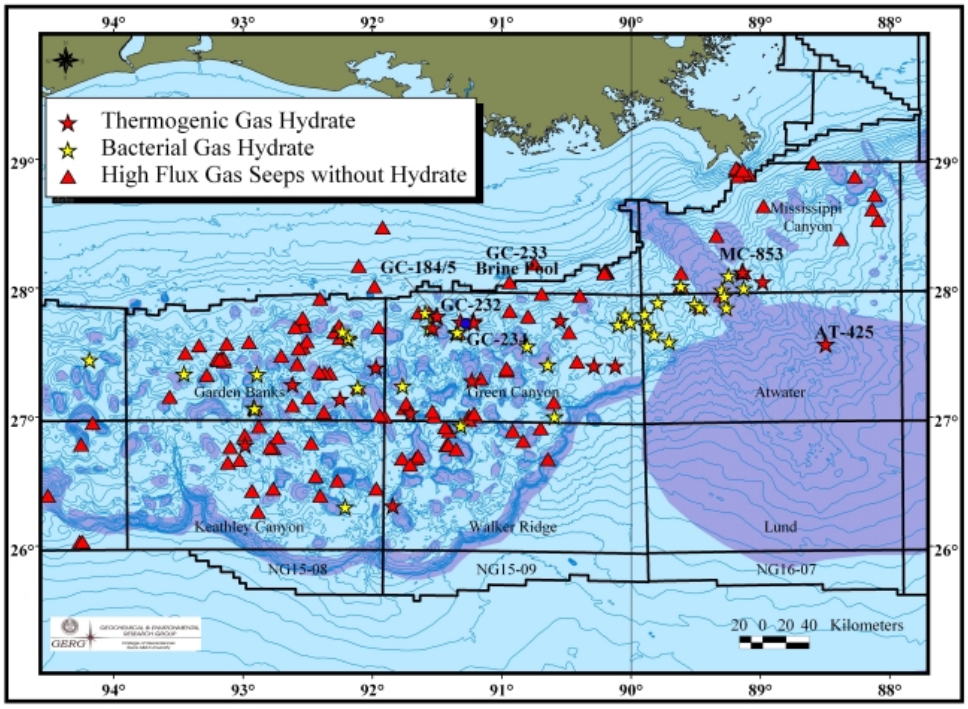

Figure 1-1: Distribution of gas hydrates (thermogenic and biogenic) and high flux gas seeps without gas hydrate in the northern slope region of the Gulf of Mexico. (Map courtesy of Dr. Roger Sassen, Geochemical & Environmental Research Group (GERG), Texas A&M University).

To date, the GoM is among only a few locations where the natural occurrence of the three known crystalline forms of gas hydrates, structure-I (sI), structure-II (sII), and structure-H (sH), has been verified.[39, 43, 44] While > 99% of naturally occurring gas hydrates contain low-molecular weight hydrocarbons ($C_1 - C_5$) formed via biogenic processes, hydrates within the GoM commonly contain hydrocarbon gas emanating from both biogenic and thermogenic sources.[1, 16, 37, 38] Thermogenic hydrates contain hydrocarbon gasses originating from deeply buried sources created by thermal degradation of geologically old organic matter, and biogenic gas hydrates contain gasses from the recent breakdown of organic material closer to the seafloor surface by bacteria and archaea.[1, 37]

Extensive faulting within the Gulf region is typically associated with salt tectonics, and results in vast conduits for fluid migration including gas and oil seepage from deeply buried sources.[23, 39, 42, 45, 46] Abundant gas flux through these conduits provides conditions suitable for gas hydrate

formation within deep sediments extending up to the seafloor and into massive hydrate outcrops/mounds.[8, 40, 45, 47] In addition, proliferate gas and oil seepage establish the foundation for thriving chemosynthetic communities, which significantly impact the cycling and sequestration of oceanic methane and carbon dioxide.[10, 15-17, 23, 26, 27, 47-49]

Oceanic gas hydrate occurrence and stability in the GoM is greatly affected by intricate relationships between dynamic and heterogeneous geophysical and biogeochemical processes surrounding fault conduits.[8, 37, 41, 45, 50-52] Despite the fairly recent discovery of gas hydrates in this region, an extensive knowledge base regarding these complex natural systems has been accumulated through intermittent observations. However, many processes remain unknown or inadequately characterized, particularly regarding the temporal dynamics, microbiological influences, and the local and regional scale distributions.[13, 37] With increasing interest in gas hydrates as a potential alternative energy resource, as submarine geohazards, and a potentially important factor in regulating global climate, it is pertinent to improve the analytical capabilities for characterizing the rates and magnitudes of gas hydrate growth, chemosynthetic activities, and authigenic carbonate formation to facilitate improved assessments of the local and global impacts of carbon cycling and sequestration within oceanic hydrate ecosystems.[2, 5, 11]

1.3 Overview and Scientific Objectives of the GOMGHRC

The GOMGHRC, managed by the Center for Marine Resources and Environmental Technology (CMRET) at the University of Mississippi, provides an extensive interdisciplinary platform facilitating collaborative research to address the complexity, diversity, and large-scale scientific objectives required for evaluating and monitoring oceanic hydrate ecosystems. The scope of the anticipated GOMGHRC seafloor gas hydrate observatory is shown schematically in **Figure 1-2**.

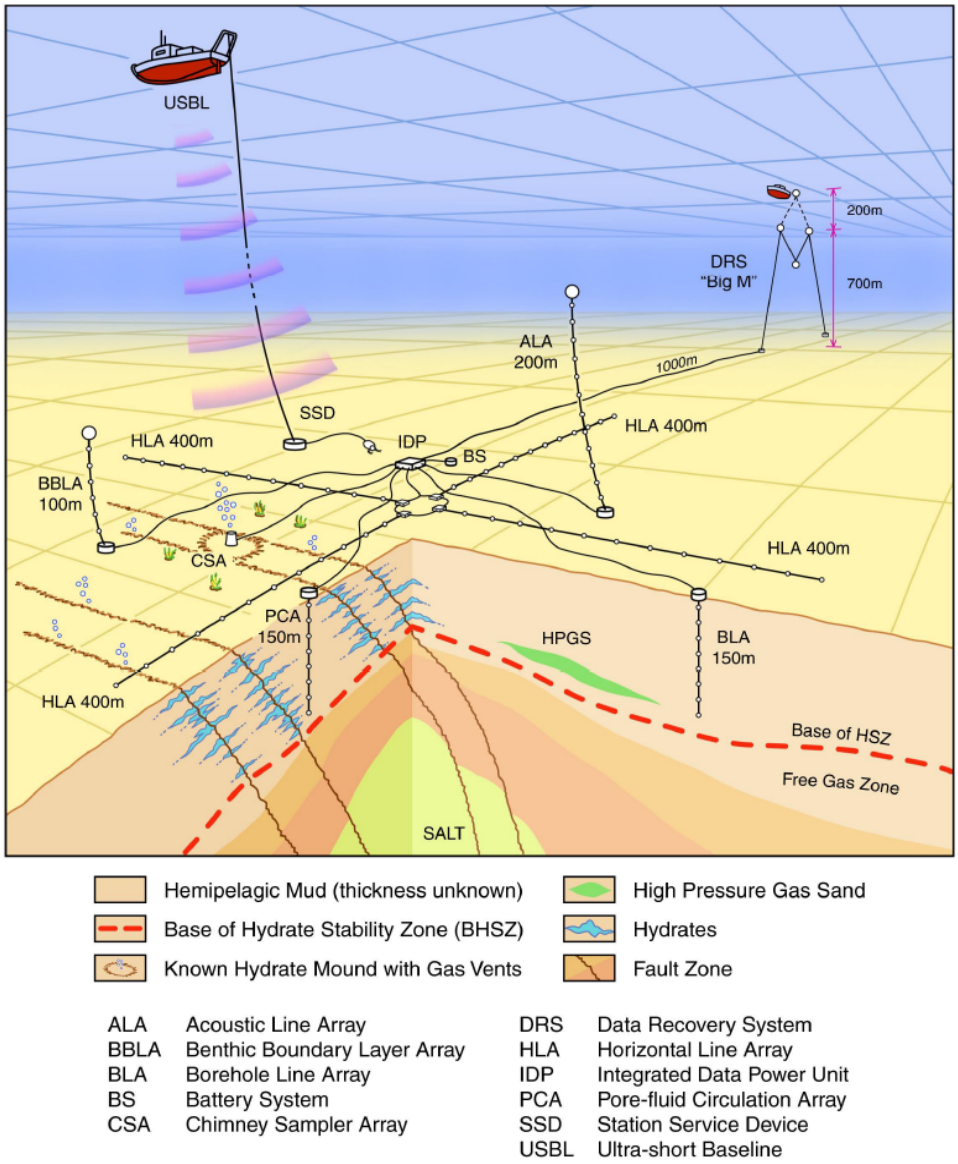

Figure 1-2: Schematic overview of the anticipated GOMGHRC seafloor observatory comprising various geophysical, microbial, and biogeochemical sensor arrays for long-term monitoring of the Mississippi Canyon 118 hydrate site. (Figure courtesy of the GOMGHRC, by Paul Mitchell, Technical Design Specialist for CMRET and the Mississippi Mineral Resources Institute (MMRI)).

The consortium consists of four focus groups to address specific goals of the seafloor observatory, which is to be stationed at a prominent and isolated gas hydrate system located in Mississippi Canyon Block 118 (MC118). The research objectives for each focus group are

outlined below, with the work described in this thesis primarily supportive of the Biogeochemistry focus group:

- **Biogeochemistry:** Focus on benthic geochemistry and biogeochemical processes (sediments and pore fluids from approx. 10 m-below-seafloor (MBSF) to approx. 10 m into the water column).
    - Pore Fluids: Depth profiles of salinity, temperature, and dissolved hydrocarbon gasses (composition, concentration, and isotopes).
    - Benthic Boundary Layer: Analysis of composition and quantity of gas flux through the seafloor, and profiling the low water column temperature, salinity, conductivity, and density.
    - Sediment and Hydrate Biogeochemistry: Characterization and profiling of gas hydrate, mineralogy, dissolved gasses, and heavy hydrocarbons (composition, concentration, quantity, morphology, distribution, dynamics, flux, and stable isotopes), as well as depth profiling sulfate reduction chemistry.
- **Microbial:** Focus on abundance, diversity, distribution, and temporal variability of chemosynthetic (bacteria and archaea) activities.
    - Rates of methane/hydrocarbon oxidation, methanogenesis, and sulfate reduction.
    - Impact on gas hydrates (gas composition, consumption, and origin).
    - Relationships between microbial byproducts and gas hydrate formation (i.e., biosurfactants).
- **Seismo-acoustic:** Focus on evaluating and monitoring the stability and temporal variability in geophysical structuring of sediments and the relationship to gas hydrate occurrences, stability, and pervasiveness.
    - Geophysical structuring of faults and fluid migration conduits.
    - Trapped gas pockets and migration routes.
    - Large-scale hydrate and seafloor stability.

- **Technology and Logistics:** Focus on developing and implementing technological and logistical support.
    - Power and data storage, recovery, and archiving.
    - Instrument deployment and recovery.
    - Providing compatible instrument networking capabilities.

1.4 Introduction to the Gas Hydrate Ecosystem at Mississippi Canyon 118

The MC118 gas hydrate site (28.852295 N; -88.491950 W) has been extensively characterized following multiple seafloor visits with manned submersibles, detailed geophysical surveys, and core sample collections to assist integration of sensor networks for a seafloor observatory.[13, 53, 54] Water depth at the site is ~890 m with seafloor temperatures averaging ~5.4° C from conductivity, temperature, and depth (CTD) casts collected during a cruise in June 2006 (more details in **Chapter 5**). Hydrocarbon gas and oil emanate at the surface through fault conduits linked to deeply buried gas and oil sources.[13] Gas vents and hydrocarbon seepage facilitate gas hydrate formation and the establishment of thriving chemosynthetic communities of bacterial mats (i.e., Beggiatoa), tube worms, and mussels.[13] Abundant sII gas hydrates amass by trapping a portion of small hydrocarbon gasses, primarily CH_4 with considerably high amounts of C_3H_8, exuding from active gas vents.[13] Additionally, substantial sequestration of CO_2 generated by microbial oxidation of hydrocarbons is evidenced by ^{13}C composition of gas and oil recovered in sediments and authigenic carbonate rock accumulations.[13] Sequestration of biogenic CO_2 is aided by robust sulfate reducing microbes that shift pore water alkalinity in favor of authigenic carbonate precipitation with pervasive production of H_2S.[13] It is estimated that the equivalent of approx. 3 billion m^3 of CO_2 at standard temperature and pressure (STP) has accumulated in the form of authigenic carbonate rock at the MC118 site.[13] **Figure 1-3** displays an autonomous underwater vehicle (AUV) survey of MC118.

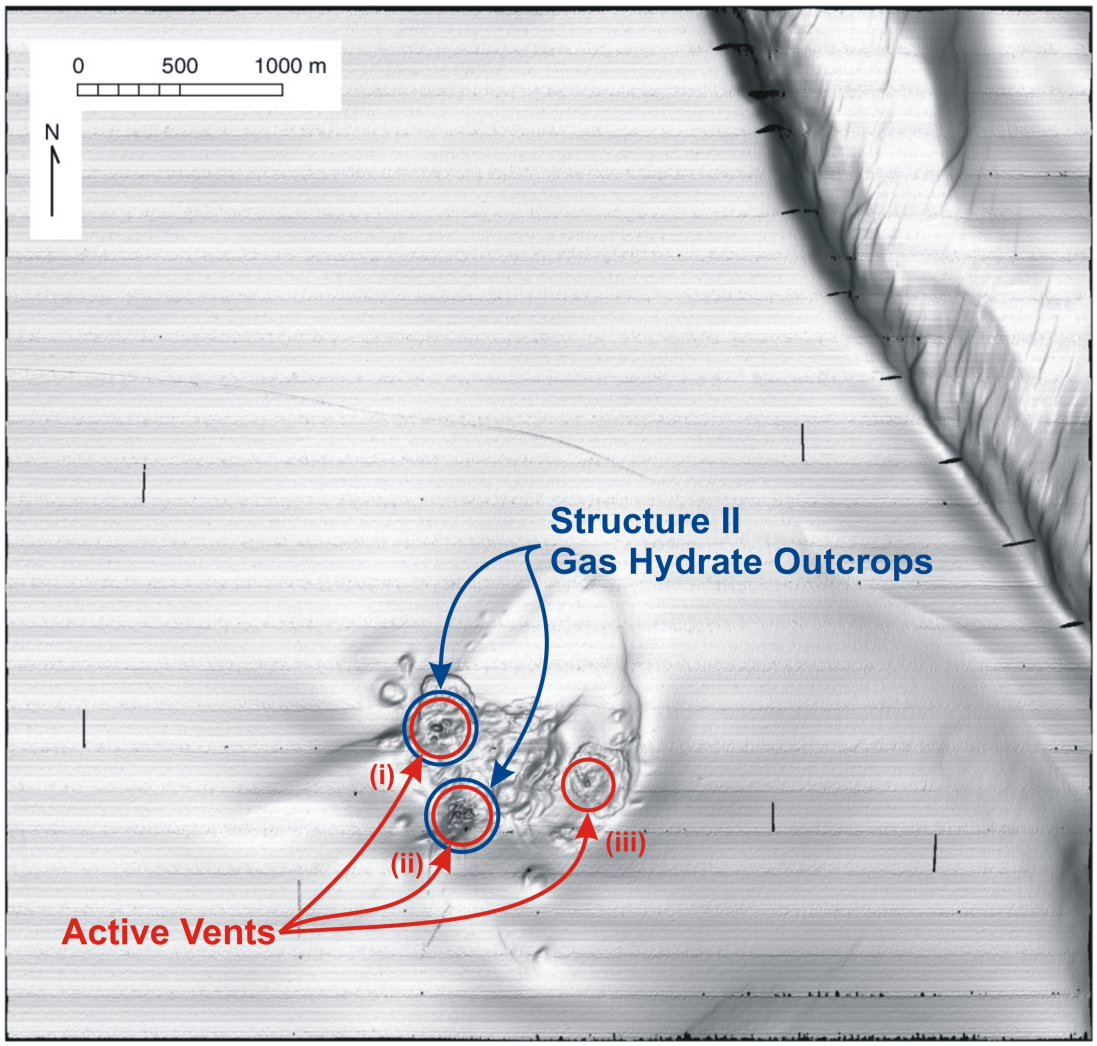

Figure 1-3: Survey of the hydrate system located in the south central area of MC118. This location is characterized by diverse topographical features with active hydrocarbon vent areas highlighted with red circles (smaller diameter). sII hydrate outcrops have been found at the NW vent (i) with recent findings of massive hydrate mounds around the SW vent (ii).13 (Swath batyhmetry shaded relief map provided courtesy of the GOMGHRC, and produced by Alessandro Bosman (University of Rome, La Sapienza) and Leonardo Macelloni (CMRET) from acoustic data collected by C&C Technologies (Lafayette, LA) with the Hugin 3000 AUV).

The hydrate system at MC118 exhibits significant fluctuations in topographical features near active hydrocarbon vents featuring massive sII hydrate outcrops surrounding the NW (i) and SW (ii) vents. A large fault associated with seismic activity lies to the east of the hydrate system stretching NW to SE. With exception of the fault, seafloor topography becomes essentially featureless a short distance away from the hydrate site.

The NW (i) and SW (ii) vent areas are locations of substantial interest as massive hydrate and carbonate formations have been observed surrounding fluid seeps. In September 2006, several dives were performed with the Johnson Sea-Link manned submersible to visually inspect seafloor morphology and to deploy and recover various scientific experiments at MC118 by members of the GOMGHRC. Audio-visual (A/V) logs and optical images were obtained during each dive. **Figures 1-4** through **1-7** provide selected images, with brief descriptions, collected around the MC118 site during manned submersible dives. All images are courtesy of the GOMGHRC and the Johnson Sea-Link Crew (Harbor Branch Oceanographic Institution).

Figure 1-4: A massive, sediment draped gas hydrate outcrop around the SW vent (ii).

Figure 1-5: Large authigenic carbonate ledges and mounds resulting from chemosynthetic activity at the hydrate site with crabs scavenging the area for food.

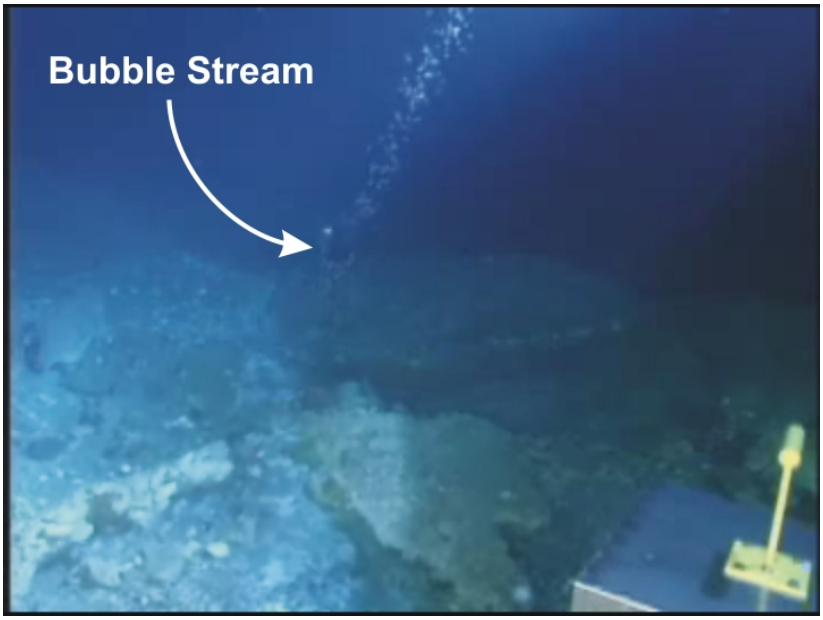

Figure 1-6: Hydrocarbon gas bubbles emerging from the seafloor characterized by hydrate, carbonate, and mollusk shell accumulations.

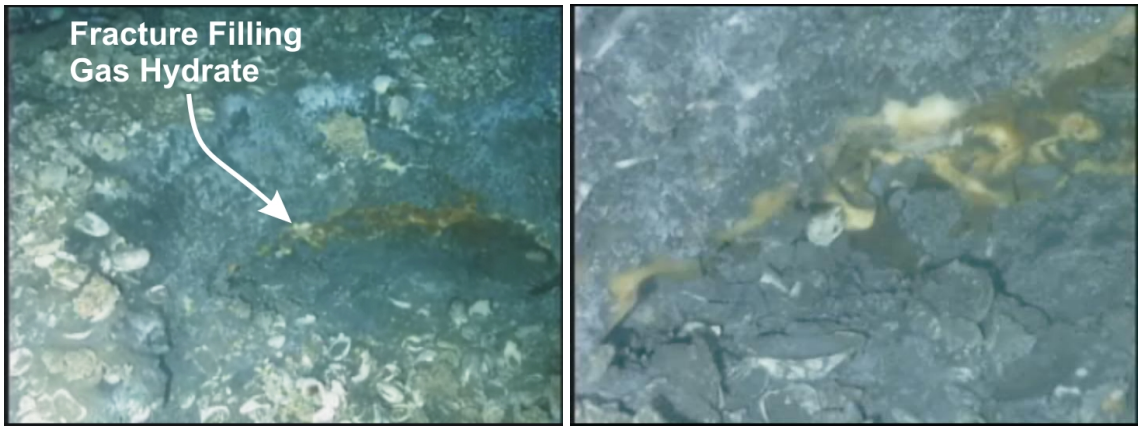

Figure 1-7: Fracture filling gas hydrate stained orange with biodegraded crude oil in an authigenic carbonate mound. Hydrate grows in the crevices of large authigenic carbonate mounds are the result of copious gas venting. Abundant aragonite shell litter is scattered and cemented into the large carbonate mass.

1.5 IR Spectroscopy and Oceanic Gas Hydrate Ecosystems

The work presented in this thesis focuses on the development and practical application of IR spectroscopic measurement and data evaluation strategies for monitoring and characterizing gas hydrates and carbonate minerals in the context of oceanic gas hydrate ecosystems. The most

significant findings reported herein include: (1) establishing the feasibility and first principles for monitoring and quantifying hydrate dynamics with IR fiber-optic evanescent field spectroscopy and (2) identifying and characterizing authigenic carbonates in surficial sediments comprised of abundant coccolith calcite surrounding the MC118 hydrate site. The respective sub-topics addressed throughout this thesis detail the fundamental principles on how the molecular specific information provided by vibrational spectroscopy can be utilized to gain direct insight into local and regional scale natural processes involved with carbon cycling and sequestration within oceanic gas hydrate ecosystems. Furthermore, the capability, feasibility, and potential for the application of submersible MIR chemical sensing platforms, as well as on-ship and laboratory based analytical and exploratory spectroscopic support modules, for evaluating and monitoring oceanic gas hydrate ecosystems is discussed.

1.6 References

1. E. D. Sloan Jr., *Clathrate Hydrates of Natural Gases*, (Marcel Dekker, Inc., New York, 1998).

2. K. A. Kvenvolden, *Methane Hydrate in the Global Organic Carbon Cycle*, Terra Nova **14**, 302 (2002).

3. K. A. Kvenvolden, *Gas Hydrates - Geological Perspective and Global Change*, Reviews of Geophysics **31**, 173 (1993).

4. K. A. Kvenvolden, *Potential Effects of Gas Hydrate on Human Welfare*, Proceedings of the National Academy of Sciences of the United States of America **96**, 3420 (1999).

5. S. Y. Lee and G. D. Holder, *Methane Hydrates Potential as a Future Energy Source*, Fuel Processing Technology **71**, 181 (2001).

6. A. V. Milkov and R. Sassen, *Economic Geology of Offshore Natural Gas Hydrate Accumulations and Provinces*, Marine and Petroleum Geology **19**, 1 (2002).

7. A. V. Milkov, *Molecular and Stable Isotope Compositions of Natural Gas Hydrates: A Revised Global Dataset and Basic Interpretations in the Context of Geological Settings*, Organic Geochemistry **36**, 681 (2005).

8. A. M. Trehu, C. Ruppel, M. Holland, G. R. Dickens, M. E. Torres, T. S. Collett, D. Goldberg, M. Riedel, and P. Schultheiss, *Gas Hydrates in Marine Sediments - Lessons from Scientific Ocean Drilling*, Oceanography **19**, 124 (2006).

9. A. V. Milkov and R. Sassen, *Thickness of the Natural Gas Hydrate Stability Zone, Gulf of Mexico Continental Slope*, Marine and Petroleum Geology **17**, 981 (2000).

10. M. J. Formolo, T. W. Lyons, C. Zhang, C. Kelley, R. Sassen, J. Horita, and D. R. Cole, *Quantifying Carbon Sources in the Formation of Authigenic Carbonates at Gas Hydrate Sites in the Gulf of Mexico*, Chemical Geology **205**, 253 (2004).

11. K. A. Kvenvolden and B. W. Rogers, *Gaia's Breath-Global Methane Exhalations*, Marine and Petroleum Geology **22**, 579 (2005).

12. J. Lelieveld, P. J. Crutzen, and F. J. Dentener, *Changing Concentration, Lifetime, and Climate Forcing of Atmospheric Methane*, Tellus, Series B: Chemical and Physical Meteorology **50B**, 128 (1998).

13. R. Sassen, H. H. Roberts, W. Jung, C. B. Lutken, D. A. DeFreitas, S. T. Sweet, and N. L. Guinasso Jr., *The Mississippi Canyon 118 Gas Hydrate Site: A Complex Natural System*, Proceedings of the Offshore Technology Conference **Paper Number: 18132**, (2006).

14. T. H. Naehr, P. Eichhubl, V. J. Orphan, M. Hovland, C. K. Paull, W. Ussler, T. D. Lorenson, and H. G. Greene, *Authigenic Carbonate Formation at Hydrocarbon Seeps in Continental Margin Sediments: A Comparative Study*, Deep-Sea Research, Part II: Topical Studies in Oceanography **54**, 1268 (2007).

15. R. Sassen, I. R. MacDonald, N. L. Guinasso, Jr., S. Joye, A. G. Requejo, S. T. Sweet, J. Alcala-Herrera, D. A. DeFreitas, and D. R. Schink, *Bacterial Methane Oxidation in Sea-Floor Gas Hydrate: Significance to Life in Extreme Environments*, Geology **26**, 851 (1998).

16. R. Sassen, S. Joye, S. T. Sweet, D. A. DeFreitas, A. V. Milkov, and I. R. MacDonald, *Thermogenic Gas Hydrates and Hydrocarbon Gases in Complex Chemosynthetic Communities, Gulf of Mexico Continental Slope*, Organic Geochemistry **30**, 485 (1999).

17. B. D. Lanoil, R. Sassen, M. T. La Duc, S. T. Sweet, and K. H. Nealson, *Bacteria and Archaea Physically Associated with Gulf of Mexico Gas Hydrates*, Applied and Environmental Microbiology **67**, 5143 (2001).

18. A. G. Judd, M. Hovland, L. I. Dimitrov, S. Garcia Gil, and V. Jukes, *The Geological Methane Budget at Continental Margins and Its Influence on Climate Change*, Geofluids **2**, 109 (2002).

19. W. S. Borowski, C. K. Paull, and W. Ussler, III, *Carbon Cycling within the Upper Methanogenic Zone of Continental Rise Sediments: An Example from the Methane-Rich Sediments Overlying the Blake Ridge Gas Hydrate Deposits*, Marine Chemistry **57**, 299 (1997).

20. R. Sassen, S. T. Sweet, A. V. Milkov, D. A. DeFreitas, and M. C. Kennicutt, II, *Thermogenic Vent Gas and Gas Hydrate in the Gulf of Mexico Slope: Is Gas Hydrate Decomposition Significant?*, Geology **29**, 107 (2001).

21. M. Hovland, *Discovery of Prolific Natural Methane Seeps at Gullfaks, Northern North Sea*, Geo-Marine Letters **27**, 197 (2007).

22. R. Botz, E. Faber, M. J. Whiticar, and J. M. Brooks, *Authigenic Carbonates in Sediments from the Gulf of Mexico*, Earth and Planetary Science Letters **88**, 263 (1988).

23. H. H. Roberts and P. Aharon, *Hydrocarbon-Derived Carbonate Buildups of the Northern Gulf of Mexico Continental slope: A Review of Submersible Investigations*, Geo-Marine Letters **14**, 135 (1994).

24. R. Sassen, H. H. Roberts, P. Aharon, J. Larkin, and E. W. Chinn, *Chemosynthetic Bacterial Mats at Cold Hydrocarbon Seeps, Gulf of Mexico Continental Slope*, Organic Geochemistry **20**, 77 (1993).

25. R. Sassen, H. H. Roberts, R. Carney, A. V. Milkov, D. A. DeFreitas, B. Lanoil, and C. Zhang, *Free Hydrocarbon Gas, Gas Hydrate, and Authigenic Minerals in Chemosynthetic Communities of the Northern Gulf of Mexico Continental Slope: Relation to Microbial Processes*, Chemical Geology **205**, 195 (2004).

26. S. B. Joye, A. Boetius, B. N. Orcutt, J. P. Montoya, H. N. Schulz, M. J. Erickson, and S. K. Lugo, *The Anaerobic Oxidation of Methane and Sulfate Reduction in Sediments from Gulf of Mexico Cold Seeps*, Chemical Geology **205**, 219 (2004).

27. B. N. Orcutt, A. Boetius, S. K. Lugo, I. R. MacDonald, V. A. Samarkin, and S. B. Joye, *Life at the Edge of Methane Ice: Microbial Cycling of Carbon and Sulfur in Gulf of Mexico Gas Hydrates*, Chemical Geology **205**, 239 (2004).

28. G. R. Dickens, J. R. Oneil, D. K. Rea, and R. M. Owen, *Dissociation of Oceanic Methane Hydrate as a Cause of the Carbon-Isotope Excursion at the End of the Paleocene*, Paleoceanography **10**, 965 (1995).

29. W. Xu, R. P. Lowell, and E. T. Peltzer, *Effect of Seafloor Temperature and Pressure Variations on Methane Flux from a Gas Hydrate Layer: Comparison between Current and Late Paleocene Climate Conditions*, Journal of Geophysical Research, [Solid Earth] **106**, 26413 (2001).

30. P. G. Brewer, C. Paull, E. T. Peltzer, W. Ussler, G. Rehder, and G. Friederich, *Measurements of the Fate of Gas Hydrates during Transit Through the Ocean Water Column*, Geophysical Research Letters **29**, 38/1 (2002).

31. I. Leifer and I. MacDonald, *Dynamics of the Gas Flux from Shallow Gas Hydrate Deposits: Interaction between Oily Hydrate Bubbles and the Oceanic Environment*, Earth and Planetary Science Letters **210**, 411 (2003).

32. C. K. Paull, P. G. Brewer, W. Ussler, E. T. Peltzer, G. Rehder, and D. Clague, *An Experiment Demonstrating that Marine Slumping is a Mechanism to Transfer Methane from Seafloor Gas-Hydrate Deposits into the Upper Ocean and Atmosphere*, Geo-Marine Letters **22**, 198 (2003).

33. Y. Zhang, *Methane Escape from Gas Hydrate Systems in Marine Environment, and Methane-Driven Oceanic Eruptions*, Geophysical Research Letters **30**, 51/1 (2003).

34. W. Xu, *Modeling Dynamic Marine Gas Hydrate Systems*, American Mineralogist **89**, 1271 (2004).

35. I. Leifer, B. P. Luyendyk, J. Boles, and J. F. Clark, *Natural Marine Seepage Blowout: Contribution to Atmospheric Methane*, Global Biogeochemical Cycles **20**, GB3008/1 (2006).

36. A. V. Shcherbakov and V. V. Malakhova, *Modeling the Distribution of the World Ocean Methane Hydrates and the Methane Flow into the Atmosphere*, Atmospheric and Oceanic Optics **19**, 477 (2006).

37. D. R. Hutchinson, C. D. Ruppel, H. S. Roberts, R. S. Carney, and M. A. Smith, in Gulf of Mexico - Its Origin (History, Archaeology, and Geology), Vol. 1 (C. W. Holmes, ed.), Texas A&M University Press, College Station, In Press.

38. J. Brooks, M. C. Kennicutt, R. R. Fay, T. J. McDonald, and R. Sassen, *Thermogenic Gas Hydrates in the Gulf of Mexico*, Science **225**, 409 (1984).

39. J. M. Brooks, H. B. Cox, W. R. Bryant, M. C. Kennicutt, II, R. G. Mann, and T. J. McDonald, *Association of Gas Hydrates and Oil Seepage in the Gulf of Mexico*, Organic Geochemistry **10**, 221 (1986).

40. I. R. MacDonald, N. L. Guinasso, Jr., R. Sassen, J. M. Brooks, L. Lee, and K. T. Scott, *Gas Hydrate that Breaches the Sea Floor on the Continental Slope of the Gulf of Mexico*, Geology **22**, 699 (1994).

41. A. V. Milkov, R. Sassen, I. Novikova, and E. Mikhailov, *Gas Hydrates at Minimum Stability Water Depths in the Gulf of Mexico: Significance to Geohazard Assessment*, Gulf Coast Association of Geological Societies Transactions **50**, 217 (2000).

42. R. Sassen, S. T. Sweet, D. A. DeFreitas, J. A. Morelos, and A. V. Milkov, *Gas Hydrate and Crude Oil from the Mississippi Fan Foldbelt, Downdip Gulf of Mexico Salt Basin: Significance to Petroleum System*, Organic Geochemistry **32**, 999 (2001).

43. R. Sassen and I. R. MacDonald, *Evidence of Structure H Hydrate, Gulf of Mexico Continental Slope*, Organic Geochemistry **22**, 1029 (1994).

44. R. Sassen and I. R. Macdonald, *Hydrocarbons of Experimental and Natural Gas Hydrates, Gulf of Mexico Continental Slope*, Organic Geochemistry **26**, 289 (1997).

45. H. H. Roberts and R. S. Carney, *Evidence of Episodic Fluid, Gas, and Sediment Venting on the Northern Gulf of Mexico Continental Slope*, Economic Geology and the Bulletin of the Society of Economic Geologists **92**, 863 (1997).

46. A. Salvador, *Late Triassic-Jurassic Paleogeography and Origin of Gulf of Mexico Basin*, American Association of Petroleum Geologists Bulletin **71**, 419 (1987).

47. H. J. Mills, C. Hodges, K. Wilson, I. R. MacDonald, and P. A. Sobecky, *Microbial Diversity in Sediments Associated with Surface-Breaching Gas Hydrate Mounds in the Gulf of Mexico*, FEMS Microbiology Ecology **46**, 39 (2003).

48. H. W. Jannasch and M. J. Mottl, *Geomicrobiology of Deep-Sea Hydrothermal Vents*, Science (Washington, DC, United States) **229**, 717 (1985).

49. I. R. MacDonald, W. W. Sager, and M. B. Peccini, *Gas Hydrate and Chemosynthetic Biota in Mounded Bathymetry at Mid-Slope Hydrocarbon Seeps: Northern Gulf of Mexico*, Marine Geology **198**, 133 (2003).

50. S. Nagihara, J. G. Sclater, L. M. Beckley, B. E.W., and L. A. Lawver, *High Heat Flow Anomalies Over Salt Structures on the Texas Continental Slope, Gulf of Mexico*, Geophysical Research Letters **19**, 1687 (1992).

51. W. Xu and C. Ruppel, *Predicting the Occurrence, Distribution, and Evolution of Methane Gas Hydrate in Porous Marine Sediments*, Journal of Geophysical Research, [Solid Earth] **104**, 5081 (1999).

52. C. Ruppel, G. R. Dickens, D. G. Castellini, W. Gilhooly, and D. Lizarralde, *Heat and Salt Inhibition of Natural Gas Hydrate Formation in the Northern Gulf of Mexico*, Geophysical Research Letters **32**, L04605/1 (2005).

53. C. B. Lutken, C. A. Brunner, L. Lapham, J. Chanton, R. Rogers, R. Sassen, J. Dearman, L. Lynch, J. Kuykendall, and A. Lowrie, *Analyses of Core Samples from Mississippic Canyon 118*, Proceedings of the Offshore Technology Conference **Paper Number: 18208**, (2006).

54. T. M. McGee and J. R. Woolsey, *A Remote Station to Monitor Gas Hydrate Outcrops in the Gulf of Mexico*, Annals of the New York Academy of Sciences **912**, 527 (2000).

CHAPTER 2

BACKGROUND

This chapter introduces the fundamental principles and theory of infrared (IR) absorption spectroscopy for transmission-absorption and attenuated total reflection measurement strategies. In addition, a general overview of oceanic gas hydrate characteristics and methods for detection and characterization are provided. This chapter concludes by summarizing classical methods and analytical techniques implemented for characterizing marine carbonates.

2.1 Infrared Spectroscopy

In general, optical spectroscopy is the investigation of interactions between light and matter. Specifically, IR spectroscopy is a common analytical tool used to probe the absorption of radiation resulting from the resonant transfer of energy through permanent dipole moments associated with fundamental vibrations and rotations of molecules respective to structure and symmetry in the spectral region from 4000 – 400 cm^{-1}.[1-4] Hence, IR spectroscopy (particularly in the fingerprint region from 1200 – 400 cm^{-1}) generates inherently molecular specific absorption patterns suited for sample characterization. In addition, the molecular specificity of this analytical strategy has lead to the development of various sensing configurations targeting single or multiple analyte species in gas, liquid, and solid sample matrices.

The underlying principle of IR spectroscopy is the frequency (or wavelength) dependent measure in the reduction of light intensity following interaction with a sample (I) relative to the intensity of incident radiation, I_0. This is often expressed as transmittance, T, which is defined as:

$$T = \frac{I}{I_0}$$

Equation 2.1

A more common expression for quantitative application is a rearrangement of **Equation 2.1** for sample absorbance, *A*, following:

$$A = -\log(T) = \log\left(\frac{I_0}{I}\right)$$

Equation 2.2

In transmission-absorption spectroscopy, light is propagated directly through a sample, and the absorbance of light is proportional to the sample thickness and analyte concentration following the Beer-Lambert law such that:

$$A = aCl$$

Equation 2.3

where *A* is absorbance, *C* is the sample concentration, *l* is the sample thickness (measurement pathlength or volume), and *a* is the sample absorptivity with inverse units corresponding to *C* and *l* such that *A* is a unitless value. The sample absorptivity is usually presented as the molar absorptivity, ε, when concentration units are expressed in moles per liter.

IR spectroscopy is often used for quantitative applications. The Beer-Lambert law illustrates that under a given set of measurement conditions where *a* and *l* remain constant, *A* varies with respect to *C* with a first order linear relationship. However, there are several fundamental limitations to the Beer-Lambert law. At high analyte concentrations, a change in the sample absorptivity can occur following a shift in the sample refractive and/or the onset of inter-molecular interactions between analyte molecules.

The term frequency (ν), wavelength (λ), and wavenumber (ω) are used interchangeably throughout this thesis to describe IR absorption characteristics of samples. The respective relationships between each are as follows:

$$\lambda = \frac{c}{\nu}$$

Equation 2.4

where c is the speed of light in vacuum, and:

$$\omega = \frac{1}{\lambda}$$

Equation 2.5

2.1.1 Infrared-Attenuated Total Reflection (IR-ATR) Spectroscopy

Attenuated total reflection spectroscopy was independently pioneered by Fahrenfort and Harrick in the early 1960's.[5, 6] This technique exploits the transfer of radiation to an absorbing sample (lossy coupling) through the surface phenomenon of the so-called evanescent field, as opposed to absorption following direct transmission of light through a sample in conventional transmission-absorption methods. The evanescent field results when light is totally internally reflected at the interface between an optically dense medium (refractive index of n_1) and optically rare medium (refractive index of n_2) where $n_1 > n_2$. The conditions for total internal reflection are achieved when the incident angle of radiation, θ, normal to the reflection interface is > the critical angle, θ_c, where:[6]

$$\theta_c = \sin^{-1} \frac{n_2}{n_1}$$

Equation 2.6

The evanescent field is a standing wave penetrating the optically rare medium normal to the reflection interface resulting from the superposition of electrical fields for incoming and reflected waves.[6] **Figure 2-1** provides a schematic representation of the evanescent field resulting from

total internal reflection of light propagated through a trapezoidal internal reflection element (waveguide).

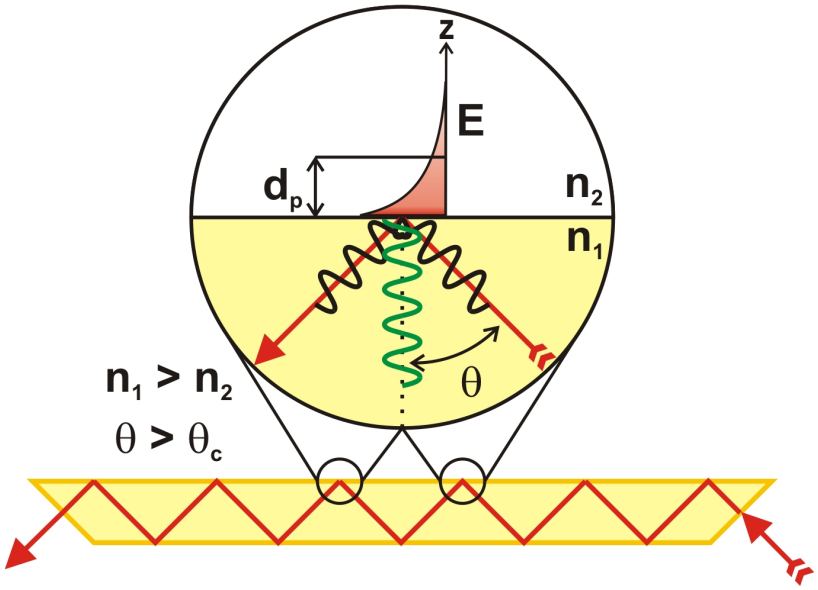

Figure 2-1: The evanescent field arising from light propagating through an optically dense waveguide via total internal reflection.

The evanescent field intensity, E, decays exponentially with increasing distance from the reflection surface following:

$$E = E_0 e^{\left(\frac{-z}{d_p}\right)}$$

Equation 2.7

where E_0 is the evanescent field intensity at the interface ($z = 0$), and d_p is the penetration depth where E_0 has decreased to a value of $1/e$.[6] The penetration depth is dependent upon θ, n_1, n_2, and the wavelength of radiation, λ, propagated through an optically "transparent" waveguide:[6]

$$d_p = \frac{\lambda}{2\pi\sqrt{n_1^2 \sin^2\theta - n_2^2}}$$

Equation 2.8

The localized surface interaction of light and sample in IR-ATR spectroscopy facilitates the interrogation of a wide variety of samples either unsuitable or difficult to analyze with transmission-absorption configurations (i.e., powders and turbid liquid media).[6] In practice the effective interaction between the evanescent field and sample extends beyond d_p; hence, an effective sample thickness, d_e, has been described.[6, 7] For ATR spectroscopy, the attenuation of reflected light, R, by sample absorption following N number of reflections respective to wavelength for constant θ, n_1, and n_2, can be expressed as:

$$\ln R(\lambda) = -aCNd_e$$

Equation 2.9

In **Equation 2.9**, ln R is comparable to the ln T for transmission-absorption spectroscopy; hence, the sample absorbance in IR-ATR spectra can be written in an adapted form of the Beer-Lambert law:

$$A(\lambda) \cong aCNd_e$$

Equation 2.10

where Nd_e is the measurement pathlength comparable to l.

2.1.2 IR-ATR Waveguides

A variety IR transparent materials and waveguide geometries enable an array of high optical throughput configurations fulfilling the conditions of total internal reflection for IR-ATR spectroscopic measurements.[8-12] IR transmitting optical fibers are typically made from chalcogenides, silver halides, and tellurium halides with diameters of 400 – 1000 μm.[13, 14] Planar ATR crystals (typical thickness > 1 mm) are usually made from ZnSe, Ge, and Si.[8-12] The effective measurement pathlength (respective to material refractive indices) can be tailored by

adjusting the number of internal reflections with waveguide geometry, thickness, length, and radiation coupling conditions. In this thesis, trapezoidal ZnSe waveguides and silver halide fibers (AgX) were utilized for IR-ATR measurements. The physical and transmission properties of ZnSe, silver halide fibers, and other waveguiding materials are commonly available from manufacturers/distributors and throughout the literature.[8-12, 14]

2.1.3 Evanescent Field Sensing Strategies

2.1.3.1 Uncoated Waveguides

The application of uncoated waveguides for sensing strategies is well-suited to evaluate major components of bulk samples through the direct interrogation of a sample matrix. Analyte sensitivity can range from parts per million[15] (ppm volume-to-volume (v/v)) to low mass percentages (~2% as in **Chapter 5** for carbonate analysis) depending on the absorption characteristics of targeted species and matrix interferences. This sensing strategy enables near real-time monitoring of a sample or measurement environment. If matrix components strongly interfere with analyte absorption features or analyte concentrations are below detection capabilities of this configuration, application of diffusion-based extraction membranes may be utilized to enhance measurement capabilities.[16] Although only uncoated waveguides were the only measurement strategy implemented in this thesis, a brief overview of surface-modified waveguides is provided below.

2.1.3.2 Surface-Modified Waveguides

Polymer or polymer-like films are often deposited onto the waveguide surface for enhancing analyte detection of small compounds.[16-18] This strategy targets the extraction and enrichment of trace amounts of volatile organic compounds (VOCs) into the polymer(-like) matrix from aqueous media. The enrichment membrane additionally facilitates the suppression of background bulk matrix interferences as the film thickness is generally > d_p. Furthermore, VOCs in general have a higher affinity for the membrane matrix than the bulk aqueous solution, which can lead to

enrichment factors from the low 100's to over 10,000.[16, 19] This significantly enhances the analyte content interrogated by the evanescent field enabling detection limits from single parts per billion (ppb) to low ppm concentrations on a v/v basis. The drawback to this strategy is the selection of a membrane material that exhibits high thermal, chemical, and physical stability while providing high analyte affinity with rapid, reversible diffusion characteristics. A wide variety of polymer, sol-gel, and, most recently, plasma-polymerized films have been utilized for detection of VOCs in the literature, including polystyrene-co-butadiene, Teflon AF 1600 and 2400, and ethylene-co-propylene.[16-20]

2.2 General Characteristics and Methods for Detecting Oceanic Gas Hydrates

A continuously increasing number of oceanic gas hydrate occurrences are reported in the literature, with most findings along continental margins.[21-25] In general, oceanic gas hydrate stability becomes favorable at pressures and temperatures corresponding to approx. 300 m below sea level.[21, 26] In most oceanic environments, hydrate stability is typically greatest at the sediment-water interface, and decreases with depth below the seafloor as a result of increasing temperatures from geothermal gradients.[21] The following sub-sections aim to provide a general overview on the fundamental characteristics of oceanic gas hydrates and a brief summary of detection methods. More extensive reviews and treatments can be found in Sloan Jr., Hutchinson et al., Trehu et al., and references therein.[21, 27, 28]

2.2.1 General Characteristics of Oceanic Gas Hydrates

Several classification schemes are commonly implemented to describe and characterize the qualities (physical and chemical) of naturally occurring oceanic gas hydrates. Established classification parameters provide general proxies for differentiating the diversity of gas hydrate morphologies and gas compositions; however, they also provide direct insight into a variety geological factors (e.g., geophysical, geochemical, and biological) directly influencing the

physical and chemical characteristics of gas hydrates. The following sub-sections provide a general overview for the most common classifications used to generate basic descriptions of naturally occurring oceanic gas hydrates.

2.2.1.1 Biogenic and Thermogenic Gas Hydrates

The classification of oceanic gas hydrates as either biogenic or thermogenic stems from the isotopic characteristics of methane carbon.[21, 27, 28] The relative abundance of ^{13}C provides insight into past physical and biological processes impacting the isotopic abundance prior to sequestration in gas hydrate structures.[21, 27, 28] Carbon isotope data is presented as $\delta^{13}C$ in parts per thousand (‰) relative to a Pee Dee Belemnite standard following:[21]

$$\delta^{13}C = \left(\frac{\left(\left[{}^{13}C \right] / \left[{}^{12}C \right] \right)_{Sample}}{\left(\left[{}^{13}C \right] / \left[{}^{12}C \right] \right)_{PDB}} - 1 \right) \times 10^{3}$$

Equation 2.11

Biogenic methane typically exhibits $\delta^{13}C$ values ranging between -60 to -85‰; whereas, thermogenic methane ranges between -25 to -55‰.[21] Hence, the isotopic composition of methane sequestered in gas hydrate correlates to methane origins and the resultant classification of gas hydrate as either biogenic or thermogenic. In addition, the concentration ratio, $[C_1/(C_2 + C_3)]$, facilitates characterization of biogenic ($> 10^3$) and thermogenic ($< 10^2$) gas hydrates.[21]

2.2.1.2 Gas Hydrate Morphologies

Several models have been proposed to describe *in situ* hydrate formation and morphological relationships between gas flux (high versus low) and gas origins (biogenic versus thermogenic).[21, 28] Currently, only a general overview of hydrate morphology and terminology is provided herein. Four general morphological groups are utilized to describe naturally occurring gas hydrates: (1) disseminated, (2) nodular, (3) layered, and (4) massive.[21] Disseminated gas hydrate describes small hydrate agglomerations, up to approx. 1 cm, widely distributed throughout the sediments.

Nodular hydrate formations include hydrate masses from approx. 1 cm to 5 cm in diameter. Layered gas hydrates are separated by thin sediment layers, and massive gas hydrates describe a wide variety of gas hydrate formations > 5 cm in size. Fracture filling gas hydrates in carbonate mounds and massive hydrate outcrops or mounds > 4 m have been observed in several locations, including the MC118 site (see **Figures 1-4** and **1-7**).[21, 29]

2.2.1.3 Gas Hydrate Structures

Oceanic gas hydrates are most frequently observed to be sI or sII (see **Section 4.1.1.2**); however, sH has also been recovered in the GoM.[21, 28, 30] Gas hydrate structure is generally inferred from the gas composition of dissociated hydrate, which is typically analyzed by gas chromatography (GC) and/or GC-mass spectrometry.[21] As a general rule, hydrates with gas compositions containing < 1% $C_3 - C_5$ are classified as sI, and sII when the $C_3 - C_5$ content is > 1%.[21] Gas compositions vary widely between gas hydrate locations, as well as the presence of sI and/or sII formations.[21] At MC118, the gas composition is reflective of sII.[29] Furthermore, the relative percentages of $C_1 - C_4$ sequestered within hydrate are substantially enriched in $C_2 - C_4$, particularly in propane, compared to the composition of thermogenic supply gases.[29] Recently, Raman spectroscopy has been extended from laboratory characterization of gas hydrate structures for deep-sea investigations at the Hydrate Ridge site (~ 780 m) off the coast of Oregon.[31] The authors demonstrated the capability for *in situ* classification of hydrate structure (sI). This was achieved using methane signatures to determine cage-occupancy ratios characteristic of sI hydrate previously observed in laboratory measurements.[31]

2.2.2 Detection, Indication, and Characterization of Oceanic Gas Hydrates

A variety of investigative methods and analysis techniques have been implemented for detecting and/or inferring the presence of oceanic gas hydrates.[21, 27, 28] A general overview of sampling methods, geophysical and geochemical indicators of gas hydrates, and common and state-of-the-art methods for detection and characterization (on-ship and *in situ*) is provided below.

2.2.2.1 Visual Observation and Hydrate Sampling Methods

The value of visual observations of gas hydrates (either *in situ* or *ex situ*) cannot be underestimated in oceanic gas hydrate research. Geochemical and geophysical anomalies, discussed in **Sections 2.2.2.2 and 2.2.2.3**, provide strong inferential evidence to the presence of gas hydrate; however, ground truthing by visual observation remains the quintessential direct confirmation of oceanic gas hydrate occurrences.[21, 27, 28] *In situ* visual observations and sample recoveries (i.e., push cores) are often facilitated by manned submersibles or ROVs (typically stimulated investigations following the collection of inferential evidence), recovery of hydrate samples from ship coring operations (gravity and piston cores), and/or continued investigations of previously documented gas hydrate sites (e.g., MC118).[21, 27, 28]

Although gas hydrates may be recovered by sediment core sampling, they are prone to rapid and potentially full dissociation, primarily disseminated and small nodules, following extraction from thermodynamically stabile conditions prior to on-ship visual investigations.[21, 27, 28] As a result, several pressure core systems have been developed to maintain sediments at *in situ* hydrostatic pressures during core recovery, thereby preserving equilibrium conditions of free gas, dissolved gas, and gas hydrate for improved characterization of hydrate-bearing sediments.[27, 32] Yun et al. developed an instrumented pressure test chamber enabling sample transfer from Fugro pressure cores with multiple access ports for measuring seismic velocities (i.e., compression (P) and shear (S)-wave), electrical conductivity, and sediment strength at *in situ* pressures.[32] In addition, track-mounted IR cameras have been recently implemented for systematic thermal imaging of all Ocean Drilling Project cores sampling within the gas hydrate stability zone.[27] Thermal imaging facilitates rapid characterization of gas hydrate structuring and layering within sediments by identifying anomalous cold spots resulting from endothermic hydrate dissociation. This method has also been utilized to aid focused, on-ship sub-sampling of recovered cores for land-based laboratory studies (e.g., pore water chemistry).[27]

2.2.2.2 Seismo-Acoustic Detection of Gas Hydrates

In addition to core sampling and submersible investigations, the occurrence of oceanic gas hydrates are most frequently indicated by hydrate-related acoustic reflections within sediments known as Bottom Simulating Reflectors (BSRs).[21, 28] A variety of seismo-acoustic methods (data collection and treatment) have been reported (e.g., shallow source deep receiver (SSDR)); however, only a brief discussion is provided herein.[21, 28] In general, a source (e.g., air gun) directs sound waves towards the sediment while a receiver (e.g., geophone) records reflected waves versus time.[21] Hydrate-related BSRs are indicated by a concomitant sharp decrease in P-wave velocity and increase in S-wave velocity.[21, 28] Seismo-acoustic sediment profiles are frequently collected in straight lines running N – S or E – W.

Seismo-acoustic methods are often implemented for aerial reconnaissance in the search for oceanic gas hydrate occurrences.[21, 28] In addition, several data treatments have also been developed for quantifying gas hydrate volumes from BSR data.[21, 28] However, BSRs are not reliable indicators for conclusive determination to the occurrence or lack of gas hydrates in oceanic environments.[21, 28] Gas hydrates have been recovered in locations without identifiable BSRs, and BSRs have been identified without gas hydrate recovery in core samples.[21, 28]

2.2.2.3 Geochemical Indicators of Gas Hydrates

In addition to the characterization of gas hydrates by analyzing gas composition and carbon isotopes, two additional geochemical factors evidence the presence of gas hydrate.[21, 28] Ions are not incorporated into gas hydrate structures; hence, recent hydrate formation leads to increased salinity/chlorinity in surrounding pore waters.[21, 28] Conversely, hydrate dissociation in sediments can be inferred from depleted values relative to baseline measurements from non-hydrate-bearing sediment fractions recovered in the same core.[21, 28] Lastly, $H_2{}^{18}O$ is preferentially incorporated into gas hydrate moieties; albeit in only small fractions such that an α value of approx. 1.0026 can be measured where:[21]

$$\alpha = \frac{\left(\left[^{18}\mathrm{O}\right]/\left[^{16}\mathrm{O}\right]\right)_{\mathrm{Hydrate}}}{\left(\left[^{18}\mathrm{O}\right]/\left[^{16}\mathrm{O}\right]\right)_{\mathrm{Liquid}}}$$

Equation 2.12

2.3 General Overview of Classical Characterization Methods for Marine Carbonates

Marine carbonates comprise a complex and diverse array of skeletal and non-skeletal formations.[33] Four general branches of characterization are implemented by geologists to facilitate a thorough description carbonate rocks and sediments: (1) texture, (2) petrography, (3) mineralogy, and (4) chemical composition.[33] For sediment analysis, texture simply refers to particle size evaluation. Particle size characterization of three size fractions is frequently sufficient for analysis; silt and clay (< 62 μm, termed mud), sand (62 – 2000 μm), and gravel (> 2000 μm).[33] Petrography is the characterization of mineral content in relationship to texture aided by visual and chemical analyses. A more thorough treatment of petrographic analysis is beyond the scope of this thesis; however, the compositional relationship of particle sizes and carbonate content has significant implications regarding IR-ATR analysis of carbonate minerals in seafloor sediments. Additional considerations of these relationships are provided in context to the studies described throughout **Chapters 5** and **6**.

Carbonate minerals are commonly classified upon visual inspection following various staining procedures utilized in petrographic analysis.[33] Reviews of common staining procedures can be found in Friedman as well as Milliman.[33, 34] Powder x-ray diffraction (XRD) is also a common method for carbonate classification via the evaluation of diffraction patterns characteristic to each mineral species.[33, 35, 36] In addition, XRD data is amenable for quantitative evaluation of carbonate constituents (i.e., calcite and dolomite) and the quantification of Mg^{2+} content in magnesian calcites.[33, 35, 36] This can be achieved with peak height and/or peak area data evaluation strategies. The quantitative accuracy of XRD typically ranges from 1 – 5%.[33, 35, 36]

Additional analytical methods have been developed for quantifying calcium carbonate composition (calcite and aragonite) including gasometry, acid-leaching, EDTA, and atomic absorption.[33] Selection of a quantification method is primarily dependant upon user needs. Elemental and isotopic analyses are also used for a thorough assessment of carbonate composition. Elemental analysis can be facilitated by x-ray fluorescence, flame atomic emission, and atomic absorption spectroscopies, whereas various mass spectrometric configurations can be utilized for isotopic characterization of C and O content relative to a standard sample.[33]

In this thesis, the general characterization of seafloor sediments has facilitated the collection of a multitude of evidence supporting IR data interpretations presented in **Chapters 5 and 6**. In addition to IR analyses presented in this work, carbonate carbon isotope analyses for several key samples were performed by external laboratories with mass spectrometry. Measurement procedures and results for isotopic analysis can be found in **Appendix A-1**. Specific discussions regarding carbonate mineralogy and oceanic hydrate ecosystems and the application of IR spectroscopy for carbonate analysis are provided in **Chapters 5** and **6**.

2.4 References

1. D. C. Harris and M. D. Bertolucci, *Symmetry and Spectroscopy: An Introduction to Vibrational and Electronic Spectroscopy*, (Dover Publication, Inc., New York, 1978).

2. D. L. Pavia, G. M. Lampman, and G. S. Kriz, *Introduction to Spectroscopy: A Guide for Students of Organic Chemistry*, (Saunders College Publishing, Fort Worth, 1996).

3. D. A. Skoog, F. J. Holler, and T. A. Nieman, *Principles of Instrumental Analsyis*, (Brooks Cole, 1997).

4. D. C. Harris, *Quantitative Chemical Analysis*, (W. H. Freeman and Company, New York, 2003).

5. J. Fahrenfort, *Attenuated Total Reflection. A New Principle for the Production of Useful Infrared Reflection Spectra of Organic Compounds*, Spectrochimica Acta **17**, 698 (1961).

6. N. J. Harrick, *Internal Reflection Spectroscopy*, (John Wiley & Sons, New York, 1967).

7. N. J. Harrick and A. I. Carlson, *Internal Reflection Spectroscopy: Validity of Effective Thickness Equations*, Applied Optics **10**, 19 (1971).

8. *Specac Inc.*, http://www.specac.com/ (July 2007).

9. *PIKE Technologies*, http://www.piketech.com/ (July 2007).

10. *MacroOptica Ltd*, http://www.macrooptica.com/ (July 2007).

11. *Remspec Corporation*, http://www.remspec.com/ (July 2007).

12. *Harrick Scientific Products, Inc.*, http://www.harrricksci.com/ (July 2007).

13. G. Holst and B. Mizaikoff, in Handbook of Optical Fibre Sensing Technology, 2002, p. 729.

14. B. Mizaikoff, *Mid-IR Fiber-optic Sensors*, Analytical Chemistry **75**, 258A (2003).

15. K. Michel, B. Bureau, C. Boussard-Pledel, T. Jouan, J. L. Adam, K. Staubmann, and T. Baumann, *Monitoring of Pollutant in Wastewater by Infrared Spectroscopy using Chalcogenide Glass Optical Fibers*, Sensors and Actuators, B: Chemical **B101**, 252 (2004).

16. P. Heinrich, R. Wyzgol, B. Schrader, A. Hatzilazaru, and D. W. Luebbers, *Determination of Organic Compounds by IR/ATR Spectroscopy with Polymer-coated Internal Reflection Elements*, Applied Spectroscopy **44**, 1641 (1990).

17. M. Janotta, A. Katzir, and B. Mizaikoff, *Sol-gel-coated Mid-infrared Fiber-optic Sensors*, Applied Spectroscopy **57**, 823 (2003).

18. G. T. Dobbs, B. Balu, C. Young, C. Kranz, D. W. Hess, and B. Mizaikoff, *Mid-infrared Chemical Sensors utilizing Plasma-deposited Fluorocarbon Membranes*, Analytical Chemistry (Accepted September 2007).

19. M. Karlowatz, M. Kraft, and B. Mizaikoff, *Simultaneous Quantitative Determination of Benzene, Toluene, and Xylenes in Water using Mid-infrared Evanescent Field Spectroscopy*, Analytical Chemistry **76**, 2643 (2004).

20. B. Murphy and P. McLoughlin, *Determination of Chlorinated Hydrocarbon Species in Aqueous Solution using Teflon Coated ATR Waveguide/FTIR Spectroscopy*, International Journal of Environmental Analytical Chemistry **83**, 653 (2003).

21. E. D. Sloan Jr., *Clathrate Hydrates of Natural Gases*, (Marcel Dekker, Inc., New York, 1998).

22. K. A. Kvenvolden, *Gas Hydrates - Geological Perspective and Global Change*, Reviews of Geophysics **31**, 173 (1993).

23. K. A. Kvenvolden, *Methane Hydrate in the Global Organic Carbon Cycle*, Terra Nova **14**, 302 (2002).

24. A. V. Milkov and R. Sassen, *Economic Geology of Offshore Natural Gas Hydrate Accumulations and Provinces*, Marine and Petroleum Geology **19**, 1 (2002).

25. A. V. Milkov, *Molecular and Stable Isotope Compositions of Natural Gas Hydrates: A Revised Global Dataset and Basic Interpretations in the Context of Geological Settings*, Organic Geochemistry **36**, 681 (2005).

26. A. V. Milkov, R. Sassen, I. Novikova, and E. Mikhailov, *Gas Hydrates at Minimum Stability Water Depths in the Gulf of Mexico: Significance to Geohazard Assessment*, Gulf Coast Association of Geological Societies Transactions **50**, 217 (2000).

27. A. M. Trehu, C. Ruppel, M. Holland, G. R. Dickens, M. E. Torres, T. S. Collett, D. Goldberg, M. Riedel, and P. Schultheiss, *Gas Hydrates in Marine Sediments - Lessons from Scientific Ocean Drilling*, Oceanography **19**, 124 (2006).

28. D. R. Hutchinson, C. D. Ruppel, H. S. Roberts, R. S. Carney, and M. A. Smith, in Gulf of Mexico - Its Origin (History, Archaeology, and Geology), Vol. 1 (C. W. Holmes, ed.), Texas A&M University Press, College Station, In Press.

29. R. Sassen, H. H. Roberts, W. Jung, C. B. Lutken, D. A. DeFreitas, S. T. Sweet, and N. L. Guinasso Jr., *The Mississippi Canyon 118 Gas Hydrate Site: A Complex Natural System*, Proceedings of the Offshore Technology Conference **Paper Number: 18132**, (2006).

30. R. Sassen and I. R. MacDonald, *Evidence of Structure H Hydrate, Gulf of Mexico Continental Slope*, Organic Geochemistry **22**, 1029 (1994).

31. K. C. Hester, R. M. Dunk, S. N. White, P. G. Brewer, E. T. Peltzer, and E. D. Sloan, *Gas Hydrate Measurements at Hydrate Ridge using Raman Spectroscopy*, Geochimica et Cosmochimica Acta **71**, 2947 (2007).

32. T. S. Yun, G. Narsilio, J. C. Santamarina, and C. Ruppel, *Instrumented Pressure Testing Chamber for Characterizing Sediment Cores Recovered at In Situ Hydrostatic Pressure*, Marine Geology **229**, 285 (2006).

33. J. D. Milliman, *Marine Carbonates*, (Springer, New York, 1974).

34. G. M. Friedman, *Identification of Carbonate Minerals by Staining Methods*, Journal of Sedimentary Petrology **29**, 87 (1959).

35. E. Gavish and G. M. Friedman, *Quantitative Analysis of Calcite and Mg-calcite by X-ray Diffraction. Effect of Grinding on Peak Height and Peak Area*, Sedimentology **20**, 437 (1973).

36. J. D. Milliman and B. D. Bornhold, *Peak Height versus Peak Intensity Analysis of X-ray Diffraction Data*, Sedimentology **20**, 445 (1973).

CHAPTER 3

EXPERIMENTAL DESIGN AND APPARATUS

The goal of this chapter is to provide detailed technical descriptions of the two primary experimental setups, including commercially available equipment, design and construction of custom-built apparatus, and control and monitoring systems, utilized throughout the course of described studies. In addition to facilitating the flow of content throughout this thesis, the reader has the option to gain a general overview of the experimental configurations by referring to **Figures 3-8, 3-10, 3-11, 3-12, and 3-14**. A mixture of International System of Units (SI) and English units are used throughout this chapter. The usage of English units facilitates easy identification of "off-the-shelf" components without requiring unit conversion. Where appropriate, units from both systems are provided side-by-side.

3.1 Experimental Setup for IR Spectroscopic Monitoring of Gas Hydrates

Experimental chambers for laboratory growth of gas hydrates have evolved substantially since the initial discovery of clathrate hydrates.[1] In principle, hydrate growth chambers must be capable of attaining and sustaining conditions at or beyond hydrate phase equilibria, while providing the means for manipulating and monitoring system parameters (i.e., temperature and pressure). Today, experimental designs typically integrate the capability for water agitation via rocking, stirring, and/or sonication, mass flowmeters for quantification of gas incorporation into hydrate structures, optical ports for visual inspection, and access ports for the interrogation of gas hydrates with additional analytical strategies.[1] A detailed overview of significant milestones in the design of experimental apparatus, methods, and measurements of gas hydrates are provided in *Clathrate Hydrates of Natural Gases* by E. Dendy Sloan Jr. and references within.[1]

The hydrate growth chamber developed for IR fiber-optic measurements of gas hydrates via evanescent field absorption spectroscopy was initially designed and described by N.A.

Pennington for studying MIR sensor concepts for assessing dissolved methane in oceanic hydrate environments.[2] To facilitate hydrate growth in a non-agitated system with visual and fiber-optic access in this thesis, several design modifications were required. In addition to a description of the pressure chamber, specifications for the cooling, imaging, and pressure and temperature monitoring sub-systems are provided. Furthermore, a complete assembly description of the hydrate chamber with identification and function of individual components is presented.

3.1.1 Initial Pressure Chamber Design

The high pressure chamber was constructed from 304 stainless steel (SS) with a sample volume of approx. 500 mL.[2] The main body (**Figure 3-1**) was fabricated from a solid piece of SS material with 6 1/4" female national pipe thread (FNPT) access ports. The cylindrical sample volume of the main body is sealed with an AS568A Dash No. 237 Viton o-ring and a 4.5" od. × 0.5" th. (od. is outer diameter, th. is thickness) circular detachable face plate secured by 12 1/4"-20 × 5/8" hexagonal (hex) head cap screws. The initial cover plate was designed to accommodate a 50 mm × 20 mm × 2 mm planar ATR waveguide allowing operation up to a pressure of approx. 300 pounds per square inch gauge (psig), 2.1 megapascal (MPa), at room temperature. Threaded anchor points at each corner on the underside of the main body enable the attachment of standard 0.5" diameter (dia.) optical posts with 1/4"-20 screw extensions.

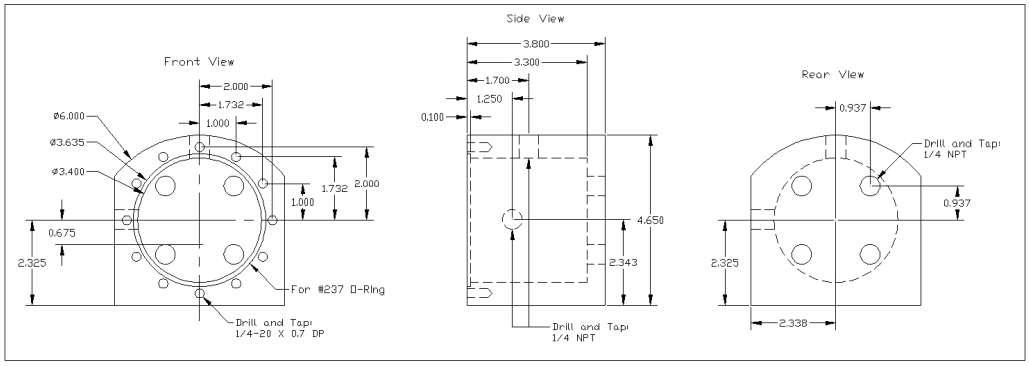

Figure 3-1: Construction drawings for the initial status of the main body for the pressure chamber. (Drawings adapted from N.A. Pennington).[2]

3.1.2 Construction Modifications to Main Body of Pressure Chamber

To facilitate growth and spectroscopic monitoring of gas hydrates with the pressure chamber described in **Section 3.1.1**, two primary construction modifications were required to incorporate temperature control and spectroscopic access to the internal sample volume. Two complementary pairs of 1/8" FNPT access ports were added to the main body for fiber-optic coupling and for integrating an internal cooling coil. In addition, one 1/4" FNPT port was added to assist fluid drainage from the underbody of the sample chamber. **Figure 3-2** displays updated construction drawings for the described main body modifications (original form depicted in **Figure 3-1**). Construction modifications were performed by the Georgia Tech College of Science Machine Shop (GTCoSMS).

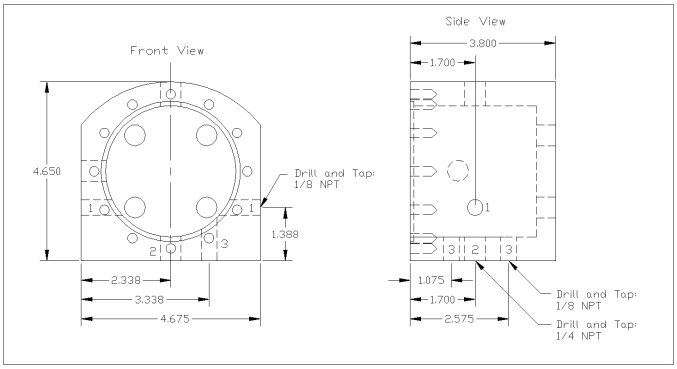

Figure 3-2: Construction drawings for modifications to the pressure chamber main body: (1) fiber-optic coupling ports, (2) liquid drain, and (3) internal cooling coil ports.

3.1.3 High Pressure Optical Viewport Design, Construction, and Specifications

Design and construction of a high pressure optical viewport provided visual access for monitoring the interior of the sample chamber during hydrate measurements. In addition, a new detachable face plate was designed and constructed for mounting and coupling the modular viewport accessory to the existing high pressure apparatus without further modification to the main body. Conceptual drawings with a cross-sectional view and three-dimensional (3-D) computer-aided design (CAD) rendering of the optical viewport are provided in **Figure 3-3**.

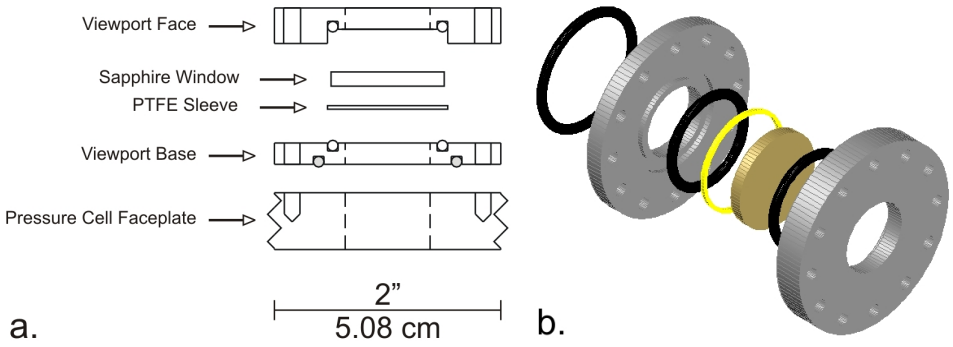

Figure 3-3: Conceptual drawings of the high pressure optical viewport with sapphire window. (a.) Cross-sectional view with labeled components, and (b.) CAD 3-D rendering of the viewport.

The viewport was designed to provide versatility, safety, and functionality. The modular construction allows detachment of the viewport from the chamber with the pressure seal maintained around the optical window, which facilitates multi-application usage for future modifications to the experimental apparatus and/or construction of a new pressure chamber. A 1/16” oversized inset, for sandwiching a 1” dia. sapphire window between the face and base components, was designed to prevent metal-sapphire contact that could result in catastrophic failure when pressurized. As a result, a thin polytetrafluoroethylene (PTFE) sleeve was manufactured to center, prevent slippage, and ensure an even crush when sealing the sapphire window with PTFE o-rings. Detailed construction drawings are provided in **Figure 3-4**.

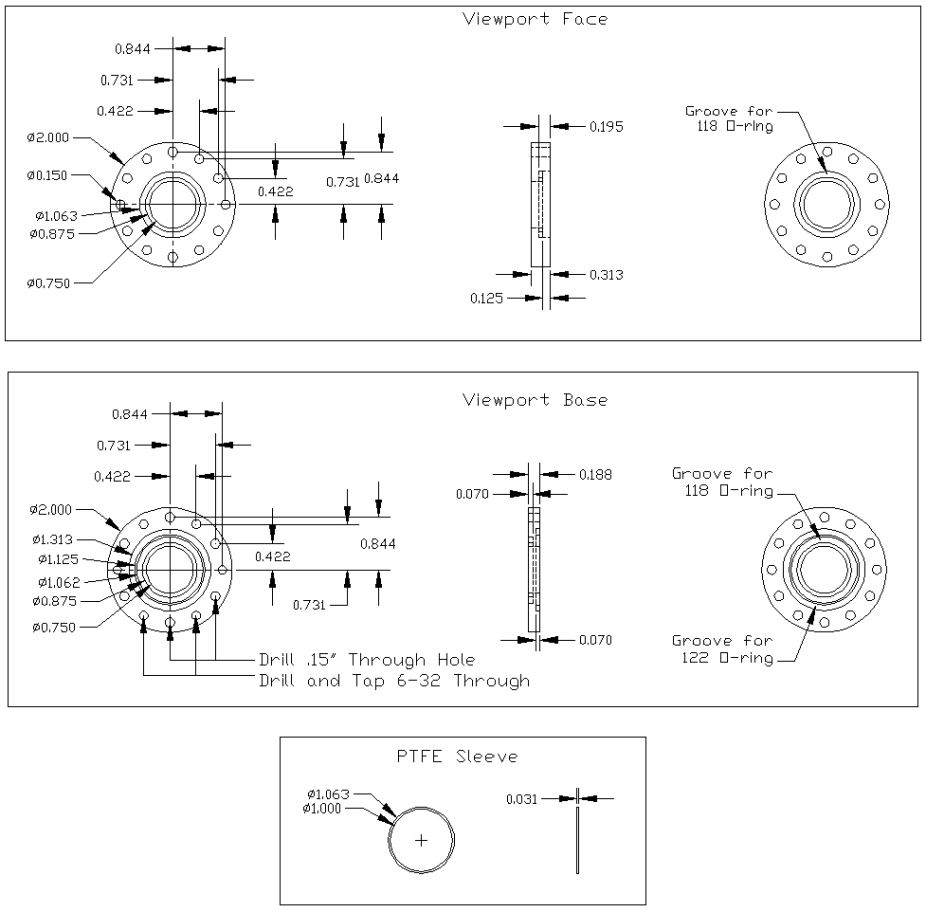

Figure 3-4: Construction drawings for the custom-designed high pressure optical viewport components.

The 1" dia. × 0.235" th. sapphire window (Meller Optics, Inc., Providence, RI) is pressure rated to 850 pounds per square inch (psi), 5.9 MPa, with a built-in 3-fold manufacturer safety factor. 12 mounting points were incorporated into the design with an alternating assembly configuration. Prior to mounting the viewport on the custom-designed detachable face plate, 6 6-32 × 1/2" hex screws were used to secure and seal the sapphire window between the face and base components with the aid of 2 AS568A Dash No. 118 PTFE o-rings. An additional 6 6-32 × 7/8" hex screws and 1 AS568A Dash No. 122 Viton o-ring lubricated with inert ultra high vacuum grease (Apiezon, Manchester, UK) ensured leak-free attachment to the face plate. Optical viewport face and base components were manufactured from 304 SS by the GTCoSMS. The PTFE sleeve was

fabricated from 1” dia. virgin electrical grade PTFE rod stock on a Minitech computer numerical control (CNC) Mini-Lathe/1 (Minitech Machinery Corporation, Norcross, Georgia).

A detachable face plate for mounting the optical viewport was designed with the same 4.5” od. × 0.5” th. form factor as the original cover plate. To add versatility to a limited 0.75” effective viewing dia., the central viewing axis was off-set by 0.625” from the face plate center. Thus, by rotating the face plate when attaching to the main body, different areas of the sample volume become visually accessible. The newly designed face plate was fabricated from 304 SS by the GTCoSMS. **Figure 3-5** provides construction drawings for the viewport face plate and an optical image of the viewport–face plate assembly attached to the modified main body of the hydrate pressure chamber.

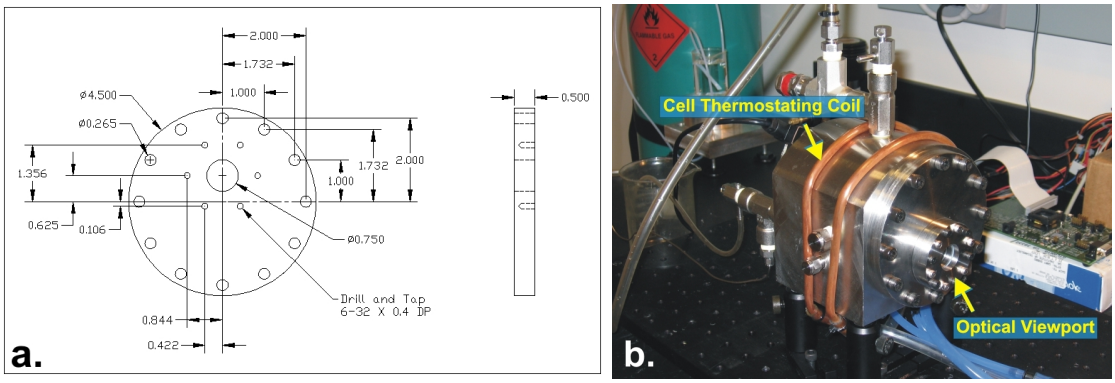

Figure 3-5: (a.) Construction drawings for the detachable viewport face plate, and (b.) optical image displaying the viewport and detachable face plate assembly attached to the main body of the pressure chamber. A cell thermostating copper coil is additionally indicated for later reference.

3.1.4 Fiber-optic Integration for IR Spectroscopic Access

To couple a 300 mm l. × 700 μm dia. (l. is length) solid-core silver halide (AgX, $X = Cl_{0.3-0.4}Br_{0.7-0.6}$) fiber for spectroscopic access through a cross-section of the hydrate chamber, a fiber coupling system with custom-made PTFE ferrules and Swagelok components (Swagelok, Solon, OH) was devised. PTFE ferrules were fashioned from 0.5” dia. virgin electrical grade PTFE rod

stock with an angle of approx. 30° to form a crimp seal around a AgX fiber with the aid of SS 1/8" Swagelok tube fitting (STF) – 1/8" male national pipe thread (MNPT) bored-through connectors. PTFE ferrules were manufactured using a Minitech CNC Mini-Lathe/1. First, a fiber-optic feedthrough was drilled into the center of PTFE rod stock with a 0.280" (#70) drill bit. Then, a CAD Drawing Interchange Format (.DXF) template file was loaded into the Mini-Lathe/1 control software to form a tool path (scaled-up by a factor of 5 for appropriate dimensioning). The tool path was traced under computer control with 0.010" incremental depths of cut with an oversized rear support to ensure material stability during ferrule fabrication. Once the dia. of the forward support was reduced to 1/8", the rear support was manually reduced until a 1/8" dia. was achieved. **Figure 3-6** provides a dimensionless and mirrored representation of the custom ferrule design and dimensioned tool path used for fabrication.

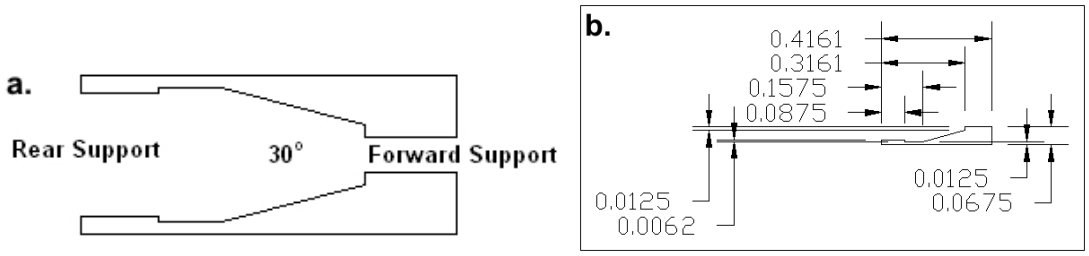

Figure 3-6: (a.) Mirrored and dimensionless representation of the custom PTFE fiber-optic coupling ferrules, and (b.) the dimensioned tool path utilized for CNC fabrication.

To date, the fiber-optic coupling system has provided leak-free IR spectroscopic access to the sample volume of the hydrate chamber throughout a wide variety of experiments with operational pressures > 750 psig (5.2 MPa) during some trials. A maximum operational pressure rating for this configuration has not been determined. Additionally, the fiber remains unsupported inside the pressure chamber beyond the two anchoring points provided by the PTFE ferrules. **Figure 3-7** contains graphical representations of the custom ferrule and Swagelok fiber-optic coupling system and assembly.

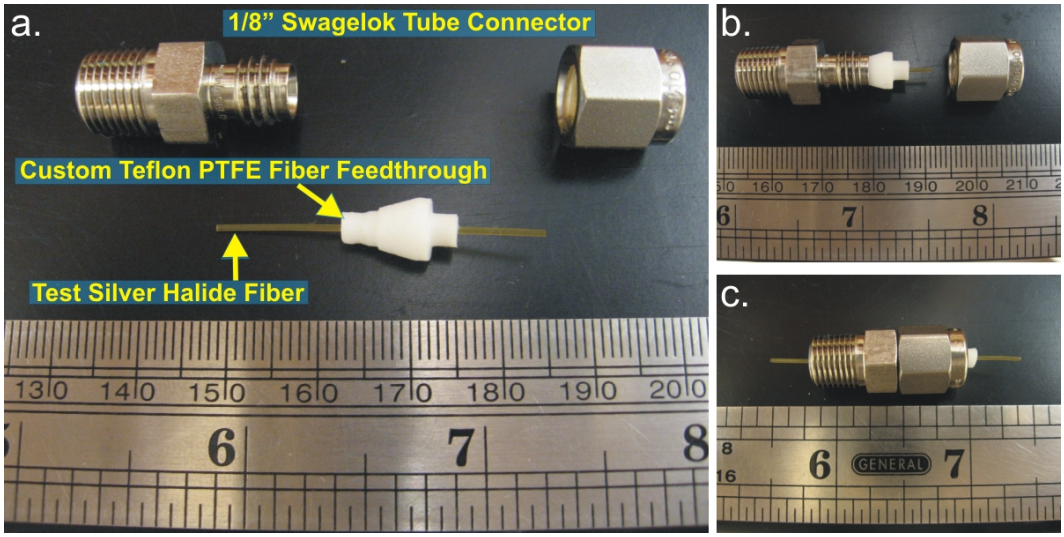

Figure 3-7: (a.) Labeled optical image of the PTFE ferrule and Swagelok fiber-optic coupling system with a 700 µm dia. test section of solid-core AgX fiber. (b. and c.) Additional images displaying assembly of the high pressure fiber feedthrough.

3.1.5 Imaging System for Hydrate Chamber

The imaging system for the hydrate growth chamber utilized an Intel PC Camera (Model CS110, Intel Corporation, Santa Clara, CA) with universal serial bus (USB) interface. The camera was interfaced with a desktop personal computer (PC) and controlled with Dorgem open source webcam capture software.[3] This simple imaging system enables continuous video collection and/or capturing of image sequences at discrete user-defined time intervals. In addition, the date and time of capture can be digitally embedded into the image. Due to the extended length of many hydrate growth and dissociation experiments (up to 28 days), webcam images were typically collected at 30 s intervals to minimize storage space requirements.

To collect optical images inside the hydrate growth chamber, the PC camera height was positioned within several cm of the optical viewport. A fiber light (Fiber-Lite Model 190, Dolan-Jenner Industries, Lawrence, MA) was positioned rearward of the camera and adjusted for coupling light into the chamber through the viewport with minimal glare. Once the hydrate chamber was filled with water, the PC camera was manually focused to ensure optimum image

quality. After hydrate nucleation, the PC camera was occasionally manipulated to re-focus or adjust the viewing angle. During initial studies, the imaging system was operated almost continuously throughout measurement series. However, spectral quality declined due to reduced IR transmission through the AgX fiber from photo-induced darkening with continuous light exposure from the visible blue to ultraviolet (UV) spectral regions.[4] Hence, usage of the imaging system was significantly reduced to intermittent visual inspections of the pressure chamber contents following initial hydrate experiments. In addition, a UV filter was placed in front of the fiber light to reduce transmission of short wavelength radiation into the hydrate chamber. **Figure 3-8** details the typical imaging system setup utilized during a hydrate growth monitoring experiment.

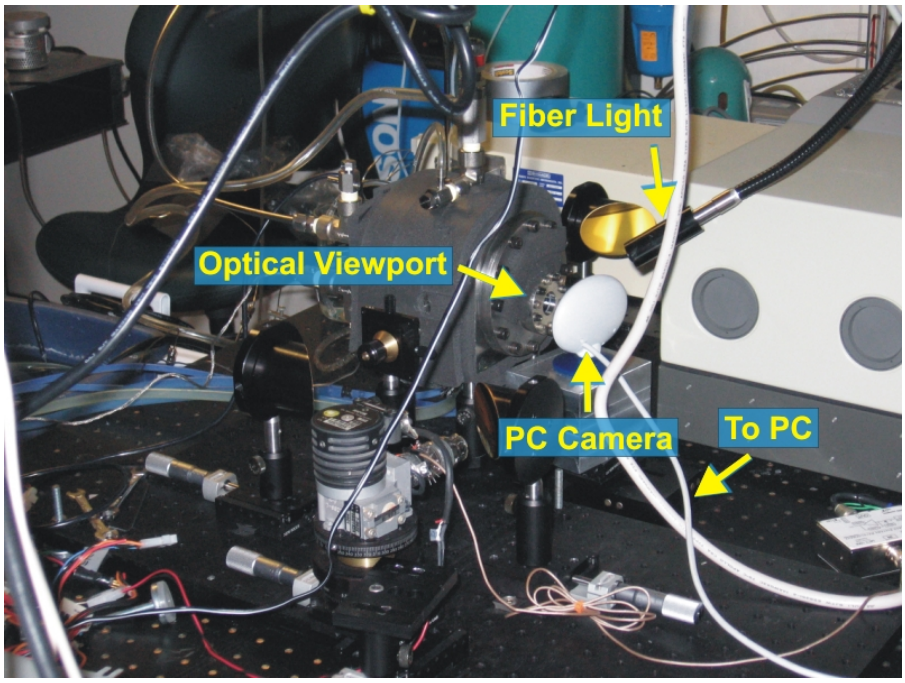

Figure 3-8: Optical image displaying labeled components of the hydrate imaging system.

3.1.6 Cooling System for Hydrate Growth Chamber

Primary cooling of the sample volume is facilitated by a tightly wrapped 1/8" od. × 0.016" wall th. 304 SS coil. The internal cooling coil, providing approx. 9 continuous

loops with 1.5” effective coil length, was formed by hand-wrapping a straight section of 304 SS tubing around a 1.0” od. rod. Loops towards the central section were splayed slightly to allow fiber-optic passage and prevent metal-fiber contact. Extended straight sections for cooling coil terminations provided pressure sealing and tubing attachment points for coolant cycling. The internal cooling coil was pressure sealed by two pairs of Swagelok 1/8” SS ferrules and 1/8” od. – 1/8” MNPT SS bored-through connectors. The semi-permanent cooling fixture was thoroughly cleaned by baking in a vacuum furnace at approx.15 mTorr and 250 °C for a period of 12 hrs. prior to sealing inside the hydrate chamber. **Figure 3-9** provides a representative image, collected by the external imaging system, of the internal cooling coil submersed in water inside the hydrate sample chamber.

Figure 3-9: Optical image of the internal cooling coil inside the sample chamber as visualized through the optical viewport and captured by the hydrate imaging system.

In addition to the internal cooling coil, 2 1/4" od. copper thermostating coils were fitted around the main body of the hydrate chamber to aid in cooling (see **Figure 3-5**). During initial hydrate measurements, insulation was not applied to the main body or rubber tubing used for coolant cycling. However, following initial measurements, 2 layers of 7/16” th. adhesive rubber foam (Thermwell Products Co., Inc., Mahwah, NJ) were applied to the main body to insulate and optimize cooling performance, minimize internal temperature gradients, and prevent moisture condensation on the external surfaces of the pressure cell. Additionally, 0.5” th. un-slit Buna-

N/PVC elastomeric foam rubber tubing insulation was added to most portions of silicone rubber tubing used for cycling coolant to improve cooling efficiency.

The external thermostating coils and the internal cooling coil were operated on individual closed-loop coolant cycles; however, each cycle utilized coolant from the same thermoregulated stock. Zip ties were used to secure silicone rubber tubing onto the terminations of both the internal cooling and thermostating coils to prevent detachment due to backpressure. During initial trials, the cooling system was driven by two submersible aquarium pumps (Models MN404 and MN606, Aquarium Systems Inc., Mentor, OH) for cycling a super-cooled salt water mixture from a manually prepared ice bath contained in a large sump tank. While several measurement series discussed in this thesis were performed with this arrangement, this strategy required continuous attention to sustain adequate system cooling for maintaining hydrate phase equilibrium conditions with respect to the system pressure and host gas supply. Currently, a low-temperature thermostat (Ecoline RE112, LAUDA, Lauda-Königshofen, Germany) with built-in recirculation pump (max. flow 17 L/min.) and a submersible, magnetic drive utility pump (Model 02527, max. flow ~43 L/min., Danner Mfg. Inc., Islandia, NY) supply a solution of an approx. 50:50 mixture of ethlyene glycol and deionized water to the copper thermostating coils and internal cooling coil, respectively. Both pumps were operated continuously to ensure reliable thermoregulated measurement conditions throughout an entire hydrate measurement cycle.

3.1.7 Pressure and Temperature Monitoring System

The pressure and temperature logging system was initially developed using a VERSA1 programmable microcontroller development kit (Goal Semiconductor Inc., Montreal, Quebec, now Ramtron International, Colorado Springs, CO) with a Windows based user interface programmed using Microsoft Visual C++ (Dr. Frank Vogt, Applied Sensors Laboratory (ASL)). The user interface and logging capabilities of the C++ program were later upgraded to record the

temperature probe resistance and enable a user-defined time interval for logging system temperature and pressure (Peter Boezerooij, ASL).

The internal temperature of the hydrate system was monitored with a Model THX-400-NPT-72 1/4" MNPT pipe-plug thermistor probe with a 2252 ohm resistance at 25 °C (Omega Engineering Inc., Stamford, CT). The temperature probe was calibrated for operation in the range of 0 - 100 °C. Curve fitting parameters from a dual exponential decay fit of the temperature calibration data were integrated into the pressure and temperature logging program. The implemented temperature monitoring system is accurate within ±0.5 °C over the calibration range.

Pressure monitoring of the hydrate chamber sample volume was facilitated by a Sensor System Solutions, Inc. (3S, Inc., Irvine, CA) Model 5100 amplified media isolated silicon pressure transducer (Part No. 5100-B2-1000-A-P1) for operation in harsh environments up to 1000 psi (6.9 MPa). The pressure and temperature logging hardware and software contained a built-in pressure calibration for an Advanced Custom Sensors, Inc. (ACSI, now merged with 3S, Inc.) Model 8030-100 pressure transducer. The 3S pressure transducer was implemented due to inadequate operation of the ACSI pressure transducer. As a result, incorrect and systematically biased output pressure values were logged by the C++ program. Hence, a manual pressure calibration was performed for each hydrate measurement series during system pressurization with the supply gas. A minimum of 5 pressure readings were obtained from the outlet pressure gauge on the gas regulator of the supply gas tank and the respective pressure output readings calculated, recorded, and displayed by the Windows based logging program. Thereby, accurate calculations of the system pressure could be made during a hydrate trial and pressure logs could be converted to the correct pressure values following completion of a hydrate measurement series. This calibration procedure provided accuracy within ±5 psi (35 killopascal, kPa). The obtained pressure and temperature accuracies were sufficient to ensure measurement conditions were achieved and sustained within hydrate phase stability for each hydrate experiment performed in

this thesis; however, the pressure and temperature monitoring system should be improved for high-precision and high-accuracy pressure and temperature monitoring during future studies.

3.1.8 Assembly of the Pressure Chamber

In addition to the face plate, 11 access ports enable the integration of various components for pressure and temperature monitoring, gas and liquid input, liquid drainage, and pressure relief valves to depressurize and prevent over-pressurization of the pressure chamber. Unless otherwise specified, all commercial components described with a SS prefix in the part number are Swagelok components made from 316 SS. **Figure 3-10** provides labeled optical images referencing all types of access ports on the main body of the pressure cell.

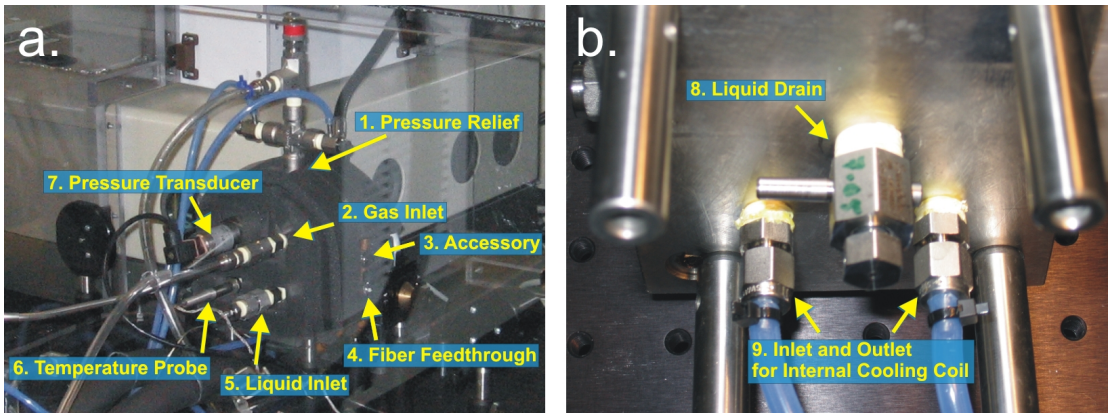

Figure 3-10: Optical images referencing each type of access port on the main body of the pressure chamber for (a.) the rear and sides of the chamber and (b.) the underside of the main body. Zip ties were used to secure silicone rubber tubing onto the inlet and outlet extensions of the internal cooling coil.

The following list describes the assembly and product numbers of components attached to the hydrate chamber for achieving system control and functionality with respect to numbering and labeling in **Figure 3-10**. All male threaded components except for the Swagelok tube fitting for the liquid inlet were wrapped with 2 layers of PTFE tape made for sealing threaded gas lines.

1. Pressure Relief: Multiple pressure relief ports are provided by a SS cross (SS-4-CS) with 4 1/4" FNPT adapters attached to the top of the hydrate chamber with a 1/4" MNPT –

1/4" MNPT hex nipple (SS-4-N). Redundant 1/4" MNPT manual bleed valves (SS-BVM4) enable gas venting while filling and draining solution from the sample chamber, system depressurization backups, and additional liquid filling ports if needed. At the SS cross apex, a proportional pressure relief valve (SS-4R3A5) is used to set the upper pressure limit of the hydrate chamber from approx. 10 – 1000 psig (69 – 6,900 kPa). If the system pressure exceeds the manually set spring tensioned pressure limit on the relief valve, excess gas is vented until pressure is reduced and the spring tension automatically reseats the bleed valve. This ensures safety by preventing over-pressurization and potential failure of the hydrate chamber.

A realistic and potentially hazardous scenario exists if the cooling system was to fail (i.e., power outage) and the internal temperature increased ≥ 8.4 °C during a methane hydrate trial. Cooling failure would result in hydrate dissociation. The phase equilibrium pressures for methane hydrate at temperatures ≥ 8.4 °C are ≥ 6.06 MPa,[1] thereby exceeding the pressure rating for the sapphire window (5.9 MPa). Hence, the maximum allowable system pressure of 1000 psig (6.9 MPa), based on specifications for a properly functioning proportional relief valve, facilitates removal of outgassing methane from the hydrate chamber while maintaining a 2.5-fold safety factor of the sapphire window.

The proportional relief valve was also utilized to initiate hydrate dissociation by gradually and manually depressurizing the hydrate chamber below hydrate phase stability. To guide gas from dissociating hydrate away from the optical setup and into a fume hood, a section of 3/8" id. rubber tubing was attached to the vent port of the proportional relief valve with a 3/8" od. male tube adapter (SS-6-TA-1-4). In addition, silicone rubber tubing extensions were attached to the bleed valve stems for guiding hydrate supply gas away from the hydrate setup from an initial sample chamber purge. Tubing extensions also facilitated leak monitoring of these high duty cycle components.

2. Gas Inlet: The hydrate chamber was brought to pressure by regulating the outlet pressure at the supply gas cylinder with the diaphragm valve of a single-stage high-purity gas

regulator. The supply gas flow rate was roughly adjusted with a needle valve at the gas outlet port. Gas was introduced into the chamber through 1/4" od. SS tubing coupled to the hydrate chamber with a 1/4" nut and ferrule system (SS-400-NFSET). The gas inlet contains a 1/4" MNPT – 1/4" MNPT check valve (SS-4CP2-1) with a 1 psi cracking pressure directly attached to the main body of the hydrate chamber. This allows gas flow into the sample chamber, and prevents depressurization if failure occurs along the gas line. A 1/4" FNPT – 1/4" FNPT hex coupling (SS-4-HCG) was attached to the check valve followed by a 1/4" MNPT – 1/4" STF bored-through connector (SS-400-1-4BT) for coupling to the gas supply tubing.

3. Accessory Port: A 1/4" FNPT port was machined during the initial pressure chamber construction to facilitate system stirring.[2] This access port was not utilized during hydrate measurements; therefore, this port was sealed with a 1/4" MNPT pipe plug (SS-4-P).

4. Fiber Feedthrough: A detailed description of the fiber-optic coupling system was provided in **Section 3.1.4**. In addition to two custom PTFE ferrules, the Swagelok components used for fiber feedthroughs were a pair of 1/8" STF – 1/8" MNPT bored-through connectors (SS-200-1-2BT) with 2 1/8" SS nuts (SS-202-1).

5. Liquid Inlet: The liquid inlet components and assembly were modeled after the gas inlet; however, a 1/4" MNPT – 1/16" STF bored-through connector (SS-100-1-4BT) was utilized for connecting 1/16" od. SS tubing with a 1/16" nut and ferrule (SS-102-1 and SS-100-SET) in replacement of the 1/4" tubing and respective adapter. Aqueous sample solutions were pumped into the pressure chamber through the liquid inlet using a Shimadzu LC-10AD high performance liquid chromatography (HPLC) pump (Shimadzu Scientific Instruments, Columbia, MD).

6. Temperature Probe: The THX-400-NPT-72 temperature probe was connected to the pressure chamber by a 1/4" MNPT fitting.

7. Pressure Transducer: The pressure transducer (Model 5100-B2-1000-A-P1) was attached to the hydrate chamber with a 1/4" MNPT fitting.

8. Liquid Drain: Liquid drainage was facilitated by a manual 1/4" MNPT bleed valve (SS-BVM4) attached to the underbody of the pressure chamber. Drainage was enhanced by opening a similar bleed valve on the pressure relief system for introducing dry air from a compressed air supply. Silicone rubber tubing was attached to the valve stem for guiding solution away from the hydrate setup.

9) Inlet and Outlet for Internal Cooling Coil: The internal cooling coil was integrated into the hydrate chamber via a pair of 1/8" STF – 1/8" MNPT bored-through connectors (SS-200-1-2BT), and sealed with 1/8" SS nuts and ferrules (SS-202-1 and SS-200-SET). The coolant inlet was selected as the port nearest to the cooling source, which was the coil extension closest to the liquid and gas inlets for all spectroscopic hydrate monitoring measurements described in this thesis.

3.1.9 Optics Layout for Hydrate Measurements

The optical setup for *in situ* spectroscopic monitoring of gas hydrate formation and dissociation was built around a Bruker IFS/66 Fourier transform-infrared (FT-IR) spectrometer (Bruker Optics Inc., Billerica, MA). Radiation modulated by the interferometer was guided outside of the spectrometer through a 45 mm od. optical port fitted with an IR transparent ZnSe window with anti-reflective coating (MacroOptica, Moscow, Russia), and then focused onto a polished in-coupling facet of a 700 μm dia. solid-core AgX fiber-optic waveguide by a 2" dia. gold-coated off-axis parabolic mirror with a 3" focal length (Janos Technology, Keene, NH). IR radiation was guided via total internal reflection inside the AgX fiber through a cross-section of the hydrate chamber until reaching the polished out-coupling facet. The emanating divergent cone of radiation was collimated with another 2" dia. off-axis parabolic mirror, and then focused onto a Stirling-cooled mercury-cadmium-telluride (MCT) detector element (Model K508, Infrared Associates, Stuart, FL) with a third 2" dia. off-axis parabaloid. The detected signal was processed with an impedance matched MCT-1000 pre-amplifier (Infrared Associates, Stuart, FL) and

connected to an external input channel at the FT-IR spectrometer. Only commercially available optical mounting components were used for the hydrate setup, which included various posts, bases, clamps, 2 optical breadboards, 5 single-axis translation stages with 25 mm of travel distance, a compact lab jack, and a pair of fiber chucks with fiber-optic positioners. **Figure 3-11** highlights the radiation path through the optical setup utilized for all fiber-optic hydrate monitoring studies reported in this thesis.

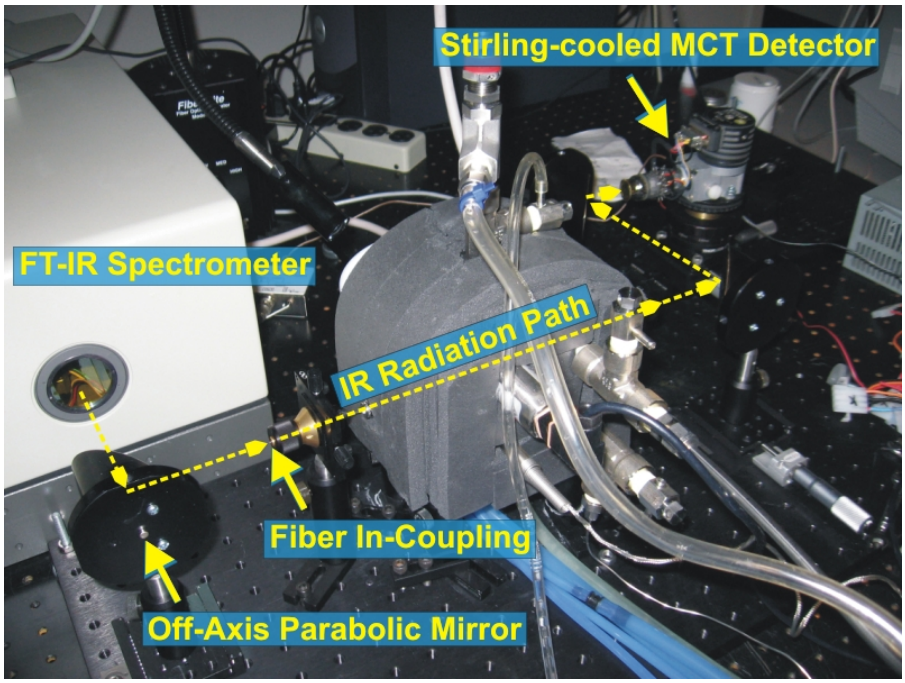

Figure 3-11: Optical image depicting the setup utilized for all IR fiber-optic spectroscopic measurements for monitoring gas hydrate growth and dissociation. The AgX fiber probes a cross-section of the pressure chamber via evanescent field absorption spectroscopy. The dashed (yellow) line indicates the radiation path.

3.1.10 Additional Features of the Hydrate Experimental Setup

Two main features of the most current hydrate setup were incorporated over the course of experimental studies for improving signal stability and the spectral quality. Firstly, a polycarbonate box was constructed to isolate and enable purging of the optical path with compressed dry air for reducing spectral interferences from environmental fluctuations in

humidity and carbon dioxide. The enclosure was constructed from 3/16" th. polycarbonate sheets with 1/2" th. x 1" w. polycarbonate reinforcement members around the edges of each side section. The purge box incorporated various electrical and tubing feedthroughs. In addition, an oversized non-reinforced lid was fitted with tubing adapters for introducing dry air. The encased hydrate setup was purged as to provide a slight positive pressure environment. Although this was not a perfectly sealed enclosure, manual regulation of air flow into the system enabled dynamic compensation for minimizing the spectral impact of environmental interferants. Secondly, the purge box was covered with custom-cut black nylon fabric coverings (0.015" th.) to minimize photo-induced degradation of the AgX fiber from exposure to overhead lighting. **Figure 3-12** displays the most current configuration of the experimental hydrate setup without drapery.

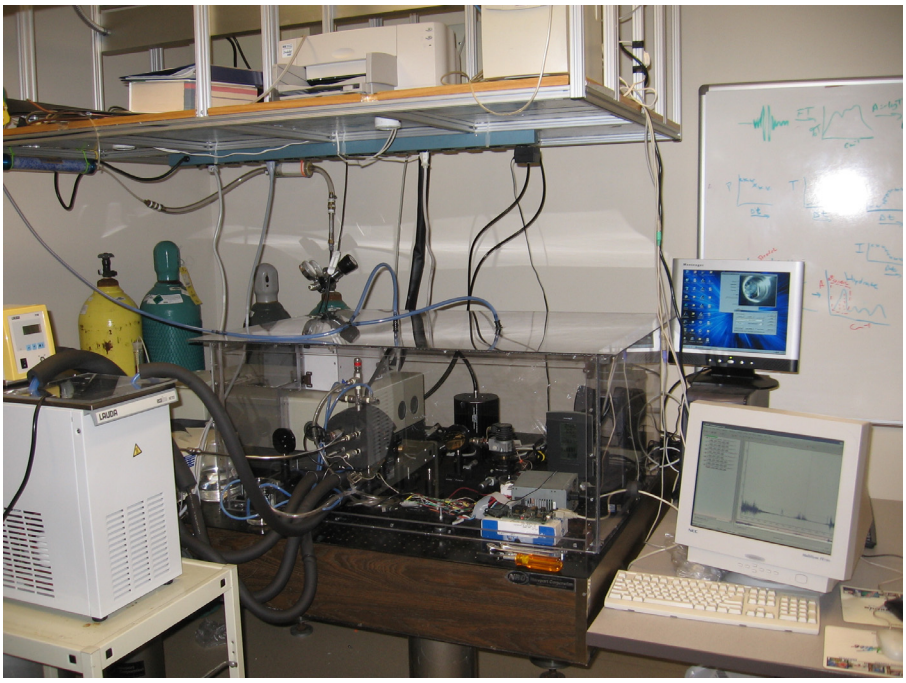

Figure 3-12: Most current configuration of the experimental gas hydrate setup. Two PCs were used during hydrate measurement trials. One PC was utilized for controlling the FT-IR spectrometer and collecting IR spectra. A second PC was used for controlling and collecting data from the imaging and pressure and temperature logging systems.

3.1.11 Concluding Remarks on the Hydrate Monitoring Apparatus

The primary function of the experimental setup developed in this thesis was to provide thermodynamically favorable conditions for gas hydrate formation, while enabling *in situ* spectroscopic monitoring of hydrate growth dynamics with IR fiber-optic evanescent field spectroscopy for the first time. As much of the hydrate work described in this thesis focuses on establishing first principles, some limitations were encountered for controlling and monitoring system pressure and temperature. However, this had minimal impact on the results presented in this thesis, and has been factored into data analysis and interpretation when appropriate in **Chapter 4**.

Although this setup was continuously improved and served well for many experiments, additional modifications can be envisioned to improve and enhance the system capabilities. Suggested areas for improving the experimental setup in continuation of studies at simulated deep-sea conditions include; (1) integrating a mass flowmeter to monitor gas incorporation into hydrate structures, (2) improving cooling efficiency and capacity by upgrading the cooling coil to larger diameter tubing with more coils, which would increase the advective surface area, improve pump efficiency, and minimize thermal gradients within the sample volume, and (3) upgrade the temperature and pressure logging hardware and software to improve accuracy for controlling and monitoring the sample chamber and enable close examination of hydrate phase equilibria.

3.2 Horizontal Attenuated Total Reflection Accessories and Optical Configuration

In addition to the application of fiber-optic waveguides for monitoring gas hydrate growth via evanescent field absorption spectroscopy, a significant number of experiments throughout this thesis have utilized planar internal reflection elements for IR-ATR spectroscopic measurements in a configuration commonly referred to as horizontal ATR (HATR). A variety of planar waveguide geometries and IR transparent materials are commercially available, thus enabling a wide array of experimental optical configurations.[5-8] This section provides a general overview and

description of the equipment and configuration frequently used for the HATR experiments described in subsequent chapters.

In this thesis, only polycrystalline trapezoidal ZnSe ($n_D = 2.43$ at $\lambda = 5$ μm) waveguides with dimensions of 72 mm × 10 mm × 6 mm (l. × w. × th.), 45° beveled radiation coupling facets, and 6 effective reflection regions along the measurement surface were used. ZnSe waveguides were mounted in commercially available HATR accessories allowing samples to be deposited onto the longer waveguide surface for spectroscopic evaluation. **Figure 3-13** provides a scaled CAD 3-D rendering of radiation propagation through a typical trapezoidal waveguide displaying discrete 'active' sensing regions along the measurement surface with respect to areas of evanescent field generation resulting from internally reflected radiation.

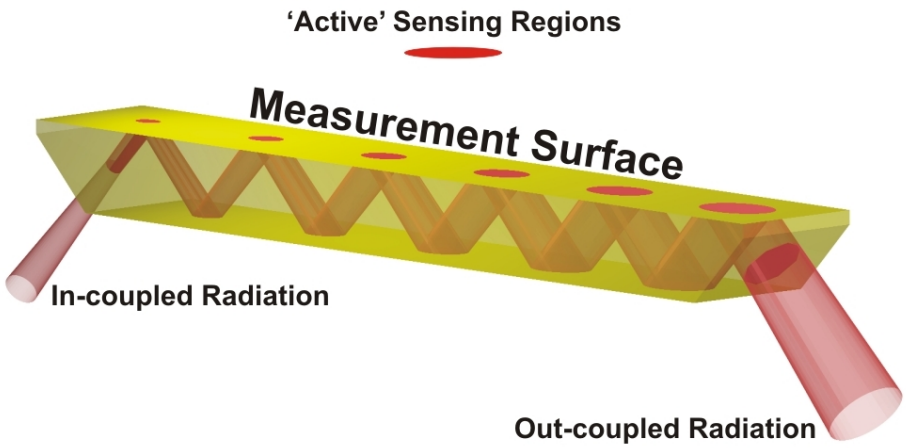

Figure 3-13: Scaled CAD 3-D rendering of a 72 × 10 × 6 mm ZnSe waveguide showing radiation focused onto the in-coupling facet and transmitted by total internal reflection until exiting the waveguide. 'Active' sensing regions are generated at each area of internal reflection where sample molecules interact with the evanescent field at the waveguide surface. **Chapter 7** provides a combined experimental and simulation approach for characterizing sensing regions along planar waveguide surfaces. (Figure adapted from Dobbs and Mizaikoff).[9]

Two equivalent Specac Gateway in-compartment HATR optics base units (Specac Inc., Woodstock, GA) were utilized for HATR measurements described in this thesis. One optics unit was aligned for use with a Bruker Equinox 55 FT-IR spectrometer (Bruker Optics, Billerica, MA), and the second base unit was aligned for use with a Bruker IFS 66/S FT-IR spectrometer.

The most commonly used crystal mounting accessory was a Specac Gateway trough top-plate (Specac Inc., Woodstock, GA). The Specac HATR accessories and Bruker Equinox 55 FT-IR spectrometer were utilized for all HATR measurements described in **Chapters 5 and 6**. For HATR measurements outlined in **Chapter 7**, a Bruker IFS 66/S FT-IR spectrometer with the respective HATR optics were used. In addition, an equivalent crystal mounting accessory was implemented for **Chapter 7** measurements by removing a fluids-coupling plate from a custom flow-cell. **Figure 3-14** contains optical images of the HATR accessories mounted in the Equinox 55 and IFS 66/S FT-IR spectrometers, and includes a schematic diagram of the radiation path through the optics unit with a mounted HATR crystal.

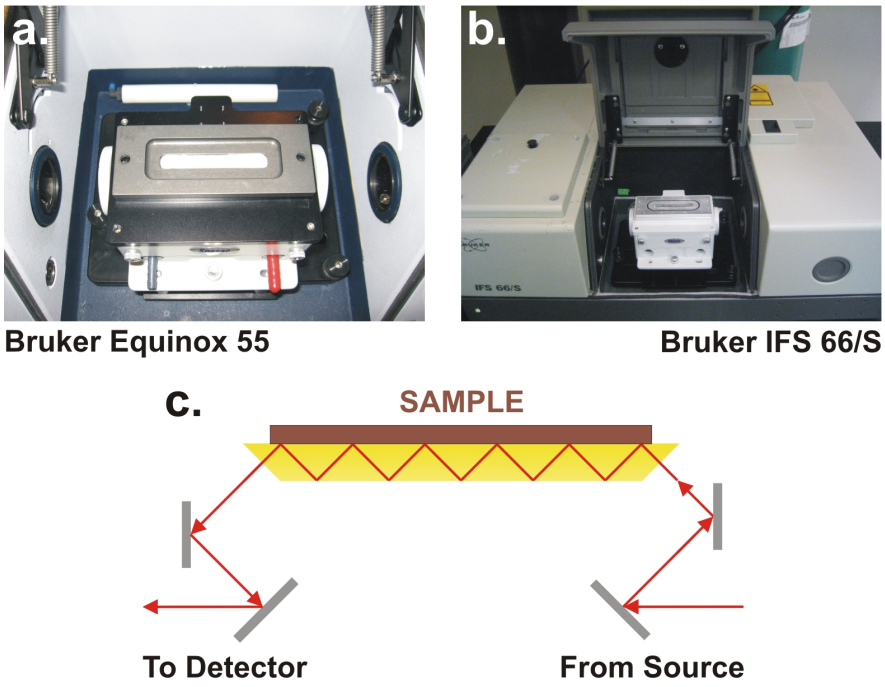

Figure 3-14: (a.) Optical image of HATR accessories placed inside the sample compartments of a Bruker Equinox 55 FT-IR spectrometer with trough-top plate assembly mounted onto the optics base unit and sample deposited onto a ZnSe crystal. (b.) Optical image displaying HATR components inside a Bruker IFS 66/S FT-IR spectrometer. (c.) Schematic diagram depicting sample placement onto a HATR waveguide with the radiation path traced through the optics base unit and HATR crystal.

HATR optical components and configurations displayed in **Figure 3-14 (a.)** and **(b.)** were used for the majority of all non-hydrate spectroscopic measurements described in the following

chapters of this thesis. Whenever an alternative configuration was used, this is indicated, and a more thorough experimental description is provided. Furthermore, specific experimental details are provided with respect to the various experiments performed throughout this thesis.

3.3 References

1. E. D. Sloan Jr., *Clathrate Hydrates of Natural Gases*, (Marcel Dekker, Inc., New York, 1998).

2. N. Pennington, *Development of Chemical Infrared Sensors for the Marine Environment: First Investigations for a Deep Oceanic Sensor for Methane*, School of Chemistry and Biochemistry, Georgia Institute of Technology, Atlanta, p. 76, (2003).

3. F. Fesevur, *Dorgem*, http://dorgem.sourceforge.net/ (August 2005).

4. R. Chen, A. Katzir, A. Levite, F. Moser, and D. Weiss, *Absorption and Luminescence of Silver Halide Optical Fibers*, Journal of the Optical Society of America B: Optical Physics **3**, 696 (1986).

5. *Harrick Scientific Products, Inc.*, http://www.harricksci.com/ (July 2007).

6. *Specac Inc.*, http://www.specac.com/ (July 2007).

7. *PIKE Technologies*, http://www.piketech.com/ (July 2007).

8. *MacroOptica LTD*, http://www.macrooptica.com/ (July 2007).

9. G. T. Dobbs and B. Mizaikoff, *Shining New Light on Old Principles: Localization of Evanescent Field Interactions at Infrared-Attenuated Total Reflection Sensing Interfaces*, Applied Spectroscopy **60**, 573 (2006).

CHAPTER 4

FIBER-OPTIC MID-IR SPECTROSCOPY FOR MONITORING GAS HYDRATES

This chapter summarizes the development and application of fiber-optic MIR sensing strategies for monitoring gas hydrate formation and dissociation grown from solution in laboratory experiments. First, a general introduction to the significance of naturally occurring gas hydrates in addition to an overview of the molecular characteristics, thermodynamics, and models describing the nucleation and growth of gas hydrates is provided. Previous applications of IR spectroscopy for investigation of different water phases, including liquid, ice, and gas hydrate, are also discussed. Detailed descriptions of data evaluation strategies, data interpretation, and data transformations for spectroscopic monitoring of gas hydrate dynamics are discussed throughout this chapter. In addition, initial feasibility assessments address various aspects regarding the potential extension of the developed monitoring strategies into oceanic environments. Finally, an expanded version of the reaction kinetics model for describing gas hydrate growth mechanisms will be introduced from considerations to published literature.

4.1 Motivation

Throughout this work, the underlying motivation for developing spectroscopic sensing strategies to monitor gas hydrate growth dynamics has centered on potential applications for the deployment of deep-sea MIR chemical sensing platforms. Due to the harsh, isolated environments in which oceanic gas hydrate deposits exist, there is a standing need to develop sensor technologies that will facilitate long-term accessibility to monitor and improve current assessments as to the occurrence, prevalence, and dynamics of gas hydrates. Currently, there is particular interest regarding the stability and dynamics of disseminated gas hydrate formations within sediment pore spaces, which are particularly susceptible to minor fluctuations in environmental conditions (i.e., hydrostatic pressure and temperature).[1] Throughout the GoM,

seasonal changes and/or sustained sub-surface loop currents or eddies can raise bottom water temperatures several °C.[1] A rise in seawater temperature has the potential to significantly alter hydrate stability, which can lead to widespread catastrophic dissociation of gas hydrate deposits throughout sediment fractions. Such events are of particular concern for seafloor stability as well as the potential for enabling the rapid escape of large quantities of methane, a primary greenhouse gas, into Earth's atmosphere.

The initial project goal consisted of the development and demonstration of IR spectroscopy as a sensing strategy for monitoring the growth and dissociation of gas hydrate structures through phase-dependent transformation in IR absorption signatures of water. From this, three primary foci are addressed within this thesis: (1) demonstrate the application of IR spectroscopy to monitor gas hydrate growth from solution within a controlled laboratory setting at relevant temperatures and pressures for oceanic gas hydrate occurrences, (2) establish robust data evaluation routines, and (3) assess the potential for extending the developed spectroscopic sensing strategy into oceanic environments.

4.1.1 Clathrate Hydrates of Natural Gases

Clathrate hydrates of natural gases (gas hydrates) describe a diverse classification of structures primarily composed of water molecules oriented in solid, cage structures that are filled by small, guest molecules (i.e., methane, ethane, and carbon dioxide).[2] The initial discovery of gas hydrate structures is credited to Sir Humphrey Davy for the initial description of chlorine hydrate in 1810.[2] Since then, an extensive amount of research has addressed many aspects of gas hydrates including the molecular characteristics, physical properties, thermodynamics, natural occurrences, and growth mechanisms.[2] The following sub-sections introduce the most important aspects of gas hydrate research relevant to the studies described in this thesis.

4.1.1.1 Naturally Occurring Gas Hydrates

Naturally occurring gas hydrates are of significance for three primary reasons: (1) as geohazards, (2) potential alternative energy sources, and (3) impact on regulation of global climate.[1-8] A wide range of estimates have been generated to quantify the amount of methane carbon sequestered in naturally occurring gas hydrates with a medial estimate of $\sim 10 \times 10^{18}$ g as reviewed by Kvenvolden in 2002.[2, 3, 5, 8] The immensity of this value becomes readily significant when contextualized; it is more than twice the amount of carbon contained in all known world-wide reservoirs of coal, oil, and natural gas, combined.[2, 3]

Kvenvolden provides an in-depth consideration regarding the three primary issues surrounding oceanic gas hydrates.[4] Currently, the greatest concern regarding oceanic gas hydrates is the potential impact as a geohazard from disruption to seafloor stability resulting from dissociation. In light of global warming trends, the significant methane quantities sequestered within gas hydrates has generated research interests focusing on assessing the relevance, significance, and potential influence of oceanic hydrates on global climate.[1, 3, 5, 7] Recent studies have revealed the capability of methane released from rapid gas hydrate eruptions to enter the atmosphere, which has significant implications concerning the role of oceanic hydrates in the global carbon cycle and the natural regulation of global climate.[1-5, 7, 9-18] Considerable research efforts are also focused on developing economically viable technologies for extraction of gas hydrates as an alternative energy resource.[2, 4, 6] Advances have been made on that front; although, realization of harvesting naturally occurring gas hydrates as a sustainable and economically feasible energy supply is likely years away.[2, 4, 6]

4.1.1.2 General Molecular Characteristics of Gas Hydrate Structures

There are currently three well-known forms of gas hydrate structures; structure-I (sI), structure-II (sII), and structure-H (sH), all of which have been found to occur naturally within the GoM.[2, 18, 19] However, sI and sII hydrates are the most commonly observed structures found in oceanic environments.[2, 8, 18] Water is the primary molecular component of gas hydrates, and each structure

is composed of different cages.[2] sI and sII hydrates have two cages (small and large), whereas sH has three cages (small, medium, and large).[2] Each cage is constructed of either square, pentagonal, and/or hexagonal faces formed by networks of hydrogen-bonded (H-bonded) water.[2] A widely adopted nomenclature for cage structures follows the description; n_i^{mi}, where n_i is the number of sides for face type "i" and m_i is the number of faces with n_i sides.[2] For example, the small cage for sI hydrate has 12 pentagonal faces represented as 5^{12}. **Table 4-1** contains the general structural characteristics for the cage units respective to each hydrate classification as summarized by Sloan.[2]

Table 4-1: Cage characteristics for the three known clathrate hydrate structures of natural gases. Table adapted from Sloan.[2]

	sI		**sII**		**sH**		
Cavity	Small	Large	Small	Large	Small	Medium	Large
Cavity Faces	5^{12}	$5^{12}6^2$	5^{12}	$5^{12}6^4$	5^{12}	$4^35^66^3$	$5^{12}6^8$
Number per Unit Cell	2	6	16	8	3	2	1
Average Cavity Radius, Å	3.95	4.33	3.91	4.73	3.91	4.06	5.71

From **Table 4-1**, the molecular structuring of cages and unit cell composition for the three types of gas hydrate are provided. Structurally, each hydrate classification is characteristically different from the most common form of solid water, ice Ih.[2] In ice Ih, one water molecule is H-bonded to four others with tetrahedral angles in lattice networks of puckered hexagonal rings (O-O-O lattice angles of 109.5°).[2] Methane hydrate can potentially store up to 164 times the quantity of an equivalent volume of methane gas at standard temperature and pressure.[2] However, gas incorporation into hydrate structures is non-stoichiometric, and as a general rule, > 95 % of small cages and > 50 % of large cages will be occupied by a guest molecule.[2] In this thesis, only sI and sII hydrates were studied; thus, only sI and sII will be considered from here on. Additionally, Sloan provides a thorough overview regarding well-established and state-of-the-art advances with respect to many aspects of gas hydrate research including; structural, molecular, and physical characteristics/properties, analytical methodologies, and naturally occurring gas hydrates.[2]

4.1.1.3 General Characteristics of Methane, Ethane, and Propane Hydrates

In this thesis, only simple gas hydrates (hydrates with one type of guest molecule) of methane, ethane, and propane were evaluated. The simple hydrates of methane, ethane, and propane have been extensively studied.[2] It has been generally well-established that the guest molecule size and the supply composition of guest molecules influence the gas hydrate structure (i.e., sI or sII).[2] The gas hydrate structure for simple hydrates of methane and ethane is sI; whereas, sII is the corresponding structure of simple propane hydrates.[2] In simple hydrates, methane fills both large and small sI cages, ethane fills only the large sI cage, and propane fills only the large sII cage.[2] In oceanic environments, sI hydrate is often found when methane, ethane, and other sI forming gases of simple hydrates (i.e., CO_2) are in abundance, typically > 99 %.[2] However, sII hydrate is often found when propane and/or other larger sII forming gases (i.e., isobutane) are present and account for as little as ~1 % of the supply gas composition.[2]

Gas hydrate stability is greatly influenced by pressure, temperature, and gas composition.[2] Extensive and multiple studies have resulted in generation of fundamental phase equilibria for methane, ethane, and propane hydrates grown from solution with deionized water, which have been reviewed in Sloan.[2] In this work, gas hydrates were grown from solution with either deionized water or surfactant solutions prepared with 380 ppm (mg/L) sodium dodecyl sulfate (SDS). SDS acts as a low entropy hydrate nucleation catalyst, and is currently not known to influence the thermodynamic stability of gas hydrates.[20]

Throughout this work, gas hydrates were typically grown at temperatures ranging between ~0 °C and ~4 °C. **Figure 4-1** provides published values (reviewed in Sloan) for liquid water (Lw)-hydrate (H)-vapor (V) phase boundaries respective to the simple hydrates of methane, ethane, and propane grown from deionized water.[2]

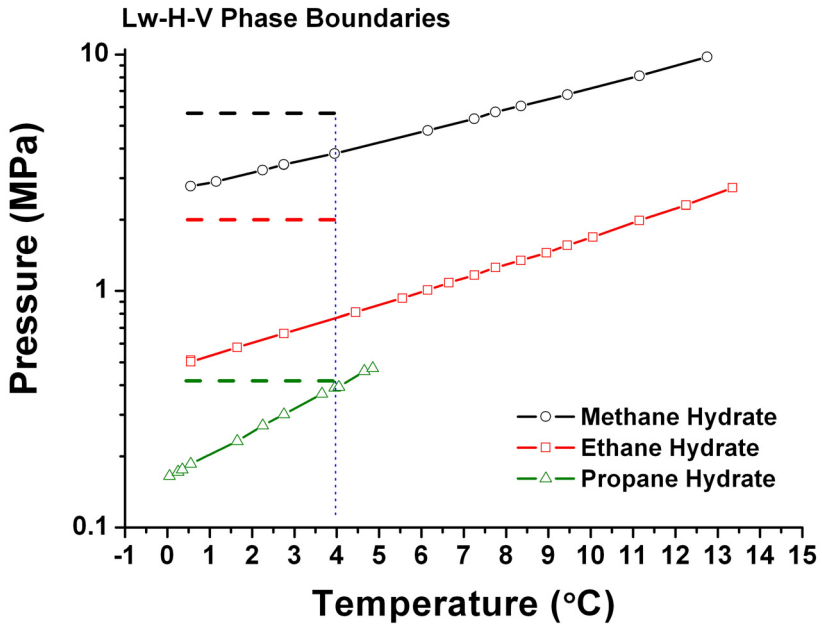

Figure 4-1: Liquid water (Lw)-hydrate (H)-vapor (V) phase boundaries for simple methane, ethane, and propane hydrates in deionized water as reviewed by Sloan.[2] In this work, gas hydrates were grown between ~0 °C and ~4 °C. Dashed lines represent ceiling operational pressures for hydrate trials with respect to each guest gas.

Targeted experimental conditions for the growth of gas hydrates in this work are indicated in **Figure 4-1** with ceiling temperature (dotted line) and pressure limits (dashed lines). Pressure limits were established prior to experiments for two reasons; to prevent liquefaction of ethane and propane gases and maintain safe operation during methane hydrate trials, which was dictated by the pressure rating of the sapphire viewing port (850 psi, 5.86 MPa). Temperatures were maintained below 4 °C to ensure favorable hydrate growth conditions during measurement trials. Although gas hydrates grown from natural gas mixtures (i.e., methane, ethane, and propane mixtures) were not examined in this work, the Lw-H-V phase boundary of simple methane hydrate requires greater pressures for hydrate stability than that required to form mixed gas hydrates with natural gas mixtures. In context to the MC118 gas hydrate ecosystem, a comparable water depth of approx. 890 m cannot be achieved with the current experimental setup due to pressure limitations. However, the experimental setup enables simulation of oceanic depths to

approx. 600 m, which exceeds environmentally relevant pressures for documented occurrences of oceanic gas hydrates at other sites within the GoM (i.e., at approx. 440 m).[1]

4.1.1.4 Cluster Nucleation and Kinetic Growth Models for Gas Hydrates

There is an extensive body of literature reviewed by Sloan addressing many aspects of gas hydrate growth and dissociation. A few examples include evaluation of factors influencing hydrate growth in natural environments (i.e., influence of biosurfactants and sediment pore spacing),[2, 21, 22] the promotion of hydrate growth in the laboratory (i.e., hydrate storage),[20] and inhibition of gas hydrate growth (i.e., preventing blockage in oil pipelines).[23-25] Despite numerous specific interests throughout the literature, two general models have been proposed to describe the processes of gas hydrate nucleation and growth mechanisms governing the kinetics of gas hydrate formation in solution.[2, 26-28] Each model will be introduced in this section to facilitate a general overview of current hypotheses and establish common terminology used throughout this chapter. In addition, an expansion of the described reaction kinetic model of Lekvam and Ruoff is proposed in **Section 4.4**.[26, 27]

The Cluster Nucleation Hypothesis for Gas Hydrates:

In gas hydrate experiments, once thermodynamic conditions amenable to hydrate stability have been achieved, a latent time period (induction time) precedes hydrate nucleation. Recently, Sloan and colleagues proposed the cluster nucleation hypothesis, which describes the nucleation of gas hydrate through the agglomeration of labile hydrate clusters until a critical cluster size has formed to initiate bulk nucleation and continued growth of gas hydrate.[2, 28] This model facilitates a generalized mechanism for hydrate nucleation whereby nucleation clusters may be formed at any location (not just the liquid-vapor interface) within a reaction vessel provided the required molecular components are present.[2, 28] **Figure 4-2** includes an adapted graphical representation of the cluster nucleation model.

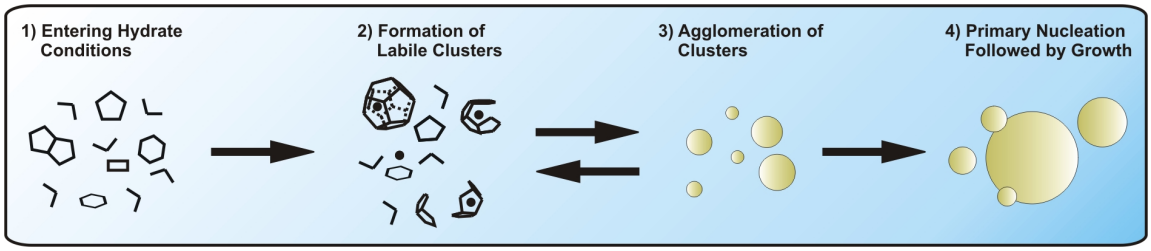

Figure 4-2: The cluster nucleation hypothesis proposed by Christiansen and Sloan.[28] Upon entering hydrate conditions with no gas in solution (1), gas is readily solvated by liquid water coupled with the formation of higher-order liquid water structures including labile hydrate cages (2), labile clusters agglomerate through sharing of hydrate-like faces and increase solution entropy (3), agglomeration continues until a critical cluster size initiates primary nucleation followed by rapid hydrate growth (4). Figure adapted from Christiansen and Sloan.[2, 28]

Following primary nucleation in laboratory experiments, hydrate growth usually ensues very rapidly (catastrophic growth) for a period of several hours. Hydrate growth eventually slows as the majority of liquid water has transformed into hydrate structures. The slow conversion of trapped water (interstitial water) can continue for many days as observed in current work.

Reaction Kinetic Model for Gas Hydrate Formation in Liquid Water:

Extensive considerations have addressed various factors influencing the rate of gas hydrate nucleation and formation with an in-depth overview provided by Sloan.[2] In 1993, Lekvam and Ruoff proposed a reaction kinetic (RK) mechanism characterizing the growth of methane hydrate from liquid water and methane gas.[26, 27] The RK model is comprised of five pseudoelementary processes describing the primary mechanisms governing the nucleation and rate of gas hydrate growth. The pseudoelementary elements contain fundamental components similar to those described by the cluster nucleation hypothesis; hence, **Figure 4-3** contains a graphical representation of the RK model with incorporation of graphical elements from the cluster nucleation hypothesis.

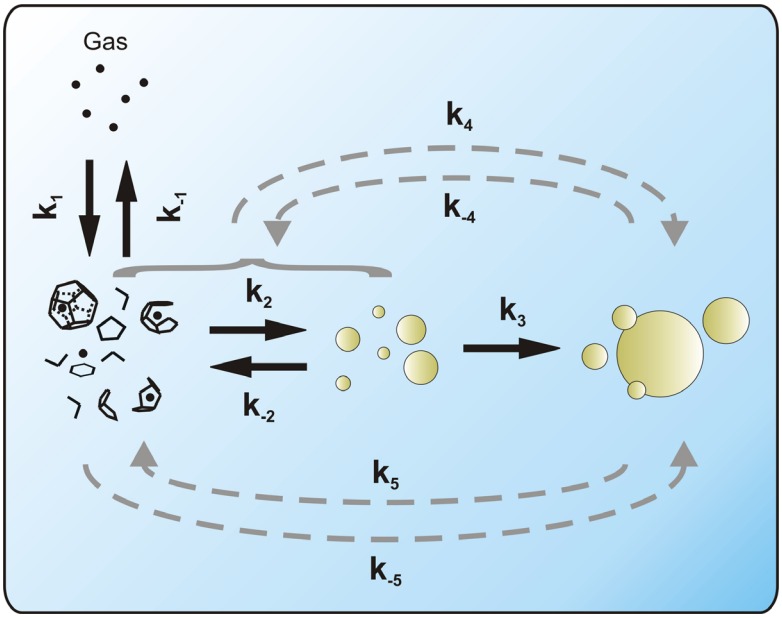

Figure 4-3: The reaction kinetic (RK) model for gas hydrates grown from liquid water as proposed by Lekvam and Ruoff with graphical representations following the cluster nucleation hypothesis.[2, 26-28] ($k_1 \leftrightarrow k_{-1}$) dissolution of gas by water in hydrate conditions with formation of oligomeric precursors (N), ($k_2 \leftrightarrow k_{-2}$) uncatalyzed formation of hydrate from N precursors, ($\rightarrow k_{-3}$) primary nucleation of gas hydrate, which results in autocatalysis of the growth mechanisms indicated with ($k_4 \leftrightarrow k_{-4}$) and ($k_5 \leftrightarrow k_{-5}$).

The RK model, with integrated cluster nucleation hypothesis (**Figure 4-3**) illustrates primary hydrate growth mechanisms with respective microscopically reversible rate constant designations, which enables generation of finite mathematical solutions.[2, 26-28] As described by Lekvam and Ruoff; after dissolution of gas in water (k_1), oligomeric precursors (N) form and hydrate (H) grows in an uncatalyzed process (illustrated as k_2) until a critical nucleus forms, which initiates primary nucleation (k_3).[26, 27] Once primary nucleation occurs, two autocatalytic growth mechanisms are activated (indicated as dashed arrows in **Figure 4-3**) accounting for the continued formation of gas hydrate.[26, 27] The predominant growth mechanism following primary nucleation is the rapid conversion of previously formed N precursors (k_4).[26, 27] This is illustrated in **Figure 4-3** to include both incomplete hydrate-like precursors and sub-critical hydrate nuclei through incorporation of cluster nucleation hypothesis descriptions.[2, 26-28] In addition, the reaction of liquid water and gas facilitates the secondary growth mechanism, which becomes rate limiting

for the conversion of trapped, interstitial waters following the initial rapid growth.[26, 27] Additional considerations and proposed expansions to this model are addressed in **Section 4.4**.

4.1.2 IR Spectroscopy and Water

With several exceptions, the application of IR spectroscopy has been historically limited in gas hydrate research, which is likely results from the strong IR absorption of liquid water encountered during conventional transmission-absorption meaurements.[2, 29-36] However, transmission-absorption configurations have been utilized to investigate clathrate hydrate films grown from vapor deposition and epitaxial growth on highly reflective surfaces in vacuum chambers.[29-36] Formation of gas hydrates in these conditions has restricted the growth of simple hydrates for many of the natural gases, such as methane.[29-36]

Recently, an IR-ATR study compared the spectral profiles of CO_2(gas) and CO_2(aqueous) with that of CO_2(hydrate) for simple, sI CO_2 hydrates grown from aqueous solution.[37] Although the phase-dependent transformation of water absorption features were not reported; a significant advance was realized by validating the capability of ATR techniques to spectroscopically interrogate gas hydrates grown from solution by circumventing sample thickness limitations of conventional transmission-absorption methods. This is achieved by confining the interaction of light and sample to the evanescent field penetration depth (typically < 2.5 μm). Despite this achievement, a detailed description of the spectroscopic setup was not provided (i.e., waveguide material, geometry, pressure coupling, etc.).

In 2004, Zhang and Ewing reported a detailed evaluation of IR-ATR spectra for simple, sI SO_2 hydrates.[38] Hydrates were grown from a liquid water film condensed on the measurement surface of a cooled, single-bounce germanium prism. The range of pressure and temperature conditions for investigating SO_2 hydrate formation were from -20 °C – 10 °C and 5 – 900 kPa (0.7 – 13 psi). In addition to a thorough treatment of SO_2 absorption features, the authors compared the IR

absorptions of water for ice (Ih) and the respective sI hydrate. Examination of the water features revealed only minor differences in the bandwidth for O-H stretch (ν_{OH}) features.[38]

4.1.2.1 The IR Absorption of Liquid Water

In this work, little or no absorption features characteristic to guest molecule occupancy in gas hydrate structures were observed in IR spectra. Hence, the focus of hydrate monitoring is centered on evaluation of the strong, phase-dependent IR absorption signatures of water. The IR spectrum of water, liquid or solid, is very complex. Many IR studies have documented the correlation of spectral changes and structuring of water with respect to temperature and phase transitioning from liquid to solid.[38-65] Various molecular level interpretations and treatments concerning the IR absorption features of water have been proposed in the literature. Molecular-descriptions respective to each absorption feature, spectral changes observed during the phase transitioning of water from liquid to solid (ice or hydrate), and a detailed account of data evaluation strategies developed for monitoring gas hydrate growth and dissociation in the presented studies are discussed in **Section 4.3**. In this section, only general band assignments and qualitative physical descriptions of the IR spectrum for liquid water are presented. **Figure 4-4** contains a representative fiber-optic IR-ATR spectrum for liquid water collected during this work for point of reference.

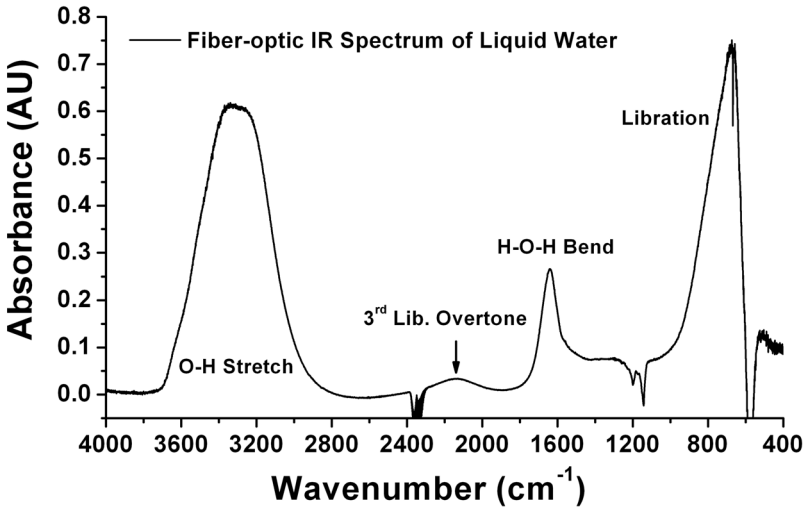

Figure 4-4: The IR spectrum of liquid water as collected with a silver halide fiber-optic waveguide in this work. Conventional vibrational mode assignments are provided, indicating the four major absorption features of water. Minor atmospheric CO_2 (~2350 cm^{-1}) and PTFE features (from fiber feedthroughs at ~1150 cm^{-1})are observed as negative absorption bands relative to a reference spectrum of air at room temperature. The detector cut-off occurs at ~680 cm^{-1}. This spectrum is an average of 250 sample scans collected at 0.5 cm^{-1} resolution. (Lib. = Libration).

The four primary IR absorption features of liquid water can be visualized in **Figure 4-4**. A very intense, broad absorption feature is observed from 3750 – 2750 cm^{-1} respective to O-H stretch (ν_{OH}) features. The second and lowest intensity absorption from approx. 2375 – 1875 cm^{-1} is labeled as the 3rd libration overtone ($3\nu_L$); however, it has also been designated as the combination band from the H-O-H bend and libration bands ($\nu_2 + \nu_L$). In this thesis, the $3\nu_L$ assignment is adopted for consistency. The strongly absorbing H-O-H bend mode (ν_2) occurs from 1750 – 1500 cm^{-1}, and the libration (ν_L) or frustrated rotation feature exhibits an intense absorption feature < 1000 cm^{-1}. The ν_L peak maximum (~675 cm^{-1})[62] cannot be fully resolved for liquid water as a result of the detector cut-off frequency.

4.1.2.2 Influences on the IR Absorption of Liquid Water

The IR absorption features of water are readily influenced by changes in temperature (i.e., $3\nu_L$ blue shifts approx. 1 cm^{-1}/°C with decreasing temperature), and have been a topic addressed within numerous studies.[39-41, 48, 50, 51, 54, 57, 60-65] Temperature influences are addressed more

specifically in the ensuing discussions. In addition to temperature, salinity, and alkalinity (or pH) are also known to perturb the IR absorption behavior of water.[66-74] In this work, only deionized water and dilute surfactant solutions were utilized for the growth of gas hydrates; hence, further considerations to the spectral impact of relevant environmental constituents are expected to enable enhanced data evaluation and interpretation upon extension of the described IR monitoring strategies into oceanic environments. Pressure has also been demonstrated to impart spectral deviations in the O-H stretch region; generally > 10 MPa.[75] In current studies, only a slight increase in the absorption intensity of water was observed during initial system pressurization. This has been attributed to the pressure seating of PTFE ferrules, whereby water was pushed into void spaces around the PTFE-fiber seal. No other discernable pressure related influences in the IR absorption behavior of water were observed throughout this work. The maximum operational pressure for the utilized experimental setup is < 5.9 MPa; therefore, the impact of pressure was not considered an influential factor in described studies. Furthermore, pressure is anticipated to have minimal spectral impact for monitoring oceanic hydrates occurring < ~1000 m of water depth (e.g., water depth at MC118 of ~ 890 m corresponds to 8.9 MPa).

Minor IR absorption features characteristic of SDS were observed following hydrate nucleation during trials with surfactant solutions (SDS features can be observed in the propane hydrate spectrum from 3000 – 2800 cm^{-1} provided for later discussion in **Figure 4-15**); however, the presence of surfactant in respective hydrate measurements had no discernable influence on the IR absorption characteristics of bulk water phases or data evaluation strategies. This was expected as SDS only serves as a low-concentration nucleation catalyst.[20] Hence, data generated from gas hydrate trials with deionized water and surfactant solutions are presented for discussion in this chapter. Although supportive evidence for the role of SDS as a low entropy nucleation catalyst (surface-surfactant-gas) was generated throughout work presented in this chapter, only results regarding the application of IR sensing strategies for monitoring gas hydrate growth dynamics are considered in this thesis.

4.2 Laboratory Growth of Simple Gas Hydrates from Solution

Simple gas hydrates for methane, ethane, and propane were investigated throughout this thesis. This section provides a general summary of typical measurement procedures performed for spectroscopic monitoring of gas hydrate growth dynamics. In addition, an overview of representative experimental data collected throughout hydrate trials are presented with exception of spectroscopic monitoring data, which is presented in **Section 4.3**.

4.2.1 Chemicals for Growth of Gas Hydrates from Solution

Aqueous solutions of 380 ± 2 ppm (mg/L) of SDS (Sigma-Aldrich, Reagent Grade, St. Louis, MO) in deionized (DI) water (R=18.2 MΩ·cm at 25 °C) or DI water with no additives were utilized to facilitate hydrate growth. SDS served as a hydrate nucleation catalyst in the respective experiments. The concentration was selected based upon the work of Zhong and Rogers, who demonstrated that ethane hydrate induction times decreased with increasing SDS concentration.[20] Induction times were reduced from approx. 600 min with 80 ppm SDS until leveling off at approx. 40 min for concentrations ≥ 242 ppm.[20] Methane (Chemically Pure, > 99.0%), ethane (Chemically Pure, > 99.0%), and propane (Instrument Grade, > 99.5%) were purchased from Air Gas (Decatur, GA).

4.2.2 General Experimental Procedures for IR Monitoring of Gas Hydrates

A full description of the experimental setup for spectroscopic monitoring of gas hydrates is provided in **Chapter 3**. Once the hydrate setup was assembled (**Figure 3-12**), the sample chamber was initially purged with a copious amount of supply gas. Following, the enclosed environment surrounding the setup was purged with dry air to stabilize atmospheric humidity and CO_2 within the open radiation path. After stabilization, a reference spectrum was collected **(Figure 4-5)**. Then, continuous spectroscopic measurements were started, and the pressure cell was filled with approx. 315 mL of aqueous solution, submersing the internal cooling coil. Once

filled, the chamber was pressurized with the supply gas followed by initiation of the cooling sub-system. Pressure and temperature data were logged throughout the entire measurement series. The hydrate setup was operated in a 'semi-closed' pressure environment; meaning hydrate growth was not under isobaric conditions. The supply gas was intermittently introduced to replace gas incorporated into hydrate lattices during hydrate growth. Hydrate dissociation was typically initiated by reducing the chamber pressure below the hydrate phase equilibrium with respect to the system temperature and supply gas.

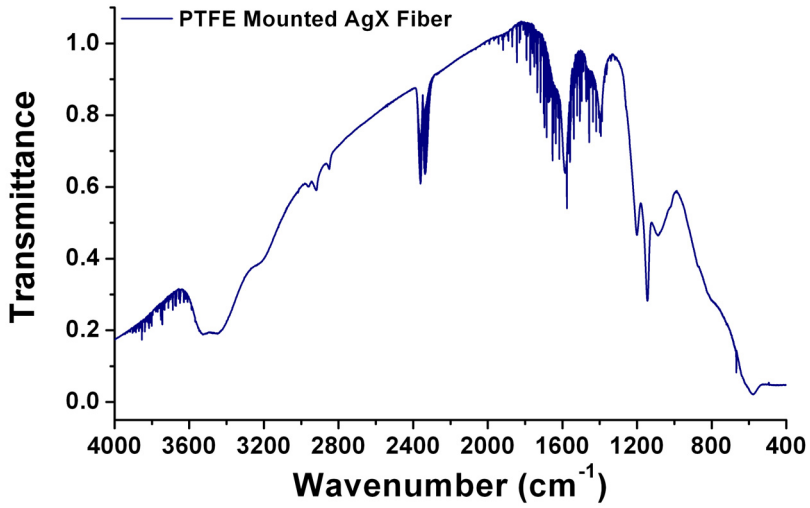

Figure 4-5: Representative IR transmittance profile from a reference spectrum (average of 250 sample scans at 0.5 cm^{-1} resolution) for a PTFE mounted AgX fiber. All reference spectra for hydrate monitoring trials were collected with an empty chamber at room temperature and atmospheric pressure.

4.2.3 Non-spectroscopic Indications of Hydrate Nucleation and Growth

Classical indicators for the nucleation of gas hydrates grown from aqueous solution include visual observation and marked pressure and temperature changes. The nucleation of gas hydrate in a closed or 'semi-closed' system is generally indicated by a rapid decrease in system pressure from the incorporation of dissolved gas into hydrate structures. In addition, a sharp increase and/or sporadic fluctuations in recorded solution temperatures are usually observed as a result from the

latent heat of fusion during the phase transitioning of water. **Figure 4-6** provides an example of pressure and temperature traces from an ethane hydrate trial (with SDS) indicating abrupt changes in the data logs characteristic of hydrate nucleation and growth in this work.

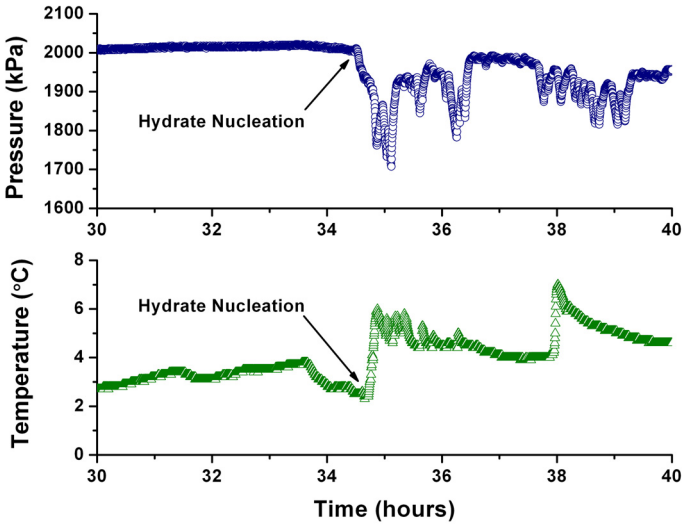

Figure 4-6: Pressure and temperature traces from an ethane hydrate trial (with SDS) indicating a rapid drop in pressure and increase in temperature at hydrate nucleation. Pressure fluctuations reflect intermittent introduction of ethane into the sample chamber. Temperature spikes likely result from localized hydrate growth in close proximity to the submersed temperature probe as opposed to bulk solution temperature changes.

At the onset of nucleation, a period of rapid hydrate growth ensues following the conversion and agglomeration of sub-critical hydrate clusters and oligomeric precursors as described by cluster nucleation theory and the RK model discussed in **Section 4.1.1.4**. **Figure 4-7** provides sequential optical images collected during a 2.5 min period covering the nucleation and initial expeditious primary growth of ethane hydrate (with SDS).

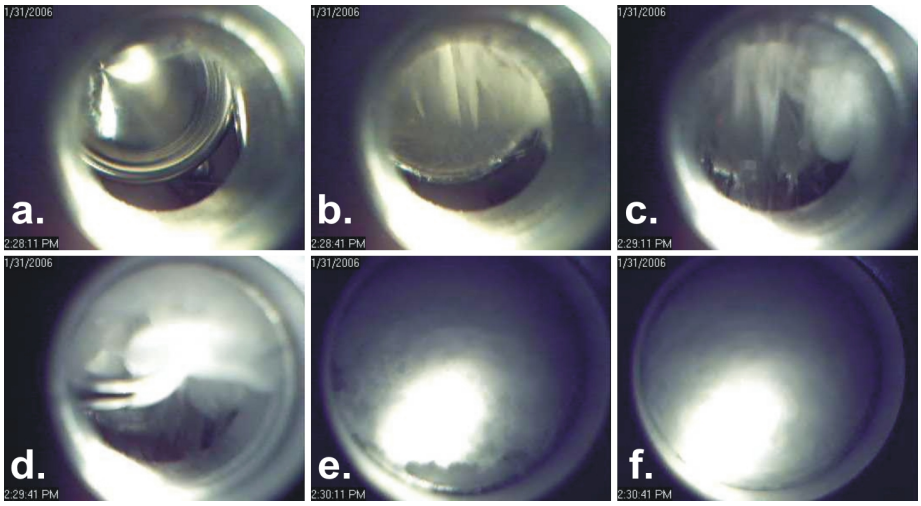

Figure 4-7: Image captures displaying the sample chamber contents from (a.) pre-hydrate nucleation, (b.) catastrophic hydrate nucleation with spindling growths, and (c. – f.) primary growth of ethane hydrate over a period of 2 mins. In images (a. – c.), the liquid water level is above the viewport, appears at the mid-line in capture (d.), and drops below the viewing region in capture (e.).

4.2.4 Visualizing Hydrate Dissociation and Comparisons with Ice

As expected, copious gas bubbles were observed during hydrate dissociation in all experiments. The addition of surfactant as a catalyst for hydrate nucleation also promoted visualization of bubble formations during hydrate dissociation. **Figure 4-8** contains three image captures collected at 2 min intervals during ethane hydrate dissociation with indication to the growth of large ethane bubbles in surfactant foam resulting from abundant outgassing during dissociation.

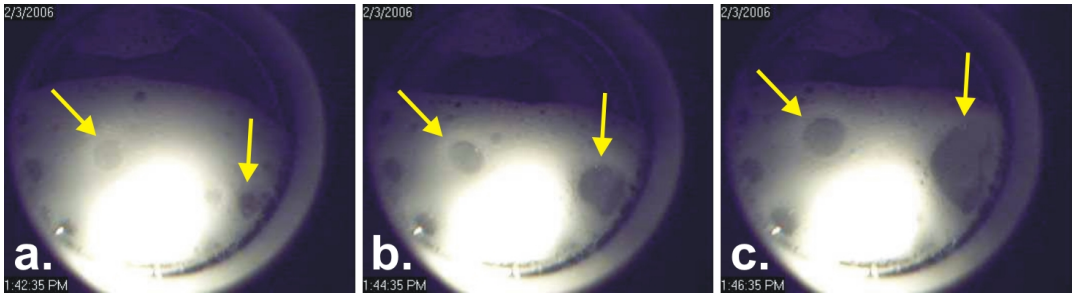

Figure 4-8: White surfactant foam formed inside the hydrate chamber from outgassing ethane during hydrate dissociation. Arrows accentuate growing ethane bubbles in sequential images collected at 2 min intervals.

Distinct cues, such as bubbles, facilitate visual differentiation of gas hydrate and ice. In addition to the growth of gas hydrates, ice was also grown from surfactant solution during this work. Image captures from pre-nucleation, growth, and the complete melting of ice (**Figure 4-9**) and dissociation of methane hydrate (**Figure 4-10**) exhibit distinct characteristics respective to each type of solid water formation.

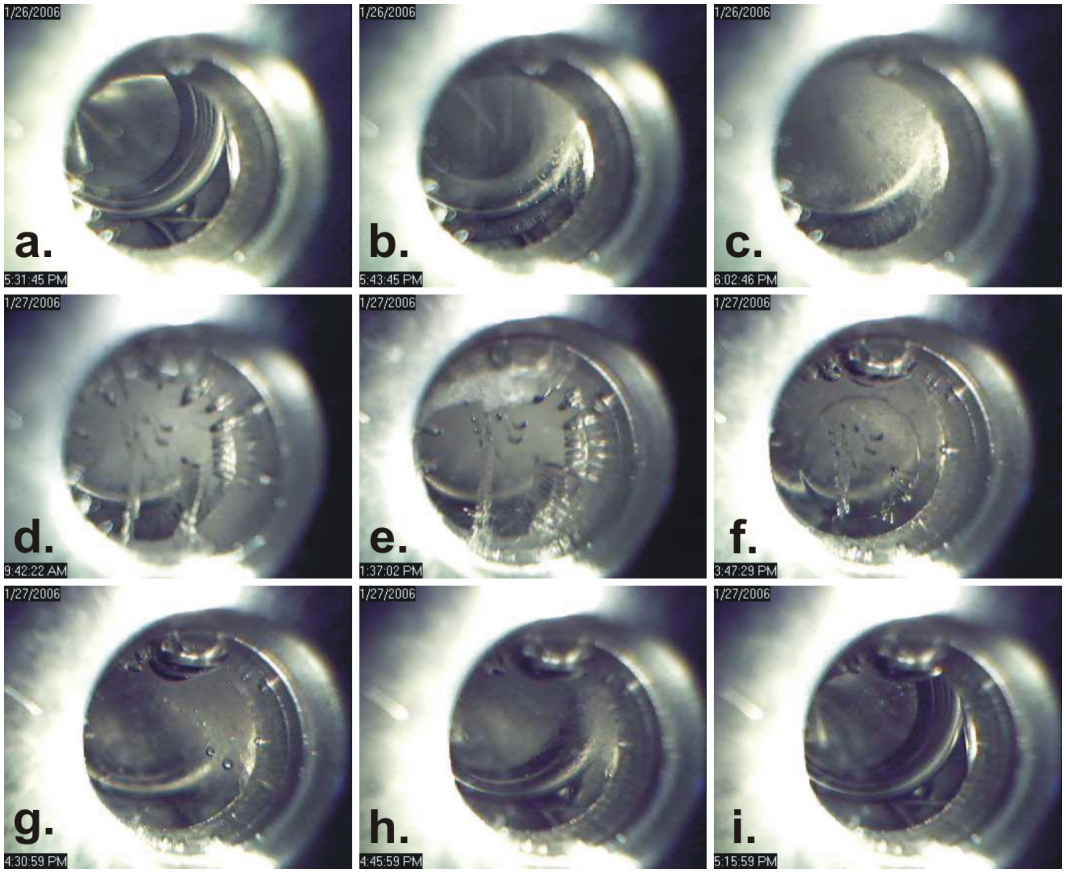

Figure 4-9: Image series displaying visual cues inside the pressure chamber throughout an ice trial with SDS solution. Chamber contents with liquid water (a.) prior to nucleation. The initial minutes of ice growth following nucleation (b.) with continued growth (c.) until completion (d.) while maintaining a clear viewing of the internal cooling coil. Melting of ice (e. – h.) with few bubble formations until finally returning to initial conditions (i.) with no surfactant foaming.

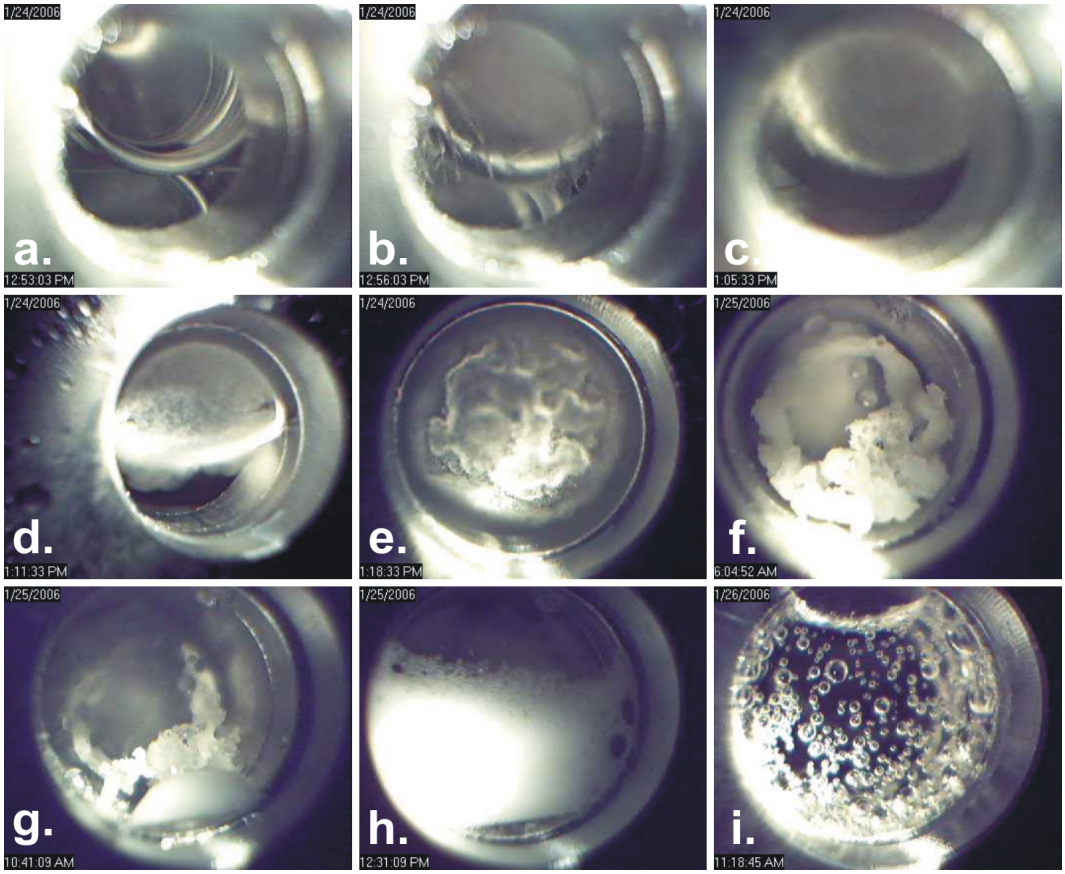

Figure 4-10: Image series depicting the sample chamber contents throughout a methane hydrate trial with SDS. Viewing of liquid water (a.) followed by hydrate nucleation (b.) and growth (c. – e). Final viewing of methane hydrate (f.) prior to initial stages of pressure induced dissociation (g.). Continuing dissociation (h.) with formation of surfactant foam until returning to initial conditions with methane bubbles attached to the sapphire viewport.

Figure 4-9 and **Figure 4-10** illustrate the distinctive visual differences observed during the growth and dissociation of ice and gas hydrate throughout this thesis, respectively.

4.2.5 Inspection of Gas Hydrates Extracted from the Pressure Chamber

In addition to monitoring of the internal sampling chamber, portions of methane, ethane, and propane gas hydrates were harvested from select experiments for closer inspection. **Figure 4-11** provides webcam images for a mass of extracted ethane hydrate.

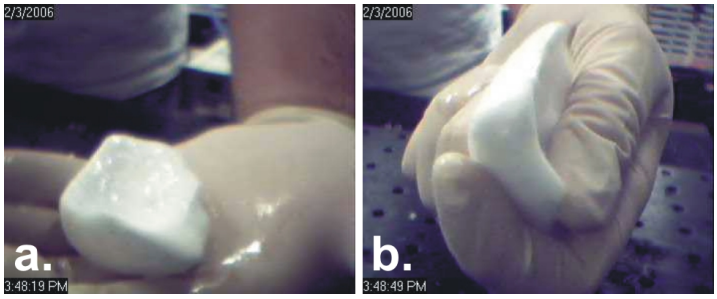

Figure 4-11: Optical images of an extracted portion of ethane hydrate from the pressure cell.

Samples for each of the harvested hydrates (each grown from a 380 ppm SDS solution) were rough to the touch as many pores formed from the outgassing of hydrocarbons during dissociation. To verify incorporation of the respective guest gases into hydrate structures, a portion of each sample was placed into the internal sample compartment of an FT-IR spectrometer for open-path IR transmission-absorption spectroscopic evaluation of outgassing constituents.

Figures 4-12 (a.), (c.), and **(e.)** provide representative IR spectra from evaluation of dissociating methane, ethane, and propane hydrate; each exhibiting characteristic IR absorption features for the respective guest gas molecules.[76] Methane spectra were collected with a Bruker IFS/66 FT-IR spectrometer (average of 100 sample scans at 4 cm^{-1} resolution) and deuterated triglycerine sulfate (DTGS) detector. Ethane and propane spectra were obtained from a Bruker 55 FT-IR spectrometer and MCT detector (average of 10 sample scans at 4 cm^{-1} resolution and average of 100 scans at 2 cm^{-1} resolution, respectively). IR spectra were collected for at least 36 mins after collection of a reference spectrum (empty sample compartment) and introduction of a beaker with dissociating gas hydrate samples. IR spectra from each measurement series were evaluated by integrating the area under C-H stretching absorption features for the respective gases. **Figures 4-12 (b.), (d.), and (f.)** graphically display absorption intensity, as integrated peak areas versus time for the expulsion of guest gases during hydrate dissociation inside the sample compartment (peak integration criteria for each species included in the respective graph).

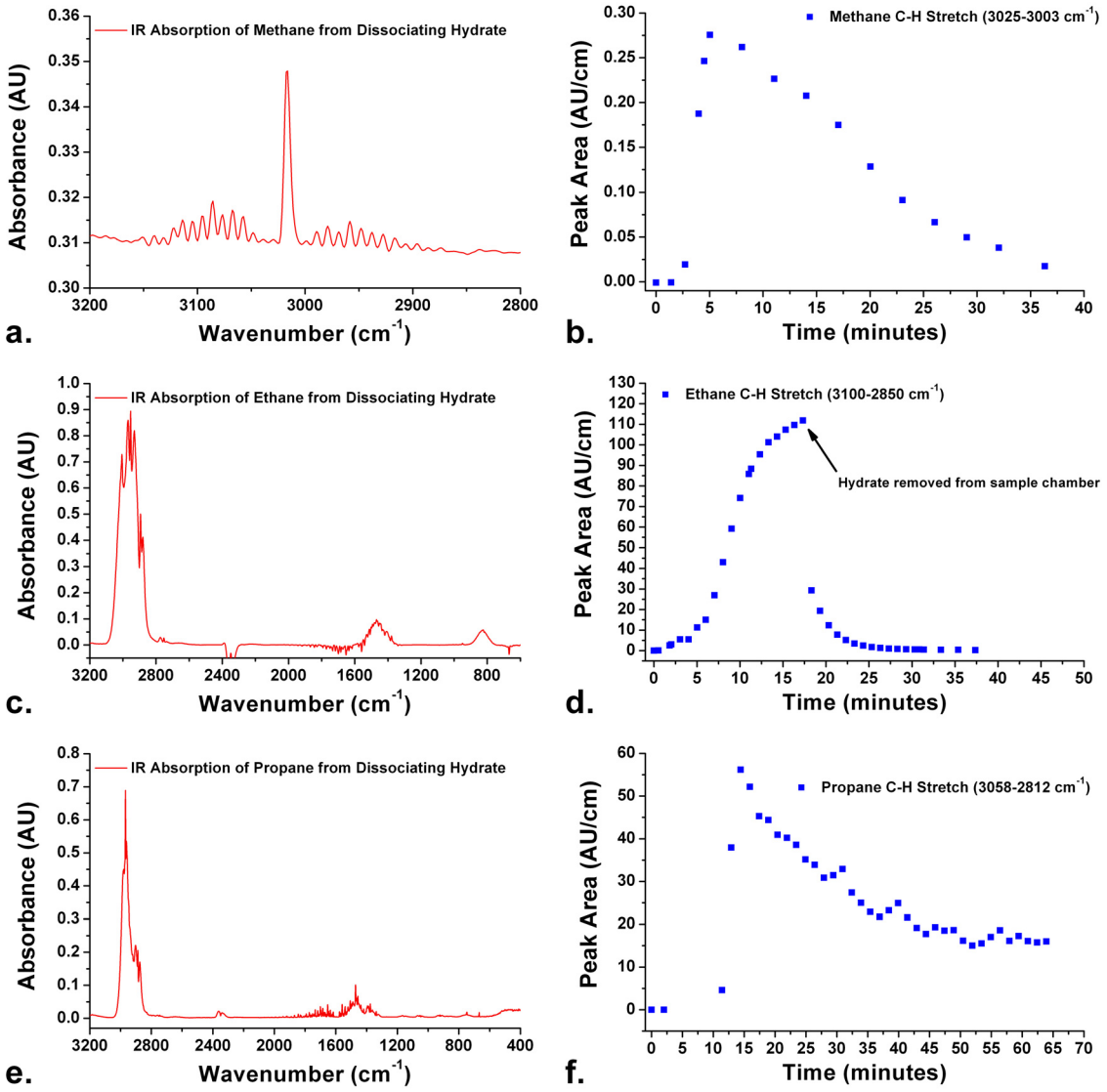

Figure 4-12: IR transmission-absorption results from the interrogation of outgassing constituents from extracted gas hydrate structures for (a. and b.) methane hydrate, (c. and d.) ethane hydrate, and (e. and f.) propane hydrate. All graphs on the left side represent selected transmission-absorption spectra from each experiment. All graphs on the right side illustrate absorption intensity for the expulsion of guest gases versus time for each measurement series (≥ 36 mins) as the peak area respective to C-H stretching features for each hydrocarbon species. Peak integration criteria are provided in the respective graphs (b.), (d.), and (f.).

Spectroscopic evaluations provided in **Figure 4-12** confirm the release of hydrocarbon gases during the dissociation of respective gas hydrate structures. The obtained IR spectra of outgassing methane (C-H stretch region displayed in **Figure 4-12 (a.)**) was comparatively weaker than gas signatures from dissociating ethane and propane hydrates, including a significant baseline shift

due to incidental obstruction of the beam path from beaker placement inside the sample chamber. In addition, a substantially larger portion of ethane hydrate was utilized compared to methane and propane experiments; hence, stronger IR absorption intensities were observed. Overall, absorption intensities subsided with time as the hydrate mass was reduced during dissociation (or the result of removal from the sample compartment in the case of ethane hydrate) and the influence of continuous purging of spectrometer sample compartments with dry air, which prevented the build-up of discharging gases. In addition to spectroscopic evaluation, the flammability of gases expelled from dissociation of extracted gas hydrates was tested, as shown in **Figure 4-13**.

Figure 4-13: Series of image captures at 1 s time intervals demonstrating the combustion of propane expulsion from gas hydrate. In capture (a.), a white foam of propane filled surfactant bubbles is observed; obstructing the view of hydrate mass contained within the 250 mL glass jar.

4.3 Fiber-optic IR-ATR Spectroscopic Monitoring of Gas Hydrates

This section contains a detailed account of fiber-optic IR-ATR spectroscopic measurements for monitoring gas hydrate formation and dissociation of simple methane, ethane, and propane gas hydrates grown from DI water (with and without SDS). First, a general discussion regarding spectral mixing during the phase transition of water from liquid to solid is provided. Following, each of the four primary water absorption features is addressed in dedicated sub-sections that include molecular level descriptions resulting in spectroscopic changes during the phase transition, explanation of data evaluation strategies, and representative results. Selected experimental results from various hydrate trials are displayed interchangeably throughout this

discussion to illustrate spectral similarities of different hydrate structures and the versatility of data evaluation strategies. A thorough analysis for a representative propane hydrate trial is then provided to emphasize the value of collective data evaluation from multiple water absorption features to assess hydrate growth dynamics. **Figure 4-14** provides representative fiber-optic IR-ATR spectra for (a.) liquid water and methane hydrate and (b.) methane, ethane, and propane hydrates to facilitate side-by-side visual comparisons.

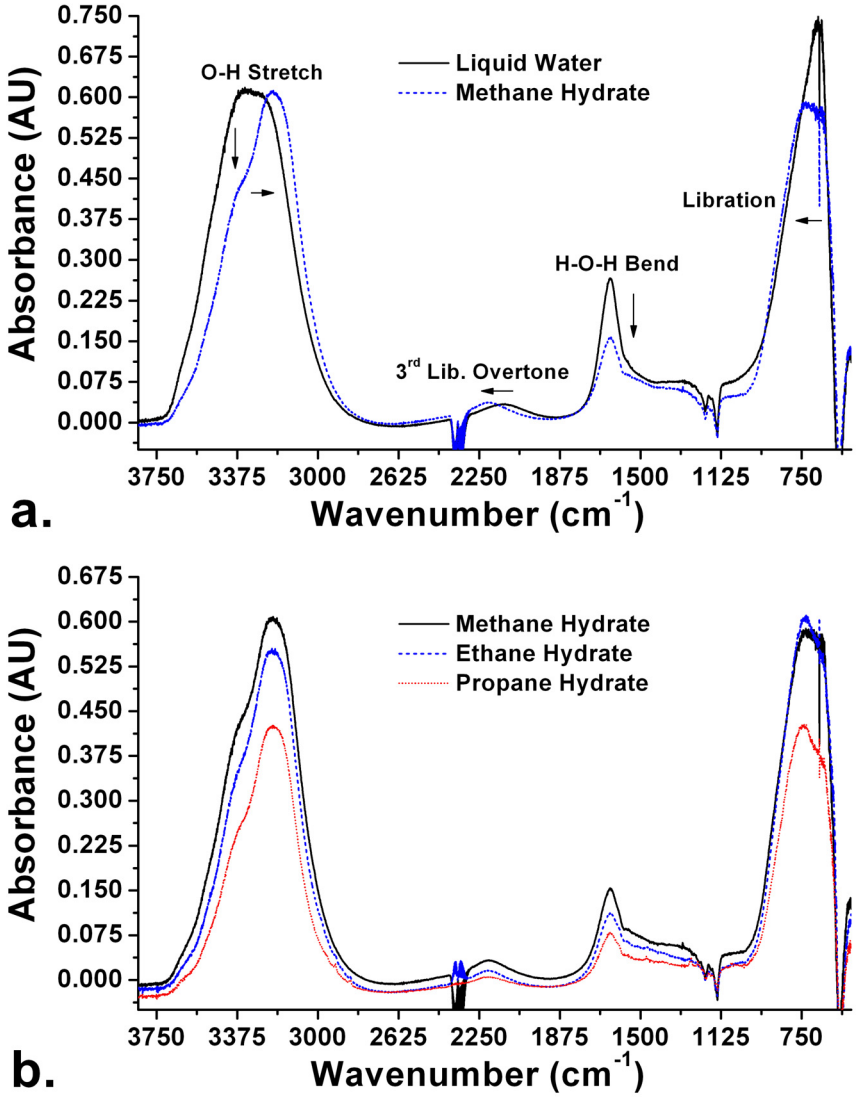

Figure 4-14: Fiber-optic IR-ATR spectra for (a.) liquid water and methane hydrate with labeled absorption features for water and indication to spectral changes during the formation of gas hydrate and (b.) methane (sI), ethane (sI), and propane (sII) hydrates illustrating the similarity in spectral shifts observed for each clathrate hydrate structure.

4.3.1 Results and Discussion

4.3.1.1 IR Spectral Mixing During the Phase Transitioning of Water

Fiber-optic IR-ATR spectra collected throughout the liquid-to-solid (and vice versa) phase transitioning of water is the sum result of spectral contributions from all sub-structures of water interacting with the evanescent field. For example, Rahman and Stillinger showed that in liquid water, ordered sub-networks of H-bonded water spontaneously form over a wide range of temperatures (primarily pentamer rings followed by hexamer and square structures); hence, the IR spectra of liquid water is a reflection of all spectral contributions from the various ordered networks (see Sloan for a review of water structuring and additional references)[2,77] The cluster nucleation and RK models indicate that incomplete hydrate cages or oligomeric precursors form as intermediates prior to the nucleation of bulk hydrate growth. For simplicity, the IR spectrum of water (W) obtained during the formation of gas hydrate can be treated as the sum of reversible, non-interacting, state-specific absorption contributions from a binary phase mixture of liquid water (Liquid) and gas hydrate (Hydrate), where liquid-like water sub-structures contribute to the Liquid portion of the IR spectrum and hydrate-like structures contribute the Hydrate portion of the IR spectrum. Thus, W can be described following the Beer-Lambert law as the equation:

$$W = A_{\text{Liquid}} + A_{\text{Hydrate}}$$

Equation 4.1

where $A = a \times C \times l$; A is the absorbance, a is absorptivity, C is the concentration (defined as mass-to-volume (m/v) in this work), and l is the measurement pathlength. The effective measurement pathlength, l, for fiber-optic ATR waveguides is the sum volume interrogated by the evanescent field by N number of reflections with an effective penetration depth, d_e, over the entire fiber measurement surface and length. Hence, l, can be defined as an effective measurement volume, where $Nd_e = V_l$. By treating Liquid and Hydrate as non-interacting species

contributing to *W*, concentration values can be rewritten with the respect to the density of each phase. Thus, during the state transformation of water, *W* varies with respect to density and the proportional volume of each phase within V_l, which can be expressed in the following form:

$$W = \left(a_{\text{Liquid}} \cdot \rho_{\text{Liquid}}\right)_{\left(T,P,\sum_{i=1}^{n-2} g_i\right)} \cdot \left(\frac{V_{\text{Liquid}}}{V_l}\right) \cdot V_l + \left(a_{\text{Hydrate}} \cdot \rho_{\text{Hydrate}}\right)_{\left(T,P,\sum_{j=1}^{n-2} h_j\right)} \cdot \left(\frac{V_{\text{Hydrate}}}{V_l}\right) \cdot V_l$$

Equation 4.2

where a_{Liquid} and a_{Hydrate} are phase-dependant absorptivities, ρ_{Liquid} and ρ_{Hydrate} are respective phase densities, and V_{Liquid} and V_{Hydrate} are the volumes of each phase within V_l, the effective measurement volume, such that:

$$V_{\text{Liquid}} + V_{\text{Hydrate}} \leq V_l$$

Equation 4.3

In addition, **Equation 4.2** enables absorbance corrections for dependencies *a* and ρ with respect to temperature *(T)*, pressure *(P)*, and any additional factors, g_i and h_j (e.g., salinity and pH), that can influence the spectral absorption of Liquid or Hydrate, respectively. The number of factors is given as $n-2$ since pressure and temperature are already indicated. Hence, under given conditions, the proportional volume of Liquid:Hydrate interacting with the evanescent field directly influences the absorption characteristics of *W*. Furthermore, V_l can be canceled out in the formulation of A_{Water} and A_{Hydrate} in **Equation 4.2** as V_{Water} and V_{Hydrate} are the effective measurement volumes respective to each phase interacting with the evanescent field and concentration units accounted by the phase densities. The consequences of this formulation are discussed in context throughout the following evaluations of spectral data obtained from hydrate monitoring series.

4.3.1.2 The O-H Stretches

The O-H stretch (ν_{OH}) region of liquid water is complex and comprised of multiple peak contributions with classical band assignments of two absorption features relating to symmetric (ν_1) and asymmetric (ν_2) vibrations.[39, 57] Recently, the ν_{OH} region has been further interpreted as the combination of three Gaussian modal contributions with respect to H-bonding.[62, 64] For this thesis, the H-bonding modal description is adopted. The three Gaussian populations for liquid water typically occur at approx. 3603 cm^{-1}, 3465 cm^{-1}, and 3330 cm^{-1} at 25 °C.[62] Poorly H-bonded water molecules, termed "multimer water" (i.e., dimers and trimers), are responsible for the high frequency component at 3603 cm^{-1} and account for approx. 10% of the ν_{OH} intensity.[62] The 3330 cm^{-1} population results from networked water with strongly H-bonded water species exhibiting coordination close to four, and are responsible for approx. 56 % of the summed ν_{OH} band intensities.[62] Finally, "intermediate water" contributes approx. 34 % to ν_{OH} absorption at 3465 cm^{-1} from medially H-bonded moieties with coordination greater than multimer water but less than networked water.[62]

The population dynamics for the three groups of liquid water are significantly influenced by temperature. With decreasing temperature, an increase in absorption intensity is observed for networked water, while decreased intensities are observed for intermediate and poorly networked water.[62] Overall, the O-H stretch region absorption intensity increases slightly with decreasing temperature, which has been primarily attributed to increased water density.[62] In addition, a red shift in the networked water band is observed upon cooling. Further red shifting and enhancement of the strongly H-bonded population with diminished populations of medially bonded and multimer water occur during the liquid-to-solid phase transitioning (formation of rigid H-bonded lattices from ice or hydrate structures), resulting in drastically altered peak shapes, positions, and intensities.[38, 62, 64, 65] Phase related absorption changes in the O-H stretch region are readily

observed in the fiber-optic IR-ATR spectra of liquid water and gas hydrates (sI and sII) provided in **Figure 4-14**.

In this study, final peak positions observed for highly networked O-H stretches from gas hydrate structures (sI or sII) typically occurred at approx. 3210 cm^{-1}, which corresponds to a red shift of approx. 120 cm^{-1} with respect to reported values from the deconvoluted O-H stretches for the liquid water spectrum at 25 °C.[62] To date, monitoring the liquid-to-solid transitioning of water through band deconvolution of the O-H stretch region has not been demonstrated in the literature. Due to the complexity of phase mixing and computation intensity of band deconvolution techniques, the implemented O-H stretch evaluation strategy for monitoring gas hydrate formation and dissociation was based on peak integration. Millo et al. reported a frequency dependent method for monitoring intensity changes due to population shifts in the O-H stretch modal contributions during the ice-to-liquid transitioning of water when referenced against the liquid water spectrum at 6 °C using fiber-optic IR-ATR spectra.[65] However, for potential environmental monitoring applications, a generic strategy was selected to monitor a summed intensity effect by evaluating the prominence of the low frequency, highly networked O-H stretch character in the ν_{OH} profile from 3310 – 3099 cm^{-1}, thus providing a singular value reflective of gas hydrate composition and growth dynamics. Peak integration provides a straight forward data evaluation strategy with minimal computation time, and is very amenable for automated, *in situ* data analysis. **Figure 4-15** contains peak integration results from a propane hydrate trial with gas hydrate grown from DI water without surfactant and highlights key features of interest.

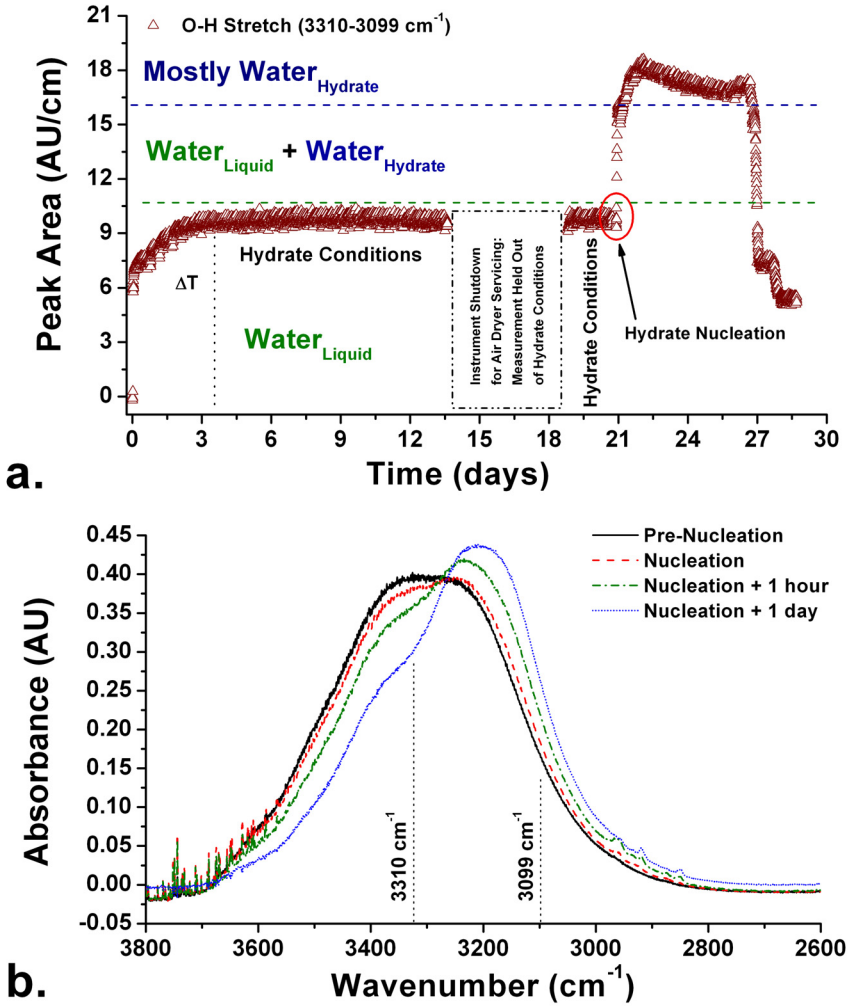

Figure 4-15: (a.) Peak integration results from spectroscopic monitoring of propane gas hydrate formation and dissociation in DI water by evaluating the population dynamics of the highly H-bonded O-H stretch feature. (b.) Fiber-optic IR-ATR spectra displaying comparable shifts in H-bonded populations during propane hydrate growth in a trial with surfactant solution (380 ppm SDS). (IR spectra were collected at 360 s intervals (a.) with an average of 250 sample scans at 0.5 cm^{-1} resolution (a. and b.).

In **Figure 14-5 (a.)**, initial rapid intensity gains are observed from filling of the hydrate chamber with liquid water followed by temperature induced H-bonding population reorganization. Once hydrate conditions were achieved, a stable signal is visualized until a gap in experimental data occurs from day 13 to day 18 due to failure of the air drying unit, which is required to drive the interferometer for collection of FT-IR spectra. During that time, temperature in the cell was raised out of hydrate conditions until remedied. Afterwards, an IR spectrum was collected and visually

inspected with no discernable negative impact; hence, data collection was continued and the cell returned to hydrate conditions. On day 21, hydrate nucleation occurred as indicated by a rapid increase in peak area from concomitant enhancement of the strongly H-bonded population and reduction of intermediately H-bonded water species. **Figure 4-15 (b.)** depicts typical O-H stretch absorption dynamics in the IR spectrum throughout the liquid-to-hydrate phase transition during a measurement series examining propane hydrates grown from a surfactant solution with 380 ppm of SDS. Indicators are also provided in **Figure 4-15 (b.)** to illustrate the peak integration region. Once hydrate nucleation occurred, propane hydrate was allowed to grow for approx. 6 days until pressure induced dissociation, which is marked by a decrease in peak area. The hydrate series was completed following full dissociation of hydrate and returning to initial system conditions. Additional subtleties regarding hydrate growth dynamics can be visualized from evaluation of the O-H stretch region in **Figure 4-15 (a.)**. A thorough, collective evaluation of all spectral changes in water absorption features during a hydrate growth trial facilitates a more coherent physical interpretation; hence, an in-depth evaluation of all water absorption features for this representative hydrate trial is provided in **Section 4.3.2**.

4.3.1.3 The H-O-H Bend

The H-O-H bend mode (ν_3) occurs at approx. 1640 cm^{-1} for liquid water at room temperature. The intensity of this band has been demonstrated to decrease slightly with decreasing temperatures with little or no observable frequency shifts.[62, 64, 65] In addition, both single-Gaussian (Brubach et al.)[62] and dual-Gaussian (Freda et al.)[64] evaluation methods of the H-O-H bend have been described in the literature. The dual-Gaussian method describes two sub-peaks at 1670 cm^{-1} and 1646 cm^{-1} for tetrahedrally arranged H-bonded (networked water) and non-H-bonded (irregularly networked) water, respectively.[64] Despite the molecular level interpretations of this vibrational mode, the overall absorption intensity becomes significantly quenched upon the phase transition and formation of rigid lattice networks of ice or gas hydrate.

The decreased ν_3 intensity results from a loss in the induced transition dipole moment from the bending motion with increased coordination in H-bonded lattices.[62] Multi-mode interpretation of the ν_3 region has been supported in the literature as this typically symmetric absorption feature becomes increasingly asymmetric throughout phase transformation.[65] However, as the primary spectral change in the ν_3 absorption during formation of solid water phases is a substantial reduction in absorption intensity, a peak integration method was utilized for evaluating phase-related amplitude fluctuations throughout hydrate formation and dissociation in this study.

Figure 4-16 (a.) contains measured ν_3 intensity values as integrated peak areas throughout formation and dissociation of ethane hydrate grown from a solution of SDS. An initial increase in peak area results from system pressurization, and is followed by a drop in intensity resulting from decreased humidity relative to environmental conditions during collection of the reference spectrum (this trial prior to incorporation of purge box). Hydrate nucleation is indicated by a sharp decrease in the peak area approx. 24 hrs after start of data collection. A relatively stable signal is observed following the conversion of liquid water into gas hydrate. Band intensity increases with progression of pressure induced dissociation starting at approx. 2.75 days.

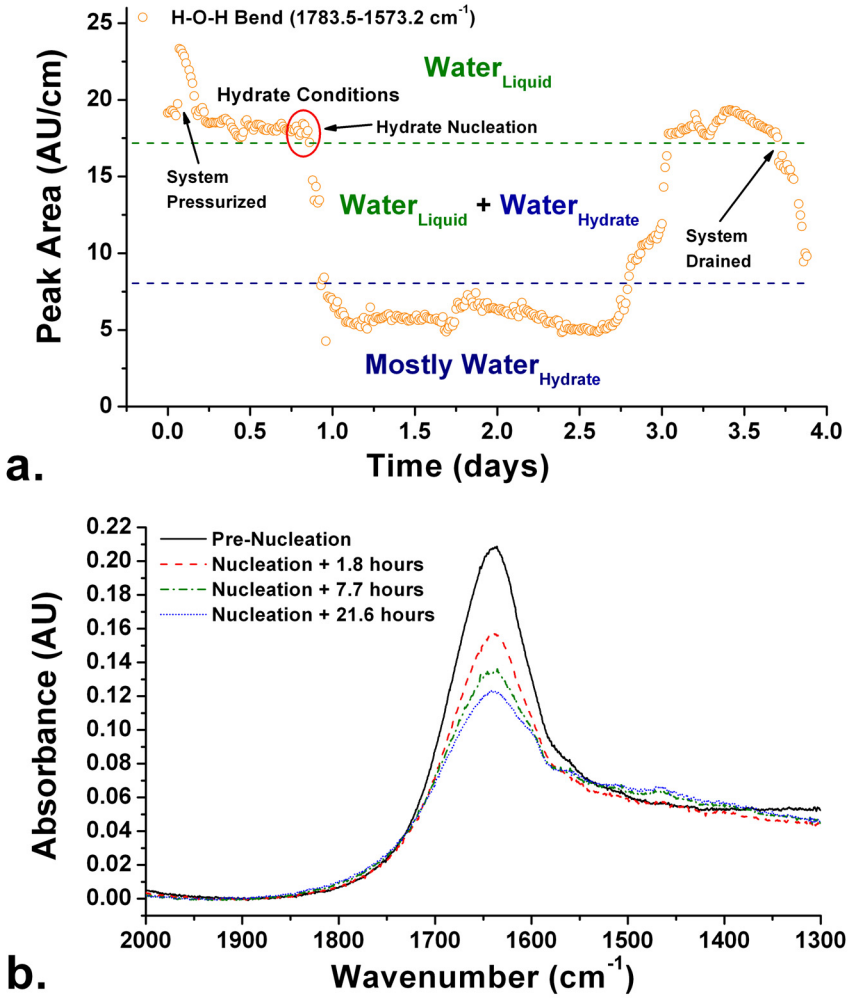

Figure 4-16: (a.) Peak integration analysis from spectroscopic monitoring of ethane hydrate formation and dissociation in 380 ppm SDS solution. (b.) IR-ATR spectra from a separate ethane hydrate trial (grown from a 380 ppm SDS solution) depicting spectral changes in the H-O-H bend throughout the liquid-to-hydrate phase transition. ((a.) IR spectra were an average of 1000 sample scans at 0.5 cm^{-1} resolution collected in 15 min intervals, and (b.) IR spectra are an average of 250 sample scans at 0.5 cm^{-1} resolution).

After gas hydrate has been formed around the fiber-optic waveguide, an asymmetric absorption profile can be observed with decreased H-O-H bend intensity (**Figure 4-16 (b.)**). Visual inspection of this region indicates contributions from a high frequency component around 1670 cm^{-1} as well as a low frequency mode at approx. 1642 cm^{-1} without deconvolution. This observation is consistent with the two-Gaussian interpretation. However, a distinct shouldering feature was also observed at approx. 1603 cm^{-1}. This absorption feature was observed in

experiments with and without surfactant, for methane, ethane, and propane hydrates, and an ice experiment grown from SDS solution. Hence, the origin of this vibrational mode may be assigned to water; however, a molecular level interpretation of this band remains unknown.

The localized measurement volume interrogated by the evanescent field was accentuated in this measurement series. Although spectroscopic data at the beginning of day 3 are indicative to the presence of only liquid water, ethane hydrate was present in the sample chamber; albeit not in intimate contact with the AgX fiber. The remaining ethane hydrate from this trial was extracted for further examination (described in **Section 4.2.4**) following drainage of liquid water contents. In addition, absorption intensities obtained from peak integration of the ν_3 region were strongly perturbed with environmental changes in humidity during this trial. Hence, a polycarbonate box was implemented for purging a restricted volume around the experimental setup following initial measurement trials for minimizing humidity induced amplitude variability. **Figure 4-16 (b.)** displays IR spectra collected throughout the formation of ethane hydrate following integration of the purge box; however, it was not possible to completely eliminate all humidity fluctuations throughout the entire course of a hydrate experiment, which could extend > 3 weeks.

4.3.1.4 The Libration Band

The libration band (ν_L) arises from small amplitude oscillations from the whole water molecule respective to H-bonding lattices.[62] In liquid water, this absorption feature has been shown to occur around 675 cm^{-1},[62] and the peak position is strongly influenced by temperature and water phase such that decreasing temperatures and/or formation of solid water structures result in a significant blue shift (peak maximum observed at 850 cm^{-1} for ice at -20 °C by Brubach et al.[62] and 750 cm^{-1} for ice at -4 °C by Millo et al.[65]).

For the current experimental setup, the peak maximum for ν_L is below the experimentally available frequency range. However, upon hydrate formation, a peak maximum for this feature becomes discernable in the IR spectrum as a result of blue shifting. Hence, two evaluation

strategies were initially implemented for evaluating the ν_L feature during formation and dissociation of gas hydrate. The first method is based upon peak fitting for elucidating the wavenumber respective to the libration peak maximum. This strategy only enables a semi-continuous evaluation as hydrate growth must progress until the peak maximum has shifted above the detector cut-off. The second method is a peak integration method similar to that implemented for assessing the prominence of the strongly H-bonded population in the O-H stretch region. The spectral region from 925 – 700 cm^{-1} was integrated for evaluating amplitude changes resulting from ν_L peak shifts. This approach enabled a continuous monitoring capability as this region swells in response to temperature induced blue shifting and hydrate formation prior to the onset of a discernable peak maximum.

Spectral monitoring of the peak maximum and peak area for the libration feature are demonstrated for a methane hydrate trial (with SDS solution) in **Figures 4-17 (a.)** and **(b.)**, respectively. IR-ATR spectra (**Figure 4-17 (c.)**) display ν_L shifts throughout the formation of ethane hydrate grown in SDS solution. The ν_L peak maximum was determined by evaluating a predominately symmetric portion of the absorption feature with a Lorentzian local least squares minimization curve fitting function (provided in Bruker's OPUS software package) for consistent, mathematical assessments. For the displayed measurement series, a fixed frequency range from 820 – 678 cm^{-1} was used for peak fitting. The typical peak maximum of ν_L from all hydrate measurements, respective to the highest obtained hydrate composition, occurred at approx. 740 ± 7 cm^{-1}. A value of 675 cm^{-1} was assigned for spectra without a discernable peak maximum.[62] Hydrate growth was detected with peak integration analysis two measurements (~30 min) prior to indication of a ν_L peak maximum. With exception of a delayed response to hydrate formation, evaluation of peak maximum or peak integration values reveal comparable information regarding hydrate growth dynamics within the sample chamber. Hence, the peak

integration method was selected as the ν_L evaluation strategy of choice for additional measurements.

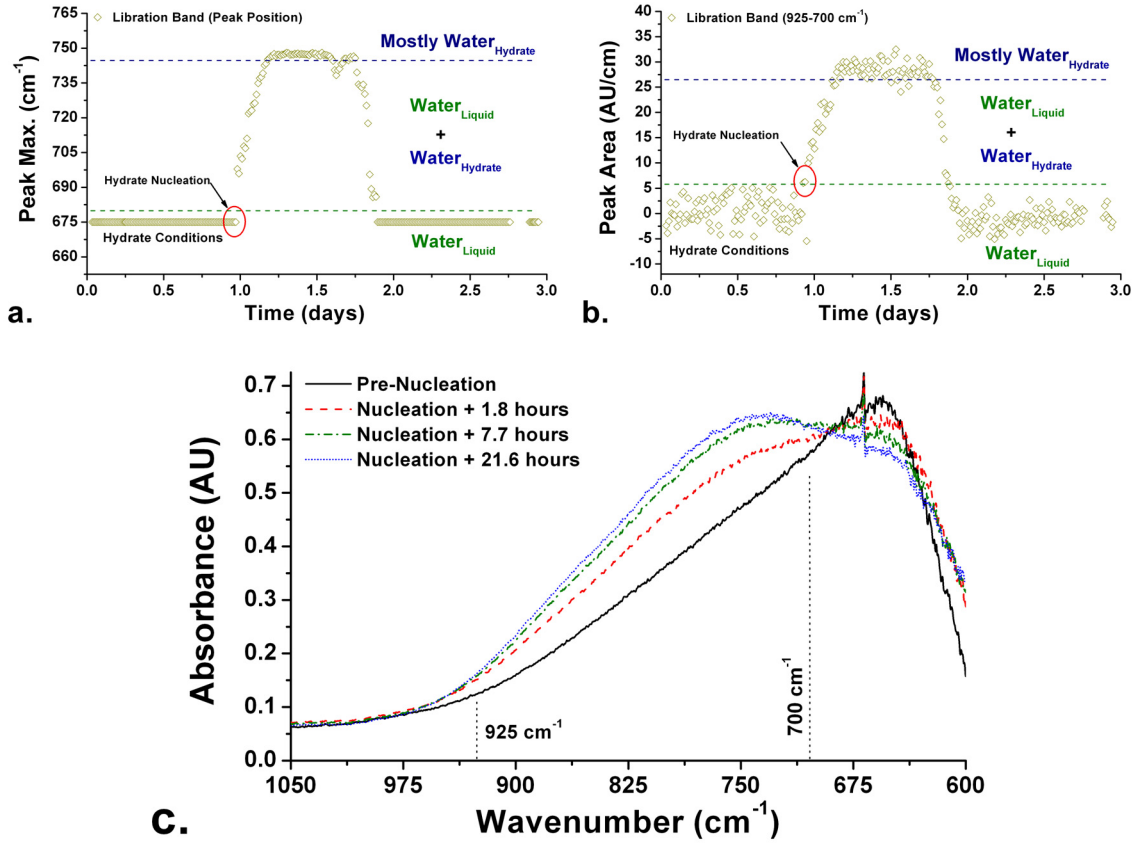

Figure 4-17: Spectroscopic results from a methane hydrate trial with SDS solution (380 ppm) for (a.) evaluation of the libration peak maximum and (b.) peak area of the libration region from 925 – 700 cm^{-1}. Representative fiber-optic IR-ATR spectra from an ethane hydrate trial (380 ppm SDS) display the shifting absorption behavior of the libration mode throughout formation of gas hydrate. ((a.) and (b.) were from analyses of IR spectra collected at 15 min intervals with an average of 1000 sample scans and 0.5 cm^{-1} resolution; (c.) IR spectra are an average of 250 sample scans at 0.5 cm^{-1} resolution).

The spectral region utilized for peak integration of ν_L is indicated (dotted lines) with IR-ATR spectra in **Figure 4-17 (c.)**. Although the detector range limits full resolution of the ν_L absorption feature, the peak integration strategy saddles near the cut-off region to take advantage of temperature and phase induced spectral shifts. In methane hydrate data displayed in **Figure 4-17 (b.)**, intensity changes from temperature induced shifts are not identified; however, temperature

induced swelling of this region upon cooling has been detected in other measurement series for methane, ethane, and propane hydrates. From all water absorption features, the libration band has limited use for environmental monitoring applications in sediment matrices due to spectral interferences from major mineral components. This is addressed in greater detail with the comparison of each data evaluation strategy to sediment spectral signatures in **Section 4.3.4**.

4.3.1.5 The 3rd Libration Overtone

The 3rd libration overtone ($3\nu_L$) is a broad absorption feature occurring at approx. 2120 cm^{-1} (room temperature). The peak maximum is strongly influenced by temperature and liquid-to-solid phase transitioning; consistent with observed changes in the libration mode.[51, 62, 65] A blue shift of approx. 0.81 cm^{-1} per °C has been reported by Libnau et al.[51] with peak maximum values for ice reported as 2190 cm^{-1} @ -6 °C,[65] 2222 cm^{-1} @ 0 °C,[39] 2235 cm^{-1} @ -175 °C,[42] with other similar values reported throughout the literature.[43, 44, 78] Intensity fluctuations have also been reported by Millo et al. during the ice-to-liquid phase transition.[65] In this thesis, evaluation of the $3\nu_L$ feature was carried out by monitoring the shift in peak maximum throughout hydrate formation and dissociation. Peak fitting strategies were similar to those utilized for evaluating the libration mode; however, the upper and lower frequency limits and frequency ranges were floated to maximize selection of the most symmetric portion of the absorption band respective to changing ratios of liquid:hydrate composition. **Figure 4-18** provides representative results from monitoring the shift in peak maximum of $3\nu_L$ during a propane hydrate trial with 380 ppm SDS.

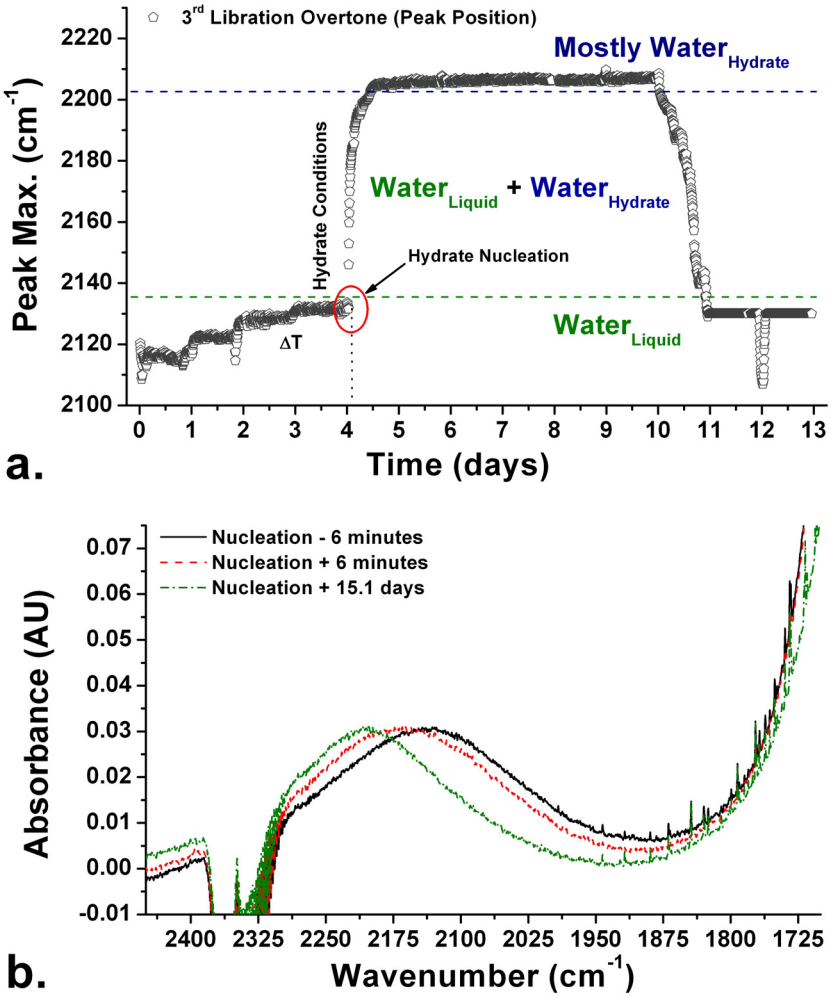

Figure 4-18: (a.) Analysis of the peak maximum for the 3rd libration overtone from IR spectra during the formation and dissociation of propane hydrate in SDS solution (380 ppm). Fiber-optic IR-ATR spectra from a methane hydrate trial (DI water) exhibit shifts in the overtone absorption feature throughout formation of gas hydrate. ((a.) is from the analysis of IR spectra collected at 6 min intervals with an average of 250 sample scans at 0.5 cm^{-1} resolution; IR spectra in (b.) were collected with an average of 250 sample scans at 0.5 cm^{-1} resolution).

A strong temperature dependence of the $3\nu_L$ peak maximum is readily observed during the first 4 days of the trial displayed in **Figure 4-18 (a.)**. In addition, a strong blue shift results upon hydrate nucleation until most liquid water interacting with the evanescent field has converted into gas hydrate. Reversibility in the peak position was observed following thermally induced dissociation, which resulted in a spiked feature at approx. 11 days due to hydrate slumping onto the unsupported fiber-optic waveguide. An additional spike was observed around 12 days from

the system temperature being warmed to approx. 40 °C before returning to room temperature. **Figure 4-18 (b.)** provides IR spectra from a methane hydrate trial with DI water, illustrating shifts in the peak maximum throughout hydrate formation. From all hydrate measurements, the observed peak maximum of $3\nu_L$ was approx. 2210 ± 10 cm^{-1}. The broad range of peak values is primarily attributed to variability in small volumes of trapped, unreacted interstitial water within the evanescent field.

The temperature dependent shift of $3\nu_L$ was compared between two propane hydrate measurement series; one with 380 ppm SDS and one with only DI water. The correlation between temperature and $3\nu_L$ peak maximum is depicted in **Figure 4-19**. **Figure 4-19 (c.)** contains the average peak positions obtained from at least 35 consecutive measurements, and displays that the presence of surfactant has minimal impact upon the observed $3\nu_L$ peak position. In addition, an approx. 1 cm^{-1} per °C shift was obtained from both measurement series comparable to literature values (a slightly higher value may result from thermal gradients within the hydrate chamber).[51] In **Figure 4-19 (b.)**, a gradual decrease in peak position is seen despite a stable system temperature at approx. 21 °C. This behavior was observed during both propane hydrate trials with and without SDS until the temperature was reduced to < 20 °C. A possible explanation for this observation comes from the reorganization of water upon solvation of gas (system was pressurized) with coincident equilibration and decrease in system temperature.[79, 80] However, further investigation is warranted to confirm the source of this behavior.

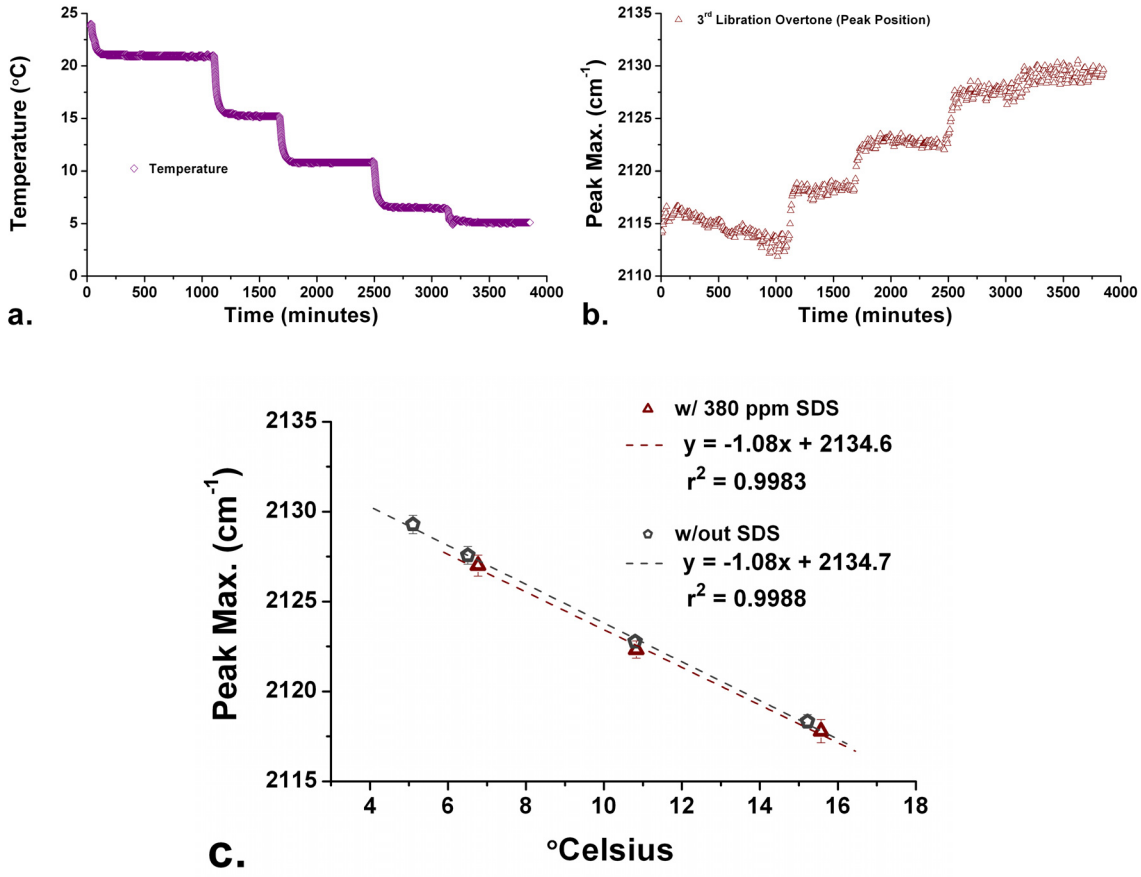

Figure 4-19: (a.) System temperature log recorded during a propane hydrate trial without SDS. (b.) Shifting peak maximum for the 3rd libration overtone in response to the corresponding temperature trace in (a.). (c.) Temperature dependent response of the 3rd libration overtone peak maximum for two propane hydrate trials; with 380 ppm SDS solution and DI water only (w/out SDS). Error bars are ± 1 standard deviation. (All spectral data were an average of 250 sample scans at 0.5 cm^{-1} resolution collected at 6 min intervals).

4.3.2 Evaluation of all Water Features during a Hydrate Trial: Model with Propane Hydrate

The collective evaluation of all major water absorption features provides the greatest amount of information regarding sample contents interacting with the evanescent field throughout the phase transitioning of water from liquid-to-hydrate and hydrate-to-liquid. **Figure 4-20** provides spectral analyses respective to each of the water absorption features following the prescribed strategies in **Section 4.3.1** for the following collective evaluation of a propane hydrate trial grown in DI water (previously discussed with regards to evaluation of O-H stretches in **Section 4.3.1.2**).

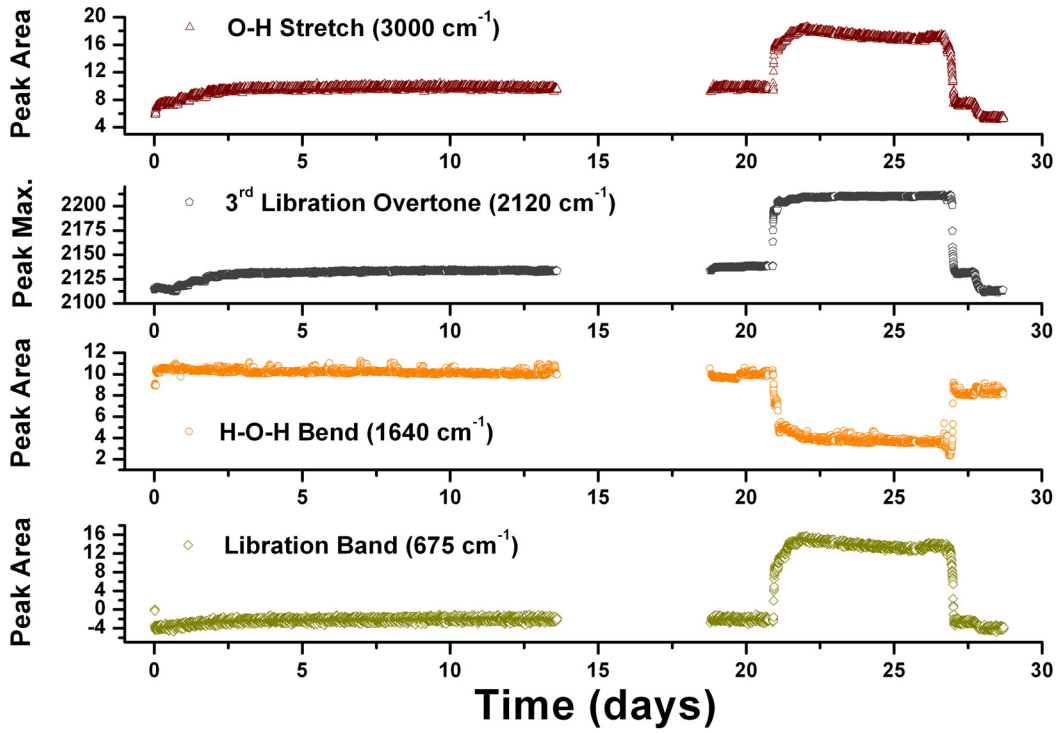

Figure 4-20: Analysis of fiber-optic evanescent field spectra with respect to each of the four absorption features of water for a propane hydrate trial grown from DI water. The data gap is the result of instrument down-time for servicing of the air dryer (see **Section 4.3.1.2**).

A qualitative consideration of analytical results depicted in **Figure 4-20** reveals comparable temporal information embedded within each of the four absorption features of water as the result of gas hydrate formation and dissociation. IR spectra collected during this measurement, as well as all hydrate measurements, provides a sum total of information regarding the influences of system temperature and hydrate content (%Hydrate) during phase transitioning resulting from changes in the absorption of water with respect to $V_{Hydrate} + V_{Liquid}$ interacting with the measurement volume of the evanescent field, V_l.

In **Figure 4-20**, the impact of temperature on liquid water absorption features can be observed in analyses for the O-H stretch absorption intensity, libration absorption intensity, and peak maximum of the 3rd libration overtone during initial cooling stages starting on day 1 and concluding on day 3. In addition, temperature influences on the absorption behavior of liquid

water are observed on day 27 (~6 °C) and day 28 (~24 °C) following hydrate dissociation. No discernable temperature influences were indicated in the H-O-H bend absorption intensity. Occasional spikes in the H-O-H bend intensity result from fluctuations in environmental humidity relative to humidity during collection of the initial reference spectrum.

Following previous discussions and depiction in **Figure 4-20**, intensity changes in the O-H stretch and libration modes provide information regarding the formation of gas hydrate, whereby increased peak areas indicate the propagation of hydrate growth. The absorption intensity of the H-O-H bend mode provides similar information; however, amplitude changes are inversely related to hydrate growth; decreased peak areas are the result of increasing hydrate content. Lastly, the peak maximum of $3\nu_L$ provides an absolute intensity independent measure of hydrate content with a functional relationship to the %Hydrate directly interacting with the evanescent field. Hence, the intensity independent evaluation of chamber contents from $3\nu_L$ coupled with inversely related amplitude responses from the respective ν_{OH}, ν_L, and ν_2 features provide a powerful combination for monitoring the overall propagation of hydrate growth and identifying spectral changes resulting from variable water content within the evanescent field.

Following hydrate nucleation for data presented in **Figure 4-20**, a gradual decrease in the absorption intensities from the O-H stretch, H-O-H bend, and libration features can be seen starting at approx. day 22 until completion of day 26. However, a subtle increase is observed in the peak maximum $3\nu_L$. Collective data evaluation is indicative of a decrease in the total water content within V_l resulting in a net proportional increase of $V_{Hydrate}$ relative to V_{Liquid}.

This result, albeit subtle in this example, illustrates the significance of collective data evaluation for interpretation of spectroscopic data collected during hydrate monitoring studies. In this example, evaluation of only $3\nu_L$ and/or the H-O-H bend can lead to two possible interpretations: (1) a net increase in %Hydrate within V_l and (2) increased $V_{Hydrate}$ with conversion of water comprising V_{Liquid}. Collective evaluation reveals that interpretation (1) is correct, whereas

interpretation (2) is incorrect. The concurrent decrease in O-H stretch intensity (very subtle) confirms increased %Hydrate in V_l is the result of a decrease in V_{Liquid} due to the liquid water level within the hydrate chamber dropping below the transected portion of the pressure cell by the fiber-optic waveguide. Hence, a continuation of initial derivations from **Section 4.3.1.1** is now provided to further depict mathematical relationships between the IR absorption of water (*W*) with respect to changes in hydrate content interacting with the evanescent field.

4.3.3 Deriving the Quantification of Gas Hydrate from IR Spectra

As described in **Equation 4.1**, the water spectrum (*W*) is the sum of water absorbance from both Hydrate ($A_{Hydrate}$) and Liquid (A_{Liquid}) phases. In this work, Hydrate and Liquid are considered the only water phases contributing to *W* such that the mixed-phase absorption characteristics of *W* follow a proportional relationship to Liquid and Hydrate content in V_l:

$$W \propto \left(\frac{V_{Liquid}}{V_l} + \frac{V_{Hydrate}}{V_l} \right) \ni \left(V_{Liquid} + V_{Hydrate} \right) = 100\% \cdot V_{Water}$$

Equation 4.4

In **Equation 4.4**, V_{Water} is the total water volume in V_l, and this relationship remains true in all described measurements although the value of V_{Water} may not remain constant with respect to **Equation 4.3** where $V_{Water} \leq V_l$. As two water phases are the only major contributors to *W* with respect to V_{Water}, then a functional relationship of *W* can be derived with respect to %Hydrate in V_l following:

$$W = f\left(\frac{V_{Hydrate}}{V_{Liquid} + V_{Hydrate}} \right)_{V_{Water}} \ni \left(\frac{V_{Hydrate}}{V_{Liquid} + V_{Hydrate}} \right)_{V_{Water}} \times 100 = \%\text{Hydrate}_{V_l}$$

Equation 4.5

For intensity based evaluations, V_{Water} is critical. If V_{Water} remains equivalent to V_l throughout a measurement series, including the phase transition, then absorption intensity (I), as an integrated peak area in this thesis, for any vibrational mode has a conserved functional relationship to %Hydrate in V_l following the general description:

$$I = f\left(\%\text{Hydrate}_{V_l}\right)_{V_{Water}}$$

Equation 4.6

Thus, %Hydrate or Δ%Hydrate in V_l can be solved provided proper mathematical relationships have been determined for each absorption feature with respect to V_{Water} under a given set of experimental conditions (i.e., temperature, V_l, etc.). In this work, %Hydrate in V_l was empirically unknown; therefore, an explicit relationship could not be determined. Furthermore, the dependence of I on V_{Water} becomes significant during spectroscopic monitoring of hydrate growth dynamics if changes in V_{Liquid} result in deviations to V_{Water}:

$$\nearrow_{+} V_{Liquid} \neq \nearrow_{-} V_{Hydrate} \ni V_{Water} \neq \text{constant}$$

Equation 4.7

If V_{Water} changes during a measurement series, as in the propane hydrate trial discussed in **Section 4.3.2**, **Equation 4.6** remains valid; however, a new mathematical relationship must be derived with respect to amplitude changes in V_{Water}.

Changes in V_{Water} can be easily discerned from spectroscopic monitoring results when the temporal change in absorption intensities from the H-O-H bend feature are not inversely related to intensity changes in the O-H stretch and libration modes. For environmental applications, this is a positive feature of IR analysis for prevenitng misinterpretation of changes in water content as the conversion of Liquid into Hydrate. However, the strong dependence of I with respect to V_{Water}

imposes a significant barrier for utilizing intensity-based evaluations for extracting values for %Hydrate in V_l.

Alternatively, evaluation of the peak maximum for the 3rd libration overtone provides an absolute intensity independent strategy for assessing %Hydrate in V_l assuming negligible scattering losses arising from the formation of hydrate. This results as boundary conditions for the $3\nu_L$ peak shift are defined by the pure phases, whereby 100% Hydrate yields the upper peak maximum limit, $\omega_{Hydrate}$, and the 100% Liquid peak maximum, ω_{Liquid}, defines the lower limit such that the phase-mixed peak position, $\omega_{(Hydrate + Liquid)}$, must follow:

$$\omega_{Hydrate} > \omega_{(Hydrate + Liquid)} > \omega_{Liquid}$$

Equation 4.8

Hence, $\omega_{(Hydrate + Liquid)}$ in the described experiments varies in response to changes in %Hydrate within V_l following the description in **Equation 4.5**; however, shifts in peak position changes are independent of changes to V_{Water}. As the peak position of the $3\nu_L$ feature is highly sensitive to temperature (T), a general functional relationship can be derived:

$$\omega_{(Hydrate+Liquid)} = f\left(\%\text{Hydrate}_{V_l}\right)_T$$

Equation 4.9

The dimensionality of **Equation 4.9** is simpler mathematically than **Equation 4.6** as the boundary conditions of this relationship are independent of V_{Water}. Assuming the Beer-Lambert law is valid from 0 - 100% Hydrate in the described measurements, the shift in $\omega_{(Hydrate + Liquid)}$ follows a first order linear relationship with respect to changes in %Hydrate within V_l. Hence, a first mathematical approximation of the relationship between $\omega_{(Hydrate + Liquid)}$ and %Hydrate in V_l can be made following additional consideration to experiments described in this thesis in addition to literature.

As discussed in **Section 4.3.1.5**, the reported peak maximum of $3\nu_L$ for ice is minimally influenced over a fairly wide range of temperatures. In literature and this work, the peak maximum of $3\nu_L$ for liquid water is strongly influenced by temperature, which has been related to the temperature dependent structuring of H-bonded networks. Thus, **Equation 4.9** must be solved with respect to the peak position of $3\nu_L$ corresponding to the bulk system temperature. Using the established relationship between ω_{Liquid} and temperature in this thesis (**Figure 4-19 (c.)**), for $T = 5$ °C (approx. that observed at MC118), an initial ω_{Liquid} (100% Liquid) value of 2129.3 cm^{-1} is obtained. If an $\omega_{Hydrate}$ (100% Hydrate) value of 2215 cm^{-1} is implemented (slightly above the 2210 cm^{-1} average reported in **Section 4.3.1.5** to offset potential influence from unreacted interstitial water), the following mathematical relationship is derived:

$$\frac{\omega_{(Hydrate+Liquid)} - 2129.3}{0.857} = \%Hydrate_{V_l}$$

Equation 4.10

For an example calculation: if an $\omega_{(Hydrate + Liquid)}$ value of 2176 cm^{-1} was measured at 5 °C, a %Hydrate value within V_l of approx. 54.5% is calculated using **Equation 4.10**. For continual assessment of %Hydrate in V_l during monitoring applications, **Equation 4.9** must be solved and implemented with respect to variations in system temperature. However, if **Equation 4.10** was implemented for temperature fluctuations of ± 4 °C (less than typical temperature changes observed at the seafloor in the GoM)[1] resulting in maximal $\Delta\omega_{(Hydrate + Liquid)}$ values ± 4 cm^{-1}, then %Hydrate values of 59.2% and 49.8% are calculated for the extremes, respectively. Thus, without correction of ω_{Liquid} with respect to system temperature, the error in predicted %Hydrate would be < 5%.

Equation 4.10 exhibits an explicit mathematical derivation for relating $\omega_{(Hydrate + Liquid)}$ and %Hydrate assuming the Beer-Lambert law remains valid throughout the transition of Liquid to

Hydrate and first order linear changes in refractive index throughout the phase transition with negligible scattering losses. In this work, the boundary conditions for Liquid and Hydrate are fairly well described. As the $3\nu_L$ peak maximum must traverse approx. 80 ± 10 cm^{-1} (defined by system temperature) over the full range of %Hydrate ($0 - 100$ %) during spectroscopic interrogation, implementation of the Beer-Labert law's first order linear relationship with proper temperature correction is predicted to facilitate the semi-quantitative assessment of %Hydrate in V_l within $\sim 10 - 15\%$ of the true value provided no significant departure in the functional relationship.

In this thesis, a multi-point calibration could not be generated to verify the first order linear derivation relating $\omega_{(Hydrate + Liquid)}$ to %Hydrate remains valid from $0 - 100$ %Hydrate due to the inability to directly control or assess the %Hydrate within V_l. Establishing an empirically derived functional form for **Equation 4.9** during future investigations is expected to improve the and confidence level of this strategy for extrapolating accurate and precise %Hydrate information in both laboratory and harsh environment measurements with evanescent field spectroscopy. Fundamentally, quantification is confined to the localized sample volume interrogated by the evanescent field, which does not guarantee representation to bulk hydrate growth behavior. Thus, this method is particularly well-suited for monitoring small-scale hydrate dynamics.

Figure 4-21 illustrates localized dynamics of methane hydrate (no SDS) as %Hydrate from evaluation of $3\nu_L$ with an average pressure corresponding to approx. 475 ± 35 m of ocean depth and average temperature of 2 ± 1.5 °C from 1.5 days into the trial until approx. day 21. For this evaluation, ω_{Liquid} was defined as 2136 cm^{-1} (average peak position for 50 measurements prior to nucleation), and $\omega_{Hydrate}$ was defined as 2215 cm^{-1}. The derived fit equation (analogous to **Equation 4.10**) was utilized for data evaluation at all system temperatures (T_{system}); therefore, -%Hydrate values correspond to 100% Liquid when $T_{system} > T$ for the defined ω_{Liquid}. From

Figure 4-21, the greatest %Hydrate valued observed in V_l during this trial was approx. 88%, which occurred around day 16.

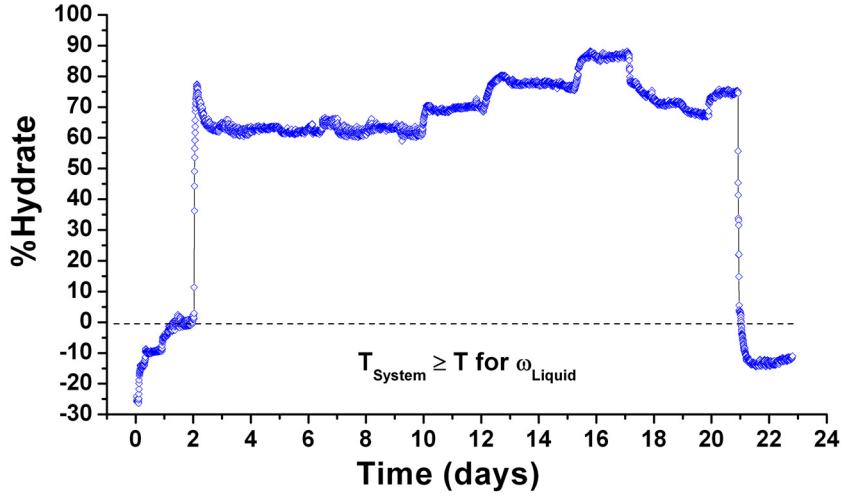

Figure 4-21: Plot of calculated %Hydrate within V_l during a methane hydrate trial (no SDS) following spectroscopic analysis of $3\nu_L$. This hydrate trial was carried out pressures comparable to oceanic environments in the GoM with documented hydrate occurrences.[1] IR-ATR spectra were an average of 250 sample scans with 0.5 cm^{-1} resolution collected at 6 min intervals. (Lines are present to assist visualization).

For quantitative applications in oceanic environments, additional factors influencing the $3\nu_L$ peak maximum other than temperature should be considered for accurate %Hydrate assessments. Salinity and alkalinity (pH) can influence ω_{Liquid}, and both can vary with time and location. However, temperature is anticipated to impart the greatest influence on ω_{Liquid} with respect to a $\Delta\omega_{Liquid}$ of ~1 cm^{-1} per °C. As salt ions are not incorporated into hydrate lattices, $\omega_{Hydrate}$ should remain relatively constant over a wide range of environmental conditions for small volumes interrogated by evanescent field sensing strategies. As a result, initial applications with only temperature considerations to the peak maximum $3\nu_L$ on ω_{Liquid} should facilitate a reasonable first approximation for changes in %Hydrate content within V_l. If salinity and pH (assuming pH facilitates a suitable correction for the spectral impact of alkalinity) are collectively monitored during real-world deployment, %Hydrate values can be corrected following improved

mathematical derivations in the relationship between $\omega_{(Hydrate + Liquid)}$ and %Hydrate with future investigations of the collective impact of the prominent factors that can influence the peak position of $3\nu_L$ (i.e., salinity, pH vs. alkalinity, and pressure) over environmentally relevant variations in oceanic gas hydrate ecosystems.

Overall, the significance for establishing this initial relationship is the potential application for scaling IR observations of Δ%Hydrate to $\Delta V_{Hydrate}$ across larger geographic areas, which could enable approximations to methane flux from dissociating hydrate. Many advances are necessary to realize the full potential of accurate IR monitoring strategies in oceanic gas hydrate ecosystems; however, the potential value of accurately quantifying changes in %Hydrate in oceanic gas hydrate ecosystems substantiates continued investigations to test and improve mathematical derivations for the described quantification strategies and the development of deployable MIR sensing platforms capable of operating in harsh, oceanic environments.

4.3.4 Feasibility for Extending Hydrate Monitoring Strategies into Oceanic Sediment Matrices

A primary objective of this work was to assess the initial feasibility for extending IR-ATR spectroscopic hydrate monitoring strategies into oceanic environments. A potential hydrate monitoring application for MIR chemical sensors could be the embedding of a sensing platform within hydrate-bearing sediments to monitor temporal hydrate dynamics. Such an application would provide valuable data for assessing hydrates in marginal stability regions (shallower depths or at the base of hydrate stability zones due to geothermal gradients), whereby minor temperature or pressure changes could stimulate wide-spread, rapid dissociation events.[1]

To assess the real-world feasibility of such an application, it was essential to screen sediment matrices for potential spectral interferences that could prevent detection and/or monitoring of gas hydrates with future deep-sea MIR chemical sensors. To facilitate this evaluation, a number of shallow (< 30 cm) box core sediment samples were collected around the MC118 gas hydrate site

for spectral analysis of sediment signatures from a variety of settings surrounding the hydrate system. Sediment samples were evaluated in their "native" hydrated condition without manipulation beyond collection, transport, and storage procedures. Hence, this strategy facilitates a close approximation as to what sediment spectral signatures would be in the natural environment. In addition, sediments were allowed to dry, enabling a full evaluation of sediment absorption features with reduced water interferences. This section provides a brief overview of sediment absorption profiles with particular consideration to spectroscopic data evaluation procedures described for monitoring gas hydrate formation and dissociation in **Section 4.3.1**. A complete description of sample collection, sample locations, and experimental procedures for sediment analyses are provided in **Section 5.3**.

Despite complex matrix compositions (e.g., quartz, clay, and carbonate), IR-ATR spectroscopic evaluation of native sediment matrices revealed accessibility to three water absorption features; the O-H stretch, the H-O-H bend, and the 3rd libration overtone. **Figure 4-22** provides representative IR-ATR spectra for hydrated and dried sediments with generic labeling of major mineral component absorption features and select spectra illustrating the diversity of native sediment signatures obtained from MC118 samples.

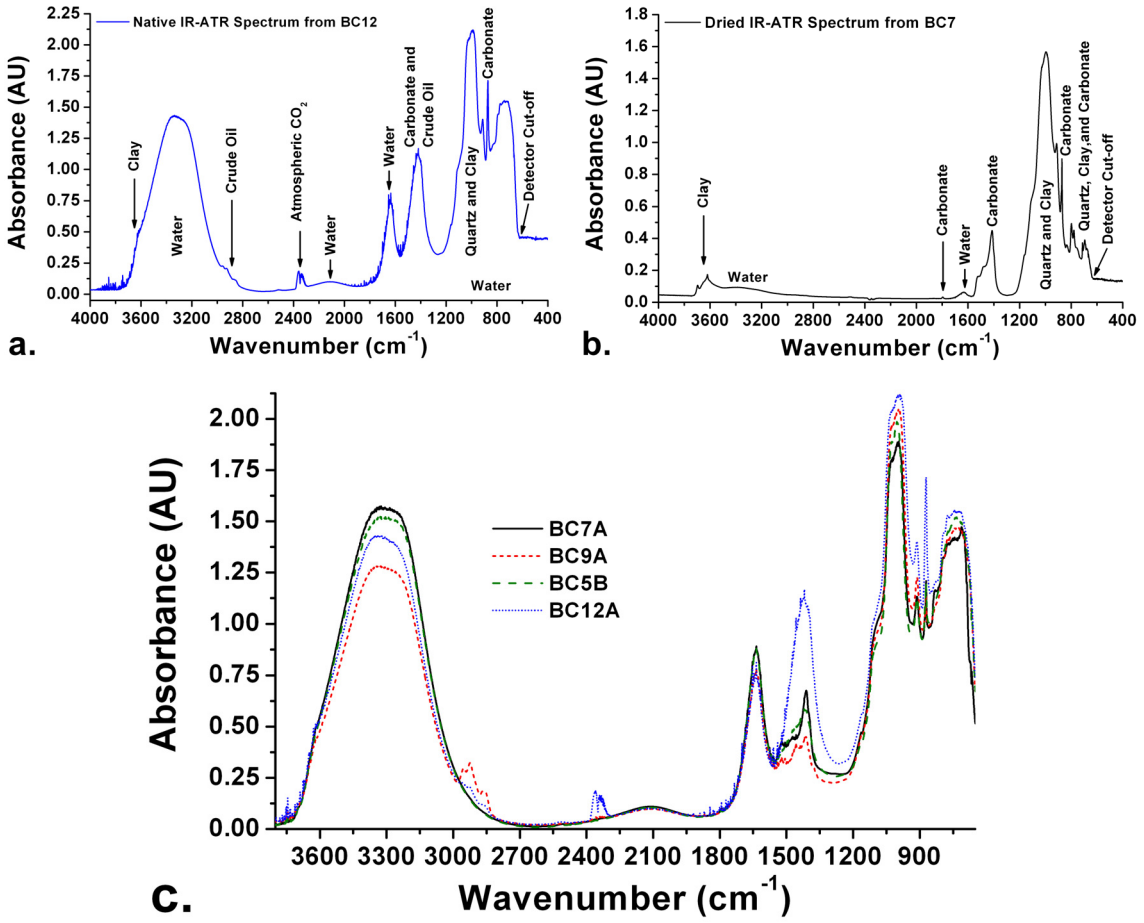

Figure 4-22: (a.) IR-ATR spectrum of hydrated sediments from the BC12 location at MC118, (b.) IR-ATR spectrum of dried sediments from the BC7 location at MC118, and (c.) selected IR-ATR spectra of hydrated sediments from different sampling locations at MC118. (All spectra were the average of 100 sample scans collected at 1 cm^{-1} resolution).

In **Figure 4-22**, the prominence of water signatures in native sediment matrices is readily apparent in **(a.)** and **(c.)**. The IR-ATR spectra provided in **Figure 4-22** enable a direct assessment of potential interferences and limitations of data analysis procedures described for monitoring water absorption features during gas hydrate formation and dissociation with respect to sediment matrix components.

In the O-H stretch region, the intermittent observation of crude oil signatures, the omnipresent clay absorption feature, and variable water absorptions must be considered. The spectral absorbance of clay minerals decreases to background levels at approx. 3500 cm^{-1}, whereas C-H

stretch features from crude oil and other potential organic interferences is primarily limited to $< 3000\ cm^{-1}$. Hence, the O-H stretch peak integration method from $3310 – 3099\ cm^{-1}$ for monitoring hydrate growth should remain unaffected by either matrix components. However, the variable strength in the IR absorption of water reveals fluctuations in the sediment water content. Thus, the collective evaluation of multiple water absorption features should facilitate the *in situ* assessment of fluctuations in the water content of sediment fractions. Furthermore, the observed variability of water absorption magnitude in the investigated sediments support the potential for quantitative evaluation of gas hydrates via analysis of the $3\nu_L$ peak position, as opposed to the peak areas from the O-H stretches and the H-O-H bend features.

Strong IR absorptions from carbonate minerals have the greatest potential to influence the longer frequency (lower wavenumber) absorption of the H-O-H bend mode. Some minor convolution of the two absorptions is observed; however, the upper wavenumber boundary of carbonate absorption for dried sediments was found to occur at $1560\ cm^{-1}$. As the H-O-H bend integration method spans from $1783.5 – 1573.2\ cm^{-1}$, this evaluation strategy should be minimally affected by the presence of carbonate minerals. In practice, the lower wavenumber limit of the H-O-H bend integration method could be shifted to $1580 – 1590\ cm^{-1}$ to minimize spectral overlap, whereby intensity changes from this evaluation procedure primarily reflect changes in either water content and/or hydrate growth.

The spectral region of the 3rd libration overtone exhibits no significant spectral contributions from sediment matrix components; therefore, this feature should provide an excellent, uninterrupted assessment of hydrate dynamics within sediments in oceanic environments. The presence of multiple, strong absorption features from sediment components below $1000\ cm^{-1}$ limits practical evaluation of the libration band for monitoring gas hydrates in sediment matrices.

Overall, sediment evaluations further support the feasibility of extending IR hydrate monitoring strategies into oceanic environments. Although the libration band has limited usefulness, the three available absorption features, each of which respond differently to hydrate growth, should

facilitate the robust evaluation of hydrate dynamics in oceanic sediments. In addition to the screening of sediment constituents, unique variations in characteristic absorption features of carbonate minerals were observed in sediment spectral signatures. **Chapter 5** and **Chapter 6** address additional developments for the application of IR-ATR chemical sensors for evaluating the complexity of carbonate mineralogy surrounding oceanic gas hydrate ecosystems.

4.3.5 Power Limitations for Extending Hydrate Monitoring Strategies into Oceanic Settings

Considering all potential limitations for extending MIR chemical sensing platforms into isolated, oceanic environments for monitoring gas hydrates, power is perhaps the most significant factor regarding the feasibility for application of a high-power instrument. The broadband FT-IR spectrometer slated for incorporation into the 2nd generation submersible sensing platform (described in **Chapter 7**) is anticipated to consume ≥ 140 W during operation. Hence, for stand-alone, battery operated monitoring applications, power limitations restrict the usage of such an instrument to either short-term deployment with high temporal resolution or long-term deployment with low temporal resolution.

With this consideration, spectroscopic data collected during the propane hydrate trial described in **Section 4.3.2** is readdressed with respect to high and low temporal resolution. During that particular hydrate trial, fiber-optic IR-ATR spectra were collected at 6 min intervals (240 spectra per day). Over the 29 day measurement campaign, a total of approx. 5450 spectra were collected. In most oceanic environments, power limitations or the cost of power would likely restrict continuous operation of an FT-IR spectrometer over such an extended period of time. Therefore, the temporal resolution of the given hydrate trial was reduced to 1 spectrum for every 10 hr period of continuous data collection (55 spectra total). **Figure 4-23** provides full and reduced data sets with respect to evaluation of $3\nu_L$.

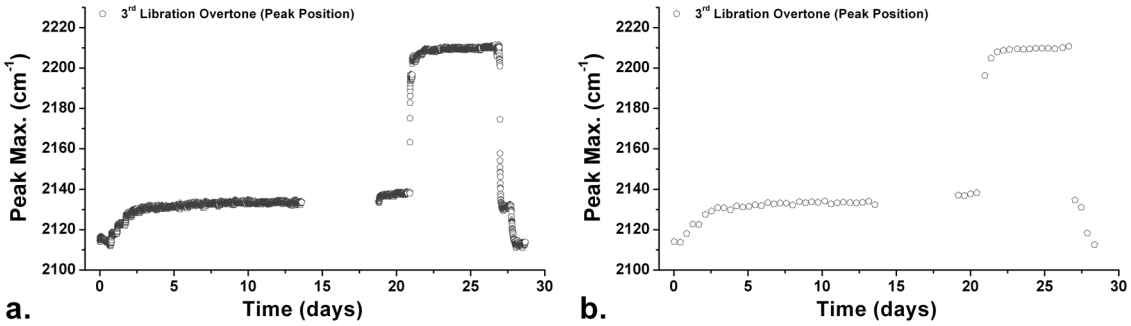

Figure 4-23: Spectroscopic analysis of the 3rd libration overtone for a propane hydrate trial (discussed in **Section 4.3.2**) with (a.) spectra collected at 6 min intervals and (b.) the same trial with reduction of data points by a factor of 100 (1 point per 600 min time interval).

From the propane hydrate data series displayed in **Figure 4-23**, expected information loss results from reduced temporal resolution throughout the hydrate series. However, the major events are still captured from this measurement series despite the reduction of temporal resolution by a factor of 100. If 20 mins were allowed for automated power-up, instrument stabilization, data collection, and shut-down (i.e., sleep mode), only 18.3 hrs of instrument operation time would be required to generate the respective 55 measurements, whereas approx. 565 hours (excluding instrument downtime) were necessary for continuous data collection of the 5450 spectra.

One potentially significant use of MIR chemical sensors is to detect substantial shifts in hydrate composition from dissociation events resulting in rapid outgassing of methane. Such information is embedded within the data presented in **Figure 4-23**, and data transformation of the temporal shift in $3\nu_L$ peak position (ΔPeak Max.) from measurement-to-measurement facilitates better assessment and visualization of rapid changes in hydrate composition. **Figure 4-24** provides such a transformation of data presented in **Figure 4-23**.

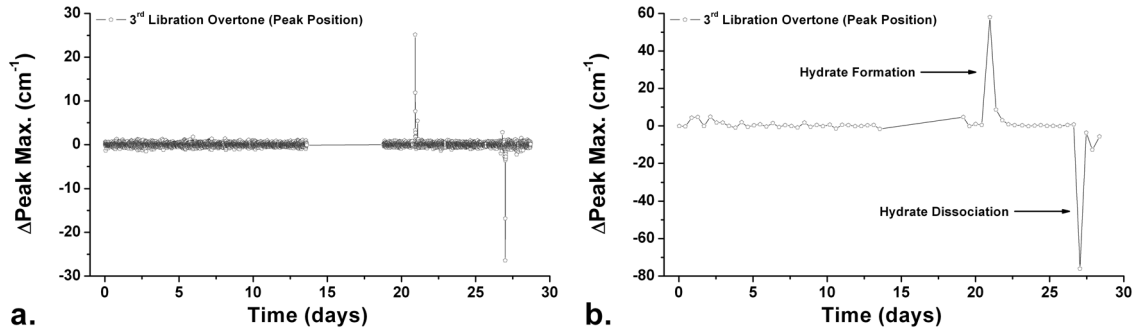

Figure 4-24: Temporal analysis of the $3\nu_L$ peak position with respect to measurement-to-measurement changes in the peak maximum during a propane hydrate series with (a.) 6 min intervals between measurements and (b.) the same data reduced to one measurement point for 600 min intervals. (Lines are present to assist visualization).

In **Figure 4-24**, the prescribed data transformation visually accentuates rapid changes in hydrate content as spiking features ((+) for hydrate growth and (-) for hydrate dissociation). Although the temporal resolution was reduced by a factor of 100 in **Figure 4-24 (b.)**, the sum shift in peak position over the time intervals of hydrate formation and dissociation are easily detected. In addition, the spike features are much stronger in the reduced data set. This is an expected result from the loss of temporal resolution; however, **Figure 24** illustrates that low temporal resolution data collections should enable the detection of rapid hydrate dissociation events at time scales with potentially significant environmental consequences from the abundant outgassing of methane (i.e., migration to the atmosphere) and/or reduced seafloor stability from gas blowouts.

For final consideration of this topic, a comparable first order relationship similar to **Equation 4.10** was derived to relate changes in $\omega_{(Hydrate + Liquid)}$ to changes in %Hydrate in V_l for both high and low temporal resolution data sets for the same hydrate trial. Initial $\omega_{(Liquid)}$ and final $\omega_{(Hydrate)}$ values of 2138 cm^{-1} (obtained prior to hydrate nucleation) and 2115 cm^{-1} were used, respectively. Following calculation and data transformation, **Figure 4-25** provides an overlay of the predicted measurement-to-measurement changes in %Hydrate within V_l from days 20 to 29.

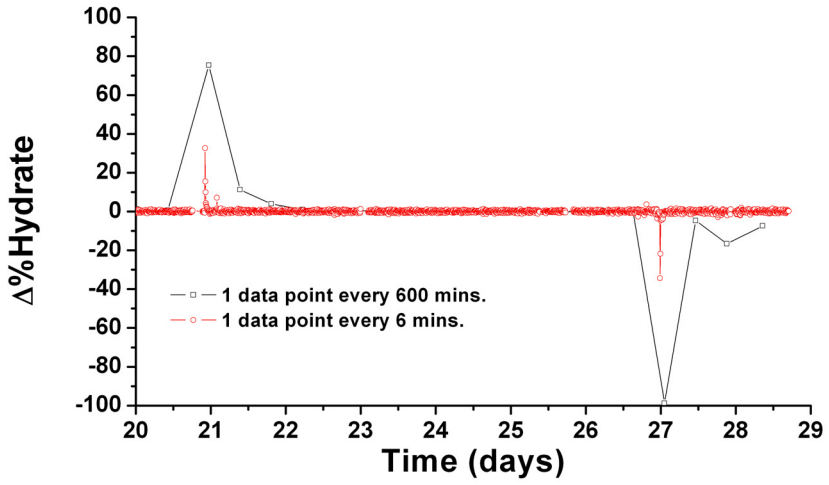

Figure 4-25: Predicted measurement-to-measurement changes in the %Hydrate within V_l during a propane hydrate series with (a.) 6 min intervals between measurements and (b.) the same data reduced to one measurement point for a 600 min. Plot generated from the transformation of the 3rd libration overtone peak position data displayed in **Figure 4-24**. (Lines are present to assist visualization).

From the transformed high and low temporal resolution data sets in **Figure 4-25**, an average of 92.6% of V_{Water} within V_l is predicted to be gas hydrate within 2.2 days following hydrate nucleation. The sum of Δ%Hydrate values for low (5 measurements) and high (512 measurements) temporal resolution data sets yield comparable values of 92.5% and 92.7%, respectively. Following initiation of hydrate dissociation, only liquid water was detected within V_l after approx. 3.1 hrs. The sum of Δ%Hydrate values throughout dissociation for low (1 measurement) and high (31 measurements) resolution data sets revealed -98.7% and -99.8%, respectively. The highest predicted hydrate composition was 95.5%; hence, the dissociation values were slightly overestimated. This difference is reflective to an increased system temperature of approx. 5 °C for hastening hydrate dissociation in this particular measurement series. Additional temperature induced change can also be observed in the low resolution data set at approx. day 28 from return of the hydrate chamber to room temperature. Overall, the low temporal resolution data set coupled with evaluation of %Hydrate throughout the propane hydrate

series demonstrates the attractiveness of IR sensing strategies for investigating the temporal dynamics of hydrate-bearing sediments in oceanic environments.

4.4 Hybridized Reaction Kinetic-Thermodynamic Model for Gas Hydrate Formation

In **Section 4.1.1.4**, two general models, the cluster nucleation hypothesis and reaction kinetic model, were described for nucleation and primary growth mechanisms of gas hydrates.[2, 26-28] Recently, it has been acknowledged that a breakthrough is needed to generate a unified hydrate kinetics model, which, to date, has been hindered as a result of stochastic nucleation.[24] Sloan provides a detailed review of nucleation theory and discusses five primary factors that influence hydrate nucleation from water: (1) displacement from thermodynamic equilibrium of hydrate stability, (2) water state and history, (3) gas composition, (4) extent of water agitation and/or turbulence, and (5) system geometry and surface area.[2]

From the aforementioned list, the multi-dimensionality required for describing and accounting for all possible influences dictating the kinetics of hydrate nucleation and growth becomes clearly evident. In **Figure 4-3**, a combination of the fundamental elements from the cluster nucleation hypothesis and RK model were depicted. Lekvam and Ruoff demonstrated the use of their proposed RK model to mathematically solve reaction rates for five microscopically reversible processes influencing the overall kinetics of methane hydrate growth in aqueous solution.[26, 27] As a result, the fundamental RK model framework provides an initial starting point for expansion and incorporation of additional elements involved in hydrate nucleation and growth processes. This section proposes an expansion of the RK model in light of current and previous works. The proposed expansion with designation of the Reaction Kinetic-Thermodynamic model (RK-T model) is depicted graphically in **Figure 4-26** for reference throughout the ensuing discussion.

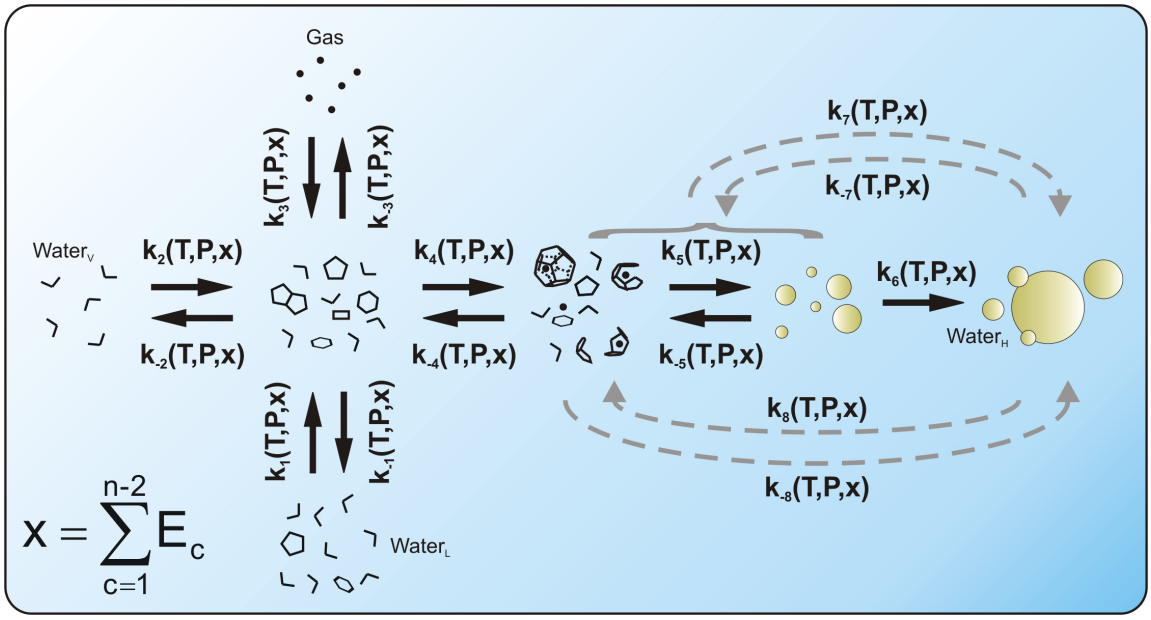

Figure 4-26: Proposed Reaction Kinetic-Thermodynamic Model expanded from the cluster nucleation hypothesis of Christiansen and Sloan and the RK model of Lekvam and Ruoff.[2, 26-28]

The primary limitations identified from expanding the cluster nucleation and RK models into a more universal framework is the restricted dimensionality; although, the established frameworks are fundamentally sound and amenable for expansion, as depicted in **Figure 4-26** with comparison to **Figure 4-2** and **Figure 4-3**.

The first proposed alteration to the RK model is the accountability for the "state" of water depicted as $k_1(T,P,x) \leftrightarrow k_{-1}(T,P,x)$ in **Figure 4-26**. This enables dimensional corrections with respect to temperature (T), pressure (P), and the sum of all other experimental factors (x) for n-2 variables as P and T have already been accounted. With respect to factors influencing hydrate nucleation, P and T are primary compensators of the water state respective to displacement from hydrate equilibrium; whereas, the factor labeled x provides the capability for further dimensional correction with respect to salinity, history of previous hydrate growth, etc. Although the significance of water structuring with temperature and the influence on hydrate stability and nucleation has been recognized, the context of this work in light of previous investigations and molecular level interpretations of temperature and phase influences on the IR spectrum of water

illustrate the need to incorporate these factors into the RK model. The kinetics of water structuring in this step is not anticipated to be a rate limiting factor to nucleation or overall hydrate growth kinetics; however, this enables dimensional correction for the structuring of water, thermal gradients, and cooling efficiency, which can influence nucleation and alter overall hydrate growth kinetics.

The second amendment, depicted as $k_2(T,P,x) \leftrightarrow k_{-2}(T,P,x)$ in **Figure 4-26**, illustrates accountability for water vapor dynamics. In laboratory experimental setups, headspace volume is necessary to facilitate gas exchange and water expansion upon hydrate formation. Hydrate nucleation is often observed at the liquid-water interface; hence, the rate and extent of water evaporation-condensation could alter water structuring at the interface and influence hydrate nucleation.[2] Furthermore, gas hydrate was often formed in the recessed portion of the viewport during this thesis. In the following days after primary growth, gas hydrate accumulations in the viewport ledge diminished from apparent dissociation, evaporation, and recondensation within the hydrate chamber. This observation is attributed to decreased thermodynamic stability of hydrate at that particular location due to thermal gradients. Hence, condensation of water vapor and conversion into gas hydrate within higher stability regions in the sample chamber appear to be an active tertiary growth process. In **Figure 4-26**, a kinetic step for this growth process was not specifically indicated as the reversible stages required for this mechanism are already depicted between the vapor phase and bulk hydrate. The overall impact on bulk hydrate growth kinetics is currently unknown; however, it is possible that this process could kinetically inhibit gas transport necessary for the conversion of trapped, interstitial water. Hence, this mechanism has been included, but further investigation is necessary to determine the significance on hydrate growth kinetics.

The third addition to the RK model, $k_3(T,P,x) \leftrightarrow k_{-3}(T,P,x)$, expands depiction for the dissolution of gas, which has been well-acknowledged as a two-step process: surface adsorption followed by solvation.[80] The RK model accounts for both steps with one kinetic variable, which likely serves

well in practical application. However, isolation of each step enables consideration of experimental factors influencing the kinetics of surface adsorption (i.e., surface area), solvation, and mass transport (i.e., temperature and volume) within the respective context. Furthermore, isolation of surface adsorption and solvation of gas coupled with the first expansion to the RK model inherently incorporates the influence of gas solubility and concentration throughout the overall model without requiring special treatment.

In practice, a reduced consideration of only the primary pseudoelementary processes described by Lekvam and Ruoff for the RK model is perhaps more suited for practical application; however, integration of P, T, and additional x factors at every kinetic step facilitates a universal dimensioning of experimental conditions to all individual elements in the RK-T model. This incorporation should not influence mathematical considerations of individual rate constants proposed by Lekvam and Ruoff; this merely places calculated values into experimental context.[26, 27] The RK-T model framework improves upon the RK model, and it is also amenable for further expansion through incorporation of additional hydrate nucleation and growth mechanisms (i.e., nucleation from ice).[2] In conclusion, the stochastic behavior of nucleation processes inherently inhibits the predictability of any proposed kinetics model; however, the inclusion and consideration of additional experimental factors influencing kinetics of nucleation and hydrate growth may facilitate a more compatible framework for experimental data considerations.

4.5 Conclusions

This chapter presented a variety of studies demonstrating the development, application, and assessment of fiber-optic IR-ATR spectroscopic sensing strategies for monitoring gas hydrate formation and dissociation in aqueous environments. Collectively, the extensive history of gas hydrate research and application of IR techniques specifically addressing the spectral absorption behavior of water have provided generally well-established frameworks facilitating the logical

extension of fiber-optic evanescent field sensing strategies in this work, with particular emphasis towards the monitoring gas hydrate dynamics in oceanic ecosystems.

The IR absorption behavior of water in response to temperature and phase transitioning has been well documented in the literature. Consistent and comparable observations were generated during this thesis. In addition, five data evaluation strategies were implemented for extracting temperature and phase related information from each of the four primary water absorption features, enabling continuous spectroscopic monitoring of gas hydrate dynamics in a controlled laboratory environment. Examination of IR spectral profiles from sediment matrices collected around the MC118 gas hydrate system revealed limited use of data evaluation strategies designed to interrogate the libration absorption mode. However, sediment components are anticipated to have minimal impact upon data evaluation strategies tailored for examination of the O-H stretch, H-O-H bend, and 3rd libration overtone features. Furthermore, it was demonstrated that collective evaluation of the unique responses from these absorption features to the phase transformation of water provides a powerful combination for assessing hydrate dynamics and delineating the differences between changes in %Hydrate due to reduced liquid water content versus the conversion of liquid water into gas hydrate.

In this thesis, a major achievement was demonstrating the use of evanescent field sensing strategies to monitor methane hydrate growth at pressures comparable to documented occurrences of oceanic gas hydrates in the GoM; experimental pressures up to an equivalent of ~510 m of ocean depth with naturally occurring hydrates reported at ~440 m. Several hydrate trials extending > 21 days demonstrated considerable long-term stability of this measurement strategy, which substantiates the potential for long-term deployments of submersible MIR chemical sensing platforms for environmental hydrate monitoring applications. Long-term deployment feasibility was further exemplified through the comparison of information extracted from data generated every 6 mins throughout a hydrate trial extending over a 29 day period to the same data and an imposed reduction of temporal resolution by a factor of 100. Although fine-scale temporal

resolution was diminished, the major formation and dissociation events were still captured during the experimental trial. The capability to detect major growth and dissociation events with limited instrument operation over long periods of time is particularly attractive for evaluating the temporal dynamics of hydrate-bearing sediments in marginal hydrate stability environments.

With consideration to literature and this thesis, the IR absorption profiles for ice (Ih), sI hydrate, and sII hydrate are strikingly similar. In 2004, Zhang and Ewing interpreted the spectral similarities of sI hydrate and ice (Ih) to be consistent with a reported enthalpy change of 1 kJ/mole from the reconfiguration of ice into empty, sI clathrate cage structures.[38] However, there is an underlying indication for the potential capability to differentiate the solid phases of water using IR spectral profiles resulting from the diverse configurations water molecules can occupy within different clathrate cages, the different cages respective to gas hydrate structures (sI, sII, and sH), and the dissimilarities of hydrate structures to the ice lattice. In this work, no indicators were readily identified that might facilitate phase identification using IR spectroscopy. This is attributed to several key factors: (1) phase-mixing during hydrate formation, (2) extent of hydrate formation, (3) broad absorption features of water, (4) temperature dependence, and (5) weak or no IR signatures from guest molecules. All five factors collectively contribute to the current assessment for limited practical usage for phase identification. The unique structural characteristics of each phase may perhaps enable identification from pure hydrate samples; however, without viable assessment as to the volume % of gas hydrate, the sensitivity of IR absorption to liquid water limits phase dependent assignments of peak positions, absorption intensities, and/or bandwidths. Furthermore, the potential for phase identification in oceanic environments is expected to be further limited due to the high probability of encountering phase mixtures of liquid and hydrate, whereby a "pure" gas hydrate spectrum would not be generated to facilitate phase identification. A currently unexplored avenue for phase identification may be through the assessment and comparison of isosbestic points in the O-H stretch region. Several reports (i.e., Millo et al.)[65] have documented isosbestic points during the liquid-to-solid and solid-

to-liquid phase transformations of liquid water and ice (Ih). Perhaps, close inspection of the O-H stretch region during the liquid-to-hydrate phase transformation will reveal unique differences with respect to each solid phase of water. In the current experimental setup, hydrate growth dynamics within the sample chamber and minor baseline shifts from gas hydrate mechanically pushing on the unsupported fiber-optic waveguide limit accurate characterization of isosbestic points.

Extended consideration of experimental results with simple derivations respective to the spectral influences of phase-mixing during hydrate growth has enabled a first approximation for relating spectral shifts in the peak position of $3\nu_L$ to %Hydrate interacting with the evanescent field. The derived first order linear relationship is hypothesized to facilitate quantification to within ~10 – 15% of the true value assuming adherence to the Beer-Lambert law throughout the complete phase transitioning of liquid water to gas hydrate; however, further investigation is warranted to verify the accuracy of this simple functional relationship. Although, with well-characterized boundary conditions dictated with respect to each phase and an approx. 80 cm^{-1} shift in $3\nu_L$ from 0 to 100% Hydrate, even minor deviations in the functional relationship should limit the total error of this derivation to < 15%. A quantification capability within this range substantiates practical use for initial evaluation and quantitative approximation to the variability of hydrate dynamics in harsh, oceanic environments. Caution should be exercised for applications demanding high levels of accuracy; however, continued investigations facilitating an appropriate functional derivation (i.e., more than two points and consideration of potential scattering losses) should enhance the precision, accuracy, and confidence level for this evaluation strategy. Furthermore, improved characterization for correction of spectral influences from variations in temperature, salinity, and pH for environmentally relevant conditions coupled with continuous, floating quantitative analysis should expand the versatility and robustness for environmental applications. The necessity for continuous dimensional corrections with respect to temperature,

salinity, and pH should remain independent of the functional relationship. Although pressure was not a primary influence on the water spectrum in this thesis, extension of this measurement strategy to pressures > 15 MPa warrants additional consideration to pressure influences.

Lastly, a proposed integration of the cluster nucleation hypothesis and reaction kinetic hydrate growth model and expansions to the RK model framework were also presented. The primary significance of the proposed Reaction Kinetic-Thermodynamic model is providing accountability for the influence of water structuring with respect to temperature and pressure (displacement from phase stability). The expanded complexity of the RK-T model may have limited practical usage for laboratory applications; however, it seems fitting to establish a multi-dimensional model incorporating the extensive knowledge of multiple experimental factors directly influencing hydrate nucleation and growth kinetics. Even without practical application, the proposed model enhances visualization to the complexity of gas hydrate growth processes. Ultimately, this model should facilitate broader multi-dimensional considerations that will advance this field towards a more unified hydrate kinetics model.

4.6 Outlook

Considering the rich history of IR spectroscopy and extensive investigations into the spectral behavior of water, it is surprising that IR techniques have had limited application in gas hydrate research. In addition to the studies performed throughout this thesis, only two additional reports demonstrate the application of IR-ATR techniques for investigating gas hydrate structures; both within the past four years. The described limitations regarding structural identification and minimal absorption contributions from methane, ethane, and propane will likely reduce the attractiveness of incorporating IR methodologies in many arenas of gas hydrate research. However, there are many potential avenues for integrating IR sensing strategies into gas hydrate research.

Although the experiments described in this thesis were restricted to well-controlled laboratory conditions, a strong emphasis was placed on assessing the feasibility for extending IR-ATR sensing platforms into oceanic environments for gas hydrate monitoring with the developed data evaluation strategies. Experimental results substantiate the potential insight that can be gained with the application of MIR chemical sensors for long-term monitoring of gas hydrate dynamics within oceanic hydrate ecosystems. Submersible fiber-optic IR-ATR sensors have been previously realized; however, limited operational depths and the known susceptibility of AgX fibers to Cl^- in aqueous solution restricts current sensing capabilities with such an instrument.[81-84] Hence, focused research efforts are necessary to realize the practical development of sensing platforms with more robust waveguiding materials (i.e., ZnSe) to access the full potential of IR-ATR sensing strategies in harsh, deep-sea environments.

In addition to engineering requirements to realize environmental applications, more thorough investigations of environmental factors known to influence the IR absorption behaviors of water are needed. Focused investigations on the spectral signature of liquid water in sediment matrices with variable temperature, salinity, and alkalinity versus pH in the laboratory should facilitate the development of multi-dimensional models for dynamic mathematical correction and extraction of %Hydrate values from the $3\nu_L$ peak position. Furthermore, controlled laboratory experiments are necessary to establish an empirical functional relationship between $3\nu_L$ peak position and %Hydrate interacting with the measurement sample volume. Improved assessment is anticipated to validate the capability of IR methods to quantify %Hydrate with an error of < 5%.

Unique insights into the role of SDS as a hydrate nucleation catalyst was revealed in data collected throughout investigations to establish and assess hydrate monitoring strategies. Although that work is not specifically addressed in this thesis, IR-ATR spectroscopic techniques display significant potential for evaluating different classifications of surfactants to elucidate molecular level mechanisms involved in catalyzing hydrate nucleation. Furthermore, there is

substantial interest for developing hydrate growth and nucleation inhibitors to prevent hydrate formation and blockage of oil pipelines. Various types of kinetic and thermodynamic inhibitors have been reported in the literature.[2, 23, 24] For example, sodium chloride is a well-known thermodynamic hydrate inhibitor due to the influence on water structuring.[24] The effect of salts on water structuring can be observed by shifts the IR spectrum of water; hence, IR techniques may facilitate rapid screening of potential thermodynamic inhibitors of gas hydrate formation and enable the prediction of concentration dependent impact on thermodynamic stability.[66, 69, 70, 72]

In conclusion, there are many potential avenues for improving and extending the application of IR spectroscopy in gas hydrate research. A particular emphasis has been placed on future environmental applications within this thesis, and all indications suggest a significant potential for the viable application of MIR chemical sensors in the exploration of oceanic gas hydrate ecusystems, including evaluation of spatial distributions, temporal dynamics, and directed investigations of acoustic anomalies generated in seismo-accoustic datasets without requiring destructive drilling of boreholes for manual inspection and validation of data interpretations. Overall, the greatest potential for *in situ* monitoring and assessment of oceanic gas hydrates follows the concurrent deployment of multiple sensor technologies, including optical sensors (IR-ATR and Raman), mass spectrometers, temperature, salinity, oxygen, accelerometers, acoustics, etc.

4.7 References

1. A. V. Milkov, R. Sassen, I. Novikova, and E. Mikhailov, *Gas Hydrates at Minimum Stability Water Depths in the Gulf of Mexico: Significance to Geohazard Assessment*, Gulf Coast Association of Geological Societies Transactions **50**, 217 (2000).

2. E. D. Sloan Jr., *Clathrate Hydrates of Natural Gases*, (Marcel Dekker, Inc., New York, 1998).

3. K. A. Kvenvolden, *Gas Hydrates - Geological Perspective and Global Change*, Reviews of Geophysics **31**, 173 (1993).

4. K. A. Kvenvolden, *Potential Effects of Gas Hydrate on Human Welfare*, Proceedings of the National Academy of Sciences of the United States of America **96**, 3420 (1999).

5. K. A. Kvenvolden, *Methane Hydrate in the Global Organic Carbon Cycle*, Terra Nova **14**, 302 (2002).

6. A. V. Milkov and R. Sassen, *Economic Geology of Offshore Natural Gas Hydrate Accumulations and Provinces*, Marine and Petroleum Geology **19**, 1 (2002).

7. K. A. Kvenvolden and B. W. Rogers, *Gaia's Breath-Global Methane Exhalations*, Marine and Petroleum Geology **22**, 579 (2005).

8. A. V. Milkov, *Molecular and Stable Isotope Compositions of Natural Gas Hydrates: A Revised Global Dataset and Basic Interpretations in the Context of Geological Settings*, Organic Geochemistry **36**, 681 (2005).

9. P. G. Brewer, C. Paull, E. T. Peltzer, W. Ussler, G. Rehder, and G. Friederich, *Measurements of the Fate of Gas Hydrates during Transit Through the Ocean Water Column*, Geophysical Research Letters **29**, 38/1 (2002).

10. G. R. Dickens, J. R. Oneil, D. K. Rea, and R. M. Owen, *Dissociation of Oceanic Methane Hydrate as a Cause of the Carbon-Isotope Excursion at the End of the Paleocene*, Paleoceanography **10**, 965 (1995).

11. I. Leifer, B. P. Luyendyk, J. Boles, and J. F. Clark, *Natural Marine Seepage Blowout: Contribution to Atmospheric Methane*, Global Biogeochemical Cycles **20**, GB3008/1 (2006).

12. I. Leifer and I. MacDonald, *Dynamics of the Gas Flux from Shallow Gas Hydrate Deposits: Interaction between Oily Hydrate Bubbles and the Oceanic Environment*, Earth and Planetary Science Letters **210**, 411 (2003).

13. C. K. Paull, P. G. Brewer, W. Ussler, E. T. Peltzer, G. Rehder, and D. Clague, *An Experiment Demonstrating that Marine Slumping is a Mechanism to Transfer Methane from Seafloor Gas-Hydrate Deposits into the Upper Ocean and Atmosphere*, Geo-Marine Letters **22**, 198 (2003).

14. A. V. Shcherbakov and V. V. Malakhova, *Modeling the Distribution of the World Ocean Methane Hydrates and the Methane Flow into the Atmosphere*, Atmospheric and Oceanic Optics **19**, 477 (2006).

15. W. Xu, *Modeling Dynamic Marine Gas Hydrate Systems*, American Mineralogist **89**, 1271 (2004).

16. W. Xu, R. P. Lowell, and E. T. Peltzer, *Effect of Seafloor Temperature and Pressure Variations on Methane Flux from a Gas Hydrate Layer: Comparison between Current and Late Paleocene Climate Conditions*, Journal of Geophysical Research, [Solid Earth] **106**, 26413 (2001).

17. Y. Zhang, *Methane Escape from Gas Hydrate Systems in Marine Environment, and Methane-Driven Oceanic Eruptions*, Geophysical Research Letters **30**, 51/1 (2003).

18. D. R. Hutchinson, C. D. Ruppel, H. S. Roberts, R. S. Carney, and M. A. Smith, in Gulf of Mexico - Its Origin (History, Archaeology, and Geology), Vol. 1 (C. W. Holmes, ed.), Texas A&M University Press, College Station, In Press.

19. R. Sassen and I. R. MacDonald, *Evidence of Structure H Hydrate, Gulf of Mexico Continental Slope*, Organic Geochemistry **22**, 1029 (1994).

20. Y. Zhong and R. E. Rogers, *Surfactant Effects on Gas Hydrate Formation*, Chemical Engineering Science **55**, 4175 (2000).

21. R. E. Rogers, C. Kothapalli, M. S. Lee, and J. R. Woolsey, *Catalysis of Gas Hydrates by Biosurfactants in Seawater-saturated Sand/Clay*, Canadian Journal of Chemical Engineering **81**, 973 (2003).

22. F. Francisca, T. S. Yun, C. Ruppel, and J. C. Santamarina, *Geophysical and Geotechnical Properties of Near-seafloor Sediments in the Northern Gulf of Mexico Gas Hydrate Province*, Earth and Planetary Science Letters **237**, 924 (2005).

23. J. P. Lederhos, J. P. Long, A. Sum, R. L. Christiansen, and E. D. Sloan, Jr., *Effective Kinetic Inhibitors for Natural Gas Hydrates*, Chemical Engineering Science **51**, 1221 (1996).

24. E. D. Sloan, *Fundamental Principles and Applications of Natural Gas Hydrates*, Nature (London, United Kingdom) **426**, 353 (2003).

25. A. P. Mehta, P. B. Hebert, E. R. Cadena, and J. P. Weatherman, *Fulfilling the Promise of Low-dosage Hydrate Inhibitors: Journey from Academic Curiosity to Successful Field Implementation*, SPE Production & Facilities **18**, 73 (2003).

26. K. Lekvam and P. Ruoff, *A Reaction Kinetic Mechanism for Methane Hydrate Formation in Liquid Water*, Journal of the American Chemical Society **115**, 8565 (1993).

27. K. Lekvam and P. Ruoff, *A Reaction Kinetic Mechanism for Methane Hydrate Formation in Liquid Water. [Erratum to document cited in CA119:142448]*, Journal of the American Chemical Society **116**, 4529 (1994).

28. R. L. Christiansen and E. D. Sloan, Jr., *Mechanisms and Kinetics of Hydrate Formation*, Annals of the New York Academy of Sciences **715**, 283 (1994).

29. J. E. Bertie and S. M. Jacobs, *Infrared Spectra from 300 to 10 cm-1 of Structure II Clathrate Hydrates at 4.3 K*, Journal of Chemical Physics **69**, 4105 (1978).

30. J. E. Bertie and J. P. Devlin, *Infrared Spectroscopic Proof of the Formation of the Structure I Hydrate of Oxirane from Annealed Low-temperature Condensate*, Journal of Chemical Physics **78**, 6340 (1983).

31. H. H. Richardson, P. J. Wooldridge, and J. P. Devlin, *FT-IR Spectra of Vacuum Deposited Clathrate Hydrates of Oxirane, Hydrogen Sulfide, THF, and Ethane*, Journal of Chemical Physics **83**, 4387 (1985).

32. F. Fleyfel and J. P. Devlin, *FT-IR Spectra of 90 K Films of Simple, Mixed, and Double Clathrate Hydrates of Trimethylene Oxide, Methyl Chloride, Carbon Dioxide, Tetrahydrofuran, and Ethylene Oxide Containing Decoupled Water-d2*, Journal of Physical Chemistry **92**, 631 (1988).

33. J. P. Devlin, *Infrared Spectra of Gas-phase Water Microparticles: Crystalline, Amorphous, and Clathrate-hydrate Clusters of Water, Water-d2, and Water/Water-d2*, Journal of Chemical Physics **91**, 5850 (1989).

34. F. Fleyfel, H. H. Richardson, and J. P. Devlin, *Comparative Sulfur Dioxide Infrared Spectra: Type I and II Clathrate Hydrate Films, Large Gas-phase Clusters, and Anhydrous Crystalline Films*, Journal of Physical Chemistry **94**, 7032 (1990).

35. F. Fleyfel and J. P. Devlin, *Carbon Dioxide Clathrate Hydrate Epitaxial Growth: Spectroscopic Evidence for Formation of the Simple Type-II Carbon Dioxide Hydrate*, Journal of Physical Chemistry **95**, 3811 (1991).

36. K. D. Williams and J. P. Devlin, *Formation and Spectra of Clathrate Hydrates of Methanol and Methanol-ether Mixtures*, Journal of Molecular Structure **416**, 277 (1997).

37. H. Oyama, T. Ebinuma, W. Shimada, S. Takeya, J. Nagao, T. Uchida, and H. Narita, *An Experimental Study of Gas-hydrate Formation by Measuring Viscosity and Infrared Spectra*, Canadian Journal of Physics **81**, 485 (2003).

38. Z. Zhang and G. E. Ewing, *Infrared Studies of the SO2 Clathrate Hydrate*, Journal of Physical Chemistry A **108**, 1681 (2004).

39. J. J. Fox and A. E. Martin, *Investigations of Infrared Spectra (2.5-7.5 m). Absorption of Water*, Proc. Roy. Soc. (London) **A174**, 234 (1940).

40. J. N. Finch and E. R. Lippincott, *Hydrogen-bond Systems: Temperature Dependence of OH Frequency Shifts and OH Band Intensities*, Journal of Chemical Physics **24**, 908 (1956).

41. J. N. Finch and E. R. Lippincott, *Hydrogen Bond Systems - Temperature Dependence of OH Frequency Shifts and OH Band Intensities*, Journal of Physical Chemistry **61**, 894 (1957).

42. N. Ockman, *The Infrared and Raman Spectra of Ice*, Advance in Phys. **7**, 199 (1958).

43. N. Ockman and G. B. B. M. Sutherland, *Infrared and Raman Spectra of Single Crystals of Ice*, Proceeding of the Royal Society of London. Series A, Mathematical and Physical Sciences **247**, 434 (1958).

44. J. E. Bertie and E. Whalley, *Infrared Spectra of Ices Ih and Ic in the Range 4000 to 350 cm-1*, Journal of Chemical Physics **40**, 1637 (1964).

45. J. E. Bertie, H. J. Labbe, and E. Whalley, *Absorptivity of Ice I in the Range 4000-30 cm-1*, Journal of Chemical Physics **50**, 4501 (1969).

46. S. G. Warren, *Optical Constants of Ice from the Ultraviolet to the Microwave*, Applied Optics **23**, 1206 (1984).

47. M. Marchi, J. S. Tse, and M. L. Klein, *Lattice Vibrations and Infrared Absorption of Ice Ih*, Journal of Chemical Physics **85**, 2414 (1986).

48. Y. Marechal, *Infrared Spectra of Water. I. Effect of Temperature and of H/D Isotopic Dilution*, Journal of Chemical Physics **95**, 5565 (1991).

49. Y. Marechal, *Infrared Spectra of Water. II. Dynamics of Water and Heavy Water Molecules*, Journal de Physique II **3**, 557 (1993).

50. Y. Marechal, *Infrared Spectra of a Poorly Known Species: Water. 3*, Journal of Physical Chemistry **97**, 2846 (1993).

51. F. O. Libnau, O. M. Kvalheim, A. A. Christy, and J. Toft, *Spectra of Water in the Near- and Mid-infrared Region*, Vibrational Spectroscopy **7**, 243 (1994).

52. Y. Marechal, *IR Spectroscopy of an Exceptional H-bonded Liquid: Water*, Journal of Molecular Structure **322**, 105 (1994).

53. J. P. Devlin and V. Buch, *Surface of Ice as Viewed from Combined Spectroscopic and Computer Modeling Studies*, Journal of Physical Chemistry **99**, 16534 (1995).

54. T. Iwata, J. Koshoubu, C. Jin, and Y. Okubo, *Temperature Dependence of the Mid-infrared OH Spectral Band in Liquid Water*, Applied Spectroscopy **51**, 1269 (1997).

55. S. Y. Venyaminov and F. G. Prendergast, *Water (H2O and D2O) Molar Absorptivity in the 1000-4000 cm-1 Range and Quantitative Infrared Spectroscopy of Aqueous Solutions*, Analytical Biochemistry **248**, 234 (1997).

56. F. Wuelfert, W. T. Kok, and A. K. Smilde, *Influence of Temperature on Vibrational Spectra and Consequences for the Predictive Ability of Multivariate Models*, Analytical Chemistry **70**, 1761 (1998).

57. Y. Y. Efimov and I. Naberukhin Yu, *On the Interrelation Between Frequencies of Stretching and Bending Vibrations in Liquid Water*, Spectrochim Acta A Mol Biomol Spectrosc FIELD Full Journal Title:Spectrochimica acta. Part A, Molecular and biomolecular spectroscopy **58**, 519 (2002).

58. J. Grdadolnik, *An Attenuated Total Reflection Infrared Spectroscopy of Water Solutions*, Internet Journal of Vibrational Spectroscopy [online computer file] **6**, No pp given (2002).

59. V. Sadtchenko and G. E. Ewing, *A New Approach to the Study of Interfacial Melting of Ice: Infrared Spectroscopy*, Canadian Journal of Physics **81**, 333 (2003).

60. M. Praprotnik, D. Janezic, and J. Mavri, *Temperature Dependence of Water Vibrational Spectrum: A Molecular Dynamics Simulation Study*, Journal of Physical Chemistry A **108**, 11056 (2004).

61. Y. Raichlin, A. Millo, and A. Katzir, *Investigations of the Structure of Water Using Mid-IR Fiberoptic Evanescent Wave Spectroscopy*, Physical Review Letters **93**, 185703/1 (2004).

62. J. B. Brubach, A. Mermet, A. Filabozzi, A. Gerschel, and P. Roy, *Signatures of the Hydrogen Bonding in the Infrared Bands of Water*, Journal of Chemical Physics **122**, 184509/1 (2005).

63. B. Czarnik-Matusewicz, S. Pilorz, and J. P. Hawranek, *Temperature-dependent Water Structural Transitions Examined by Near-IR and Mid-IR Spectra Analyzed by Multivariate Curve Resolution and Two-dimensional Correlation Spectroscopy*, Analytica Chimica Acta **544**, 15 (2005).

64. M. Freda, A. Piluso, A. Santucci, and P. Sassi, *Transmittance Fourier Transform Infrared Spectra of Liquid Water in the Whole Mid-infrared Region: Temperature Dependence and Structural Analysis*, Applied Spectroscopy **59**, 1155 (2005).

65. A. Millo, Y. Raichlin, and A. Katzir, *Mid-infrared Fiber-optic Attenuated Total Reflection Spectroscopy of the Solid-Liquid Phase Transition of Water*, Applied Spectroscopy **59**, 460 (2005).

66. F. Vogt, M. Kraft, and B. Mizaikoff, *First Results on Infrared Attenuated Total Reflection Spectroscopy for Quantitative Analysis of Salt Ions in Seawater*, Applied Spectroscopy **56**, 1376 (2002).

67. J. Baril, J.-J. Max, and C. Chapados, *Infrared Titration of Phosphoric Acid*, Canadian Journal of Chemistry **78**, 490 (2000).

68. J.-J. Max and C. Chapados, *Subtraction of the Water Spectra from Infrared Spectra of Acidic and Alkaline Solutions*, Applied Spectroscopy **52**, 963 (1998).

69. J.-J. Max and C. Chapados, *Interpolation and Extrapolation of Infrared Spectra of Binary Ionic Aqueous Solutions*, Applied Spectroscopy **53**, 1601 (1999).

70. J.-J. Max and C. Chapados, *Infrared Spectra of Cesium Chloride Aqueous Solutions*, Journal of Chemical Physics **113**, 6803 (2000).

71. J.-J. Max and C. Chapados, *Infrared Titration of Aqueous NaOH by Aqueous HCl*, Canadian Journal of Chemistry **78**, 64 (2000).

72. J.-J. Max, S. De Blois, A. Veilleux, and C. Chapados, *IR Spectroscopy of Aqueous Alkali Halides. Factor Analysis*, Canadian Journal of Chemistry **79**, 13 (2001).

73. J.-J. Max, C. Menichelli, and C. Chapados, *Infrared Titration of Aqueous Sulfuric Acid*, Journal of Physical Chemistry A **104**, 2845 (2000).

74. J.-J. Max, M. Trudel, and C. Chapados, *Subtraction of the Water Spectra from the Infrared Spectrum of Saline Solutions*, Applied Spectroscopy **52**, 234 (1998).

75. J. Abe, N. Hirano, and N. Tsuchiya, *Experimental Apparatus for Measurement of IR and Raman Spectrum at High Temperatures and Pressures*, AIP Conference Proceedings **833**, 129 (2006).

76. *NIST Standard Reference Database 69, June 2005 Release: NIST Chemistry WebBook*, http://webbook.nist.gov/chemistry/ (December 2005).

77. A. Rahman and F. H. Stillinger, *Hydrogen-bond Patterns in Liquid Water*, Journal of the American Chemical Society **95**, 7943 (1973).

78. P. A. Giguere and K. B. Harvey, *The Infrared Absorption of Water and Heavy Water in Condensed States*, Canadian Journal of Chemistry **34**, 798 (1956).

79. P. Buchanan, N. Aldiwan, A. K. Soper, J. L. Creek, and C. A. Koh, *Decreased Structure on Dissolving Methane in Water*, Chemical Physics Letters **415**, 89 (2005).

80. K. Y. Song, G. Feneyrou, F. Fleyfel, R. Martin, J. Lievois, and R. Kobayashi, *Solubility Measurements of Methane and Ethane in Water at and near Hydrate Conditions*, Fluid Phase Equilibria **128**, 249 (1997).

81. M. Kraft, *Mid-Infrared Spectrosocpy using Optical Waveguides in the Marine Environment*, Technische Universitat Wien, (2000).

82. M. Kraft, M. Karlowatz, B. Mizaikoff, R. Stuck, M. Steden, M. Ulex, and H. Amann, *Sensor Head Development for Mid-infrared Fiber-optic Underwater Sensors*, Measurement Science and Technology **13**, 1294 (2002).

83. M. Kraft, M. Jakusch, M. Karlowatz, A. Katzir, and B. Mizaikoff, *New Frontiers for Mid-infrared Sensors: Towards Deep Sea Monitoring with a Submarine FT-IR Sensor System*, Applied Spectroscopy **57**, 591 (2003).

84. R. Goebel, R. Krska, R. Kellner, and A. Katzir, *Development of Protective Polymer Coatings for Silver Halide Fibers and Their Application as Threshold Level Sensors for Chlorinated Hydrocarbons in Seawater*, Fresenius' Journal of Analytical Chemistry **348**, 780 (1994).

CHAPTER 5

IR-ATR EVALUATION OF CARBONATE MINERALS IN SEAFLOOR SEDIMENTS

In this chapter, the application of IR-ATR spectroscopy for evaluating carbonate minerals in seafloor sediments is presented along with a background on the general application of IR spectroscopy for carbonate mineralogy. The primary focuses of this chapter are direct qualitative characterization of carbonate minerals and the semi-quantitative evaluation of calcite and dolomite compositions in marine sediment samples without pre-treatment. To establish the context for presented studies, the scope and complexity of carbonate mineralogy with respect to gas hydrate ecosystems in the GoM will be described following a general introduction to carbonate mineral classification.

5.1 Motivation

The application of IR spectroscopy for analyzing carbonate minerals is an enduring research topic with roots extending back to the early 1950's with establishment of spectral databases for a wide range of naturally occurring minerals.[1-3] In the mid-1960's, the capability of IR methods to quantify carbonate minerals in marine sediments was demonstrated and acknowledged for the potential value as an on-ship research tool.[4, 5] Recently, the application of IR spectroscopy for carbonate mineralogy has gained relevance in areas ranging from the characterization of synthetic formation of magnesian calcite (Mg-calcite) to evaluating Sr and Mg concentrations in biogenic calcites.[6, 7]

IR-ATR spectroscopic evaluation of seafloor sediments for this thesis was initiated as a next-step to assess the potential of MIR chemical sensors for monitoring hydrate dynamics in oceanic environments (see **Chapter 4**). Preliminary sediment analyses were performed with samples collected from MC118 in October 2005 as provided by Dr. Carol Lutken of the University of Mississippi. Following initial screenings, significant spectral variations observed in the IR

absorption profiles of carbonate minerals stimulated a breadth of studies to further address and understand the nature and spectral differences of carbonate minerals in context to oceanic gas hydrate ecosystems in the GoM.

5.1.1 Introduction to the Classification of Carbonate Minerals

Carbonate minerals are a diverse group of naturally occurring rock formations containing the carbonate ion, CO_3^{2-}.The most common anhydrous carbonate minerals in the primary Dana classification 14 were predominately studied in this work.[8, 9] Within Dana 14, the anhydrous carbonate minerals are subdivided by general chemical formula, crystal system, and final classification based on specific chemical formula.[8, 9] **Table 5-1** summarizes the Dana classifications for carbonate minerals examined in this thesis.

Table 5-1: Dana classification of carbonate minerals addressed with IR-ATR spectroscopy in this thesis.

Dana Classification of Carbonate Minerals
14 Anhydrous Carbonate Minerals
14.1 Anhydrous Carbonates with Simple Formula A+ CO_3
14.1.1 Calcite Group (Trigonal – Hexagonal Scalenohedral)
14.1.1.1 Calcite, $CaCO_3$
14.1.1.2 Magnesite, $MgCO_3$
14.1.1.3 Siderite, $Fe^{++}CO_3$
14.1.1.4 Rhodochrosite, $MnCO_3$
14.1.1.6 Smithsonite, $ZnCO_3$
14.1.3 Aragonite Group (Orthorhombic – Dipyramidal)
14.1.3.1 Aragonite, $CaCO_3$
14.1.3.2 Witherite, $BaCO_3$
14.1.3.3 Strontianite, $SrCO_3$
14.1.3.4 Cerussite, $PbCO_3$
14.2 Anhydrous Carbonates with Compound Formula A+ B++ $(CO_3)_2$
14.2.1 Dolomite Group (Trigonal – Rhombohedral)
14.2.1.1 Dolomite, $CaMg(CO_3)_2$

In addition to the carbonate species listed in **Table 5-1**, the anhydrous carbonate phase of Mg-calcite will be discussed throughout this body of work. Mg-calcite is not classified in the Dana scheme; however, it is a common carbonate phase often encountered in marine environments, including oceanic gas hydrate ecosystems.[10-12] Mg-calcite will be described and discussed in more detail when relevant within ensuing sections.

5.1.2 Carbonate Mineralogy of Oceanic Gas Hydrate Ecosystems in the GoM

Carbonate minerals are ubiquitous throughout many marine environments, and are extremely diverse and complex with respect to origin, composition, diagenesis, and distribution.[10] While the focus of carbonate mineralogy throughout this thesis primarily targets gas hydrate ecosystems in the GoM, it is prudent to address more generalized regional, even global, characteristics of the origins and distributions of carbonates throughout marine environments. This aspect is particularly important for disseminating and contextualizing the findings presented in this chapter and **Chapter 6**. The following sub-sections provide a fundamental and descriptive background to the scope, complexity, and diversity of carbonate minerals throughout the GoM along with the relevance to gas hydrate ecosystems.

5.1.2.1 Authigenic Carbonate Production

The term authigenic refers to minerals formed in-place as opposed to being transported into a geologic system from an external source. Roberts and Aharon have described three basic categories for carbonate buildups on the northern shelf edges and continental slopes in the GoM: (1) reefs, (2) bioherms, and (3) lithoherms.[11] Reef formations consist of biogenic and inorganically cemented carbonates containing frame-building organisms (i.e., coralline algae) typically found in the photic zone of warm, tropical to sub-tropical waters. Bioherm mounds are much less geographically restricted, and are primarily comprised of biogenic carbonates from organisms such as mussels and clams, which are not frame-building species. Lithoherms form by submarine lithification (i.e., compaction and cementation) in deepwater environments, and may

contain some biogenic carbonate. Recently, the term chemoherm has been introduced to differentiate formations resulting from authigenic carbonate precipitation driven by chemosynthetic processes surrounding hydrocarbon vents.[11]

In the GoM, authigenic chemoherms can greatly modify the seafloor surrounding cold hydrocarbon seeps (i.e., at or near ambient seawater temperatures), and are frequently coincident with gas hydrate occurrences.[11, 13-16] Chemoherms are strongly linked to the microbial oxidation of exuding hydrocarbons as evidenced by strong depletions in ^{13}C, which typically range from approx. -14 ‰ to -55 ‰ PDB (per mille relative to a sample standard such as the Chicago Belemnite Standard).[11, 15, 17] Chemosynthetic mediated authigenic carbonate formation surrounding seep environments is driven by the concomitant production of CO_2 from the anaerobic oxidation of methane and other hydrocarbons (i.e., crude oil) and enhanced sulfate reduction resulting in pore water saturation of bicarbonate and hydrogen sulfide.[15, 16, 18-23] In these circumstances, pore water chemistry strongly favors inorganic (i.e., abiotic) authigenic carbonate precipitation following the generalized formula:[16]

$$2HCO_3^- + (Ca^{2+}, Mg^{2+}) \rightarrow (Ca, Mg)CO_3 + H_2O + CO_2$$

Equation 5.1

Roberts and Aharon provide an extensive overview on authigenic carbonate formations found throughout the full depth range of the northern GoM slope.[11] The importance of microbially driven chemoherm accumulations is two-fold: (1) massive carbonate accumulations greatly modify seafloor morphology,[11, 12, 15, 23] and (2) the magnitude of carbon/carbonate cycling and sequestration of greenhouse gases within these environments are significant for consideration at a global scale, and in effect, buffer the migration of seeping greenhouse gases into the atmosphere.[23-27] Furthermore, the significance of chemoherms are not exclusive to the GoM.[12, 19, 20, 28]

In highly-active areas of carbonate precipitation, diverse morphological authigenic formations, including large mounds, isolated slabs, hardgrounds, nodules, and microcrystals, can be found.[11, 20, 23] Occasionally, massive carbonate buildups can extend 10 – 20 m in relief of the surrounding environment, and can be easily detected in seismic profiles as a result of their high acoustic density.[11] However, as the distance increases away from a seep system, the seafloor morphology typically tapers off to a comparatively barren landscape with a significant decrease in biodiversity (i.e., the MC118 gas hydrate site).[23]

The most common marine carbonate minerals, including those found within GoM hydrate ecosystems, are calcite, dolomite, aragonite, and Mg-calcite.[10, 11, 14, 16, 20, 29] However, the mineralogy, genesis, and diagenesis of marine carbonates can be highly variable and complex.[10, 12, 30] In deep-sea environments, many geophysical and biogeochemical factors such as pore water chemistry (i.e., alkalinity, $[Ca^{2+}]$, and $[Mg^{2+}]$), pCO_2, temperature, etc. can greatly affect the kinetics and thermodynamics of inorganically precipitated carbonate minerals.[10, 12, 20, 30-32] Berner described that general carbonate phase stability within marine environments follows the order: dolomite > calcite > Mg-calcite (< 8.5 mole% $MgCO_3$) > aragonite > high Mg-calcite (> 8.5 mole% $MgCO_3$).[31]

In addition to older, larger authigenic carbonate accumulations, ranging from small nodule formations of several millimeters up to massive mound-like formations, incipient authigenic carbonate formation occurs throughout fine grained sediment fractions surrounding hydrate locations in the GoM, whereby background biogenic carbonate content can be > 75% by mass.[11, 14, 15, 23, 29, 30] In this thesis, IR-ATR spectroscopy has been applied to gain insight into the distribution and variance of carbonate minerals and their origins within sediments and nodule formations surrounding the gas hydrate system at MC118. Results presented throughout this chapter and **Chapter 6** are relevant for evaluating carbon cycling and sequestration within hydrate ecosystems and display the potential utility of IR-ATR spectroscopy for guiding more

detailed investigations into the complexity and buffering capabilities of chemosynthetic communities associated with cold hydrocarbon seeps.

5.1.2.2 Dolomitization

Dolomitization is the diagenetic conversion of calcium carbonate into dolomite within Mg-rich environments. Experimental evidence supports the fact that dolomitization processes occur in variety of marine settings, including intertidal, supratidal, and deep-sea environments.[10] In deep-sea environments, dolomitization is typically considered a gradual process occurring over geologic time (i.e., burial dolomitization), which can greatly alter the calcite-dolomite composition of sediments.[10, 30] However, as dolomite can also form as a primary precipitate in marine environments, the capability to characterize and/or differentiate dolomites as the product of primary precipitation or diagenetic conversion is frequently enigmatic.[10, 30, 33]

The occurrence of dolomite has been documented within cold seep environments in the GoM; however, the processes of authigenic/sedimentary dolomite formation are yet to be fully understood.[11, 15, 30] Botz et al. have reported at least two generations of calcite and dolomite formations in GoM sediments from several coring locations, including one core near gas hydrate occurrence in Green Canyon Block 183.[30] Multiple formation generations are evidenced by carbon isotope ratios ($\delta^{13}C$) ranging from "normal-marine" values of 0 ‰ to "microbially altered" carbonates with depleted ^{13}C values of -14.6 ‰ PDB. Within this work, dolomite was observed in shallow (< 30 cm) sediments, deep (> 30 cm) sediments, and several nodule formations. The capabilities, limitations, and potential application of IR-ATR spectroscopy as a characterization tool for marine dolomites will be further discussed in **Section 5.5.2.5**.

5.1.2.3 Biological Sources of Carbonates

Milliman provides an extensive overview of skeletal and non-skeletal biological sources (biogenic) of marine carbonates.[10] Despite the diversity of biogenic sources, the primary contributors to carbonates in deep-sea sediments originate from planktonic foraminifera, coccolithophores, and pteropods. Regional distributions and characteristics of calcium carbonate

composition in sediments throughout the GoM were mapped by Balsam and Beeson from 186 core samples.[29] In general, the northern (Texas-Louisiana) and western (East Mexico) continental shelf regions (shelf water depths < 200 m) typically contained < 10% carbonate by mass, and a continuous region extending from the eastern shelf (West Florida) onto the southern shelf (Campeche-Yucatan) exhibited > 75% carbonate. In the northern and western GoM provinces, carbonate composition increased from 10 – 25% on the upper slopes and rises to 25 – 50% entering into the plain regions of the GoM basin (Sigsbee and East Gulf Plains). The eastern and southern shelves exhibited the greatest diversity of biogenic carbonates, which included non-skeletal (lithoclasts, pelletoids, and ooids) and skeletal (mollusks, foraminifera, algae, echinoids, corals, and bryozoans) components. However, the diversity of biogenic carbonate sources decreased down slope from the continental shelves into the GoM basin. In these settings, planktonic foraminifera and coccolithophores were the primary contributors to biogenic carbonate formations found within the seafloor sediments.[29, 34]

Planktonic foraminifera and coccolithophores are widely distributed organisms that thrive in photic waters throughout Earth's oceans and seas.[10, 35, 36] Foraminifera are single-celled protists that commonly produce calcareous shells, referred to as tests, above the thermocline.[10] Foraminiferal tests contribute primarily to the sand sized sediment fractions (62.5 μm – 2 mm on the Wentworth Scale).[10, 36] Coccolithophores are single-celled photosynthetic organisms that produce calcite "shields", termed coccoliths, with diverse, complex, and exotic morphologies that generally range from 2 – 20 μm.[10, 35-37] Coccoliths are the dominant biogenic carbonate structures in sediment fractions < 6 μm.[10, 36] As in the GoM, carbonate generated from foraminifera and coccolithophores are frequently coincident.[10, 29] It is significant to note the ubiquitous, regional presence of foraminiferal tests and coccolith formations throughout GoM sediments, including settings that are conducive for gas hydrate formation (water depths > 300 m).[15, 29, 34] In addition, considerably smaller coccolith formations have greater potential for contributing to sediment IR-

ATR spectral signatures than foraminiferal tests. This results as coccoliths in the very fine sediment fractions provide a better particle size match for interaction with the evanescent field (penetration depth ~750 nm @ 1335 cm^{-1} with $n_1 = 2.42$ and $n_2 = 1.3$; < 2.5 μm) throughout the evaluated spectral region with the implemented ATR configuration in this thesis. The spectral impact of coccolith calcite is only briefly discussed in this chapter; however, a more thorough treatment of this significant carbonate source for detecting authigenic carbonate precipitation with IR-ATR spectroscopy is discussed in **Chapter 6**.

In addition to the abundant sedimentation of biogenic carbonates from foraminifera and coccolithophores, additional sources of biogenic carbonates surrounding gas hydrate systems in the GoM arise from the accumulation of fossil shell material (predominately aragonite).[11, 15, 17, 23] Aragonite shells originate from large chemosynthetic organisms including mussels and clams. At MC118, shell material litters the seafloor and often contributes to chemoherm formations (see **Figure 1-7**).[23] The size of shell material (commonly whole pieces or fragments > 1 mm) inhibits the potential for significant interaction with the evanescent field during IR-ATR evaluation. The lack of significant spectral contributions from these particular carbonate sources is addressed throughout this chapter.

5.1.2.4 Mg-Calcite

In **Section 5.1.1**, Mg-calcite was introduced as an anhydrous carbonate phase not classified in the Dana system. Mg-calcite is of particular relevance, since: (1) Mg-calcite (authigenic and biogenic) is commonly found in low-temperature marine environments, such as hydrate systems in the GoM,[10-12, 14-16, 20, 23, 30, 38] and (2) Mg^{2+} incorporation into calcite lattices imparts finite changes in the characteristic IR spectrum of calcite with increasing Mg^{2+} content,[39] as discussed in **Section 5.2.2**.

In 1975, Berner investigated the role of Mg^{2+} in seeded precipitation of inorganic calcite and aragonite in seawater to establish an explanation for the impact of Mg^{2+} on inorganic carbonate

formation in marine environments.[31] Under consideration of previously published literature, the author formulated several generalizations including the finding that aragonite growth in seawater is essentially unaffected by the presence of dissolved Mg^{2+}; however, Mg^{2+} is incorporated into calcite crystals following surface adsorption resulting in significant perturbation of crystal growth. In addition, Mg-calcite precipitation can be seeded by Mg-free calcite. The most thermodynamically stable forms of magnesian calcite were also predicted to contain between 2 and 7 mole% $MgCO_3$, and Mg-calcite containing greater than 8.5 mole% $MgCO_3$ are unstable relative to aragonite at the average Mg/Ca ratio commonly found in seawater.

Within gas hydrate ecosystems in the GoM, authigenic formation of Mg-calcite is intimately connected with microbial activity.[11, 14-16, 30] In addition, authigenic carbonate in sediments and nodule formations in these ecosystems can exhibit diverse carbonate mineralogy, morphology, and geologic history, even within single rock formations.[11, 12, 15, 40] **Chapter 6** presents the IR-ATR spectroscopic evaluation of nodule formations collected from the MC118 hydrate site, and exemplify the complexity and diversity of carbonates encountered within a single gas hydrate ecosystem.

5.1.3 IR Spectroscopy and Carbonate Mineralogy

The feasibility of IR spectroscopic techniques for classifying and differentiating anhydrous carbonate minerals was recognized over 50 years ago.[1-3, 41] One of the earliest thorough reports on the IR spectra of carbonate minerals was by Hunt et al. in 1950 with the presentation of transmission-absorption spectra for calcite, dolomite, magnesite, aragonite, rhodochrosite, siderite, and smithsonite.[2] Sample preparation required grinding, isolation of particulates with an average particle size < 5 μm via sedimentation and centrifugation procedures, sample drying, and the application of a thin particulate film onto NaCl windows from approx. 0.2 g of powdered sample. IR transmission-absorption spectra were then recorded with a dual-beam, grating spectrophotometer. In addition to reporting the IR spectra, the authors acknowledged the

capability to discriminate each carbonate species based on unique vibrational frequencies for a carbonate absorption band occurring between 752 and 714 cm^{-1}. Since then, IR spectroscopy has gained recognition as a powerful tool for carbonate research. Resulting, a variety of IR spectroscopic methodologies, sample preparation procedures, and data evaluation strategies have been implemented to take advantage of the molecular specific nature of this analytical technique.[4, 7, 39, 42-46] The following sub-sections provide a detailed overview on the application of IR spectroscopy for evaluating carbonate minerals with particular emphasis on topics relevant to this thesis.

5.1.3.1 Classification of Carbonate Minerals with IR Spectroscopy

IR spectra of anhydrous carbonate minerals exhibit several absorption features characteristic to fundamental vibrational modes of the carbonate ion, which collectively provide discriminatory signatures with respect to the crystal system and molecular composition.[5, 47-50] Chester and Elderfield extensively discussed the utility of carbonate spectral features from transmission-absorption measurements for identifying common anhydrous carbonate minerals.[5] In practice, the collective use of fundamental absorption features, with exception of the ν_3 mode (see **Figure 5-1**), typically enables the unambiguous identification of these minerals. This section provides a generic description for the practical usage of IR absorption features to identify and discriminate carbonate minerals. Furthermore, a summary of carbonate identification utilizing an IR-ATR spectral database generated for this thesis is provided (experimental details in **Section 5.2**). As a first guideline, **Figure 5-1** contains a representative IR-ATR spectrum for witherite ($BaCO_3$), which is classified in the aragonite group.

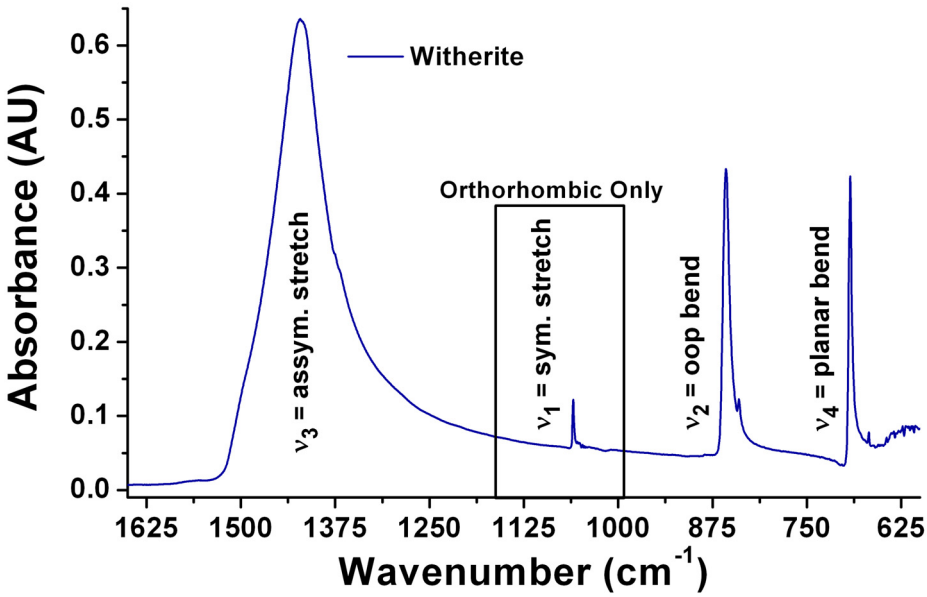

Figure 5-1: IR-ATR spectrum of witherite ($BaCO_3$) mined from Illinois, USA with carbonate vibrational mode assignments. The spectrum is an average of 100 sample scans collected at a spectral resolution of 1 cm^{-1}. This representative spectrum was collected for the IR-ATR spectral database described in **Section 5.2**. (Abbreviations are assym = asymmetric, sym. = symmetric, and oop = out-of-plane).

Four fundamental absorption modes are IR active for carbonate minerals with the conventional band assignments provided in **Figure 5-1**. However, the ν_1 symmetric C-O stretch is typically only observed for anhydrous carbonates in the aragonite group.[5, 49, 50] Hence, observation of this spectral feature is generally indicative of the presence of aragonite group mineral(s). The ν_1 vibration resonates between 1085 and 1050 cm^{-1}, and its fundamental frequency is unique to each aragonite group species (aragonite, witherite, strontianite, and cerussite). Therefore, this absorption feature is frequently applied for identifying the four aragonite group minerals classified under Dana 14.1.3.

For all anhydrous carbonates investigated in this thesis, a major and minor ν_2 absorption feature can be observed. The minor ν_2 absorption occurs in the range of 860 – 820 cm^{-1} as a weak protrusion shouldering at the longer frequency flank of the major ν_2 peak. The minor band is not commonly utilized for carbonate species identification; however, this feature may assist the

classification process.[5] Using IR-ATR spectra and the requirement for a spectral separation of at least 3 cm^{-1} to facilitate unambiguous species identification, calcite and cerussite can be clearly distinguished, and the remaining minerals narrowed to three sub-groups: (1) siderite and rhodochrosite, (2) aragonite, witherite, strontianite, and smithsonite, and (3) dolomite and magnesite. Despite the prominence of the major ν_2 band compared to the minor feature, it also has limited capability for unambiguous carbonate identification. Transmission-absorption spectra indicate that mineral speciation using this feature is restricted to magnesite, smithsonite, rhodochrosite, and cerussite.[5] However, from the collected IR-ATR spectra and the 3 cm^{-1} criterion, it was found that classification with the major ν_2 band produces similar results from evaluation of the minor feature. Consequently, cerussite and calcite can be discriminated with formation of three remaining sub-groups: (1) aragonite, witherite, and strontianite, (2) rhodochrosite, siderite, and smithsonite, and (3) dolomite and magnesite.

The ν_3 asymmetric carbonate stretch region (1550 – 1350 cm^{-1}) is the strongest carbonate absorption feature active in all hexagonal and rhombohedral carbonates, and it is comprised of multiple vibrational contributions.[5] This absorption region is not typically used for species classification due to the broad spectral characteristics and similar frequencies of peak maxima for several carbonate minerals.[5] However, ν_3 peak absorption frequencies in the 1400 cm^{-1} regime are frequently reported in literature for confirming the presence of carbonate mineral(s) and/or quantitative analysis.[4-6, 39, 42, 46, 50, 51]

The fundamental ν_4 planar bending vibration (750 – 695 cm^{-1}) is the most utilized absorption feature for identifying carbonate minerals. From the IR-ATR spectral database in this thesis, the 3 cm^{-1} criterion enables unambiguous classification of all evaluated carbonate species except calcite and aragonite. The differentiation of calcite and aragonite, as well as dolomite and rhodochrosite, is limited with evaluation of the ν_4 band in transmission-absorption spectra.[5] Hence, collective evaluation of the ν_1, ν_2, and ν_4 absorption features facilitates the qualitative

diagnosis to the sole presence or potential co-occurrence of calcite and aragonite. Furthermore, each aragonite group mineral is expected to exhibit two ν_4 absorption features;[50] however, two absorption bands are typically only observed for aragonite and strontianite (also within current studies).[5, 50]

In addition to the four fundamental carbonate absorption features, two combination bands, $(\nu_1 + \nu_3)$ and $(\nu_1 + \nu_4)$, can be observed at approx. 2525 cm^{-1} and 1800 cm^{-1}, respectively.[39] Although the combination bands have previously been found to contain mineral specific information with use for quantitative analysis, these absorption features are comparatively very weak.[39, 45] As unambiguous identification of the investigated anhydrous carbonates can be achieved from the other more prominent absorption bands, including the species frequently encountered in GoM gas hydrate ecosystems, only the four fundamental and the minor ν_2 absorption bands will be addressed throughout the remainder of this thesis.

5.1.3.2 Quantification of Carbonate Minerals with Infrared Spectroscopy

In addition to utilizing IR spectroscopy for identification of carbonate minerals, a variety of quantitative evaluation strategies have been developed using both transmission-absorption and ATR techniques.[4, 5, 41, 44-46, 51-56] Two quantitative approaches demonstrated in the literature relevant to this thesis include the quantification of calcite and dolomite as percentages of the total carbonate composition within a sample and the quantification of total carbonate mass percent within in a sample.[4, 5, 46, 52] Quantitative evaluation of calcite and dolomite as partial percentages of the total carbonate content involves evaluation of the ν_4 bands via ratioing the respective peak heights.[5] In contrast, essentially every carbonate IR absorption feature, including the weak combination bands, has been utilized to demonstrate the capability of quantifying total carbonate composition in either natural or synthetic samples.[4, 41, 44-46, 51-56]

Reported accuracies for the quantitative evaluation of carbonate minerals with IR spectroscopy range from < 1% up to approx. 10%.[4, 5, 41, 46, 51-54, 56] Hence, IR analyses compare favorably with

powder XRD as the widely accepted quantitative reference technique providing typical accuracies in the range of 1 – 5%.[10, 57, 58] For both transmission-absorption and ATR techniques, control of the particle size is essential for facilitating accurate quantitative analysis.[4, 5, 46, 59] Particle size is particularly important to ensure representative assessment of the sample composition for both techniques and to minimize scattering effects during transmission-absorption measurements.[4, 5, 59] Therefore, sample grinding and/or physical separation are frequent preparatory procedures implemented prior to sample analysis.[4, 5, 41, 45, 46, 52, 54, 56] Average particle sizes < 2 μm typically enable accurate quantification for the various types of samples analyzed with IR techniques and validated via XRD analysis.[4, 5, 41, 45, 46, 52, 54, 56]

An abundance of literature demonstrates the capabilities of IR spectroscopy for characterizing and quantifying marine carbonates.[4-7, 39, 41, 42, 44, 46, 52, 60-62] However, only a few of those reports are directed towards evaluation of carbonate minerals in marine sediment or rock formations.[4, 46, 52] Chester and Elderfield demonstrated accurate quantification of the total carbonate mass in various types of calcareous marine sediments and terrestrial sedimentary rocks (i.e., calcareous oozes, dolomite limestone, etc.) via ratiometric comparison of peak amplitudes from the ν_3 carbonate absorption band and "clay" features between 1100 – 900 cm^{-1} obtained in transmission-absorption spectra.[4] In 1992, Herbet et al. used transmission-absorption spectra and similar evaluation methods to quantify the major components of deep-sea sediments (clays, quartz, and carbonates).[52] Mecozzi et al. utilized the ν_3 peak area derived from IR-ATR spectra to quantify total carbonate mass percentages in various marine solid samples; however, the authors only examined sodium carbonate added to samples following an acid pretreatment to decarbonate the natural sample matrices.[46]

5.1.3.3 IR Spectral Characteristics of Mg-Calcite

Mg-calcite is frequently present in both biogenic and authigenic marine carbonates as discussed in **Section 5.1.2.4**. The random occlusion of Mg^{2+} into biogenic or authigenic/inorganic

precipitated magnesian calcite formations introduces positional disorder of CO_3^{2-} in the crystal matrix, which results in unit-cell contraction of the calcite lattice as the M^{2+}-O bond length decreases with increasing Mg^{2+} substitution.[63, 64] Disruption of the calcite lattice with Mg^{2+} substitution leads to a blue shift in characteristic calcite absorption bands.[6, 7, 39, 60] In 1997, Bottcher et al. used transmission-absorption IR spectroscopy to analyze 57 biogenic and inorganic magnesian calcite samples with previously quantified Mg^{2+} mole fractions (X_{Mg}).[39] It was found that the ν_4 vibrational mode increased linearly with respect to increased Mg^{2+} content following; $\nu_4(cm^{-1}) = 39.40 \times X_{Mg} + 712.20$, where $0 < X_{Mg} < 0.23$.[39] Furthermore, it was observed that the derived linear trend predicted the endmember ν_4 absorption frequencies for calcite (712 cm^{-1}), dolomite (729 cm^{-1}), and magnesite (748 cm^{-1}) with Mg^{2+} mole fractions of 0, 0.5, and 1, respectively.[39] Hence, for homogeneous Mg-calcite samples, it is possible to determine the mole fraction of Mg^{2+} using IR spectroscopy via calibration with the three endmember ν_4 frequencies for calcite, dolomite, and magnesite.

Recently, it has been shown that Mg-calcite can form via an amorphous calcium carbonate (ACC) precursor phase during laboratory synthesis with significant implications to the modality of biologically produced Mg-calcites.[65-67] Shortly thereafter, Politi et al. confirmed that sea urchin spine calcite forms after initial precipitation of amorphous calcium carbonate with identification of ACC aided by IR spectroscopy.[62] In addition, IR-ATR spectroscopy has been utilized to assess the role of Mg^{2+} on the stability of precipitated ACC, which has a strong influence on calcite morphologies precipitated under various Mg^{2+} concentrations.[6, 68-71] Next to the importance of understanding biomineralization processes, several of the previously referenced articles further demonstrate the capability of detecting Mg-calcite with IR spectroscopic techniques.

5.2 IR-ATR Spectral Database for Identifying Carbonate Minerals

Since the pioneering studies of the 1950's and 60's utilizing transmission-absorption IR spectroscopy for identifying the most common anhydrous carbonate minerals, a variety of IR-ATR applications for evaluating carbonate minerals have been reported in the literature.[1-3, 5, 43, 46, 49-51, 72] However, the generation of a comparable spectral database for carbonate identification via IR-ATR methods has yet to be reported. Consequently, research grade carbonate minerals were obtained to facilitate the establishment of an IR-ATR spectral library for ten of the most common anhydrous normal carbonate minerals within this thesis. The following sub-sections describe the applied measurement strategies and provide a side-by-side comparison of carbonate absorption features useful for identifying the carbonate minerals. IR-ATR spectra for the examined carbonate specimens are provided in **Appendix A-2**.

5.2.1 Experimental

5.2.1.1 Materials

Naturally occurring carbonate mineral specimens were obtained from several suppliers. Research grade calcite, aragonite, dolomite, magnesite, rhodochrosite, siderite, smithsonite, and strontianite were purchased from WARD'S Natural Science (Rochester, NY). A cerussite sample was purchased from World-Wide Minerals, a WWW-based mineral supplier (http://www.wmtn.biz/wwm.html, location unknown). A witherite specimen was purchased from FREDROCK Rock Shop (www.fredrockonline.com, Waterford, MI). Although mineral purity is not available for each of the specimens, the collected IR spectra revealed that each sample was generally of high quality with slight to non-detectable contaminations. As small variations in the fundamental absorption frequencies have been reported in literature,[5] **Table 5-2** provides the source locations for each species as provided by the suppliers along with indication of potential contaminations.

Table 5-2: Source locations and qualitative contamination assessments for carbonate specimens examined for IR-ATR spectral database. The qualitative purity assessment follows from highest to lowest as: No Identifiable Contamination > Very Minor Contamination > Slight Contamination.

Mineral	Source Location	Spectral Quality
Calcite	Unknown	No Identifiable Contamination
Magnesite	Brumado, Bahia, Brazil	Very Minor Dolomite Contamination
Siderite	Ivigtut, Greenland	Slight Unidentified Contamination
Rhodochrosite	Sweet Home Mine in Alma, CO	Very Minor Unidentified Contamination
Smithsonite	Bingham, NM	No Identifiable Contamination
Aragonite	Minglanilla, Cuenca, Spain	Slight Unidentified Contamination
Witherite	Illinois	No Identifiable Contamination
Strontianite	Mathilde Mine, Westphalia in Asheberg, Germany	Very Minor Dolomite Contamination
Cerussite	Mibladen, Morocco	Slight Unidentified Contamination
Dolomite	Butte, Montana	No Identifiable Contamination

5.2.1.2 IR-ATR Instrumentation

The IR-ATR spectra of all carbonate minerals were recorded from 4000 - 400 cm^{-1} using a Bruker Equinox 55 FT-IR spectrometer (Bruker Optics Inc., Billerica, MA) equipped with a liquid nitrogen (LN_2) cooled MCT detector (Infrared Associates, Stuart, FL) and a Specac Gateway in-compartment horizontal ATR unit (Specac Inc., Woodstock, GA). Each sample was directly deposited onto a trapezoidal ZnSe ($n_D = 2.43$ at $\lambda = 5$ μm) ATR crystal (MacroOptica, Moscow, Russia) with 6 effective reflection regions (72 × 10 × 6 mm; 45 °). A 3/16" th. polycarbonate sheet was custom cut and used to replace the spectrometer sample compartment cover. The custom cover was modified to allow direct purging of the sample compartment with dry air in order to stabilize atmospheric humidity and CO_2 as well as expedite sample drying times. Additional details on the experimental setup are provided in **Section 3.2**.

5.2.1.3 IR-ATR Measurement Procedures

Each carbonate specimen was first hand ground into a fine powder with a ceramic mortar and pestle. Deionized water (R = 18.2 MΩ·cm at 25 °C) was then added (approx. 1 mL per 600 mg of sample) to form a suspension for application to the waveguide surface. Prior to sample

deposition, the sample chamber was purged with dry air for at least 10 mins for reducing atmospheric CO_2 and water vapor interferences followed by collection of a reference spectrum with a clean, dry ZnSe crystal. After collection of the reference spectrum, approx. 1 mL of the sample suspension was pipetted onto the waveguide to fully cover the surface. Spectra were recorded at either 90 s or 120 s intervals throughout the drying process until a stable spectral signature was acquired. IR-ATR reference and sample spectra were generated by averaging 100 scans at a spectral resolution of 1 cm^{-1}.

The application of carbonate suspensions prepared with acetone onto ATR waveguides has been demonstrated to increase spectral quality and reproducibility by improving the sample-waveguide contact, which is attributed to the formation of a cast-like film.[46, 73] Although acetone is preferable to water for minimizing solubilization or reaction of carbonate minerals in liquid suspensions, acetone was avoided during these experiments to allow monitoring of the drying process, to ensure a higher quality reference measurement, and to minimize vapor interferences inside the sample compartment.

5.2.2 Results and Discussion

Representative IR-ATR spectra of all examined carbonate specimens for the database are provided in **Appendix A-2**. Here, the fundamental vibration frequencies (i.e., peak maxima) for ν_1 (**Table 5-3**), ν_2 (**Table 5-4**), minor ν_2 (**Table 5-5**), and ν_4 (**Table 5-6**) absorptions are presented in table format alongside previously published values obtained by transmission-absorption techniques.

Table 5-3: Absorption frequencies in wavenumbers (cm^{-1}) for the ν_1 carbonate feature for aragonite group minerals.

ν_1 Symmetric Stretch (Aragonite Group Only)			
Mineral	**This Work**	**Adler et al. 1963**[50]	**Chester et al. 1967**[74]
Aragonite	1082.8	1084.6	1083.4
Witherite	1059.6	1061.6	1060.4
Strontianite	1071.8	1073	1069.5
Cerussite	1051.5	1052.6	1050.4

Table 5-4: Absorption frequencies in wavenumbers (cm^{-1}) for the major ν_2 carbonate feature for all examined carbonate minerals. (* no reported value, or mineral not evaluated in the respective study).

Major ν_2 OOP Bend				
Mineral	**This Work**	**Hunt et al. 1950**[2]	**Adler et al. 1951**[3]	**Chester et al. 1967**[5]
Calcite	873.7	877.2	874.1	876.4
Magnesite	882.3	888.9	883.4	885
Siderite	865.2	869.6	*	*
Rhodochrosite	863.4	869.6	867.3	869.6
Smithsonite	867.8	871.8	870.3	870.3
Aragonite	855.8	877.2	859.8	856.9
Witherite	857.2	*	859.8	856.9
Strontianite	856.7	*	859.8	856.9
Cerussite	838.5	*	840.3	839.6
Dolomite	879.5	885	880.3	878.7

Table 5-5: Absorption frequencies in wavenumbers (cm^{-1}) for the minor ν_2 carbonate feature for all examined carbonate minerals. (* no reported value, or mineral not evaluated in the respective study).

Minor ν_2 OOP Bend			
Mineral	**This Work**	**Hunt et al. 1950**[2]	**Chester et al. 1967**[5]
Calcite	848	847.5	850.3
Magnesite	855.7	854.7	852.5
Siderite	835.2	836.8	*
Rhodochrosite	837	836.8	847.5
Smithsonite	841	840.3	858.4
Aragonite	843.5	858.4	840.3
Witherite	840	*	835.4
Strontianite	842.9	*	840.3
Cerussite	823.6	*	838.2
Dolomite	852.9	854.7	852.5

Table 5-6: Absorption frequencies in wavenumbers for the ν_4 carbonate features for all examined carbonate minerals. (* no reported value, or mineral not evaluated in the respective study).

ν_4 Planar Bend				
Mineral	**This Work**	**Hunt et al. 1950**[2]	**Adler et al. 1951**[3]	**Chester et al. 1967**[5]
Calcite	712.4	713.3	712.3	710.2
Magnesite	748	750.2	747.4	746.3
Siderite	737.1	740.7	*	*
Rhodochrosite	725.6	728.9	727.3	727.3
Smithsonite	743.6	746.3	741.8	742.9
Aragonite	712.5, 699.8	713.3, 699.3	712.3	710.2, 694.9
Witherite	692.5	*	693	686.8
Strontianite	706.1, 699.1	*	699.8	702.2, 697.4
Cerussite	677.2	*	678.9	678.9
Dolomite	728.8	729.9	728.9	726.7

Some variations between the current study and previous reports on the fundamental vibration frequencies for carbonate minerals are readily apparent in the presented tables. While in most cases the spectral deviations were < 4 cm^{-1}, deviations up to 17 cm^{-1}, as for the minor ν_2 band of smithsonite, were also observed. Generally, this should not present a significant problem for identifying carbonate species in moderate to high purity samples with collective evaluation of the multiple carbonate absorption bands. However, spectral mixing could reduce the reliability of species elucidation when evaluating samples containing low carbonate content and/or multiple carbonate minerals.

The spectral database provides diagnostic peak information for identifying all major carbonates anticipated to occur in gas hydrate ecosystems in the GoM with the exception of Mg-calcite. By extending the work of Bottcher et al. described in **Section 5.1.3.3**,[39] the endmember fundamental frequencies from the spectral database for calcite, dolomite, and magnesite were used to derive the following equation for characterizing Mg-calcites with IR-ATR spectroscopy:

$$\frac{\nu_4(\mathrm{cm}^{-1})_{\mathrm{Exp}} - 711.93}{35.6} = X_{\mathrm{Mg}}$$

Equation 5.2

The derived equation is a simple rearrangement from a linear fit ($R^2 = 0.998$) to enable extraction of the Mg^{2+} mole fraction (X_{Mg}) using an experimentally obtained ν_4 vibrational frequency ($\nu_4(cm^{-1})_{Exp}$). In addition, the linear fit equation can be used to predict fundamental ν_4 band positions for varying Mg^{2+} mole fractions. **Table 5-7** summarizes a range of expectation values for the ν_4 peak position for various ranges of X_{Mg}.

Table 5-7: Predicted fundamental ν_4 band positions for various ranges of Mg^{2+} mole fractions as generated from data obtained from IR-ATR spectra of calcite, dolomite, and magnesite in the ATR spectral database. (* the predicted peak location for $X_{Mg} = 0.00$ of 711.93 is less than the experimental value for calcite, expected $X_{Mg} = 0.00$, at 712.4).

X_{Mg}	Predicted $\nu_4(cm^{-1})$
0.00 – 0.10	712.4* - 715.5
0.10 – 0.20	715.5 – 719.1
0.20 – 0.30	719.1 – 722.6

The predicted ν_4 peak locations for different Mg^{2+} mole fractions displays the range of spectral shifts that could potentially be encountered with the occurrence of magnesian calcites. Using the derived equation to calculate X_{Mg} for the examine calcite standard ($\nu_4 = 712.4$), a X_{Mg} value of 0.013 was obtained. This demonstrates minor error using this strategy; however, this method should facilitate a suitable first quantitative evaluation of homogeneous magnesian calcite samples. Furthermore, the calibration only requires spectral analysis of the three endmember samples, calcite, dolomite, and magnesite, which are readily available as high-purity, research grade specimens.

5.3 Seafloor Sediment Collections from the GoM

Three sediment collections from two gas hydrate ecosystems in the Mississippi Canyon region of the GoM were examined with IR-ATR spectroscopy throughout progression of this thesis. Detailed information regarding each collection is provided in the following sub-sections.

5.3.1 Box Core Sediment Collections from MC118 in June 2006

Shallow sediment box cores (< 30 cm deep) were collected at various locations around the hydrate system at MC118 on June 9 and June 11 of 2006 on-board the R/V Pelican (owned and operated by the Louisiana Universities Marine Consortium, Chauvin, LA). The cruise was conducted by the GOMGHRC, and was funded by the Minerals Management Service (MMS, U.S. Department of the Interior). The first phase of this cruise focused on completing geophysical seismo-acoustic grid profiles of the MC118 hydrate site. Six CTD casts and several preliminary instrument tests for the GOMGHRC seafloor observatory were additionally conducted throughout this cruise. **Figure 5-2** displays a global positioning system (GPS) trace of the cruise plotted with Google Earth software.

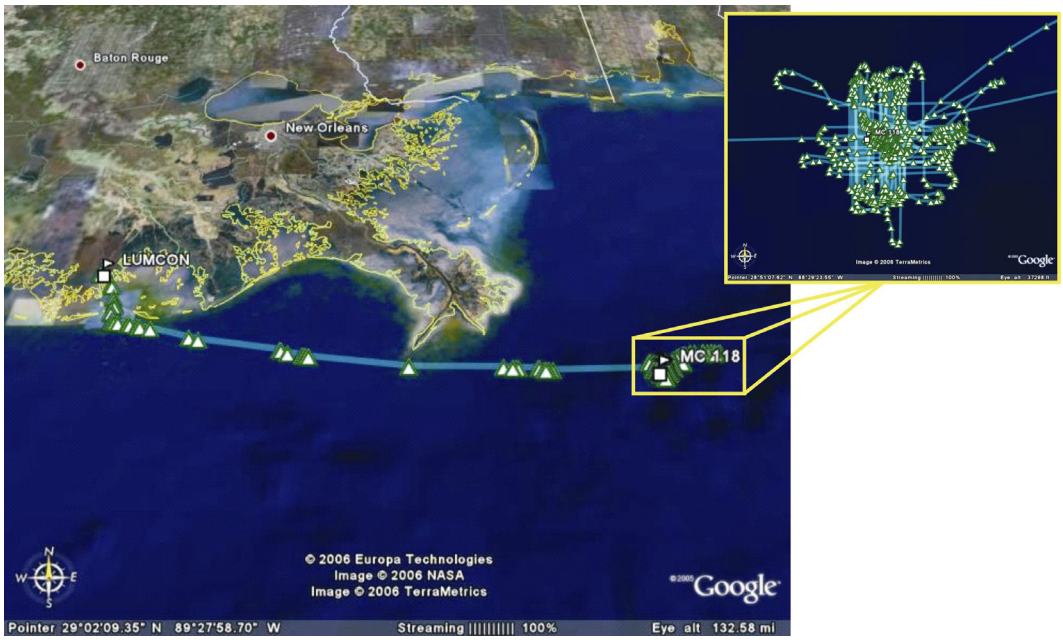

Figure 5-2: GPS trace of the June 2006 GOMGHRC cruise to MC118 aboard the R/V Pelican. The inset provides an accentuated view of grid profiles from the collection of geophysical lines for mapping acoustic reflections throughout the sediments.

The box core sampler (**Figure 5-3**) had a 30.5 × 30.5 × 45.7 cm trap for collecting sediments. Real-time positioning and monitoring of the box core unit was enabled from an attached Ultra-short baseline (USBL) transponder relaying coordinates back to the ship mounted transceiver

(Model 5000HA, Linkquest Inc., San Diego, CA). USBL feedback was then overlaid onto a seafloor map of the MC118 area (C&C Technologies, Lafayette, LA) using the TrackLink software package (Linkquest Inc., San Diego, CA).

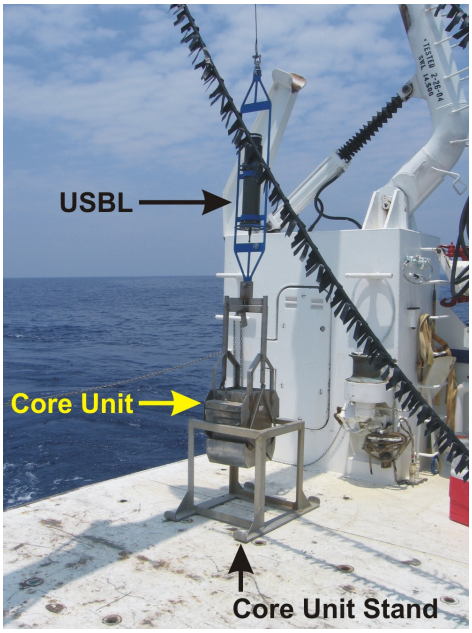

Figure 5-3: Box core unit equipped with USBL navigational component (blue frame with black cylinder) utilized to collect seafloor sediments during the June 2006 GOMGHRC cruise to MC118 on the R/V Pelican.

Box core samples were collected with the following procedures: (1) The coring unit was lowered from the ship's A-frame to approx. 50 m above the seafloor. (2) The ship went into a controlled drift for maneuvering the core unit over a targeted sampling location. (3) Once positioned, the core unit was rapidly deployed to the target. (4) After the core unit struck bottom, USBL coordinates were recorded followed by retrieval of the box core. On average, each collection took approx. 1.5 hrs. With calm seas during core collection, target accuracy was typically within 10 m. Overall accuracy was influenced by sub-surface currents and line drag resulting in a substantial distance offset between the ship and core unit. Despite such difficulties, this coring strategy resulted in considerable target accuracy. **Figure 5-4** provides a representative screen shot of the navigation screen following a successful box core collection.

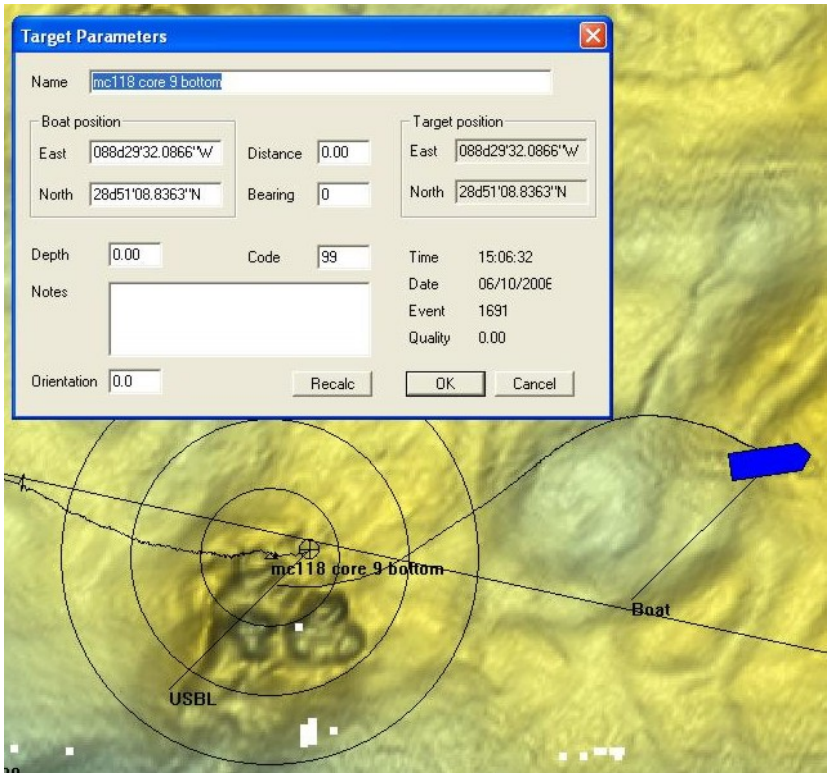

Figure 5-4: Screen capture of navigational feedback for the ship and box core unit locations following a successful sampling event. The sample location is indicated by the bull's-eye with triangular center. The rings surrounding the bull's-eye are 100, 200, and 300 m in diameter. Screen shots were recorded for each target location containing the date, time, and coordinates for each sample location.

Upon retrieval of the box core unit, sediments were sub-sampled by push-coring with 5.1 cm id. clear polyvinylchloride (PVC) pipe followed by separation of marked color stratifications within the sediment. The depth of push-cores ranged from 13 to 29 cm with 2 – 4 observable color changes within each sub-sample. Sub-samples identified within the text are distinguished as Top, Mid, and Bot where Mid = Middle, Bot = Bottom, and depth below seafloor follows the order Top < Mid < Bot. A detailed list of sediments collected from MC118 during this cruise is provided in **Appendix A-3**. **Figure 5-5** provides an optical image displaying 4 color stratifications within a sub-sampled push-core.

Figure 5-5: Representative image of a push-cored sub-sample with a 5.1 cm id. clear PVC pipe capped with rubber stoppers. Four distinct color changes within the sediments can be visualized in the pipe section next to the graduated ruler. The light brown layer in this image corresponds to the top sediment layer at the sediment-seawater interface.

After subdivision, all samples were placed in plastic bags, frozen on-ship, transported to the laboratory in cooled ice chests, and maintained in freezer storage at -80 °C prior to IR-ATR evaluation. Before spectroscopic evaluation, samples were thawed at approx. 4 °C, 6 – 10 mL of sediment was transferred into a 15 mL glass vial for refrigerated storage at 4 °C, and the remaining sample was returned to freezer holding at -80 °C. Box core samples are designated as BC# corresponding to the respective sampling locations. **Table 5-8** provides the coordinates of box core sampling sites from the June 2006 GOMGHRC cruise including field notes collected during sample collection.

Table 5-8: USBL coordinate locations and field notes for box core samples (BC#) collected from MC118 in June 2006. All coordinates are referenced to Zone 16 in Universal Transverse Mercator (UTM) meters of the North American Datum of 1927 (NAD27) based on the Clarke ellipsoid of 1866.

	Latitude (N)			Longitude (W)			
Sample	**Degrees**	**Minutes**	**Seconds**	**Degrees**	**Minutes**	**Seconds**	**Field Notes**
BC1	28	51	28.5923	88	29	33.8671	Shells, Gassy Mud
BC2	28	51	21.8532	88	29	28.5801	Slight Oil Sheen
BC3	28	51	8.2715	88	29	31.5127	Spilled, Oil, Shells, Nodules; Sediment Not Sampled
BC4	28	51	14.1734	88	29	18.7122	Shells at Bottom
BC5	28	51	29.4959	88	29	36.9823	Shells, Nodules, and Gassy Mud
BC6	28	51	31.1223	88	29	39.4490	
BC7	28	51	11.7656	88	29	23.0113	
BC8	28	51	8.4233	88	29	24.5590	Oil
BC9	28	51	8.8363	88	29	32.0866	Shells, Oil
BC10	28	51	18.7126	88	29	37.9212	Not Sampled, Oil
BC11	28	51	7.6325	88	29	20.7956	
BC12	28	51	7.4440	88	29	30.8883	Oil
BC13	28	52	44.9218	88	28	30.0892	No Sediment Retrieved in BC

5.3.2 Gravity Core Sediment Collections from MC118 in October 2005

In addition to the sediments collected for this thesis during the 2006 GOMGHRC, sediments previously collected from three locations at MC118 were provided by Dr. Carol Lutken at the University of Mississippi. Gravity core samples were collected during a GOMGHRC conducted and MMS funded cruise in October 2005.[75] Three sediment samples were provided with the designations Core 21, Core 26, and Core 38; the sediments reflected sub-samples at intervals of 100 – 105, 30 – 34, and 52 – 56 centimeters below seafloor (cmbsf), respectively. Coordinates for the sampling locations are; Core 21: 28 51.258 N, 88 29.6028 W (117 cm core; No USBL, core location is ship's location.), Core 26: 28 51.1551 N, 88 29.4879 W (54 cm core, USBL on coring unit), and Core 38: 28 51.0431 N, 88 29.5633 W (89 cm core, USBL on coring unit). Both samples from Core 21 and Core 26 contained nodule formations that were additionally evaluated with IR-ATR spectroscopy as discussed in **Section 6.2**.

5.3.3 Sediments from Piston Core MD02-2570

Piston core sediments from sampling location MD02-2570 were provided by Dr. Rudy Rogers at Mississippi State University. These samples were initially donated by scientists from a cruise partially funded by the U.S. Department of Energy, and jointly conducted by the Institut Polaire Francais, Paul-Emile Victor and the U.S. Geological Survey. Piston cores were collected from the French vessel R/V Marion Dufresne during a cruise from July 1 – 8, 2002. Sampling locations were around a gas hydrate mound in the Mississipi Canyon area of the GoM at 28.57100N, 89.68983W (water depth of 641 m).[76, 77] The piston core was sub-sampled from 0 to approx. 30 meters below seafloor (mbsf). Samples were provided in plastic bags and stored at 4 °C. The site location for this core sample was designated as MD02-2570 at the time of collection. Sediments from the same set of samples provided by Dr. Rogers were previously utilized to evaluate the influence of organic and inorganic sedimentary components on gas hydrate induction and formation rates.[76] Additional information from this cruise can be found in Paull et al.[77]

5.4 IR-ATR Spectroscopic Screening of Sediment Samples

IR spectroscopic analysis of sediment collections for this thesis focused on three primary goals: (1) rapid characterization of sediment samples in their "native" hydrated state for closely emulating sediment signatures in their native environments to assess *in situ* analytical capabilities of future submersible IR chemical sensing platforms, (2) qualitative and semi-quantitative evaluation of carbonate mineral compositions in native and/or dried samples, and (3) assessment and possible correlation of compositional and/or spectral variances to assist characterization of the geological settings with respect to the sediment collection environment(s). Sediment samples were not manipulated beyond the described collection, transport, and storage procedures outlined in **Section 5.3**. In select cases, additional experiments were performed to further characterize sample composition (i.e., carbon isotope ratios). Spectroscopic data collected during sediment analysis is discussed in detail throughout the remainder this chapter as well as in **Chapter 6**.

5.4.1 Experimental

The same instrumentation and experimental setup described in **Section 5.2.1.2** for generating IR-ATR spectra of carbonate minerals for the spectral database was also utilized for spectroscopic evaluation of all sediment samples.

For IR-ATR screening of sediments, sufficient sample was deposited onto the waveguide to ensure coverage of the entire measurement surface following collection of a reference spectrum with a clean, dry ZnSe crystal after stabilized conditions within the sample compartment from purging for at least 10 mins with dry air. Reference and sample spectra were collected from $4000 - 400\ cm^{-1}$ by averaging 100 sample scans at a spectral resolution of $1\ cm^{-1}$, unless otherwise specified. Sequential spectroscopic measurements were typically collected at 60, 90, or 120 s intervals until a stabilized signal was obtained for dried sediments. Following each sample evaluation, dried sediment was rinsed off the waveguide surface with a stream of deionized water without mechanical rubbing to minimize scratching of the measurement surface. Once the majority of sediment was removed, a moistened Kimwipe (Kimberly-Clarke Professional, Neenah, WI) was utilized to gently clear away any residual particles.

5.4.2 Results and Discussion

5.4.2.1 Assessment of Sediment Compositions from Native Samples

IR-ATR spectra collected within the first few minutes following sediment deposition onto the waveguide surface are close representations of the expected spectroscopic signatures if samples were to be evaluated in the natural environment. Although strong absorption features from water occur around 3300, 2100, 1640, and below $1100\ cm^{-1}$, a significant amount of information can still be obtained respective of the sediment composition. **Figure 5-6** contains a representative IR-ATR spectrum for sediments collected from BC12 with generic labeling of the major absorption characteristics observed in the native hydrated sediment.

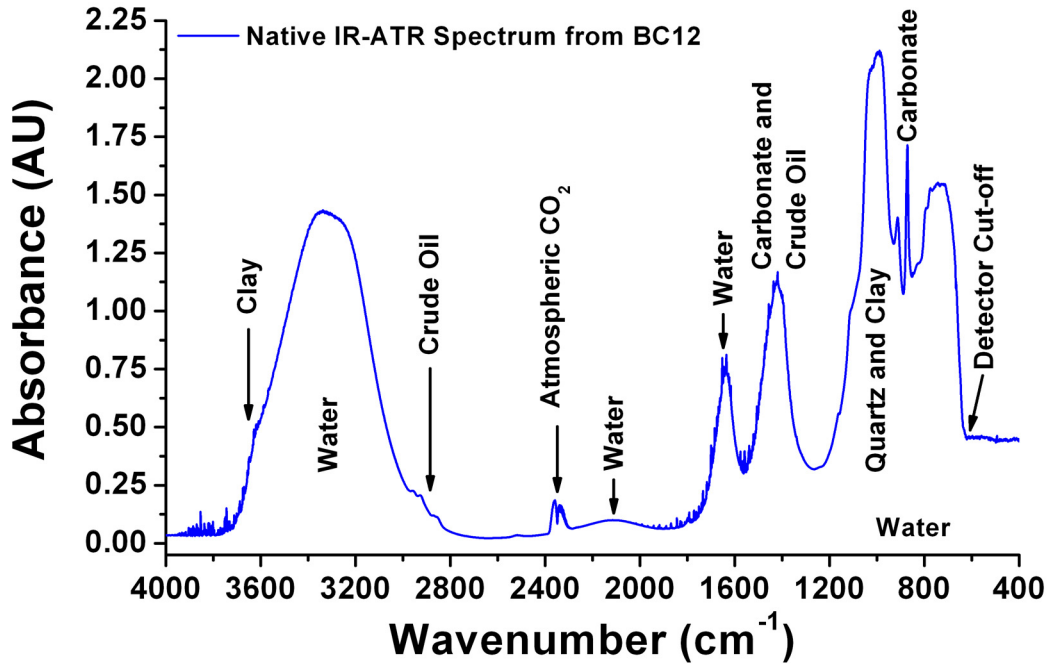

Figure 5-6: IR-ATR spectrum of hydrated BC12 sediments. General absorption characteristics are labeled for point of reference. This spectrum contains substantial absorption features from water, carbonates, quartz, and clays. Additional minor C-H stretch features above 2800 cm^{-1} resulting from the presence of crude oil are also observed. Sample: BC12B Bot.

For native sediments examined within this work, the most notable and variable spectral features of interest are: (1) water absorption features at approx. 3300, 2100, and 1640 cm^{-1}, (2) the strong ν_3 carbonate absorption feature in the region of 1550 – 1350 cm^{-1}, and (3) the C-H stretch and bend features from crude oil above 2800 cm^{-1} and approx. 1460 cm^{-1}, respectively. **Figure 5-7** exhibits the diversity of spectral profiles obtained for hydrated sediments from four MC118 box core locations.

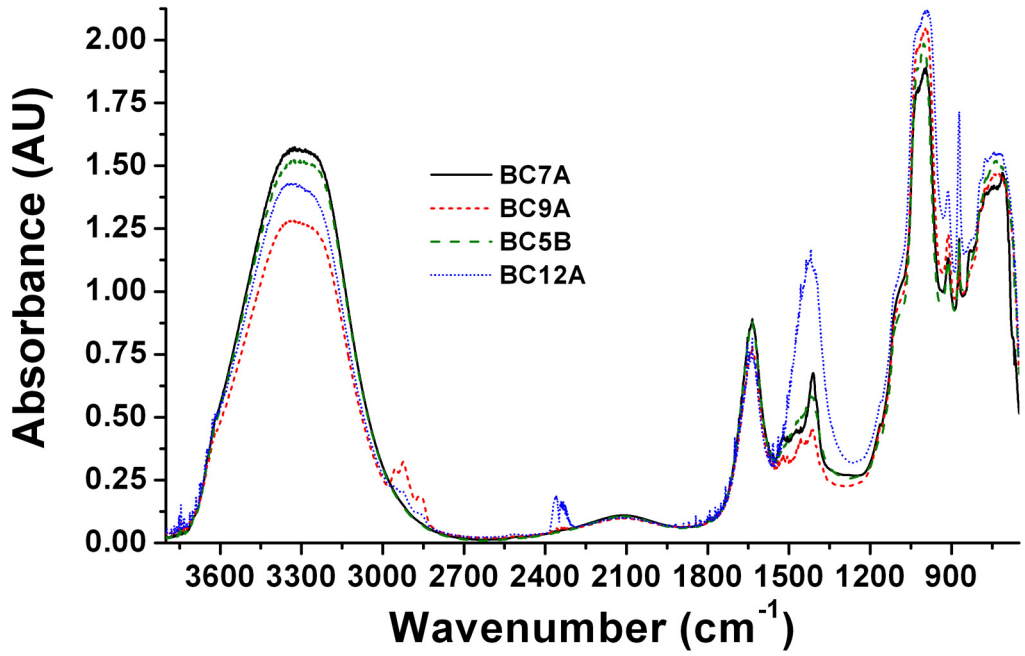

Figure 5-7: IR-ATR spectra from four box core locations at MC118. Variations in the spectral profiles for water, crude oil, and carbonates are readily apparent. Samples: BC7A Bot, BC9A Bot, BC5B Bot, and BC12A Bot.

Spectral variation in the absorbance of water bands from sediment samples was previously discussed in detail concerning the potential application of MIR chemical sensors for monitoring gas hydrate dynamics in **Chapter 4**. Hence, the following discussion will focus on fluctuations in crude oil and carbonate signatures.

Among all sediment samples evaluated in this study, C-H stretch signatures from crude oil were only observed in box core sediments collected from BC9 and BC12. Previous carbon isotope evaluations of gas and oil hydrocarbons in the sediments surrounding MC118 revealed substantial microbial alteration via depleted ^{13}C isotope ratios.[23] Although biodegraded crude is widely dispersed around MC118 as indicated in the field notes provided in **Table 5-8**, spectroscopic detection of oil in the sediment spectral profiles from BC9 and BC12 has been interpreted to result from the close proximity to higher seep prone areas linked to the fault conduits throughout MC118. The C-H features observed in BC9 and BC12 sediments are relatively weak and suggest only a minor overall mass contribution of crude oil to the sediment composition. However, if

localized pockets of highly concentrated crude oil are deposited onto the waveguide surface, the potential for generating related IR spectral features significantly increases. **Figure 5-8** displays the presence of two localized and highly concentrated pockets of biodegraded crude oil in sediments recovered from BC9.

Figure 5-8: Pockets of highly concentrated biodegraded crude oil (brown stains circled in red) in push-cored BC9 sediments from MC118 collected in June 2006. Although the crude appears to be a low mass percentage of the overall sediment composition, enough oil is present to generate absorption features in IR-ATR spectra when within evanescent field sensing regions. For scale, the diameter of this push-core tube is approx. 7.6 cm.

In addition to the spectroscopic signatures of biodegraded crude oil in a few sediment samples, substantial variations in the spectral profile of ν_3 carbonate absorption features were immediately evident. **Figure 5-9** contains an accentuated view of ν_3 carbonate signatures from native MC118 sediments, which were previously displayed as full spectra in **Figure 5-7**.

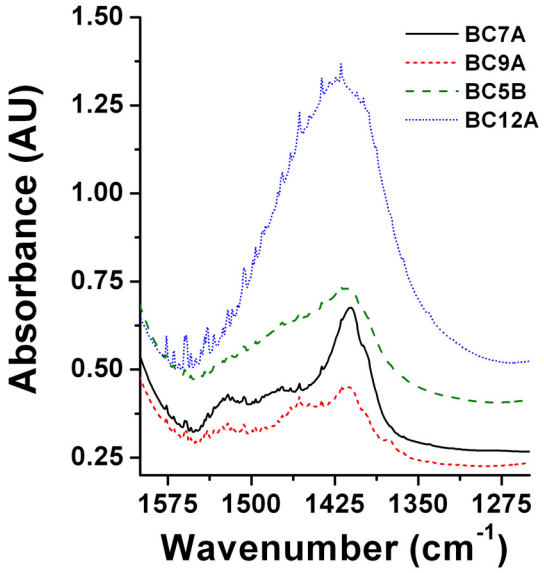

Figure 5-9: Accentuated view of ν_3 carbonate profiles in the IR-ATR spectra of native box core sediments collected from MC118. The spectral signature from each sample exhibits unique absorption characteristics. Samples: BC7A Bot, BC9A Bot, BC5B Bot, and BC12A Bot.

The ν_3 carbonate profiles displayed in **Figure 5-9** reveal a significant amount of information regarding differences in the sediment composition from each sampling location. First, the ν_3 profile of sample BC7A was the most commonly observed signature in surficial sediments collected at MC118. From additional experiments described in **Chapter 6**, it has been found that the strong, sharp peak at 1413 cm^{-1} is characteristic to sediments containing substantial accumulations of coccoliths. BC9A exhibits very similar features to the coccolith laden BC7A sediment; however, the presence of biodegraded crude in this sample leads to an additional sharp absorption protrusion at 1460 cm^{-1}. Furthermore, the broadened ν_3 spectral characteristics observed in sediments from BC5B and BC12A samples have been directly linked to areas of authigenic carbonate formation connected to chemosynthetic activities evidenced by $\delta^{13}C$ measurements described in **Appendix A-1** and **Chapter 6**. Partial broadening of the BC12A features can also be attributed to the presence of biodegraded crude, as indicated by the observance of C-H stretch absorptions.

Although the abundance of information contained within the spectral region of the ν_3 carbonate absorption has been briefly discussed here, **Chapter 6** provides more detailed considerations on the spectral consequences with respect to biogenic and authigenic carbonate formations. The focus of this section was primarily to acknowledge the extent of detailed information readily extracted from IR-ATR spectra of native sediment samples, which has significant implications for future applications of MIR chemical sensors in these environments.

5.4.2.2 IR-ATR Characterization of Dried Sediment Samples

Although detailed information can be generated from IR-ATR spectra of hydrated sediments, a more thorough characterization of the sediment composition can be extracted when water interferences are minimized. **Figure 5-10** provides a representative IR-ATR spectrum from dried BC7 sediments with the labeling of general absorption features.

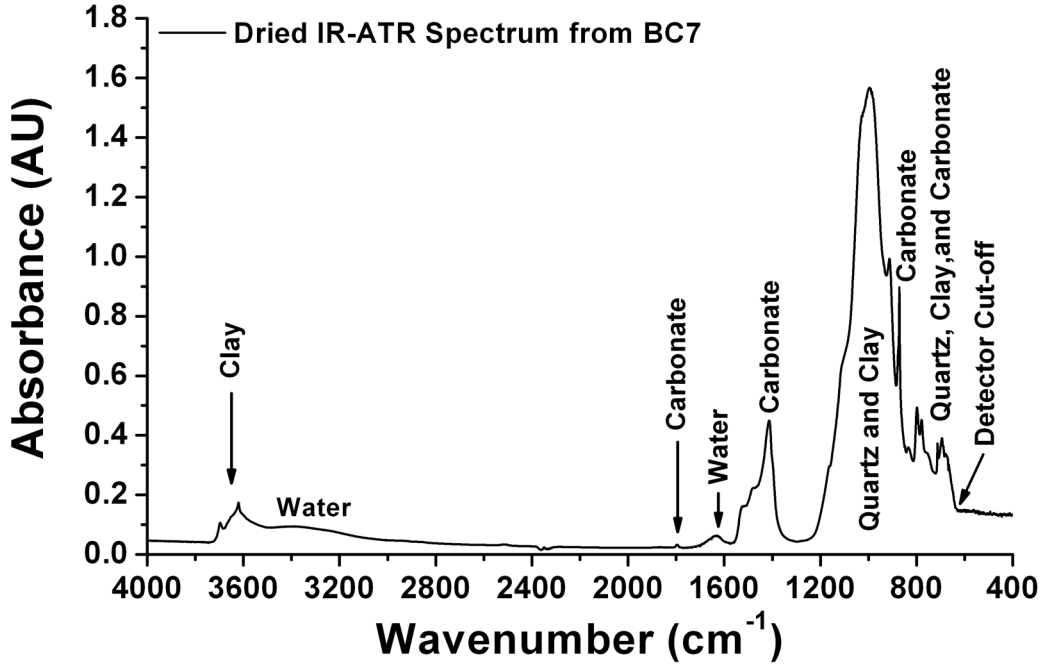

Figure 5-10: Representative IR-ATR spectrum of dried BC7 sediments collected from MC118. General absorption characteristics are labeled for reference. This spectrum displays improved spectral access to sediment components following the reduction of water interferences by drying. Sample: BC7A Bot.

Figure 5-10 displays significantly improved spectral access to compositional information after reduction of water interferences surrounding clay (i.e., smectite, illite, kaolinite, etc.) absorption features characteristic of O-H stretches from the aluminum silicate matrix at approx. 3600 cm^{-1} and the fingerprint region below 1600 cm^{-1}.[78, 79] As clay absorption features are only of generic interest for this thesis, the discussion will now focus on the fingerprint region (1600 – 400 cm^{-1}). **Figure 5-11** provides an expanded view of the fingerprint region from **Figure 5-10**.

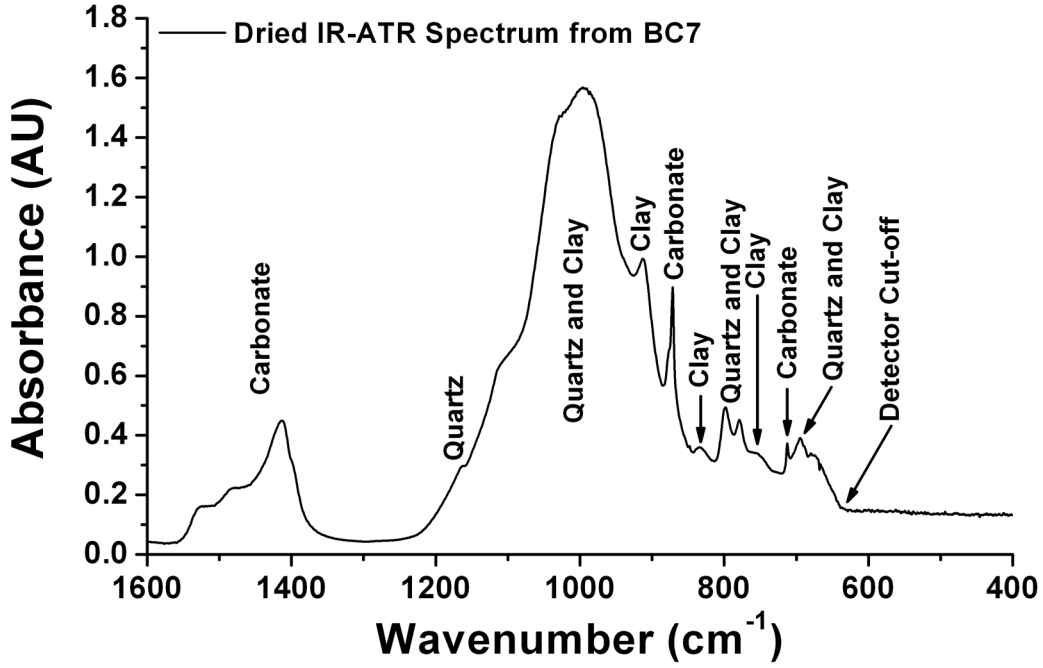

Figure 5-11: Labeled view of the fingerprint region for an IR-ATR spectrum of dried BC7 sediments. Quartz and clay exhibit similar absorption features resulting from Si-O moieties. Improved spectral access to fundamental carbonate absorption bands is clearly observed. Sample: BC7A Bot.

The fingerprint region contains a high density of information on the mineral composition, which becomes readily accessible following the drying process. Quartz and clays exhibit multiple absorption bands with several similar Si-O features that congest the spectral region from 1200 – 850 cm^{-1}; although, strong ν_2 carbonate signatures can still be observed. Additional mineral spectral features are also apparent below 850 cm^{-1}. In the scope of current work, the primary concern with regards to clay and quartz absorption features arises from their close proximity to ν_4

carbonate signatures that occur in the range of 735 – 700 cm^{-1}. The IR absorptions of quartz and clay leads to some minor overlap with ν_4 carbonate spectral features, which can constrain the accuracy of IR methods for quantitative evaluation of carbonate minerals. In the present work, the IR evaluation of sediments has primarily focused on qualitative and semi-quantitative methods for characterizing carbonate compositions and their differences within the geological context of gas hydrate ecosystems. Hence, clay and quartz interferences are discussed where relevant; however, further development of IR methods for evaluating these types of samples will require more careful consideration to the consequences of spectral interferences from these major mineral constituents.

The carbonate features of primary interest for GoM sediment evaluations are the ν_3 absorption the 1550 – 1350 cm^{-1} region and the ν_4 mode occurring from 735 – 700 cm^{-1}. In general, the ν_4 carbonate absorption region remains accessible for IR-ATR evaluation despite minor IR absorptions of clay and quartz minerals. The ν_2 carbonate bands strongly overlap with spectral contributions from clay and quartz at 1200 – 850 cm^{-1}; therefore, this carbonate feature is of limited practical usage for carbonate speciation in these particular sediment samples. However, shifts in the absorption profile of the ν_2 vibrational mode were found to correlate with variations observed in the ν_3 carbonate region. A complete description of the observed ν_3 and ν_2 spectral anomalies is provided in **Chapter 6**.

Among all GoM sediments evaluated, calcite and dolomite were the most frequently observed carbonate minerals with calcite being the only species detected in all samples. Aragonite shells litter the seafloor surrounding the MC118 site, and were recovered in several box core collections. However, no discernable spectral contributions from aragonite were observed in any of the IR-ATR spectra of sediment samples, including sediments with recovered shells and/or authigenic carbonate nodules. This is attributed to the large shell sizes as discussed in **Section 5.1.2.3**, and suggests the relative instability of aragonite within the very fine surficial sediment

fractions (< 62.5 μm) and/or undersaturated pore waters with respect to aragonite at the sampling locations surrounding MC118. The only unambiguous spectral detection of Mg-calcite among all sediments was in BC12 samples. **Figure 5-12** provides accentuated views of ν_4 carbonate features exemplifying the diversity of carbonate signatures observed in sediment samples with examples from the three sample collections described in **Section 5.3**.

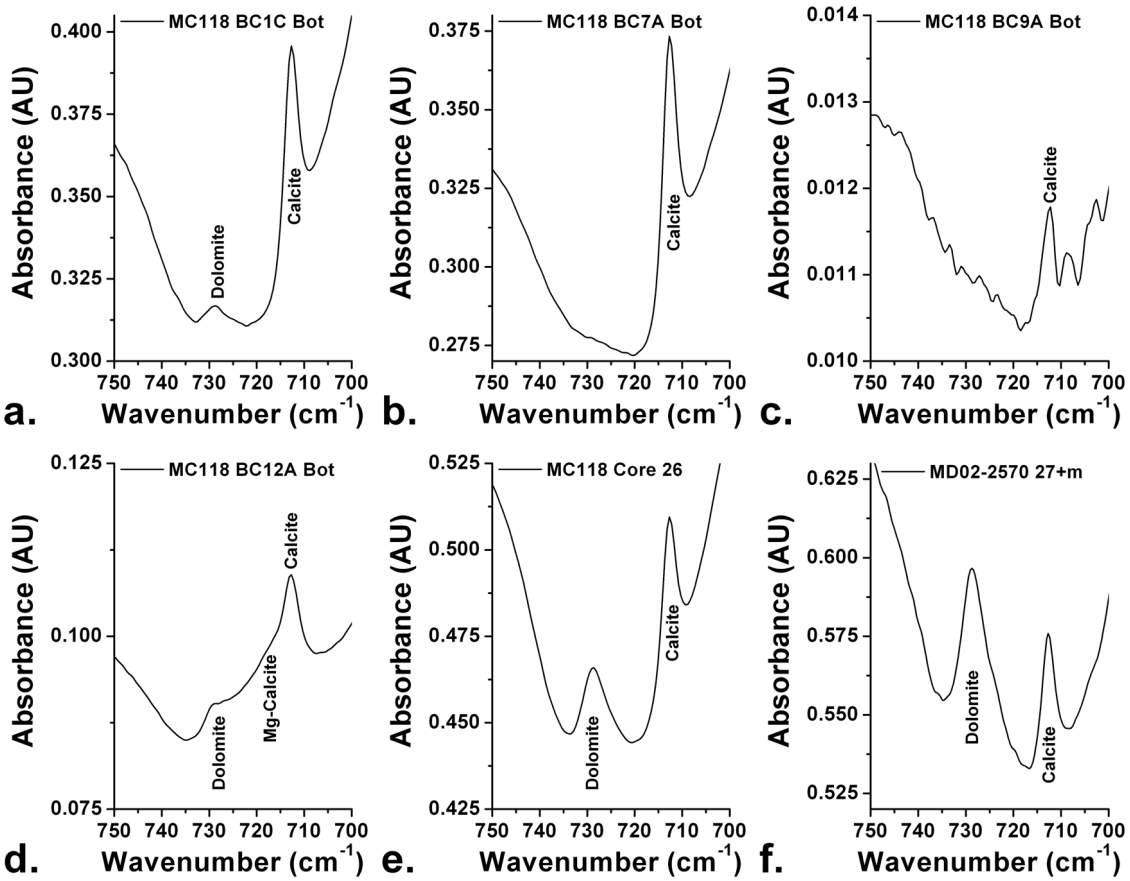

Figure 5-12: Selected views of ν_4 carbonate absorption features for IR-ATR spectra obtained from (a.) BC1C Bot, (b.) BC7A Bot, (c.) BC9A Bot, (d.) BC12A Bot, (e.) MC118 Core 26, and (f.) 27+m sediments from core MD02-2570. The ν_4 absorption characteristic to calcite was observed in all samples. Dolomite is clearly present in BC1C Bot, BC12A Bot, and Core 26 sediments from MC118, as well as in 27+m sediments from MD02-2570. Mg-calcite was only observed in BC12 sediments, as indicated in (d.).

In **Figure 5-12**, spectra **(a.) – (d.)** display the extent of variability obtained for ν_4 carbonate features in box core sediments collected from MC118 in June 2006. The most common ν_4

signature can be observed in spectrum **(b.)** for BC7A Bot sediments. MC118 samples exhibiting only calcite-related ν_4 features provide the first indication of sediments with biogenic coccoliths as the primary carbonate source within the very fine sediment fraction and no further indication of authigenic carbonate available from this absorption feature, as discussed in **Chapter 6**.

In **Section 5.4.2.1**, the spectral profiles of BC9 and BC12 were shown to contain measurable amounts of biodegraded crude oil. The presence of crude oil in sediment samples was coincident with noticeably reduced IR absorption intensities, as these sediment samples coalesced during the drying process (see Y-scales in **Figure 5-12 (b.)** and **(c.)**). As sediments clumped together while drying, they delaminated from the waveguide surface, thereby resulting in decreased spectral intensity from reduced evanescent field interactions. This phenomenon appears to correlate with the relative mass fraction of crude oil in these samples. BC9 sediments typically exhibited stronger C-H absorption features, indicative of higher crude content, and lower spectral intensities compared to BC12 sediments. Despite the presence of crude and apparent sample detachment from the ATR crystal surface in BC9 samples, calcite was still detected with no indication of additional carbonate species.

Calcite, dolomite, and Mg-calcite were detected in sediments from BC12, as labeled in **Figure 5-12 (d.),** thereby indicating the presence of authigenic carbonate. The IR absorption of Mg-calcite appears as a shouldering feature covering the spectral region between calcite and dolomite features. The ν_4 region from other representative spectra provided in **Figure 5-12** serve as excellent comparisons to aid visualization of the spectral absorption of Mg-calcite. Using **Equation 5-2**, Mg^{2+} mole fractions (X_{Mg}) can be estimated to range from $0.1 - 0.2$. Spectral mixing from the presence of calcite and dolomite limit the capability to provide an exact X_{Mg} value, and it has previously been recognized that effective quantification of X_{Mg} requires a homogeneous sample.[39] Furthermore, Mg-calcites with a wide range of X_{Mg} compositions are

likely to be present within a single sample matrix, as the degree of Mg^{2+} incorporation can vary with precipitation over long periods of time and temporal fluctuations in pore water conditions.

Sediments from two of the three MC118 gravity cores, Core 21 and Core 26, contained significant dolomite contributions, as evident in their IR-ATR spectra. Core 38 did not exhibit any significant dolomite absorption features in the ν_4 region. Furthermore, the carbonate absorption characteristics (ν_3 and ν_4) from Core 38 sediments closely resembled those obtained in the IR-ATR spectra of BC7A Bot sediments, as displayed in **Figures 5-11 and 5-12 (b.)**. All samples evaluated from the MD02-2570 piston core collected in Mississippi Canyon during 2002 contained strong dolomite and calcite signatures.

In all spectra displayed in **Figure 5-12**, overlapping spectral interferences are observed for both calcite and dolomite absorption bands arising from clay and quartz features. Calcite exhibited stronger spectral overlap due to tailing from the quartz and clay absorption bands centered below 700 cm^{-1}, whereas only minor overlap was typically observed for dolomite and the clay absorption centered at approx. 750 cm^{-1}. A wide range of calcite-dolomite compositions relative to the overall carbonate mass fraction are observed in the IR-ATR spectra displayed in **Figure 5-12 (a.), (d.), (e.), and (f.)**. **Section 5.5** addresses the semi-quantification of the relative mass percentages of calcite and dolomite to the total carbonate mass for all sediment samples evaluated in this study. In addition, the impact of spectral interferences from clay and quartz features with respect to data interpretation will be further addressed within **Section 5.5**.

5.5 Calcite-Dolomite Ratios from Sediment Collections

In 1967, Chester and Elderfield described an IR method to determine the relative mass percentage contributions from calcite and dolomite to the total carbonate composition in rock samples utilizing absorption intensities at the peak maxima of the respective ν_4 features.[5] After examining a series of 7 calcite-dolomite standards ranging from 5% to 95% calcite with 100% sample mass

from the combined composition, a first order linear calibration function was generated to extract the relative mass percentages of calcite and dolomite with respect to the total carbonate content. The X-axis of the calibration plot was obtained by the ratio of calcite absorption intensity divided by the sum of intensities for calcite and dolomite (C/(C+D)), where C = calcite and D = dolomite. Dual Y-axes represented the inverse relationship in composition enabling simultaneous calculation of the respective mass % contributions such that higher C/(C+D) values corresponded to greater calcite composition. This evaluation strategy is resilient to potential sample-to-sample absolute absorption intensity fluctuations (i.e., change in effective sample pathlength, particle density, etc.) resulting from the normalization and ratiometric calculation yielding a unitless value. Since 1967, several reports have expanded on this initial method for quantifying carbonate minerals for various applications.[55, 60] In this work, similar methods have been developed for semi-quantitative evaluation of the relative mass percentages of calcite and dolomite in the carbonate composition of marine sediment samples using ν_4 peak area analysis of IR-ATR spectra.

5.5.1 Experimental

5.5.1.1 Materials and Instrumentation

The instrumental setup and equipment is identical to that described in **Section 5.2.1.2** for generating IR-ATR spectra of carbonate minerals. Additionally, the same research grade calcite and dolomite specimens described in **Section 5.2.1.1** were utilized to establish a calibration method for estimating the mass percent composition of calcite and dolomite with respect to total carbonate mass.

Standardized calcite-dolomite samples were prepared as aqueous suspensions similar to that described for evaluating single carbonate mineral specimens. However, for quantitative evaluation, it was pertinent to ensure that reaction or dissolution of calcite was minimized. Hence, an aqueous solution was prepared by adjusting the pH of deionized water (R = 18.2 MΩ·cm at

25°C) to approx. 8.5 for generating standard sample suspensions. This stock solution (~200 mL) was prepared following the drop-wise addition of a highly concentrated potassium hydroxide solution after the addition of 3 KOH pellets (J.T. Baker, Phillipsburg, NJ) to ~25 mL of deionized water. Drops were added until a stable pH reading of approx. 8.5 was obtained with a calibrated pH meter (ThermoOrion Model 555A, Thermo Fisher Scientific Inc., Waltham, MA).

5.5.1.2 Sample Preparations and IR-ATR Measurement Procedures

Calcite and dolomite specimens were separately hand ground into a fine powder with a ceramic mortar and pestle to generate stocks utilized for all calibration standards. In addition to preparing five standard samples, four blind samples were prepared for evaluating the calibration method. Three blind samples were prepared using the same ground calcite and dolomite stocks for concocting calibration mixtures. The remaining blind sample was purposefully prepared from secondary and separately ground calcite and dolomite stocks as a rough measure of calibration robustness.

Following preparation of calcite and dolomite stocks, each sample was vigorously mixed before preparing calcite-dolomite calibration standards ranging from 10% to 90% calcite with approx. 1.8 g total mass. The four blind samples (designated as BS1 – BS4) were prepared in similar fashion. **Table 5-9** summarizes the calcite-dolomite compositions for calibration standards and blind samples (obtained after spectroscopic analysis).

Table 5-9: Composition information for calcite-dolomite calibration standards and blind samples. Mass % values represent both the absolute and relative mass compositions for each species with respect to the total sample and total carbonate content. (D = dolomite and C = calcite).

Calibration Standards	**Mass (g)**		**Mass (%)**	
%D:%C	**Dolomite**	**Calcite**	**Dolomite**	**Calcite**
90:10	1.6068	0.1796	89.95	10.05
70:30	1.2611	0.5504	69.62	30.38
50:50	0.9003	0.9001	50.01	49.99
30:70	0.5433	1.2603	30.12	69.88
10:90	0.1805	1.6135	10.06	89.94
Blind Samples	**Mass (g)**		**Mass (%)**	
BS#; %D:%C	**Dolomite**	**Calcite**	**Dolomite**	**Calcite**
BS1; 32:68	0.5786	1.2246	32.09	67.91
BS2*; 46:54	0.8298	0.9738	46.01	53.99
BS3; 7:93	0.1163	1.6821	6.47	93.53
BS4; 78:22	1.4033	0.3937	78.09	21.91

Prior to the initial spectroscopic evaluation of each calibration mixture or blind sample, 4.5 mL of the prepared KOH solution was added with a 0.10 – 1.00 mL calibrated Eppendorf pipette (Eppendorf North America Inc., New York, NY). The sample compartment was purged for at least 10 mins with dry air prior to collecting a reference spectrum of a clean, dry ZnSe crystal for each sample evaluation. Upon completion of the reference spectrum, the respective calibration mixture or blind sample suspension was aspirated and dispensed from a single-use disposable plastic pipette for approx. 15 s to ensure sample homogeneity. Afterwards, approx. 1 mL of the sample mixture was delivered and distributed onto the waveguide, fully covering the measurement surface. IR-ATR spectra were then continuously recorded at 90 s intervals throughout the drying process until approx. 25 spectra were obtained following spectral stabilization of dried, powdered residues. This measurement strategy required approx. 3 hrs per individual sample analysis. IR-ATR reference and sample spectra were generated by averaging 100 sample scans at a spectral resolution of 1 cm^{-1}. The calibration set was generated over a three day period without any disturbance to the experimental apparatus. Each calibration sample was

evaluated only once per day without any prescribed order. Blind samples were evaluated the day following completion of the calibration measurements. Each blind sample was evaluated only once. Statistical evaluation for the reproducibility of blind sample evaluations was performed by pooling analytical information from all four sample analyses.

5.5.2 Results and Discussion

5.5.2.1 Calibration for Determining Mass % of Calcite and Dolomite to Total Carbonate

Figure 5-13 contains representative IR-ATR spectra from the ν_4 spectral region for calcite-dolomite standards used for calibrating the relative mass % of calcite and dolomite to the total carbonate composition.

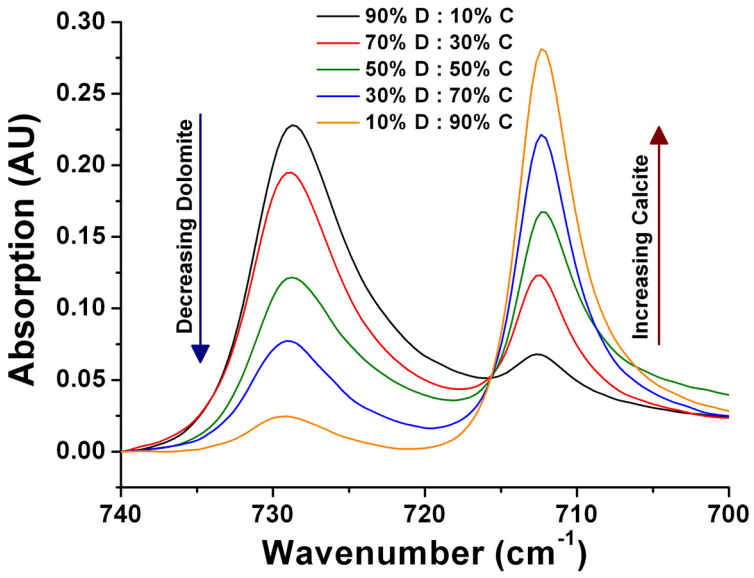

Figure 5-13: IR-ATR spectra highlighting the ν_4 carbonate region for calibration standards used to establish the correlation of peak areas to the mass % of each component. Spectra were uniformly shifted to a zero baseline at 740 cm^{-1}. As expected, the intensity of calcite and dolomite absorption features varied according to the relative mass fraction present in each sample. (D = dolomite and C = calcite).

A "valley-to-valley" peak integration method was developed to evaluate the ν_4 spectral absorptions of calcite (716.3 – 705.2 cm^{-1}) and dolomite (733.9 – 721.9 cm^{-1}), while limiting

overlap between the two components. This integration method was utilized for evaluating all calcite-dolomite compositions for standard, blind, and sediment samples.

For each standard and blind sample, the average of 25 consecutive integrated peak areas (PAs) was calculated and used to represent the sample specific PA value for each component used for further calculations. Proportional PA ratios (Prop. PAs) for calcite-dolomite analysis were determined following two possible combinations; (1) D/(C+D) and (2) C/(C+D) where D = dolomite PA and C = calcite PA. This calculation is identical to that described by Chester and Elderfield; however, PAs were utilized in this study, as opposed to absorption maxima.[5] For calibration standards, the average Prop. PA was calculated from triplicate evaluations of each respective sample standard. **Table 5-10** provides a reduced data analysis table with calcite-dolomite Prop. PAs used to generate standard calibration curves and calibration fit parameters utilized for correlating the mass % of calcite and dolomite with respect to the overall carbonate content present in the sample; full data tables are provided in **Appendix A-4**.

Table 5-10: Data table for IR-ATR analysis of standard samples. Prop. PAs were calculated from the average of triplicate analyses. The standard deviation (SD) of Prop. PAs are provided in addition to the % Error calculated using the linear calibration fit equation with the SD. The SD and % Error are the same for both Prop. PA calculation methods. Linear calibration fit parameters are provided. In addition, an approximation of the dynamic range for each Prop. PA calculation strategy is presented. The reported dynamic range is only valid for samples where the sum of the mass from (calcite+dolomite) = 100% of the sample mass. The % calcite and dolomite in each sample standard were calculated from mass values. (D = dolomite PA and C = calcite PA).

Calibration Standard	**Prop. PA**	**Prop. PA**		
% Dolomite:% Calcite	**D/(C+D)**	**C/(C+D)**	**SD**	**% Error from SD**
89.95:10.05	0.916	0.084	0.003	0.28
69.62:30.38	0.714	0.286	0.002	0.20
50.01:49.99	0.496	0.504	0.006	0.60
30.12:69.88	0.300	0.700	0.003	0.28
10.06:89.94	0.103	0.897	0.001	0.19
	Linear Calibration Fit Parameters			
	Fit from D/(C+D)		**Fit from C/(C+D)**	
	y = A + B*x		**y = A + B*x**	
	A	0.565	**A**	1.796
	B	97.639	**B**	97.639
	R^2	0.9995	**R^2**	0.9995
	Dynamic Range Estimated from 6*AvgSD			
	From D/(C+D) Calibration		**From C/(C+D) Calibration**	
	2.3 – 97.7% Dolomite		3.6 – 96.4% Calcite	

From **Table 5-10**, evaluation of the Prop. PA ratios from IR-ATR spectra was very reproducible resulting in high quality linear regression functions with the capability to quantify both carbonate species over an estimated dynamic range from approx. 3 – 97 mass % with this sample matrix. The % relative standard deviation (%RSD) of Prop. PA ratios averaged < 1.2% despite average %RSDs of approx. 7.5% from absolute PA values (see full data tables in **Appendix A-4**). Hence, usage of Prop. PA ratios provides inherent resilience against sample-to-sample intensity fluctuations, which is desirable for practical applications. **Figure 5-14** displays linear calibration plots generated for determining the mass % contributions of calcite and dolomite to the total carbonate composition along with results for the spectral analysis of 4 blind samples.

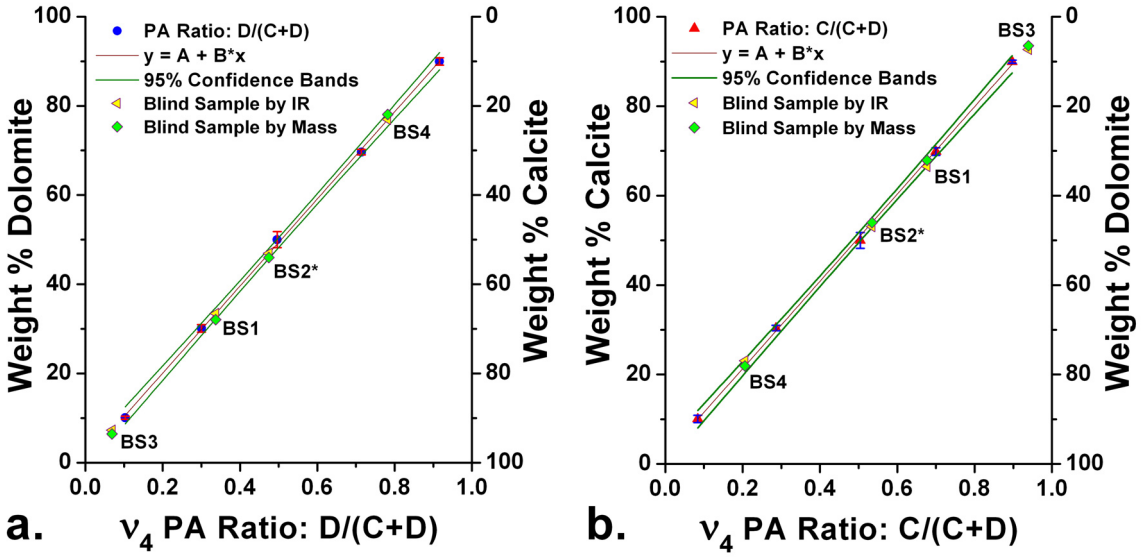

Figure 5-14: Calibration functions for determining the mass % of calcite and dolomite contributions to the total carbonate content using Prop. PA ratios for ν_4 absorptions (a.) D/(C+D) and (b.) C/(C+D). Error bars represent the mass % error calculated from three times the SD of triplicate measurements. In addition, the mass % determinations of calcite and dolomite from IR analysis for four blind samples (BS#) are plotted along with actual mass % values calculated from the recorded mass composition. (BS2* was prepared from secondary calcite and dolomite stocks).

The quality of linear regressions generated by Prop. PA ratio analysis of standard samples is readily observed in **Figure 5-14**. In addition, the experimentally determined and actual mass % values calculated from the sample masses for calcite and dolomite for all blind samples are plotted. Prop. PA ratios obtained from IR evaluation are plotted along the calibration function based on the calculation of D/(C+D) or C/(C+D). Actual mass values were plotted using the experimentally determined Prop. PA ratio versus the actual mass %s determined from the sample composition. The largest absolute deviation from the true value using the described IR method was < 1.4%. In addition, the composition of BS3 (6.5% D : 93.5% C) was determined within 1% of the actual value, although it was slightly beyond range of the calibration standards. This result was consistent with respect to the estimated dynamic range from **Table 5-10**. Furthermore, the mass composition of the BS2* sample prepared from secondary calcite and dolomite stocks was determined within 1% of the actual value. The purpose for single evaluations of blind samples

was to simulate the practical application for rapid on-ship sample assessment. Analytical confidence in single trial evaluations is desirable if time is limited and costly. A reduced data table summarizing IR-ATR evaluation of blind samples is provided in **Table 5-11**; the full data table is provided in **Appendix A-4**.

Table 5-11: Data table for IR-ATR analysis of blind samples. The average PA for calcite and dolomite, Prop. PA ratio calculated as either D/(C+D) or C/(C+D), and calculated mass % for calcite and dolomite are included. An excellent agreement is obtained by the comparison of sample mass % (determined from mass composition) with the mass % determination by IR analysis. The largest error in % determination was less than 1.4% of the respective mass composition. (BS2* was prepared from secondary calcite and dolomite stocks).

	Blind Sample Analysis: Sum(C+D) = 100% Sample Mass							
	Mass (%)		**PA**	**SD**	**D/(C+D)**	**% (C or D) by IR**		**% Error**
ID	**D**	**C**	**D**	**D**	**D**	**D**	**C**	**(C or D)**
BS1	32.09	67.91	0.3375	0.0023	0.3370	33.47	66.53	1.38
BS2*	46.01	53.99	0.5402	0.0023	0.4750	46.94	53.06	0.93
BS3	6.47	93.53	0.0809	0.0019	0.0690	7.30	92.70	0.83
BS4	78.09	21.91	0.9469	0.0030	0.7822	76.94	23.06	1.15

	PA	**SD**	**C/(C+D)**
ID	**C**	**C**	**C**
BS1	0.6640	0.0025	0.6630
BS2*	0.5971	0.0022	0.5250
BS3	1.0907	0.0019	0.9310
BS4	0.2636	0.0020	0.2178

To establish this calibration, it was not required to control the total sample mass deposited onto the waveguide surface. This is one particular advantage of utilizing proportional ratios coupled with the Beer-Lambert law. Hence, experimental results should remain highly reproducible as the absorption of all matrix components shall be affected equally provided that: (1) packing of the residual sample powder within the evanescent field is reproducibly representative of the sample composition following evaporation of the aqueous matrix, and (2) any absolute intensity fluctuations occur irrespective to the relative mass % of calcite and dolomite to the total carbonate composition. Absorption intensity fluctuations were apparent from sample-to-sample evaluation as indicated by the %RSD in absolute PA values of approx. 7.5%; however, intensity fluctuations appeared to occur irrespective of the calcite and dolomite composition as the %RSD

for Prop. PA ratios was < 1.2%. Thus, this calibration method provides a robust analytical evaluation strategy, which is significant for supporting the practical application of this technique; not only for studies presented in this thesis, but also for real-world application such as on-ship sediment analysis. The capabilities, advantages, and limitations of this analysis strategy are further discussed in **Section 5.5.2.5**.

5.5.2.2 Evaluating Calcite and Dolomite in MC118 Sediments (June 2006 Cruise)

IR-ATR spectra of box core sediments collected from MC118 in June 2006 were obtained over a period of nine months. Calcite and dolomite compositions with respect to the total carbonate content in sediment samples have been calculated as prescribed by the calibration equations using the Prop. PA ratios. Analytical results have been compressed and integrated into a site map (**Figure 5-15**) with each sample location identified and significant findings indicated.

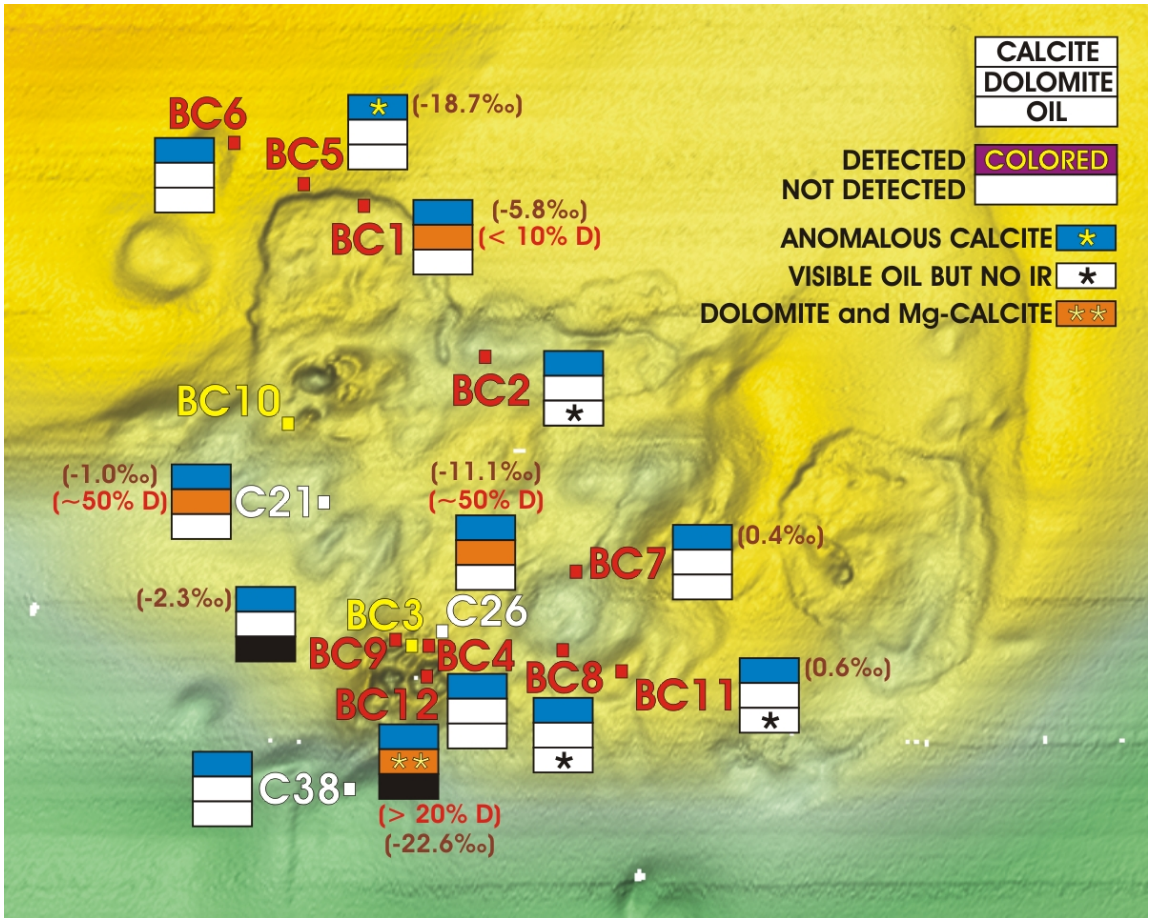

Figure 5-15: Condensed summary of IR-ATR spectral analyses of MC118 sediments collected in June 2006 (BC#) and October 2005 (C#). Each sampling location and significant findings are provided. Variability with respect to hydrocarbon detection and carbonate mineral diversity around the MC118 system is readily visualized and accentuated around the SW hydrate mound and the NW ridgeline. Dolomite mass % (red text with % D) are averages relative to the total carbonate mass, not sample mass. δ13C values (V-PDB scale as brown text with ‰) are also provided as discussed in **Appendix A-1** and **Chapter 6**. (Swath batyhmetry color-shaded relief map provided courtesy of the GOMGHRC, and produced by Alessandro Bosman (University of Rome, La Sapienza) and Leonardo Macelloni (CMRET) from acoustic data collected by C&C Technologies (Lafayette, LA) with the Hugin 3000 AUV).

Calcite was clearly detected in all box core sediment samples collected at MC118. Sediments from BC2, BC4, BC6, BC7, BC8, and BC11 exhibited very similar absorption profiles with no indication of dolomite from ν_4 evaluations via visual inspection or peak area analysis. Peak area analysis of ν_4 absorption features for calcite and dolomite in IR-ATR spectra for these samples resulted in calculated relative mass % values for dolomite to the overall carbonate composition

ranging between -5% – < 1%. The artifact of calculated negative mass % values was frequently obtained via the prescribed data evaluation strategy when calcite was the only detected carbonate species in the IR-ATR spectra of sediment samples (i.e., C = 100% and D = 0% based on IR-ATR analysis). **Figure 5-16** visually displays that the origin of negative mass % values resulting from mathematical artifacts due to the peak integration method evaluating the dolomite absorption region, which spans a dip in the spectrum related to interference from the clay absorption feature centered at approx. 750 cm^{-1}.

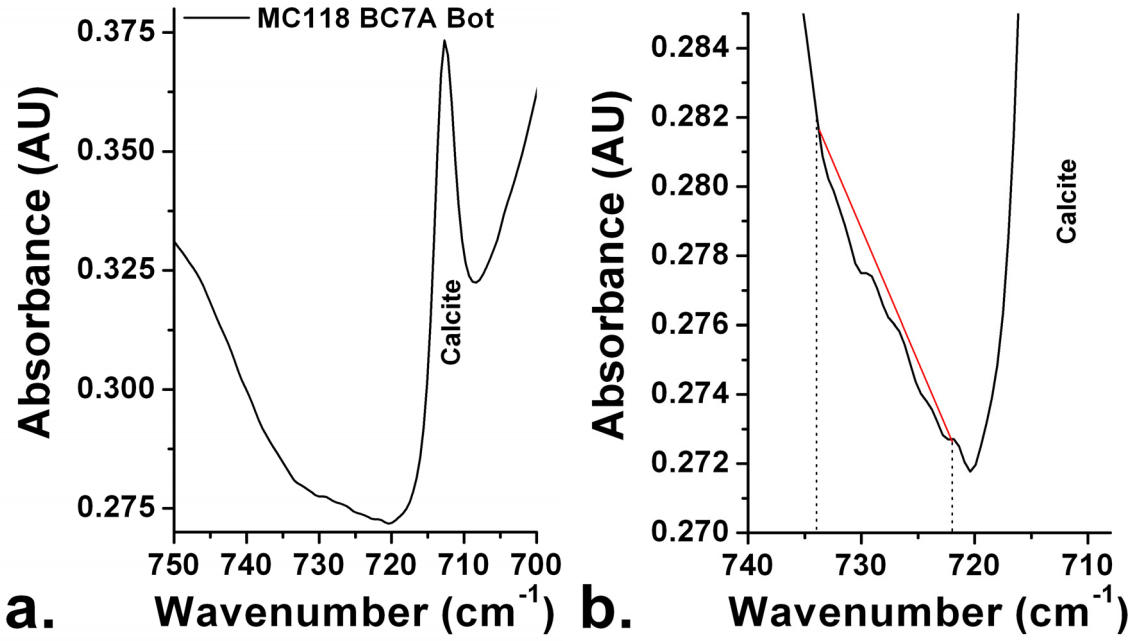

Figure 5-16: Selected viewings of an IR-ATR spectrum for BC7A Bot sediments. (a.) IR-ATR spectrum displaying calcite-only carbonate absorption features and tailing of the clay absorption feature centered at ~750 cm^{-1} readily apparent. (b.) Accentuated view of the dolomite integration region imposed on the same IR-ATR spectrum from (a.). The red (solid) line illustrates a small gap below the baseline imposed during peak integration analysis resulting in the calculation of negative mass % values for dolomite in the total carbonate composition in sediment samples. Thus, C = 100% and D = 0% when this occurs during sediment analysis with the prescribed evaluation strategy.

The implemented peak integration method for evaluating carbonate absorption features imparts a straight line spanning the defined spectral region for analysis. Then, the area between the imposed line and the IR spectral signature is calculated. Hence, when dolomite is not present at a threshold

level to overcome the influence of the spectral dip resulting from the clay absorption feature, as in **Figure 5-16**, a negative peak area is obtained from IR-ATR spectral analysis. Therefore, when calculating the mass % of dolomite from a negative peak area, regardless of using either C/(C+D) or D/(C+D), an artifactual negative mass % value arises. The mathematical calculation of (C+D) amplifies the magnitude of this artifact in the mass % values with increasing negative peak area values. Calculated negative mass % values are interpreted as 0% dolomite and 100% calcite in the overall carbonate mass fraction. All mass % values are presented in this thesis as the output values from the prescribed evaluation procedure to illustrate the effect of spectral interference from clay on the quantitative evaluations. Although negative mass % values were frequently returned from this evaluation procedure, the IR-ATR spectra for all sediment samples were visually inspected to confirm the absence/presence of dolomite, aragonite, and/or Mg-calcite.

Although the presence of dolomite and/or other carbonate minerals was not detected via IR-ATR spectroscopy in BC2, BC4, BC6, BC7, BC8, and BC11 samples, low mass %s could be present in the sediment sample in addition to calcite. In calibration samples, the lower quantification range for dolomite was approx. 3% of the sample mass without matrix dilution or interference from clay mineral absorption features. Hence, spectral sensitivity to the detection of multiple carbonate minerals in marine sediment samples is expected to be lower depending upon the carbonate mass contribution to the overall sample mass. Additional examination of the ν_3 spectral profile, as discussed in **Chapter 6**, revealed no significant indication to the presence of additional carbonate species other than coccolith calcite for these particular samples. **Table 5-12** provides representative peak area results from spectral evaluation of the ν_4 absorption feature assessing the calcite-dolomite composition in BC7 sediments; full data tables from the analysis of all marine sediments from the GoM are provided in **Appendix A-5**.

Table 5-12: Analytical results from evaluating ν_4 carbonate absorption features to determine the relative mass % of calcite and dolomite in the total carbonate content for sediments from push-core A of BC7 sediments. The negative values result from matrix interference indicating that calcite is the only carbonate species contributing to the IR-ATR spectrum (i.e., C = 100% of the carbonate composition). Similar values were obtained for BC2, BC4, BC6, BC8, and BC11 sediment samples. Visual inspections confirmed that calcite was the only carbonate species detected within IR-ATR spectra.

Calculated Mass % of Calcite and Dolomite from $\Sigma(CO_3)$ in BC7 Sediments					
Push-core Sub-sample	**D PA**	**D SD**	**D/(D+C)**	**% D**	**% C**
BC7A Top (1)	-0.0057	0.0027	-0.0560	-4.90	104.90
BC7A Top (2)	-0.0080	0.0014	-0.0491	-4.23	104.23
BC7A Top (3)	-0.0064	0.0017	-0.0413	-3.46	103.46
BC7A Bot (1)	-0.0048	0.0022	-0.0179	-1.18	101.18
BC7A Bot (2)	-0.0083	0.0019	-0.0355	-2.90	102.90
BC7A Bot (3)	-0.0100	0.0020	-0.0417	-3.51	103.51

Although this quantification strategy yielded artifactual negative mass % values indicative of 100% calcite, the representative results provided in **Table 5-12** illustrate the consistent analysis of IR-ATR spectra from both BC7A Top and Bot sub-samples collected over a span of eight months in the laboratory. Minor variability is observed, which is attributed to the heterogeneous nature of sediment matrices.

As seen in **Figure 5-15**, biodegraded oil is widely distributed throughout the hydrate system at MC118 including BC3 and BC10 sediments, which were not sampled for evaluation with IR-ATR spectroscopy. Spectral detection of crude oil in BC9 and BC12 sediments were previously described. However, visual inspection of the ν_4 carbonate absorption features revealed different results. BC9 sediments exhibited only calcite features, whereas BC12 sediments contained calcite, Mg-calcite, and dolomite absorption bands (see **Figure 5-12 (c.)** and **(d.)**). With exception of crude oil absorptions, the IR-ATR spectra of BC9 sediments closely resembled those obtained for BC2, BC4, BC6, BC7, BC8, and BC11 samples. Semi-quantitative analysis of calcite and dolomite compositions in the total carbonate mass provided conflicting results with calculated values ranging from approx. -19% up to approx. 26%. Upon closer visual inspections of the IR-ATR spectra, calcite was confirmed to be the only carbonate mineral contributing to the obtained

spectra (i.e., C = 100% and D = 0%). The conflicting quantitative ν_4 analyses are attributed to the combination of two factors: (1) significantly reduced absorption intensities for all sample components in BC9 sediments resulted from the enhanced detachment of sample from the waveguide surface with the presence of crude oil, and (2) the average spectral noise, typically insignificant in the mass composition analysis, becomes a significant factor impacting the outcome of mass analysis as a result of sample delamination (see **Figure 5-12 (c.)**). Visual inspection of the IR-ATR spectra throughout the drying process confirmed that calcite was the only detected carbonate species within BC9 sediments.

Although BC12 sediments also contained measurable amounts of crude oil, unambiguous spectral identification of dolomite, calcite, and Mg-calcite was possible in the ν_4 region. The presence of Mg-calcite further complicates the characterization of calcite and dolomite compositions to the overall carbonate mass. Highly variable mass % values were obtained for dolomite composition in BC12 sediments, which ranged from approx. 10 to 30% with an average > 20% (this value was assigned to BC12 sediments in **Figure 5-15**). The range of variance is partly attributed to the presence and spectral interference of Mg-calcite. However, the detection and variability of multiple carbonate species surrounding the SW hydrate mound signifies the detection of authigenic carbonate formation. This assessment is complemented by the visual confirmation of abundant authigenic formations surrounding the SW hydrate mound during manned submersible dives. Further evaluation and considerations to the significance of spectral features exhibited by BC12 sediments for detecting authigenic carbonate formation is discussed in **Chapter 6**.

The only additional box core sediment samples exhibiting identifiable dolomite absorption features were those collected from the BC1 location. Calculated mass % values for dolomite contribution to the overall carbonate mass ranged from not detectable (≤ 1%) up to approx. 10.5% with the average < 10%, as indicated in **Figure 5-15**. These findings, coupled with the recovery

of ‘gassy’ mud and aragonite shells, are consistent with the detection of authigenic carbonate formation driven by chemosynthetic communities.

Lastly, sediments collected from BC5, specifically the bottom sediments from the B push-core, exhibited unique spectral characteristics. Deviations in the ν_3 absorption profile followed trends characteristic to authigenic carbonate formation observed in BC1 and BC12 samples; however, calcite was the only identifiable carbonate species from visual inspection of the ν_4 region. Highly variable calculated mass % values for dolomite were obtained from BC5 sediments, which ranged from approx. -50% to approx. -10%. As previously mentioned, the negative mass % values are a mathematical artifact, and confirm calcite identifiable contributor to the IR-ATR spectra. Considering the broadened ν_3 spectral characteristics combined with recovered authigenic carbonate nodules and shells indicative to chemosynthetic activity, the IR-ATR spectra for BC5B Bot sediments strongly supports the detection of localized authigenic carbonate formation at this sampling site.

This section provided a focused discussion regarding qualitative and semi-quantitative analyses of calcite-dolomite compositions in box core sediment collections. The calculation of negative mass % values throughout this section underscores a shortcoming in this data evaluation procedure, which is discussed further in **Section 5.5.2.5**. However, the most significant finding in this chapter stems from the diversity of carbonate minerals and the spectral deviations observed from BC1, BC5, and BC12 samples, which provided the initial insight for the capability to detect authigenic carbonate formation with IR-ATR spectroscopy. Additional analyses of nodule samples and coccoliths are discussed in **Chapter 6**, which focuses on the detection of authigenic carbonate via qualitative assessment of unexpected characteristics and changes in the ν_3 carbonate absorption signature.

5.5.2.3 MC118 Gravity Core Sediments (October 2005 Cruise)

IR-ATR spectroscopic analysis of MC118 sediments collected from gravity cores revealed several interesting results (see **Figure 5-15** for locations). **Figure 5-17** includes representative IR-ATR spectra focused on the ν_4 region for each of the investigated sediment samples.

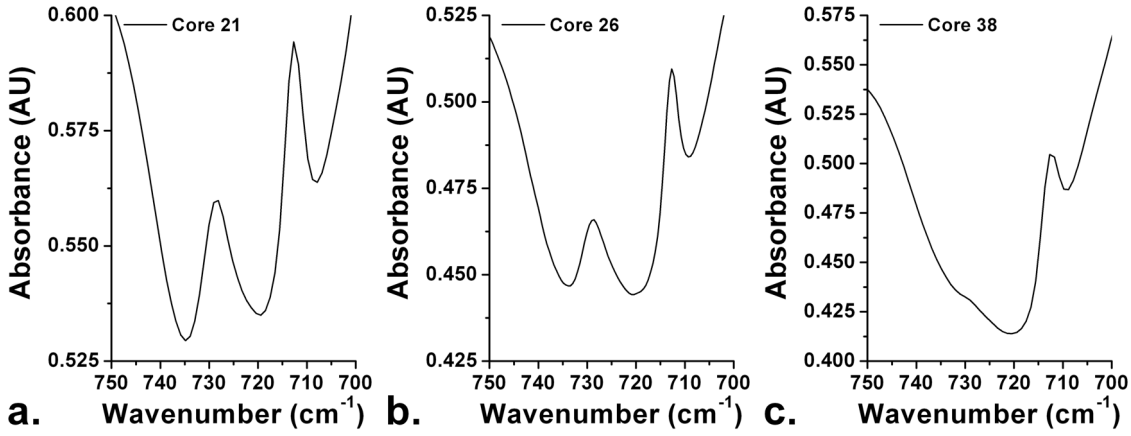

Figure 5-17: Representative IR-ATR spectra for sediments from gravity cores 21, 26, and 38. Strong dolomite signatures are observed near 730 cm^{-1} in core 21 and core 26 sediments. While not clearly evident, a minor hump may indicate the presence of dolomite in core 38.

Gravity core sediment samples examined in this study were collected further below the water-sediment interface than those evaluated from box core collections. In addition, the sediment samples from core 21 and core 26 were accompanied by authigenic carbonate nodule formations. Analysis of the carbonate mass composition in cores 21 and 26 indicate that approx. 50% of the carbonate mass fraction is comprised of dolomite with no quantifiable amount in core 38 sediments (see full data tables in **Appendix A-5**). The detection of strong dolomite signatures in core 21 and 26 sediments coupled with presence of authigenic nodules is strongly indicative to the detection of authigenic carbonate within the very fine sediment fractions. The high dolomite composition and sediment recovery depths suggest that dolomite has either accumulated from prolonged periods of primary precipitation and/or diagenetic conversion of calcite by dolomitization. Detailed isotopic, petrographic, and porewater analyses are necessary to better assess the genesis/diagenesis of dolomite from these particular coring locations. The slight hump

near 730 cm^{-1} in the IR-ATR spectrum of core 38 sediments may indicate minor dolomite composition; however, calcite was identified as the primary spectral contributor further indicated by visual inspection of the ν_3 region. Additional consideration to these samples is provided in **Chapter 6**.

5.5.2.4 Sediments from Piston Core MD02-2570

Access to piston core sediments collected from site MD02-2570 in Mississippi Canyon provided an excellent opportunity to better assess the potential application for rapid depth profiling of sediments with IR-ATR spectroscopy. Overall, the carbonate absorption features in the IR-ATR spectra from sediment samples in this piston core resembled those obtained for sediments from gravity cores 21 and 26 from MC118 (see **Figure 5-17 (a.)** and **(b.)**). All analyzed sediments from 1 mbsf to approx. 30 mbsf (sample designation as 27+m) are characterized by strong dolomite and calcite signatures without detection of additional carbonate minerals. **Figure 5-18** summarizes the semi-quantitative relative % contributions from dolomite and calcite to the total carbonate mass fraction with respect to the depth of each sediment sample.

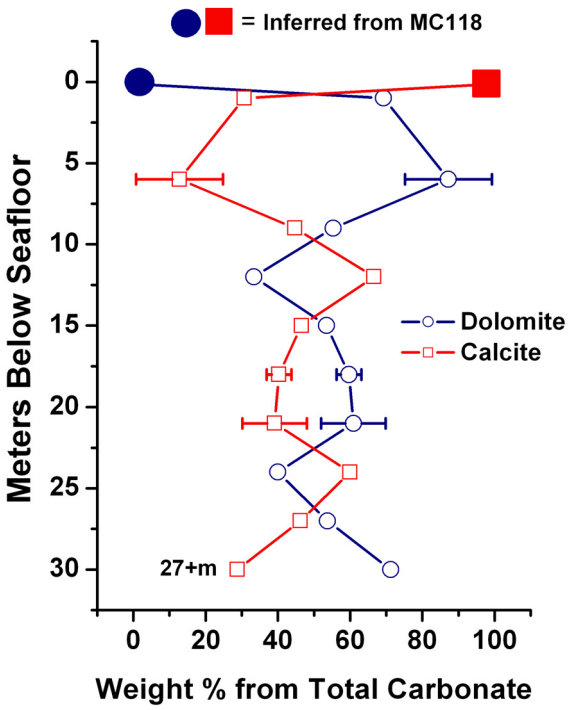

Figure 5-18: Semi-quantitative assessments from IR-ATR spectra for the mass % of dolomite and calcite in the total carbonate fraction of piston core sediments collected from MD02-2570. For each sediment depth, the calcite and dolomite mass % are plotted with the sum equal to 100% of the carbonate fraction. Error bars for 6, 18, and 21 mbsf samples are twice the SD from triplicate evaluation. Lines are present to assist visualization.

A wide range of calcite-dolomite mass fractions from the MD02-2570 piston core sediments is clearly evident in **Figure 5-18**. The dolomite mass % in the overall carbonate composition ranged from approx. 30 to 90% (see **Appendix A-5**). The greatest variability was observed within the first 12 m. The shallowest sediments obtained from this core were from 1 mbsf; therefore, the dolomite composition for surficial sediments (< 15 cmbsf) was designated as 100% calcite based on the most common results obtained from box core sediments at MC118. These sediments were collected around a gas hydrate location in the Mississippi Canyon region (not at MC118); therefore, it is hypothesized that dolomite could be present within surficial sediments at the MD02-2570 site. To gauge the analytical reproducibility, sediments from 6, 18, and 21 mbsf were analyzed in triplicate resulting in standard deviations < 6%. This range was not beyond the expectation for heterogeneous natural sediments. The most significant findings from these

experiments are the extent of variability in calcite-dolomite compositions and the consistently high dolomite mass fractions. Although IR-ATR analysis is not expected to facilitate direct elucidation of the specific processes of dolomite formation, the detection and depth profiling of changes in dolomite composition supports the practical application of MIR chemical sensors for assisting the characterization of authigenic/diagenetic dolomites in marine sediments.

5.5.2.5 Advantages, Limitations, and Potential of Quantitative Evaluations

The primary objective for characterizing the calcite-dolomite compositions with IR-ATR in this thesis was to establish a first semi-quantitative approximation of the relative compositional variability throughout sediment samples with particular emphasis on the MC118 hydrate site. However, some limitations on the quantitative accuracy for analyzing calcite-dolomite compositions were found despite the quality and robustness of Prop. PA ratio calibrations, which are addressed in this section.

Advantages of Ratiometric Calibration:

In **Section 5.4.2.2**, the clumping and delamination of samples from the waveguide surface were correlated to the presence of crude oil. However, sediment delamination was observed upon drying of essentially all native sediment samples, albeit at varying degrees. Clay minerals have a high water sorption capacity; thus, clumping and surface detachment is primarily attributed to the contraction of clay mineral moieties upon drying, which appears amplified in samples containing crude oils.[80] Second, sediment samples were evaluated over a period of approx. 11 months for this thesis. The potential sample-to-sample variance in absolute intensity fluctuations due to sample delamination and instrumental drift could lead to obscure evaluation results for quantitative evaluations based upon absolute intensities without correction for instrumental drift and the effective sampling pathlength. However, assuming that the investigated sediment samples are somewhat homogeneous, absorption intensity fluctuations resulting from sample delamination and/or instrumental drift should proportionally affect the absorbance of all components. Thus, a ratiometric evaluation method should provide consistent sample-to-sample results regardless of

variance in the effective sample-waveguide contact and/or instrumental drifts. In this work, consistent mass % values for calcite and dolomite relative to the total sample carbonate composition were obtained for all samples irrespective to the period each sample was evaluated despite inherent variance in sample-waveguide contact (see results in **Appendix A-5**). Hence, any observed variability is mostly attributed to compositional variance and sample inhomogeneities in the marine sediments. Consistent quantitative values were obtained without manipulating the sediment samples, which further demonstrates the robust nature of ratiometric data evaluation.

Current Limitations and Restrictions:

There are two primary factors that must be further addressed regarding the quantitative analysis of carbonate minerals in marine sediment samples for improving the accuracy of data evaluation methods described in this thesis.

The first consideration to ensure consistent and accurate quantitative analysis of carbonates in marine sediments with IR-ATR spectroscopy is by controlling the mean particle size (PS). It has been established in the literature that the sample PS characteristics directly affects the analytical accuracy of IR techniques when evaluating carbonate minerals in natural samples (see discussion in **Section 5.1.3.2**). The key particle size limit reported to ensure a high confidence in analytical accuracy is < 2 μm. In transmission-absorption measurements, a PS well below the wavelength of radiation is necessary to minimize scattering affects in non-absorbing regions. For ATR methods, the scattering of light in non-absorbing regions is essentially absent regardless of PS; therefore, uniform PS is required to ensure dense and uniform particle packing within the evanescent field representative of the compositional mass fractions within a sample.[59] Thus, it is required to maintain constant PS characteristics across both the calibration standards and natural samples. Without homogenizing the investigated sample matrix, quantitative results can be systematically biased against the overall sample composition. In this work, the quantitative analysis of calcite-dolomite content in marine sediments focused on the evaluation of non-manipulated sediments following an *in situ* drying process, which is preferable for rapid, semi-quantitative on-ship

sediment analysis. Without previously drying and homogenizing the sample by grinding, the quantitative results presented in this work are biased against the presence of carbonate minerals from larger particulates (i.e., foraminiferal tests, pelletoids, mollusk shells etc.) due to a size mismatch with the evanescent field (see **Section 5.1.2.3**). As a result, the reported quantitative values are predominately reflective of finer grained sediments, which limit quantitative accuracy in calcite and dolomite composition assessments relative to the bulk sediment matrix.

The second factor currently limiting the quantitative accuracy of carbonate minerals in marine sediments with IR-ATR spectroscopy is the impact of clay, quartz, and Mg-calcite absorption features. The overlapping nature of these bands with the calcite and dolomite ν_4 vibrational modes reduces the accuracy for a straightforward calibration established for only the two components of interest. Hence, it is necessary to further address the absorption influences from these interfering matrix components to migrate from semi-quantitative to quantitative results characterizing multiple carbonate mineral compositions in marine sediments. This should be facilitated in the future with the establishment of multivariate data evaluation routines considering the spectral influences from all major sediment matrix constituents.

Potential of the Method:

Due to the current limitations, the results presented in this thesis provide a first semi-quantitative measure for characterizing the calcite and dolomite compositions in complex marine sediment matrices utilizing IR-ATR spectroscopy. With the variety of samples collected from the GoM, this method has been confirmed as a useful strategy for evaluating the wide range and variability of carbonate minerals encountered in complex oceanic gas hydrate ecosystems, which is an imperative initial step towards improving the quantitative capabilities of this methodology in the future. In addition, **Chapter 6** will focus on the practical application of IR-ATR spectroscopy as a qualitative characterization tool with immediate significance for detecting and characterizing the occurrence and distribution of authigenic carbonates driven by chemosynthetic communities associated with cold hydrocarbon seeps in the GoM.

5.6 Conclusions

This chapter has covered the fundamental application of IR-ATR spectroscopy for characterizing carbonate minerals with particular focus on the diversity and variability encountered in gas hydrate ecosystems within the GoM. The first task addressed was the establishment of an IR-ATR spectral database for 10 of the most common anhydrous carbonate minerals. This database is useful for assisting the identification of carbonate minerals within complex matrices such as marine sediments. Although a reference specimen of a homogenous Mg-calcite was not acquired for compilation of the spectral database, sufficient evidence was obtained from the literature to confirm the spectroscopic detection of Mg-calcite in BC12 sediments.[39] Furthermore, the IR-ATR carbonate spectral database enabled a functional derivation, following the work of Bottcher et al., enabling the evaluation of Mg^{2+} compositions of homogenous Mg-calcite samples.[39]

The second major application of IR-ATR spectroscopy for assessing carbonate minerals in marine sediments was the qualitative evaluation of sediments in their 'native' and dried states. As demonstrated throughout **Section 5.4**, an abundance of information can be quickly obtained via the qualitative assessment of wet and dry samples. This was particularly useful for evaluating the diversity and variability of carbonate mineralogy surrounding the MC118 system and aiding the elucidation of indicators for the spectroscopic detection of authigenic carbonates, which is the focus of **Chapter 6**. The ability to contextualize IR-ATR spectroscopic data from MC118 throughout this chapter was significantly enhanced via several key factors: (1) accurate mapping of sediment collection locations with respect to the site geography, (2) accumulation of context clues such as 'gassy' or oil stained sediments and the recovery of shells and/or authigenic carbonate nodules, and (3) previous characterization studies of the MC118 hydrate site from GOMGHRC members (i.e., isotopic compositions of authigenic carbonate nodules[23]) and extensive literature archives addressing the complexity of gas hydrate ecosystems.

The third focus of this chapter was establishing the semi-quantitative analysis of calcite-dolomite compositions relative to the overall carbonate content in sediment samples. Although in **Section**

5.5.2.1 it was confirmed that a high quality analytical calibration can be generated to evaluate calcite and dolomite composition with IR-ATR techniques comparable to other IR techniques in the literature, there were several factors limiting highly accurate quantitative assessments in this thesis (described in **Section 5.5.2.5**). However, based on the findings in this thesis, two primary factors were identified that should facilitate improvement to the quantitative characterization of carbonate minerals in marine sediments from complex hydrate ecosystems with IR-ATR techniques in the future. In addition, the obtained semi-quantitative results generated during these studies provide a first approximation as to the characteristic variability of dolomite compositions in marine sediments surrounding the MC118 gas hydrate site, thus providing an initial guideline for improving the quantitative capabilities to address environmentally relevant compositional variations. Furthermore, the presented results allude to potential pitfalls for the more generic application of quantitative IR methods for evaluating carbonate minerals in natural samples without specifically considering the potential interferences of major sediment components surrounding the sampling environment.

An additional key finding from these initial sediment screening studies was the limited spectral sensitivity to hydrocarbons despite the wide distribution and frequent visual observation of crude oil surrounding the MC118 hydrate site. The enhanced presence of biodegraded crude in sediments from BC9 and BC12 was accentuated by identifiable C-H stretch absorption features in the IR-ATR spectra. However, visual observation coupled with the lack of IR-ATR detection of crude signatures in sediments from BC2, BC8, and BC11 displays the resilience of this measurement technique to potential interferences from natural organic matter in the sediments surrounding MC118. The IR-ATR sediment analyses presented in this chapter additionally facilitated an initial assessment of potential spectral interferants from the MC118 site with respect to IR gas hydrate monitoring strategies described in **Chapter 4**. The findings from such evaluations (discussed in **Section 4.3.4**) support the future application of IR techniques to monitor gas hydrate growth dynamics in sediment matrices.

Overall, the particular significance to the studies described in this chapter was establishing the initial connection between IR-ATR spectral signatures and the presence of authigenic carbonates associated with chemosynthetic communities that thrive on energy from hydrocarbon seepage emanating through fault conduits at the MC118 site. Collectively, chemosynthetic activity and gas hydrates play an important role in the global cycling and sequestration of carbon, carbonate, and greenhouse gases. As IR-ATR spectroscopy has been demonstrated as a useful strategy for characterizing carbonate minerals in marine sediments and gas hydrate growth dynamics, the realization of deep-sea MIR chemical sensors is anticipated to facilitate improved access for assessing and characterizing the significance of 'small' scale distributions and dynamics of localized authigenic carbonate formation and gas hydrates within complex oceanic gas hydrate ecosystems. **Chapter 6** will address the application of IR-ATR spectroscopy for characterizing the origins and variability of carbonate minerals within context of oceanic gas hydrate ecosystems and the GoM.

5.7 Outlook

As discussions of IR-ATR spectroscopy and carbonate mineral analysis will continue in **Chapter 6**, only a brief outlook is provided herein. From this chapter, it is of paramount importance to define the analytical objectives for the application of IR-ATR spectroscopy when evaluating carbonate minerals in marine sediments. Much information can clearly be obtained simply through qualitative application with many avenues for practical application. However, the quantitative evaluation of carbonate minerals in marine sediments requires additional research to facilitate improved accuracy of the described IR-ATR analysis. To attain improved accuracy, it is pertinent to generate a robust multivariate calibration, while ensuring conservation of PS characteristics between calibration standards and sediment samples. The multivariate calibration should focus on the accountability for spectral influences from major sediment components, such as quartz and clay minerals. More thorough characterization of major sediment components from

various geographic regions coupled with advanced data evaluation routines is anticipated to facilitate accurate quantitative assessment of carbonate minerals within diverse marine settings and highly variable sediment matrices.

5.8 References

1. F. A. Miller and C. H. Wilkins, *Infrared Spectra and Characteristic Frequencies of Inorganic Ions*, Analytical Chemistry **24**, 1253 (1952).

2. J. M. Hunt, M. P. Wisherd, and L. C. Bonham, *Infrared Absorption Spectra of Minerals and other Inorganic Compounds*, Analytical Chemistry **22**, 1478 (1950).

3. H. H. Adler, E. E. Bray, N. P. Stevens, J. M. Hunt, W. D. Keller, E. E. Pickett, and P. F. Kerr, in Reference Clay Minerals; American Petroleum Institute Research Project 49. Preliminary Report No. 8, Columbia University, New York, 1951, p. 7.

4. R. Chester and H. Elderfield, *The Infra-red Determination of Total Carbonate in Marine Carbonate Sediments*, Chemical Geology **1**, 277 (1966).

5. R. Chester and H. Elderfield, *The Application of Infra-red Absorption Spectroscopy to Carbonate Mineralogy*, Sedimentology **9**, 5 (1967).

6. E. Loste, R. M. Wilson, R. Seshadri, and F. C. Meldrum, *The Role of Magnesium in Stabilising Amorphous Calcium Carbonate and Controlling Calcite Morphologies*, Journal of Crystal Growth **254**, 206 (2003).

7. Y. Dauphin, *Infrared Spectra and Elemental Composition in Recent Carbonate Skeletons: Relationships between the n2 Band Wavenumber and Sr and Mg Concentrations*, Applied Spectroscopy **51**, 253 (1997).

8. R. V. Gaines, H. K. Skinner, E. E. Foord, B. Mason, and A. Rosenzwieg, *Dana's New Mineralogy: The System of Mineralogy of James Dwight Dana and Edward Salisbury Dana*, (Wiley, New York, 1997).

9. D. Barthelmy, *Mineralogy Database*, http://www.webmineral.com/dana/V-14.shtml (July 2007).

10. J. D. Milliman, *Marine Carbonates*, (Springer, New York, 1974).

11. H. H. Roberts and P. Aharon, *Hydrocarbon-Derived Carbonate Buildups of the Northern Gulf of Mexico Continental slope: A Review of Submersible Investigations*, Geo-Marine Letters **14**, 135 (1994).

12. T. H. Naehr, P. Eichhubl, V. J. Orphan, M. Hovland, C. K. Paull, W. Ussler, T. D. Lorenson, and H. G. Greene, *Authigenic Carbonate Formation at Hydrocarbon Seeps in Continental Margin Sediments: A Comparative Study*, Deep-Sea Research, Part II: Topical Studies in Oceanography **54**, 1268 (2007).

13. R. Sassen, H. H. Roberts, P. Aharon, J. Larkin, and E. W. Chinn, *Chemosynthetic Bacterial Mats at Cold Hydrocarbon Seeps, Gulf of Mexico Continental Slope*, Organic Geochemistry **20**, 77 (1993).

14. M. J. Formolo, T. W. Lyons, C. Zhang, C. Kelley, R. Sassen, J. Horita, and D. R. Cole, *Quantifying Carbon Sources in the Formation of Authigenic Carbonates at Gas Hydrate Sites in the Gulf of Mexico*, Chemical Geology **205**, 253 (2004).

15. R. Sassen, H. H. Roberts, R. Carney, A. V. Milkov, D. A. DeFreitas, B. Lanoil, and C. Zhang, *Free Hydrocarbon Gas, Gas hydrate, and Authigenic Minerals in Chemosynthetic Communities of the Northern Gulf of Mexico Continental Slope: Relation to Microbial Processes*, Chemical Geology **205**, 195 (2004).

16. D. R. Hutchinson, C. D. Ruppel, H. S. Roberts, R. S. Carney, and M. A. Smith, in Gulf of Mexico - Its Origin (History, Archaeology, and Geology), Vol. 1 (C. W. Holmes, ed.), Texas A&M University Press, College Station, In Press.

17. R. Sassen, S. Joye, S. T. Sweet, D. A. DeFreitas, A. V. Milkov, and I. R. MacDonald, *Thermogenic Gas Hydrates and Hydrocarbon Gases in Complex Chemosynthetic Communities, Gulf of Mexico Continental Slope*, Organic Geochemistry **30**, 485 (1999).

18. P. Aharon and B. Fu, *Microbial Sulfate Reduction Rates and Sulfur and Oxygen Isotope Fractionations at Oil and Gas seeps in Deepwater Gulf of Mexico*, Geochimica et Cosmochimica Acta **64**, 233 (2000).

19. C. L. Zhang and B. Lanoil, *Geomicrobiology and Biogeochemistry of Gas Hydrates and Cold Seeps*, Chemical Geology **205**, 187 (2004).

20. J. Peckmann and V. Thiel, *Carbon Cycling at Ancient Methane-Seeps*, Chemical Geology **205**, 443 (2004).

21. S. B. Joye, A. Boetius, B. N. Orcutt, J. P. Montoya, H. N. Schulz, M. J. Erickson, and S. K. Lugo, *The Anaerobic Oxidation of Methane and Sulfate Reduction in Sediments from Gulf of Mexico Cold Seeps*, Chemical Geology **205**, 219 (2004).

22. B. N. Orcutt, A. Boetius, S. K. Lugo, I. R. MacDonald, V. A. Samarkin, and S. B. Joye, *Life at the Edge of Methane Ice: Microbial Cycling of Carbon and Sulfur in Gulf of Mexico Gas Hydrates*, Chemical Geology **205**, 239 (2004).

23. R. Sassen, H. H. Roberts, W. Jung, C. B. Lutken, D. A. DeFreitas, S. T. Sweet, and N. L. Guinasso Jr., *The Mississippi Canyon 118 Gas Hydrate Site: A Complex Natural System*, Proceedings of the Offshore Technology Conference **Paper Number: 18132**, (2006).

24. R. Sassen, S. T. Sweet, A. V. Milkov, D. A. DeFreitas, and M. C. Kennicutt, II, *Thermogenic Vent gas and Gas Hydrate in the Gulf of Mexico Slope: Is Gas Hydrate Decomposition Significant?*, Geology **29**, 107 (2001).

25. K. A. Kvenvolden, *Methane Hydrate in the Global Organic Carbon Cycle*, Terra Nova **14**, 302 (2002).

26. A. Boetius and E. Suess, *Hydrate Ridge: A Natural Laboratory for the Study of Microbial Life Fueled by Methane from Near-Surface Gas Hydrates*, Chemical Geology **205**, 291 (2004).

27. K. A. Kvenvolden and B. W. Rogers, *Gaia's Breath-Global Methane Exhalations*, Marine and Petroleum Geology **22**, 579 (2005).

28. C. Pierre and J.-M. Rouchy, *Isotopic Compositions of Diagenetic Dolomites in the Tortonian Marls of the Western Mediterranean Margins: Evidence of Past Gas Hydrate Formation and Dissociation*, Chemical Geology **205**, 469 (2004).

29. W. L. Balsam and J. P. Beeson, *Sea-Floor Sediment Distribution in the Gulf of Mexico*, Deep-Sea Research, Part I: Oceanographic Research Papers **50**, 1421 (2003).

30. R. Botz, E. Faber, M. J. Whiticar, and J. M. Brooks, *Authigenic Carbonates in Sediments from the Gulf of Mexico*, Earth and Planetary Science Letters **88**, 263 (1988).

31. R. A. Berner, *Role of Magnesium in the Crystal Growth of Calcite and Aragonite from Sea Water*, Geochimica et Cosmochimica Acta **39**, 489 (1975).

32. E. Busenberg and L. N. Plummer, *Thermodynamics of Magnesian Calcite Solid-Solutions at 25 DegC and 1 Atm Total Pressure*, Geochimica et Cosmochimica Acta **53**, 1189 (1989).

33. H. G. Machel, *Concepts and Models of Dolomitization: A Critical Reappraisal*, Geological Society Special Publication **235**, 7 (2004).

34. R. W. Pierce and G. F. Hart, *Phytoplankton of the Gulf of Mexico: Taxonomy of Calcareous Nannoplankton*, (LSU Press, Baton Rouge, 1979).

35. A. Winter and W. G. Siesser, eds., *Coccolithophores*, (Cambridge Universtiy Press, Cambridge, 1994).

36. H. R. Thierstein and J. R. Young, eds., *Coccolithophores - From Molecular Processes to Global Impact*, (Springer, Berlin, 2004).

37. J. R. Young, M. Geisen, L. Cros, A. Kleijne, C. Sprengel, I. Probert, and J. Ostergaard, *A Guide to Extant Coccolithophore Taxonomy*, Journal of Nannoplankton Research **Special Issue**, 125 (2003).

38. F. Lippman, *Sedimentary Carbonate Minerals*, (Springer, New York, 1973).

39. M. E. Bottcher, P.-L. Gehlken, and D. F. Steele, *Characterization of Inorganic and Biogenic Magnesian Calcites by Fourier Transform Infrared Spectroscopy*, Solid State Ionics **101-103**, 1379 (1997).

40. R. Sassen, *Personal Communication*, (2007).

41. J. M. Hunt and D. S. Turner, *Determination of Mineral Constituents of Rocks by Infrared Spectroscopy*, Analytical Chemistry **25**, 1169 (1953).

42. O. Gomez-Martinez, D. H. Aguilar, P. Quintana, J. J. Alvarado-Gil, D. Aldana, L. L. Diaz-Flores, and M. Yanez-Limon, *Infrared Spectroscopy Characterization of Marine Shells*, Materials Research Society Symposium Proceedings **711**, 325 (2002).

43. C. K. Huang and P. F. Kerr, *Infrared Study of the Carbonate Minerals*, American Mineralogist **45**, 311 (1960).

44. E. L. Compere, Jr. and J. M. Bates, *Determination of Calcite/Aragonite Ratios in Mollusc Shells by Infrared Spectra*, Limnology and Oceanography **18**, 326 (1973).

45. A. G. Xyla and P. G. Koutsoukos, *Quantitative Analysis of Calcium Carbonate Polymorphs by Infrared Spectroscopy*, Journal of the Chemical Society, Faraday Transactions 1: Physical Chemistry in Condensed Phases **85**, 3165 (1989).

46. M. Mecozzi, E. Pietrantonio, M. Amici, and G. Romanelli, *Determination of Carbonate in Marine Solid Samples by FTIR-ATR Spectroscopy*, Analyst (Cambridge, United Kingdom) **126**, 144 (2001).

47. M. Donoghue, P. H. Hepburn, and S. D. Ross, *Factors Affecting the Infrared Spectra of Planar Anions with D3h Symmetry. V. Origin of the Splitting of the Out-of-plane Bending Mode in Carbonates and Nitrates*, Spectrochimica Acta, Part A: Molecular and Biomolecular Spectroscopy **27**, 1065 (1971).

48. H. Elderfield and R. Chester, *Effect of Periodicity on the Infrared Absorption v2 Frequency of Anhydrous Normal Carbonate Minerals*, American Mineralogist **56**, 1600 (1971).

49. H. H. Adler and P. F. Kerr, *Infrared Spectra, Symmetry, and Structure Relations of Some Carbonate Minerals*, American Mineralogist **48**, 839 (1963).

50. H. H. Adler and P. F. Kerr, *Infrared Absorption Frequency Trends for Anhydrous Normal Carbonates*, American Mineralogist **48**, 124 (1963).

51. S. H. Lee, Z. U. Bae, K. W. Kim, D. K. Yang, and S. S. Choi, *Determination of Calcium Carbonate in Limestone by Attenuated Total Reflectance Fourier Transform Infrared Spectrometry*, Analytical Sciences **13**, 93 (1997).

52. T. D. Herbet, B. A. Tom, and C. Burnett, *Precise Major Component Determinations in Deep-Sea Sediments using Fourier Transform Infrared Spectroscopy*, Geochimica et Cosmochimica Acta **56**, 1759 (1992).

53. M. A. Legodi, D. De Waal, J. H. Potgieter, and S. S. Potgieter, *Rapid Determination of CaCO3 in Mixtures utilising FT-IR Spectroscopy*, Minerals Engineering **14**, 1107 (2001).

54. F. B. Reig, J. V. G. Adelantado, and M. C. M. Moya Moreno, *FTIR Quantitative Analysis of Calcium Carbonate (Calcite) and Silica (Quartz) Mixtures using the Constant Ratio Method. Application to Geological Samples*, Talanta **58**, 811 (2002).

55. N. V. Vagenas, A. Gatsouli, and C. G. Kontoyannis, *Quantitative Analysis of Synthetic Calcium Carbonate Polymorphs using FT-IR Spectroscopy*, Talanta **59**, 831 (2003).

56. M. Tatzber, M. Stemmer, H. Spiegel, C. Katzlberger, G. Haberhauer, and M. H. Gerzabek, *An Alternative Method to Measure Carbonate in Soils by FT-IR Spectroscopy*, Environmental Chemistry Letters **5**, 9 (2007).

57. E. Gavish and G. M. Friedman, *Quantitative Analysis of Calcite and Mg-calcite by X-ray Diffraction. Effect of Grinding on Peak Height and Peak Area*, Sedimentology **20**, 437 (1973).

58. J. D. Milliman and B. D. Bornhold, *Peak Height versus Peak Intensity Analysis of X-ray Diffraction Data*, Sedimentology **20**, 445 (1973).

59. N. J. Harrick, *Internal Reflection Spectroscopy*, (Harrick, Ossining, N.Y., 1979).

60. Y. Dauphin, *Infrared Spectra and Elemental Composition in Recent Biogenic Calcites: Relationships Between the n4 Band Wavelength and Sr and Mg Concentrations*, Applied Spectroscopy **53**, 184 (1999).

61. K. V. Narasimhulu and J. Lakshmana Rao, *EPR and IR Spectral Studies of the Sea Water Mussel Mytilus conradinus Shells*, Spectrochimica Acta, Part A: Molecular and Biomolecular Spectroscopy **56A**, 1345 (2000).

62. Y. Politi, T. Arad, E. Klein, S. Weiner, and L. Addadi, *Sea Urchin Spine Calcite Forms via a Transient Amorphous Calcium Carbonate Phase*, Science (Washington, DC, United States) **306**, 1161 (2004).

63. W. D. Bischoff, S. K. Sharma, and F. T. Mackenzie, *Carbonate Ion Disorder in Synthetic and Biogenic Magnesian Calcites: A Raman Spectral Study*, American Mineralogist **70**, 581 (1985).

64. J. Paquette and R. J. Reeder, *Single-crystal X-ray Structure Refinements of Two Biogenic Magnesian Calcite Crystals*, American Mineralogist **75**, 1151 (1990).

65. L. Addadi, S. Raz, and S. Weiner, *Taking Advantage of Disorder: Amorphous Calcium Carbonate and Its Roles in Biomineralization*, Advanced Materials (Weinheim, Germany) **15**, 959 (2003).

66. E. Loste and F. C. Meldrum, *Control of Calcium Carbonate Morphology by Transformation of an Amorphous Precursor in a Constrained Volume*, Chemical Communications (Cambridge, United Kingdom)901 (2001).

67. S. Raz, S. Weiner, and L. Addadi, *Formation of High-magnesian Calcites via an Amorphous Precursor Phase. Possible Biological Implications*, Advanced Materials (Weinheim, Germany) **12**, 38 (2000).

68. N. Spanos and P. G. Koutsoukos, *Kinetics of Precipitation of Calcium Carbonate in Alkaline pH at Constant Supersaturation. Spontaneous and Seeded Growth*, Journal of Physical Chemistry B **102**, 6679 (1998).

69. D. Kralj, J. Kontrec, L. Brecevic, G. Falini, and V. Noethig-Laslo, *Effect of Inorganic Anions on the Morphology and Structure of Magnesium Calcite*, Chemistry--A European Journal **10**, 1647 (2004).

70. J. Kontrec, D. Kralj, L. Brecevic, G. Falini, S. Fermani, V. Noethig-Laslo, and K. Mirosavljevic, *Incorporation of Inorganic Anions in Calcite*, European Journal of Inorganic Chemistry4579 (2004).

71. P. K. Ajikumar, L. G. Wong, G. Subramanyam, R. Lakshminarayanan, and S. Valiyaveettil, *Synthesis and Characterization of Monodispersed Spheres of Amorphous Calcium Carbonate and Calcite Spherules*, Crystal Growth & Design **5**, 1129 (2005).

72. J. Louisfert and T. Pobeguin, *Differentiation of Calcium Carbonates by Means of Infrared Absorption Spectra*, Compt. rend. **235**, 287 (1952).

73. N. Dupuy, M. Meurens, B. Sombret, P. Legrand, and J. P. Huvenne, *Multivariate Determination of Sugar Powders by Attenuated Total Reflectance Infrared Spectroscopy*, Applied Spectroscopy **47**, 452 (1993).

74. R. Chester and H. Elderfield, *Application of IR Absorption Spectroscopy to Carbonate Mineralogy*, Sedimentology **9**, 5 (1967).

75. J. R. Woolsey, P. Higley, L. Lapham, J. Chanton, C. Lutken, K. Sleeper, S. Sharpe, A. Durbin, and L. Macelloni, *Operations Report of Cruise GOM3-05-MC118: Installation, Calibration, Testing and Use of the LinkQuest Ultra-Short Baseline System, CTD Survey and Coring at the Mound, Mississippi Canyon 118*, http://www.olemiss.edu/depts/mmri/programs/GOM3-05-MC118.pdf (2005).

76. B. P. Kelleher, A. J. Simpson, R. E. Rogers, J. Dearman, and W. L. Kingery, *Effects of Natural Organic Matter from Sediments on the Growth of Marine Gas Hydrates*, Marine Chemistry **103**, 237 (2007).

77. C. K. Paull, W. Ussler, III, T. Lorenson, W. Winters, and J. Dougherty, *Geochemical Constraints on the Distribution of Natural Gas Hydrates in the Gulf of Mexico*, Geo-Marine Letters **25**, 273 (2005).

78. D. Bougeard, K. S. Smirnov, and E. Geidel, *Vibrational Spectra and Structure of Kaolinite: A Computer Simulation Study*, Journal of Physical Chemistry B **104**, 9210 (2000).

79. J. Madejova, *FTIR Techniques in Clay Mineral Studies*, Vibrational Spectroscopy **31**, 1 (2003).

80. K. S. Katti and D. R. Katti, *Relationship of Swelling and Swelling Pressure on Silica-Water Interactions in Montmorillonite*, Langmuir **22**, 532 (2006).

CHAPTER 6

SPECTROSCOPIC DETECTION OF AUTHIGENIC CARBONATES IN MARINE SEDIMENTS CONTAINTING COCCOLITH CALCITE

This chapter extends upon the experimental applications of IR-ATR spectroscopy for characterizing carbonate minerals in seafloor sediments previously discussed in **Chapter 5**. However, the focus shifts towards the diagnostic identification of chemosynthetically driven authigenic carbonate precipitation within the very fine sediment fractions of surficial marine sediments surrounding gas hydrate ecosystems. To facilitate this objective, a variety of qualitative investigations concerning the origin of spectral variability among ν_3 IR vibrations of carbonate minerals in the IR-ATR spectra of sediments are presented. Topics discussed include evaluation of recovered authigenic carbonate nodules and spectral characterization of coccoliths produced from laboratory cultures of coccolithophores. This chapter demonstrates the capability to identify chemosynthetically driven authigenic carbonate precipitation through the disruption of peculiar carbonate absorption features in marine sediments traceable to coccolith accumulations originating from the photic zone over 800 m above the seafloor. Furthermore, concluding remarks summarizing the breadth of IR-ATR spectroscopic analyses of samples collected from the MC118 gas hydrate ecosystem are provided.

6.1 Motivation

In **Chapter 4**, the initial motivation for spectroscopic investigations of marine sediments was to facilitate a feasibility assessment for extending evanescent field sensing strategies for hydrate monitoring into oceanic environments. During the first sediment characterization experiments, striking contrasts were observed in the ν_3 carbonate profiles of IR spectra collected for MC118 sediments. This simple observation stimulated a variety of studies to further understand spectral data and the application of IR-ATR spectroscopic techniques for addressing the relationships,

consequences, and connections between carbonate mineralogy within the context and complexity of oceanic gas hydrate ecosystems, particularly in the Gulf of Mexico. IR studies described in **Chapter 5** focused on the initial assessment of inter- and intra-site characteristics of carbonate minerals in the described sediment collections. During sediment studies and concurrent spectral analysis of recovered authigenic carbonate nodule samples (discussed in this chapter), a correlation was observed for spectral broadening of ν_3 carbonate signatures with the occurrence of chemosynthetically driven authigenic carbonate formations. This hypothesis was further supported through the association of spectral similarities of sediments in close proximity to the recovery of authigenic carbonate nodules and the combination of context clues suggestive of chemosynthetic activities intimately connected to authigenic carbonate precipitation.

As discussed in **Chapter 5**, the combination of gas hydrate formation and the influence of associated chemosynthetic communities play a significant role in the global cycling and sequestration of greenhouse gasses in extreme oceanic environments; in effect buffering the migration of greenhouse gasses from oceanic sources into the atmosphere. Hence, the potential capability for utilizing IR-ATR spectroscopy as a tool for characterizing the spatial occurrence and enabling *in situ* assessment to the significance of authigenic carbonate precipitation within marine sediment fractions warranted further consideration. The potential value for such a tool was further accentuated with the current lack of data regarding the dynamics, distributions, and/or significance of authigenic carbonate formation and associated chemosynthetic organisms within fine sediment fractions surrounding oceanic gas hydrate systems. However, to substantiate this hypothesis, it was essential to establish a definitive explanation for the omnipresent carbonate signature observed throughout surficial sediments hypothesized to be unaffiliated with authigenic carbonate and provide a valid explanation as to the governing nature of spectral differences.

Initial evidence capable of providing an explanation for the occurrence and nature of IR carbonate signatures in sediment samples originated through the examination of scanning electron microscope (SEM) images of MC118 sediments, which revealed the presence of coccoliths,

which are highly structured biogenic carbonate particulates produced by single-celled planktonic organisms that thrive throughout many of Earth's oceans and seas (**Figure 6-1**). This realization provided the context for consideration to the regional effects of natural processes that can directly and significantly impact sediment compositions with molecular level consequences to spectral observations. Resulting, this chapter presents the experimental studies and findings that substantiate the capability for IR-ATR spectroscopy as a tool for detecting the occurrence of chemosynthetically driven authigenic carbonate precipitation within surficial sediments surrounding gas hydrate ecosystems. The findings presented in this chapter provide a significant advancement towards improved characterization and understanding of authigenic carbonate formations and associated chemosynthetic organisms within oceanic gas hydrate ecosystems.

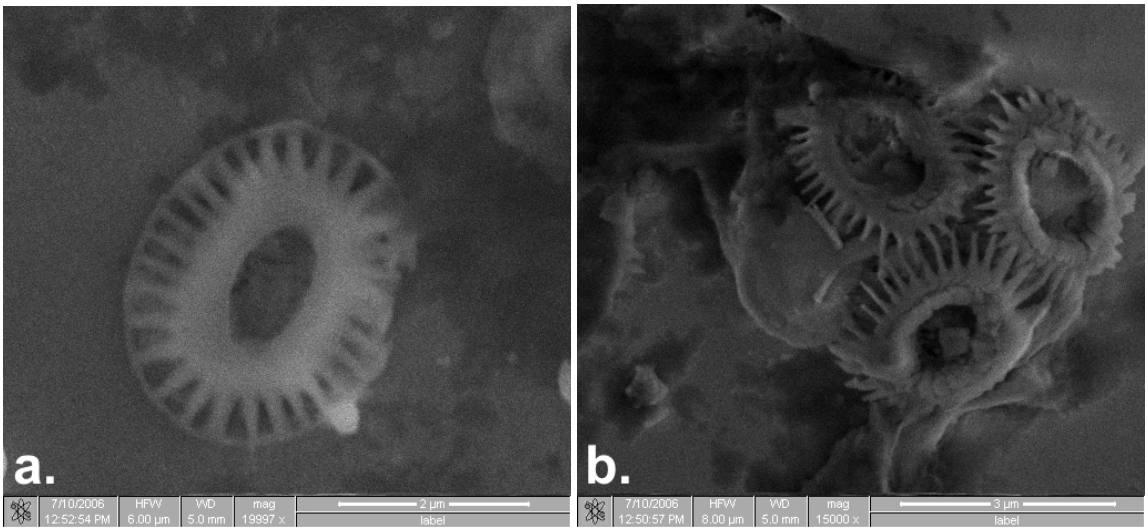

Figure 6-1: SEM images of coccoliths from MC118 gravity core 38 sediments. A small sediment portion was smeared onto a glass microscope slide and allowed to dry before collection of images with a Nova Nanolab 200 (FEI Company, Hillsboro, OR). Coccolith shield morphologies are characteristic of the coccolithophore species *Emiliania huxleyi* (*E. huxleyi*).[1-4]

6.1.1 Coccolithophores and Coccoliths

Coccolithophores are a diverse group of single-celled, photosynthetic planktonic algae with an average size between 10 to 100 µm in diameter.[2, 4, 5] Most species are covered by a coccosphere

comprised of small 2 – 20 μm sized calcite plates known as coccoliths, which are formed within the coccolith vesicle inside the cell body.[2, 4, 6] Coccolith morphologies are characteristic to individual species and commonly used for taxonomic identification.[1-4, 7] Coccolithophores are an abundant life form in the photic zone of Earth's oceans and seas; that cycle and drive globally significant fluxes of organic carbon and carbonate in marine environments through photosynthetic conversion of CO_2 into O_2 and organic carbon in addition to the generation of CO_2 and carbonate during coccolith formation.[2, 4, 8-10]

Coccolithophore cell densities typically range between several thousand to many hundreds of thousands per L of seawater.[2, 4, 7] Occasionally, algal blooms occur whereby cell densities exceeding 1,000,000 per liter of seawater have been observed, which can be visualized in satellite imagery by significant shifts to the color of ocean waters.[2, 4, 11] Coccolithophore activity and coccolith sedimentation flux have been shown to vary seasonally. A study by Ziveri et al. exemplifies the variability and magnitude of coccolith fluxes from sediment traps placed in the San Pedro Basin, Southern California Borderlands.[12] The authors reported coccolith fluxes ranging from as low as 30,000 coccoliths per m^2 per day to as high as 866,390,000 coccoliths per m^2 per day (equivalent to approx. 81 mg of carbonate accumulation per m^2 per day) between January 7 and July 26, 1988. In this thesis, the impact of coccolithophores and coccolith sedimentation on the composition of surficial marine sediments is of particular importance with the focus centered on the Gulf of Mexico region.

6.1.1.1 Coccolithophores in the Gulf of Mexico

In 1972, Hulbert and Corwin reported average coccolithophore concentrations throughout the GoM from 1,500 – 9,000 cells per L with highs between 5,000 – 20,000 cells per L from samples collected between November 1965 and December 1969.[13] A more recent and thorough investigation of coccolithophores in the GoM was documented in the doctoral work of Vita Pariente, which includes a review of previous coccolithophore water column studies in the GoM

region.[7] In general, water column coccolithophore concentrations in the GoM were found to range from 1,500 cells per L to as high as 155,000 cells per L.[7]

The work of Pariente was primarily concerned on seasonal and vertical differences in coccolithophore community structuring within the GoM between October 1990 and March 1991.[7] The standing coccolithophore crop during the study interval was generally less than 10^5 cells per L with the greatest densities found in March of 1991 (by a factor of 2 to 3) primarily from the abundance of *E. huxleyi*. Despite the diversity of coccolithophore species observed during that work, four primary species where found to dominate seasonal populations. In October, the dominant species were; *Umbellosphaera irregularis*, *Umbellosphaera tenuis*, *Florisphaera profunda*, and *E. huxleyi*. In March, *E. huxleyi* was the prevalent species in most samples; however, *F. profunda* was observed at most sampling locations, often surpassing *E. huxleyi* populations for samples collected in the nutricline. **Table 6-1** summarizes temporal observations of the most prominent coccolithophores found in the GoM water column by Pariente.[7]

Table 6-1: Coccolithophore species accounting for ≥ 50% of the population in at least one sample as reported by Pariente.[7] Percent values in parenthesis reflect the maximum observed relative abundance from all samples with respect to each individual species. Despite the single sample reference, these four species were prevalent throughout most sampling locations. Table adapted from Pariente.[7]

Abundance	**≥ 50% (max. relative abundance)**
Period	October 1990
Species	*F. profunda* (84%)
	U. irregularis (69%)
	U. tenuis (64%)
	E. huxleyi (56%)
Period	March 1991
Species	*E. huxleyi* (99%)
	F. profunda (64%)

6.1.1.2 Coccolith Distributions in Gulf of Mexico Sediments

As previously discussed in **Section 5.1.2.3**, biogenic carbonate formations from planktonic foraminifera and coccolithophores are widely distributed and dominate the carbonate composition of sediments throughout the GoM off of the continental shelves.[14] Pierce and Hart characterized

the regional taxonomic distributions and variability of coccolith morphologies in surficial bottom sediments throughout the GoM with exception to the continental shelves.[1] From their investigations, coccoliths from 11 primary taxa were identified to comprise > 0.5% of coccolith accumulations in sediments from all observed taxa (35 extant and 21 extinct) with *E. huxleyi* coccoliths representing the dominant species (> 75% on averagae). **Table 6-2** summarizes the overall observation frequencies for the 11 primary coccolith taxa reported by Pierce and Hart.[1]

Table 6-2: The overall relative % observation of coccolith taxa contributing > 0.5% from all surficial sediment samples collected throughout the Gulf of Mexico as reported by Pierce and Hart. Table adapted from Pierce and Hart.[1] (* Updated taxonomic classificatiion as *Calcidiscus leptoporus*).[2, 3]

Taxa	Observed %
E. huxleyi	76.32
Gephyrocapsa oceanica	5.65
Umbilicosphaera mirabilis	4.83
U. irregularis	2.01
*Cyclococcolithina leptopora**	1.74
Syracosphaera pulchra	1.57
U. tenuis	1.40
Scapholithus fossilis	1.06
Rhabdosphaera stylifera	0.85
Discosphaera tubifera	0.57
Thoracosphaera hemii	0.53
Sum Observed %	96.53

In addition to characterizing the community structuring of coccolithophores in the GoM water column, Pariente also compared the relative prominence of coccolithophore water column populations observed from October 1990 and March 1991 with consideration to the 10 most abundant coccolithophore species found within GoM sediments as reported by Pierce and Hart.[1, 7] A general overview of this comparison revealed that the combined abundance of water column coccolithophores from October and March with respect to the 10 most abundant species found in sediments accounted for only 74.41% of the total coccolithophore population (with exclusion of *F. profunda* from water column data). There are several contributing factors to the variation of comparing water column organisms to sedimented coccoliths as discussed in detail by Pariente.[7]

Perhaps the most prominent reasons suggested by Pariente for such variations included: (1) Time; water column samples are a single record in space and time, whereas sediments are a sum geologic record of the past, and (2) the number of coccoliths generated varies from species to species.[7]

Additional considerations were also offered by Pariente as to why *E. huxleyi* dominates the coccolith accumulations throughout GoM sediments: (1) the number of coccoliths produced and shed by *E. huxleyi* is more than most other species, (2) *E. huxleyi* has probably been more abundant over longer time periods throughout the water column, (3) *E. huxleyi* may have been more abundant in the past as sediment compositions are a reflection of the past, (4) transport of coccoliths from shelf regions where *E. huxleyi* is a dominant species, (5) rapid and abundant coccolith formation from past, sporadic *E. huxleyi* blooms, (6) the high cell multiplication rate of *E. huxleyi*, and (7) a sum influence of all factors.[7] Essentially, *E. huxleyi* is currently the preeminent coccolithophore species in the GoM, and that is directly reflected in the taxonomic composition of coccoliths in GoM sediments.

6.1.1.3 General Characteristics of Coccolith Shields

There are two main classifications of coccoliths, heterococcoliths and holococcoliths.[2, 4, 5] Heterococcoliths are formed of various shapes and sizes of fundamental crystal units, whereas holococcoliths are comprised of many small crystals of the same type.[2, 4] Holococcoliths are typically more soluble than heterococcoliths; hence, heterococcoliths dominate the coccolith record in deep-sea sediments.[2, 4, 5] Much research has focused on understanding the cellular mechanisms involved during coccolith calcification, as well as describing the structures and morphologies of coccoliths.[2, 4, 6, 8, 10, 15-20] In general, the biomineralization of coccolith shields is a highly controlled, molecular-level process initiating with the nucleation of single calcite crystals specifically oriented (respective to the C-axis of a calcite rhombohedron) around an organic-based template to form a proto-coccolith ring.[15] The continued growth of crystals around the proto-coccolith ring continues by the addition of various single-crystal units with complex

morphologies, which are believed to be controlled by several factors including spatial constraints from growth vesicles within the cell and interaction with organic molecules until the final coccolith morphology is realized.[2, 4, 6, 10, 15-20] Ultimately, heterococcolith shields are composed of many interlocking single-crystal units that exhibit exceptional molecular and crystalline uniformity giving rise to diverse coccolith morphologies between $2 - 20$ μm respective to individual coccolithophore species.[2-4, 6, 10, 15-20]

6.1.1.4 Coccoliths versus Foraminifera Tests

Biogenic carbonate formations from planktonic foraminifera and coccolithophores are widely distributed throughout sediments in the GoM.[1, 14] Combined, they produce the dominant carbonate contributions to surficial sediments off of the continental shelves.[14] In sediments comprised of both foraminifera and coccoliths, the calcareous foraminiferal tests contribute mostly to carbonates in the sand size particle fractions from $62.5 - 2{,}000$ μm with fragments composing silt portions from $4 - 62.5$ μm. On the other hand, coccolith carbonate dominates the very fine sediment fractions < 6 μm.[2, 4, 5] Hence, coccolith carbonate is more apt to influence the IR-ATR spectrum than foraminiferal carbonate as coccoliths provide an excellent 'size' match for interaction with the evanescent field penetration depth (~700 nm @ 1335 cm^{-1} with $n_1 = 2.42$ and $n_2 = 1.3$). In this thesis, coccoliths were addressed as the most probable contributor of peculiar carbonate absorption features observed within MC118 sediment; facilitated through SEM investigations that revealed abundant coccolith assemblages.

6.2 Correlating Spectral Profiles of Authigenic Carbonate Nodules with Select Sediments

In addition to the characterization of MC118 sediments with IR-ATR spectroscopy as described in **Chapter 5**, a number of authigenic carbonate nodules ($\delta^{13}C$ values between -24 and -34‰, see **Appendix A-1**) recovered from MC118 box cores BC3 and BC5 and gravity cores 21 and 26 were also analyzed. The following sub-sections focus on the characterization of carbonate

minerals and spectral signatures obtained from authigenic carbonate nodules exhibiting strong depletions in ^{13}C from the inheritance of C generated from the chemosynthetic oxidation of seeping hydrocarbons at MC118. Furthermore, spectral similarities between authigenic nodules and select sediments from MC118 are described. Nodule sizes generally ranged from approx. 3 mm up to 3 cm. **Figure 6-2** contains optical images of several recovered authigenic carbonate nodules from MC118.

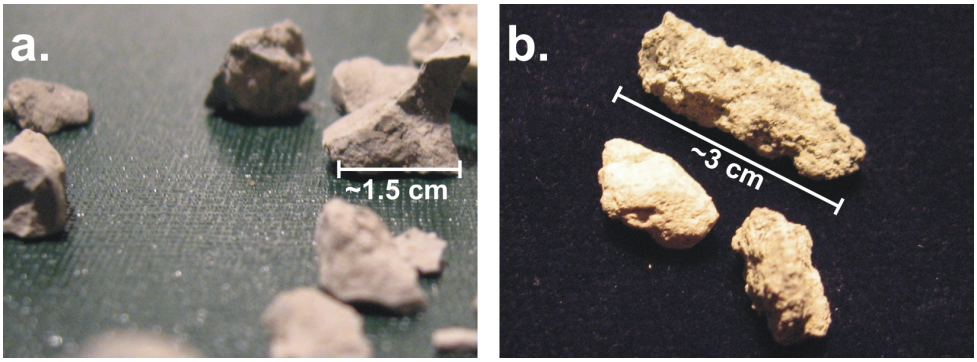

Figure 6-2: Authigenic carbonate nodules collected from (a.) BC3* and (b.) BC5 MC118 samples. (* nodules provided courtesy of Dr. Roger Sassen, GERG, Texas A&M University).

6.2.1 Experimental

6.2.1.1 IR-ATR Instrumentation

IR-ATR spectra of carbonate nodules were recorded from $4000 - 400\ cm^{-1}$ using a Bruker Equinox 55 FT-IR spectrometer (Bruker Optics Inc., Billerica, MA). The spectrometer was equipped with a LN_2 cooled MCT detector (Infrared Associates, Stuart, FL) and Specac Gateway in-compartment horizontal ATR unit (Specac Inc., Woodstock, GA). For spectral analysis, each sample was deposited directly onto a trapezoidal ZnSe ($n_D = 2.43$ at $\lambda = 5\ \mu m$) ATR crystal (MacroOptica, Moscow, Russia) with dimensions of $72 \times 10 \times 6$ mm and 45 ° end facets. A custom cut 3/16" th. polycarbonate cover allowed purging of the sample compartment with dry air to stabilize background water and CO_2 and expedite sample drying. Additional physical

descriptions of the optical path and components used in the experimental setup can be found in **Section 3.2**.

6.2.1.2 Sample Preparations and IR-ATR Measurement Procedures

Nodule specimens were first isolated from the sediment matrix and rinsed with an aqueous potassium hydroxide (J.T. Baker, Phillipsburg, NJ) solution (pH ~9.5 to protect aragonite) as to remove loose sediment particulates from the larger carbonate mass. Solution preparation procedures followed that described in **Section 5.5.1.1**. After rinsing, nodule samples were allowed to air dry for at least 48 hrs before being hand ground into a fine powder with a ceramic mortar and pestle. Once ground, particulates were placed in a glass vial with plastic cap and stored at room temperature until further use.

Prior to the spectroscopic evaluation of each sample, a sufficient volume of KOH solution (pH ~9.5) was transferred into the sample vial to form a viscous particulate suspension while ensuring minimal solvation and reaction of the carbonate minerals, particularly aragonite. A reference spectrum with a clean, dry ZnSe crystal was collected after purging the sample compartment for at least 10 mins with dry air. After collection of the reference spectrum, the sample suspension was thoroughly mixed by pulling and ejecting sample contents from a single-use disposable plastic pipette for approx. 15 s. Approx. 1 mL of the sample mixture was delivered and distributed as to fully cover the waveguide surface. IR-ATR spectra were then continuously recorded, typically at 90 s intervals, throughout the sample drying process. Once spectral stabilization for dried, powdered residue was observed, measurements were continued until approx. 25 spectra were obtained for each sample. Each individual sample analysis required approx. 3 hrs. IR-ATR reference and sample spectra were generated by averaging 100 sample scans at a spectral resolution of 1 cm^{-1}. Each specific sample was evaluated only once. In select cases, a small portion of unwetted sample was isolated for carbon isotope characterization studies. Following IR analysis of each sample, powdered residue was rinsed off the waveguide surface with deionized water. Once most of the sample residue was removed, a moistened

Kimwipe (Kimberly-Clarke Professional, Neenah, WI) was used to clear away any residual particulates.

6.2.2 Results and Discussion

Several key observations were made throughout the spectroscopic evaluation of authigenic carbonate nodules: (1) as expected, much stronger carbonate features were observed with comparatively lower intensity absorptions from clay and quartz minerals than sediment matrices, (2) highly variable carbonate mineral compositions, (3) Mg-calcite signatures were observed in all nodule samples, (4) no less than two carbonate species were observed in any sample, and (5) the ν_3 carbonate region always exhibited characteristically broad absorption features. **Figure 6-3** contains an IR-ATR spectrum for an authigenic carbonate nodule collected from BC5 sediments.

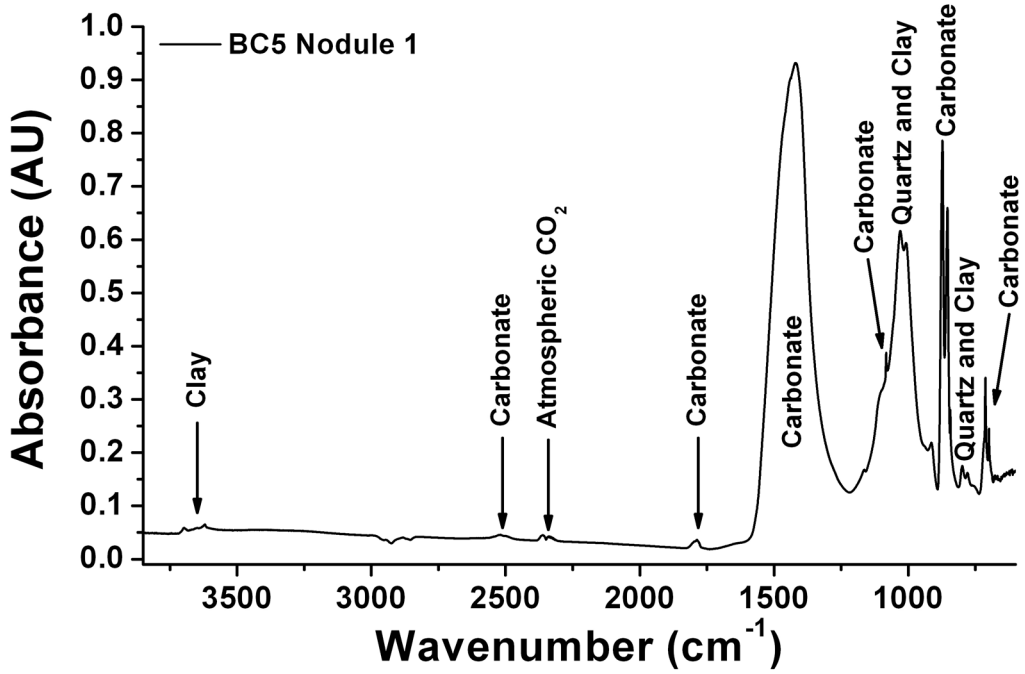

Figure 6-3: An IR-ATR spectrum for an authigenic carbonate nodule recovered from BC5 sediments. Notice very strong carbonate absorption features in addition to minor spectral abosrptions from clay and quartz minerals. Of particular importance is the broad ν_3 carbonate absorption profile around 1500 cm^{-1}.

In general, three compositional classifications of authigenic nodules were found: (1) High Aragonite ($\delta^{13}C$ of -26.6‰ for representative sample); medium to high aragonite signatures with medium to low calcite and Mg-calcite features, (2) Medium Dolomite ($\delta^{13}C$ of -34.0‰ for representative sample); medium to low dolomite absorption intensities with medium to high calcite and Mg-calcite contributions, and (3) High Mg-Calcite ($\delta^{13}C$ of -24.0‰ for representative sample); a single nodule sample exhibiting a strong Mg-calcite profile, medium to low calcite signature, and very low to no dolomite absorption character. The usage of qualitative terms high, medium, and low do not describe the composition of Mg-calcite, but are in reference to qualitative IR signal strengths respective to individual carbonate species. **Figure 6-4** provides IR-ATR spectra centered on the ν_4 carbonate absorption region to display characteristic signatures for the three generalized nodule classifications based on spectroscopic analysis of carbonate mineral compositions.

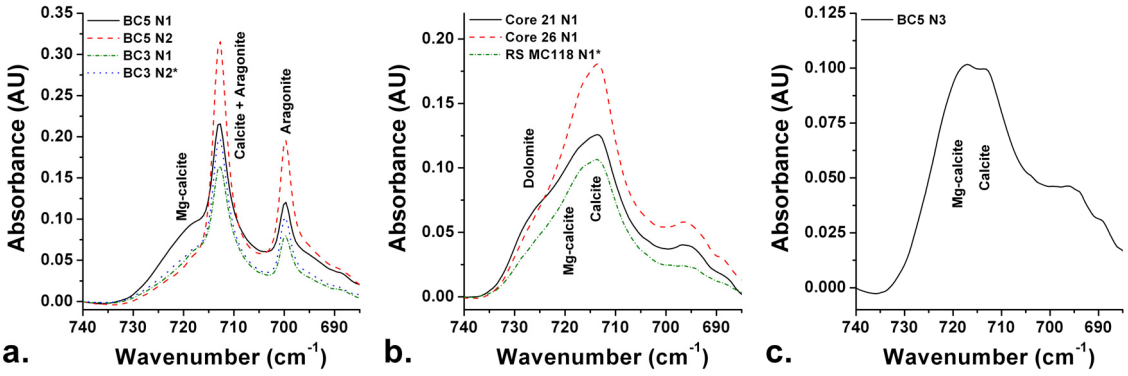

Figure 6-4: IR-ATR spectra of 7 nodule samples from MC118 demonstrating the diversity of carbonate mineral compositions observed for (a.) High Aragonite nodule samples, (b.) Medium Dolomite nodule samples, and (c.) a High Mg-calcite nodule sample. Spectra were uniformly shifted to and absorbance of 0.0 at 740 cm^{-1} to aid visualization. (* Sample provided courtesy of Dr. Roger Sassen, GERG, Texas A & M University).

The diversity of carbonate mineral constituents in authigenic nodule samples was readily observed despite IR-ATR spectroscopic evaluation of only several samples. It is anticipated that continued spectroscopic analysis of additional samples coupled with the development of high-

precision quantification methods will reveal a continuous range of carbonate compositions. However, the current primary significance of these IR-ATR spectroscopic measurements is revealed by the broad ν_3 carbonate spectral profiles observed from all examined nodule samples. **Figure 6-5** compares the ν_3 carbonate spectral region for selected samples from each general nodule classification and two characteristic ν_3 absorption profiles observed in surficial sediments from box core collections at the MC118 hydrate site.

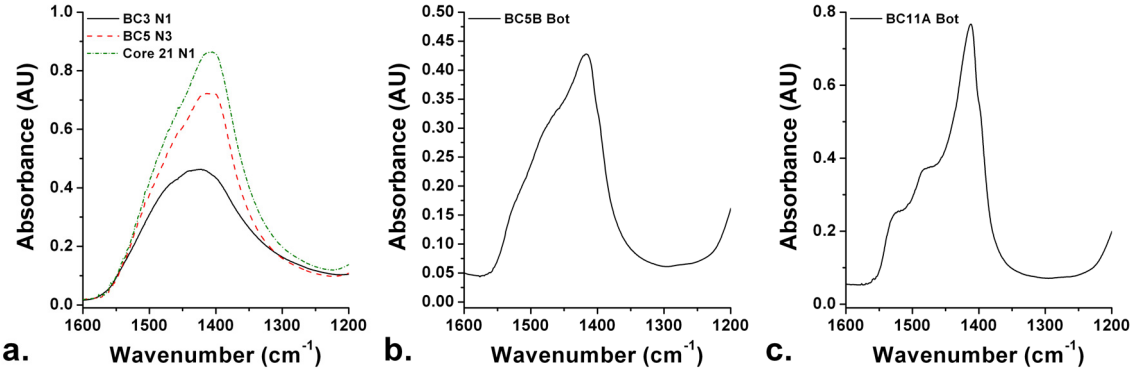

Figure 6-5: Observed ν_3 carbonate absorption features from IR-ATR spectra of (a.) authigenic carbonate nodules from three general composition classifications (average $\delta^{13}C$ of -28.98‰ for 4 examined nodule specimens), (b.) sediments in close proximity to recovered nodules from BC5B Bot sample ($\delta^{13}C$ of -18.7‰), and (c.) sediments from BC11A Bot sample displaying sharp, well-defined absorption characteristics with no significant context clues indicative to authigenic carbonate formation at this sample collection (average $\delta^{13}C$ of 0.50‰ for BC7 and BC11 sediments).

In **Figure 6-5**, rather broad ν_3 carbonate absorption profiles are observed in the selected spectra representing authigenic carbonate nodules from each general composition classification (a.) and sediments from the BC5B Bot sample (b.), which was in close proximity to authigenic nodule formations. The BC11 sample collection was collected with no significant context clues suggestive to the potential for chemosynthetically driven authigenic carbonate formation (i.e., shells or nodules). The ν_3 carbonate profile from sample BC11A Bot (**Figure 6-5 (c.)**) exhibits a very sharp absorption feature at 1413 cm^{-1} and three distinctive, albeit minor, shoulders at approx. 1485 cm^{-1}, 1520 cm^{-1}, and 1398 cm^{-1}. A close examination of the ν_3 spectral signature for the

BC5B Bot sample reveals similar characteristics to the BC11A Bot sample; however, the profile is considerably broadened with diminished features characteristic to the BC11A Bot sample.

A quick overview of ν_3 carbonate absorption profiles from box core sediments, described in **Chapter 5**, reveals that sediments from BC2, BC4, BC6, BC7, BC8, BC9, and BC11 collections were found to exhibit similar spectral features exemplified by the BC11A Bot sample in **Figure 6-5 (c.)**. Sediments from BC1, BC5, and BC12 were the only collection locations to contain samples with broadened ν_3 carbonate absorption characteristics similar to those displayed in **Figure 6-5 (a.)** and **(b.)** for authigenic nodules and the BC5B Bot sample, respectively. IR spectroscopic results summarized in this section facilitated establishment of the initial correlation between ν_3 carbonate absorption characteristics and the detection of chemosynthetically driven authigenic carbonate formation.

6.3 Coccoliths Observed in MC118 Samples

To characterize coccolith assemblages in MC118 samples, samples were evaluated visually with the assistance of a SEM. The following sub-sections summarize the significant findings from brief characterization studies of MC118 samples.

6.3.1 Experimental

MC118 samples were characterized with use of the SEM from a Nova Nanolab 200 (FEI Company, Hillsboro, OR) and the assistance of Dr. Christine Kranz (ASL, Georgia Tech). Sediment samples were smeared onto either a small portion of a glass microscope slide or gold-coated glass cover slip. Sediment samples were allowed to dry for at least 12 hrs prior to SEM examination. Sediments from the BC7 sampling location were used for the characterization of coccolith assemblages in sediment matrices. In addition, the surface of a small (~3 mm) authigenic carbonate nodule recovered from BC3 sediments was examined. Prior to nodule

analysis, the sample was lightly rinsed with an aqueous KOH solution (pH ~9.5) and allowed to dry at room temperature for approx. 72 hrs. Glass slides and the nodule sample were secured onto standard, aluminum SEM pin stub specimen stages with the aid of PELCO carbon conductive tabs (Ted Pella, Inc., Redding, CA) in order to minimize sample charging.

6.3.2 Results and Discussion

6.3.2.1 Taxonomic Characterization of Coccoliths in MC118 Samples

Coccolith morphologies are very diverse and commonly used for taxonomic classification of coccolithophore species.[1-3] In **Section 6.1.1.4**, results from an extensive study of coccolith distributions throughout the surficial sediments in the GoM by Pierce and Hart were summarized.[1] In this thesis, only brief characterization studies of coccoliths present in MC118 samples were carried out, and coccolith identification was facilitated with the use of taxonomy guides of Pierce and Hart, Winter and Siesser (eds.), and Young et al.[1-3]

From approx. 25 SEM imaging locations in three sediment samples and one nodule sample, coccoliths from 4 of the 11 primary taxa found in surficial sediments throughout the GoM by Pierce and Hart were identified with high confidence.[1] The 4 coccolith taxa were *Emiliania huxleyi*, *Gephyrocapsa oceanica*, *Calcidiscus leptoporus*, and *Thoracosphaera heimii*. Coccolith morphologies characteristic of *E. huxleyi* were the most abundant formations observed within MC118 samples; consistent with findings reported by Pierce and Hart.[1] **Figure 6-6** contains SEM images illustrating the various coccolith taxa observed during coccolith characterization studies in this thesis.

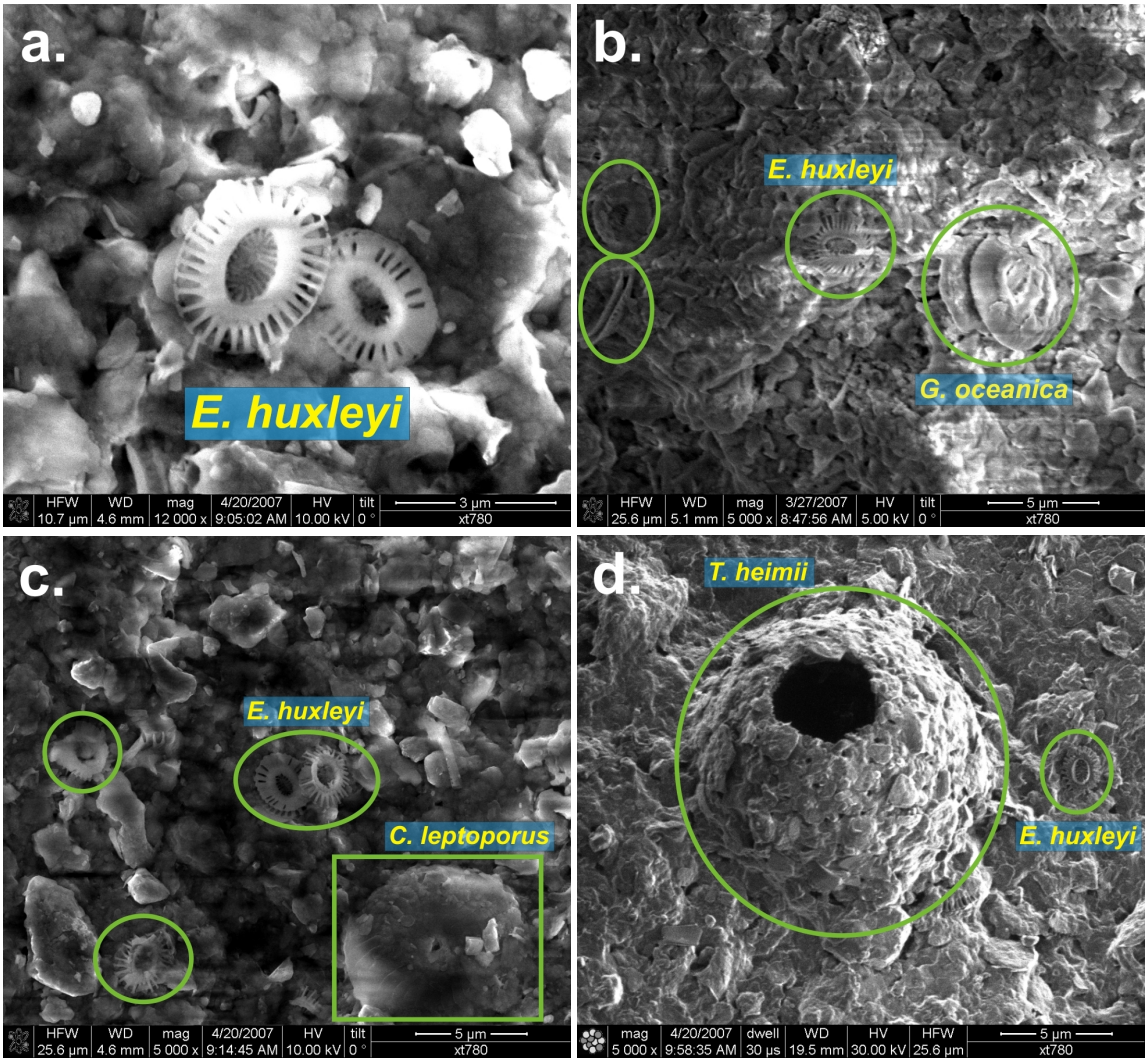

Figure 6-6: SEM images exhibiting coccoliths with taxonomic identification of 4 primary taxa found in GoM sediments. Images (a.), (c.), and (d.) were collected from BC7 sediments, and image (b.) was collected during surface evaluation of an authigenic carbonate nodule collected from BC3. In images (b.) and (c.), well-preserved *E. huxleyi* coccoliths are also indicated without an identification tag. More coccoliths and coccolith fragments can be observed in each image.

6.3.2.2 Coccolith Density in MC118 Sediments

Coccoliths characteristic of *E. huxleyi* were observed in abundance during SEM investigations. **Figure 6-7** contains two SEM images illustrating the abundance of readily identified coccoliths and coccolith fragments superficially distributed from the BC7 sediment sample.

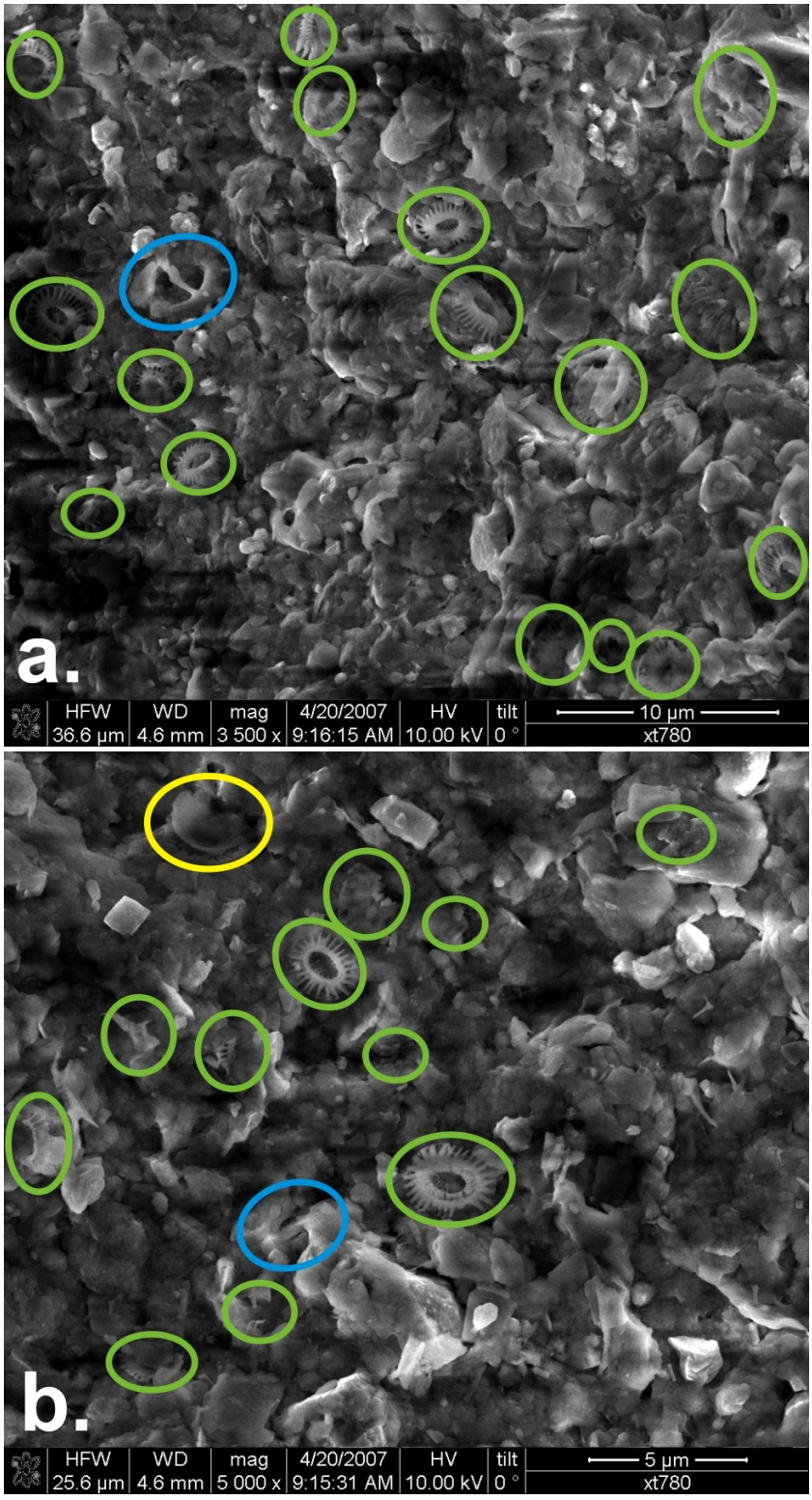

Figure 6-7: SEM images with highlighted whole coccoliths and coccolith fragments from BC7 sediments; *E. huxleyi* (green), *G. oceanica* (blue), and an unidentified taxa (yellow).

In **Figure 6-7**, a reasonable estimation of eight coccoliths (whole, nearly whole, and summed minor fragments) per 25 μm × 25 μm can be made. Using values from **Chapter 7** to describe 'active' sensing regions along the waveguide surface for IR-ATR measurements with a similar experimental setup as that used for sediment studies (radiation cone angle of 2 ° and source radius of 0.1278 cm from **Table 7-3 in Section 7.3.3.2**), approx. 215 mm^2 of the measurement surface participates in spectral generation. Hence, a rough approximation indicates that $> 2.5 \times 10^6$ coccoliths (equivalent to approx. 25 mg)[12] would be subject to full or partial interaction with the evanescent field, which is ample particle density and sufficient mass for significant contribution to IR-ATR spectra. Results summarized in this section confirmed the feasibility for characteristic carbonate signatures, specifically displayed in **Figure 6-5 (c.)**, to originate from accumulated coccoliths within sediments collected from the MC118 gas hydrate site.

6.4 IR-ATR Spectroscopic Evaluation of Coccoliths from Coccolithophore Cultures

To confirm the capability for detecting authigenic carbonate precipitation within very fine sediment fractions with IR-ATR spectroscopy, it was imperative to establish a direct connection of ν_3 carbonate infrared absorption signatures displayed in **Figure 6-5 (c.)** with coccolith formations. This section provides a detailed overview of experiments and results for the generation of IR-ATR absorption spectra of coccoliths produced by cultured coccolithophores.

6.4.1 Experimental

6.4.1.1 Coccolithophore Cultures

Coccolithophore cultures were purchased from Ward's Natural Science (Rochester, NY). In total, 9 vials with approx. 20 mL (each) of coccolithophores in marine culture media were obtained. After initial receipt of the coccolithophore cultures, optical microscope (OM) (Olympus BX41, Olympus America Inc., Mellville, NY) and SEM images (Nova Nanolab 200, FEI Company,

Hillsboro, OR) were taken to confirm the presence of coccolith shields and assist taxonomic identification. To reduce interference from salt recrystalization, approx. 1 mL of culture was diluted with 12 mL of KOH solution (pH ~9.5) and centrifuged (IEC Clinical Centrifuge, International Equipment Company, now Thermo Scientific, Waltham, MA) for 2 hrs. Following, all but ~0.5 mL of supernate was discarded, and the sedimented coccolith/coccolithophore condensate was re-suspended in the remaining solution. Several droplets of the condensate were pipetted onto a glass microscope slide and gold-coated glass cover slip and allowed to dry for OM and SEM imaging, respectively. **Figure 6-8** provides confirmatory images of generous coccolith production by coccolithophore cultures of *Pleurochrysis carterae*.[3]

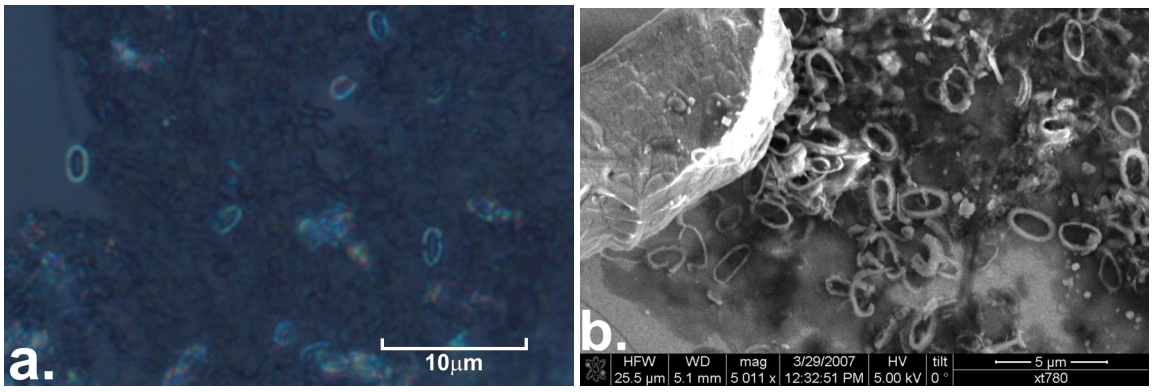

Figure 6-8: Optical microscope image at x100 magnification (a.) and SEM image (b.) of coccoliths produced by *Pleurochrysis carterae*. The coccoliths are ellipsoidal shaped rings approx. 2 μm in length along the major axis.

The primary objective for culturing coccolithophores was to generate a sufficient mass of coccoliths for IR-ATR spectroscopic evaluation. Hence, elementary culturing methods were utilized compared to highly controlled coccolithophore culture studies.[4, 21, 22] Cultures were maintained in uncovered vials between 21 – 25 °C in a partially shaded, eastward facing window for 4 – 6 weeks prior to harvesting for spectroscopic evaluation. Each vial was sealed and gently swirled each morning for approx. 10 s to mix culture contents. Following, the vials and flasks were uncovered to facilitate gas exchange.

6.4.1.2 Sample Preparation

During collection of coccoliths for IR-ATR spectroscopic evaluation, similar treatments for concentrating coccoliths while reducing the potential for salt interferences for OM and SEM images were carried out. First, culture vial contents were transferred into 6 glass centrifuge tubes and brought to equivalent volumes with KOH solution (pH ~9.5). Following centrifugation for approx. 2 hrs, all but approx. 1 mL of culture media was carefully removed and discarded. Then, approx. 12 mL of KOH solution was added to achieve equivalent volumes before centrifuging for another 2 hrs. After rinsing and concentrating coccoliths (with coccolithophores), the supernatant from each centrifuge tube was carefully removed until approx. 1 mL of condensate remained. Condensates from each vial were then re-suspended and transferred into 2 clean centrifuge tubes. Before centrifuging the combined contents, 2 mL of KOH solution was added to each of the initial tubes and vigorously shaken to maximize coccolith/coccolithophore collection. KOH recovery solutions were then added to the final 2 tubes. Final collection tubes were brought to an equivalent volume with additional KOH solution, and then centrifuged for approx. 1 hour. Supernate was removed until approx. 2 mL of condensate and solution remained. Finally, each sample was capped and stored at room temperature.

6.4.1.3 IR-ATR Instrumentation and Spectroscopic Measurement Procedures

The IR-ATR spectra of coccolith/coccolithophore samples were collected using the same experimental configuration as described in **Section 6.2.1.1**.

IR-ATR spectroscopic measurements were carried out for aliquots of each sample tube with condensed coccoliths and coccolithophores. Prior to loading each sample, the internal sample compartment was purged for at least 10 mins before collecting a reference spectrum. Following, the coccolith/coccolithophore matrix was re-suspended and mixed with the 2 mL of remaining solution before dispensing approx. 1 mL of sample to fully cover the waveguide surface. After sample deposition, IR-ATR spectra were collected at 90 s intervals while drying until a minimum

of 30 spectra were collected following signal stabilization after water evaporation. All reference and sample spectra were 100 sample scan averages at 1 cm^{-1} resolution.

6.4.2 Results and Discussion

In SEM images of GoM sediments (as seen in **Figure 6-7**), accumulated coccolith shields were found as detached particulates; a common result of sloughing from living organisms and separation from expired organisms during detrital sedimentation.[2, 7] From published SEM photos, a single *P. carterae* cell is generally covered with > 70 coccoliths.[3, 16] Considering the difference between cell size (~10 μm) to coccolith size (~2 μm) with at least a 70:1 coccolith:coccolithophore ratio, only minor organic-based spectroscopic signatures were expected during evanescent field measurements. Hence, no additional treatments were taken to further isolate the coccoliths from organic remnants of the culture matrix. Representative IR-ATR spectra for each of the prepared coccolith condensates are provided in **Figure 6-9**.

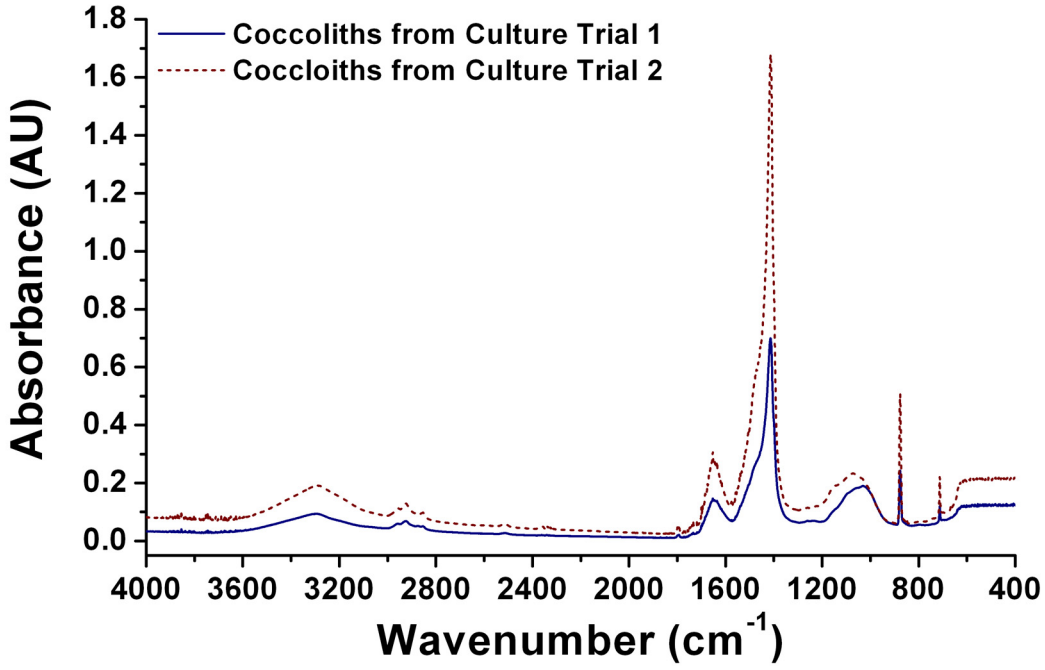

Figure 6-9: IR-ATR spectra for each sample of coccolith condensates from cultured coccolithophores of *P. carterae*.

As expected, the IR-ATR spectra of coccolith condensates were dominated by calcite absorption features (ν_4; 713 cm^{-1}) with only minor spectral contributions from organic coccolithophore debris and/or remnants from the parent culture media around 3000 – 2820 cm^{-1} and 1200 – 950 cm^{-1}. Additionally, minor water absorption features were observed in the O-H stretch and H-O-H bend regions. However, the most significant finding was the absorption characteristics of the ν_3 carbonate region in both cultured coccolith samples. The IR-ATR spectra exhibit an intense, sharp absorption band at 1413 cm^{-1} resembling the ν_3 carbonate profiles from MC118 sediments inundated with coccoliths. Accentuated views of the ν_3 carbonate absorption regions for coccoliths from culture (CfC) and a graphical overlay with coccolith loaded BC7A Bot sediments ($\delta^{13}C$ of 0.4) are provided in **Figure 6-10**.

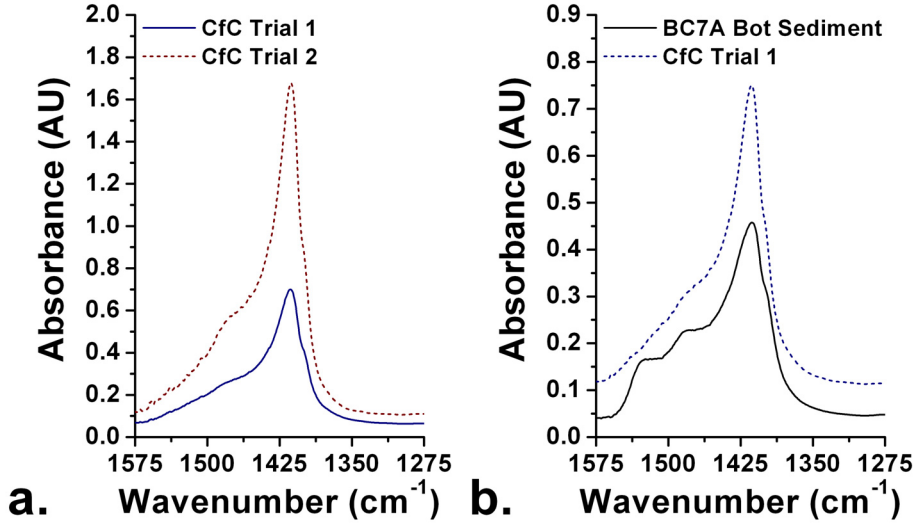

Figure 6-10: IR-ATR spectra displaying accentuated views of the ν_3 carbonate region for (a.) coccoliths from culture (CfC) for evaluated condensate samples and (b.) overlays of CfC and coccolith rich BC7A Bot sediments collected from MC118. Each carbonate profile exhibits an intense, narrow absorption feature centered at 1413 cm^{-1}.

In addition to the intense band at 1413 cm^{-1}, the spectra of *P. carterae* coccoliths exhibit two partially defined shoulders similar to MC118 sediment signatures. Shouldering absorption features were observed at approx. 1485 cm^{-1}, 1520 cm^{-1}, and 1398 cm^{-1} in MC118 sediments, and

at approx. 1484 cm^{-1} and 1399 cm^{-1} from cultured coccoliths. A comparable, distinctive absorption feature at 1520 cm^{-1} was not observed for the cultured coccoliths. This is currently attributed to a slight inter-species variance in single-crystal calcite units contributing to the overall coccolith morphology; primarily between *E. huxleyi* and *P. carterae* as *E. huxleyi* coccoliths are dominant throughout GoM sediments. A more thorough consideration to molecular, structural, and environmental factors contributing to spectral differences in the ν_3 carbonate profiles is provided in **Section 6-5**.

Following IR-ATR spectroscopic evaluation, OM images were collected for dried coccolith assemblages on demounted ZnSe waveguides. **Figure 6-11** contains an OM image displaying a high surface density of condensate residue contrasted against a bare portion on the ZnSe waveguide. The zonal boundary between coccolith remnants and clean surface resulted from dismounting the waveguide; a small edge portion of ZnSe crystal is masked by a Viton mat when mounted in the ATR assembly to prevent solution leakage.

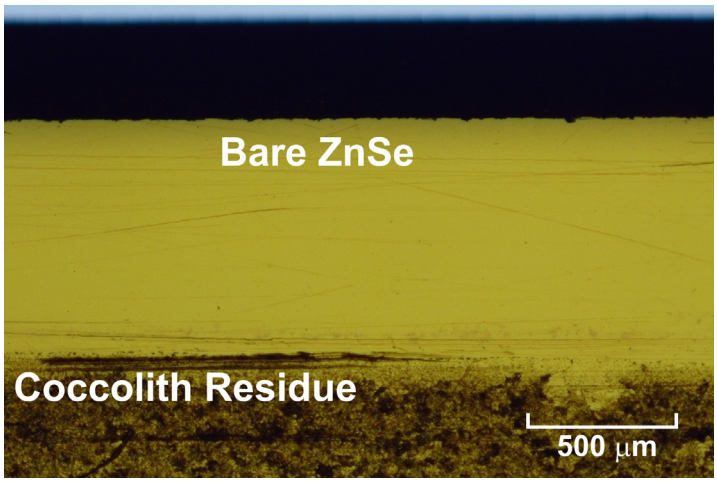

Figure 6-11. OM image (x2.5) contrasting a bare portion of ZnSe crystal with a high surface density of coccolith/coccolithophore residue after IR-ATR measurements.

Additional OM images were collected at x50 magnification for visual confirmation of coccolith structures on the ZnSe waveguide surface following spectroscopic evaluation. Representative images from each condensate sample are contained in **Figure 6-12**.

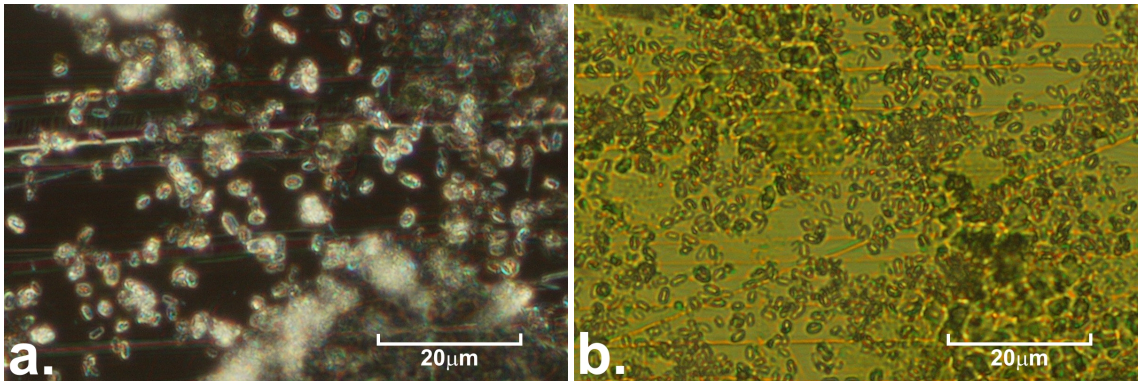

Figure 6-12: OM images of dried coccolith accumulations on ZnSe crystals following spectroscopic evaluation of (a.) CfC trial 1 at x50 magnification in dark-field lighting and (b.) CfC trial 2 at x50 magnification. Copious coccoliths are observed on the ZnSe waveguide surface in both images.

The ν_3 carbonate spectral signatures from cultured coccoliths exhibited a direct correlation to many of the IR-ATR profiles from surficial MC118 sediment collections with abundant coccoliths, which was further corroborated with SEM imagery and carbon isotope evaluation of BC7 and BC11 samples (average $\delta^{13}C$ of 0.5). The traceability of coccolith signatures from IR spectra in most MC118 sediment samples is consistent within established context. Coccolith accumulations account for a significant mass fraction of sediment compositions off of the continental shelves in the GoM as a product of thriving coccolithophore crops throughout photic waters in the Gulf region (expected $\delta^{13}C$ of carbonate close to normal seawater values of 0). At the MC118 hydrate site, this signal is disrupted by the culmination of geophysical and biogeochemical processes driving authigenic carbonate formation (expected depletion of ^{13}C from the inheritance of C from seeping thermogenic hydrocarbons with strongly negative $\delta^{13}C$ values). Although direct correlations have been established and experimentally validated, it is important to understand the underlying molecular level consequences giving rise to the observed spectral differences. Hence, **Section 6.5** provides a thorough examination as to the origins of characteristically 'sharp' ν_3 carbonate profiles of biogenic coccoliths and the consequences of authigenic carbonate precipitation leading to broadened spectral features. Then, final conclusions

from IR-ATR spectral analyses of MC118 sediment and nodule samples examined throughout the described studies are provided in **Section 6.6**.

6.5 Traceability of Coccolith IR Absorption Signatures in Sediments with and without Authigenic Carbonates

A variety of topics must be considered to understand the spectral consequences of authigenic carbonate formation on the alteration of carbonate absorption signatures from coccolith laden sediments. This section will first focus on delineation of the nature of IR absorption features characteristic to coccolith formations. Then, the spectral impact of authigenic carbonates as disruptive elements that decompose the traceability of coccolith signatures in sediment samples will be discussed. The ν_3 carbonate absorption feature will be of primary interest, but absorption characteristics of the ν_2 carbonate signature are also considered.

6.5.1 Molecular Characteristics of Coccoliths and Relationship to IR Absorption Features

In **Section 6.1.1.3**, the molecular level control coccolithophores impart during the biomineralization of coccoliths was described.[2, 4, 6, 10, 15-20] IR absorption characteristics of solid samples are strongly influenced by molecular composition, the molecular uniformity throughout crystalline lattices, and mixed-crystal formations.[23, 24] The IR spectral consequences to calcite absorption features from Mg^{2+} incorporation during the formation of Mg-calcite (**Section 5.1.3.3**) is a specific example of the impact molecular composition can impart upon crystal uniformity and resultant IR absorption characteristics of carbonate minerals.[25-27] In contrast, the IR absorption characteristics of carbonate crystals should also be indicative of considerable uniform molecular composition coupled with highly ordered crystalline lattices. Although molecular composition is important, spectral comparison of coccolith calcite and non-biogenic, naturally occurring calcite mineral (also referred to as inorganic calcite) reveals that the crystalline structure is perhaps more

influential to the ν_3 carbonate profile. **Figure 6-13** contains an overlay from the IR-ATR spectra of cultured coccoliths and naturally occurring inorganic calcite.

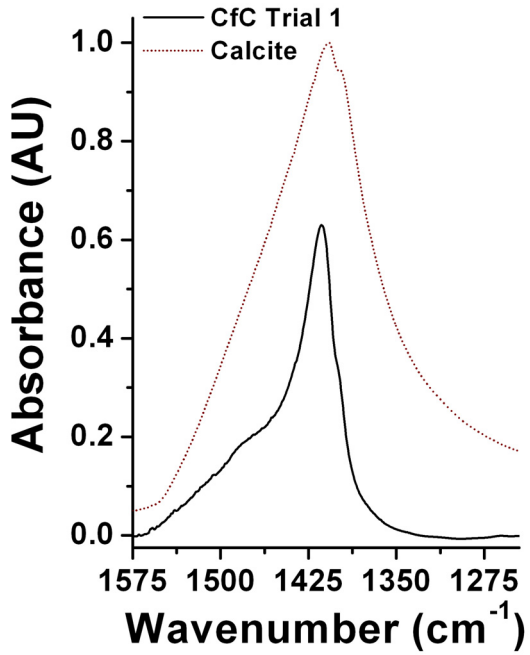

Figure 6-13: IR-ATR spectra focused on the ν_3 carbonate absorption features for calcite for coccoliths from culture (CfC) and hand ground non-biogenic calcite (calcite). The calcite spectrum was obtained from the IR-ATR spectral database described in **Section 5.2**.

The ν_3 calcite absorption profiles from coccoliths and inorganic calcite mineral are quite different despite both specimens being composed of high purity calcite. The observation of broadened features from the non-biogenic mineral, also observed in other calcite spectra in the literature,[28-34] can result from disruption to well-ordered crystalline lattices during grinding (results in peak height variations in XRD measurements[35]). Furthermore, although large single-crystals can form naturally, the absence of biologically templated growth can increase the susceptibility to lattice defects or alteration, which can directly influence IR absorption characteristics (i.e., the formation of Mg-calcite as discussed in **Section 5.1.3.3**). Hence, the well-defined ν_3 carbonate absorption features characteristic of coccolith formations are attributed to the high degree of organismal

control over the molecular composition and, most importantly, the crystallographic uniformity of 'nano'-sized single-crystal building blocks that form the coccolith shield.[4, 10, 15-20]

The IR-ATR spectral features obtained following the concentration of millions of cultured coccoliths further reflects the conservation of precise control in templated crystal formation among organisms of the same species. In this work, coccoliths from *E. huxleyi* were found to be the most abundant coccolith morphology within MC118 sediments; however, the direct connection of sediment spectral features to coccolith formations was based upon the absorption characteristics from cultured *P. carterae* coccoliths. The cellular calcification mechanisms of coccolith formation and coccolith structuring have been extensively studied for both *E. huxleyi* and *P. carterae*.[4, 10, 15-20] Although cellular components involved in coccolith calcification mechanisms have been shown to vary between *E. huxleyi* and *P. carterae*, coccolith growth from both species (as well as other heterococcolith producing species) initiate through what has been described as a proto-coccolith ring.[4, 10, 15-20] The proto-coccolith ring is comprised of two types of alternating single calcite crystals; V and R scaffolding units having their *c*-axis oriented either vertically or radially to the coccolith plane, respectively. Once formed, growth propagates through the addition of other single crystal units until the species specific coccolith morphology is achieved.[4, 10, 15, 16, 18-20]

The extreme similarities of ν_3 carbonate profiles, particularly the sharp, strong absorption at 1413 cm^{-1}, in the IR-ATR spectra of MC118 sediments and cultured coccoliths reflects an inherent inter-species conservation for generating coccoliths with highly uniform molecular composition and ordered single crystal structures. However, slight differences in the overall ν_3 profiles were observed, such as the absence of a distinctive shoulder at approx. 1520 cm^{-1} from cultured coccoliths (additional spectral details provided in **Section 6.4.2**). This is currently attributed to differences in the basic single-crystal building blocks contributing to the overall coccolith morphologies primarily respective to *E. huxleyi* and *P. carterae*; although, the coccolith

dominated sediment signature may also reflect contributions from accumulated coccoliths of other taxa (i.e., morphologies from *G. oceanica*). Additionally, the presence of organic matter in cultured coccolith samples could overshadow accentuation of such a shouldering feature due to spectral mixing.

6.5.2 Disruption to ν_3 Carbonate Signatures of Sediments Laden with Coccolith Calcite due to Authigenic Carbonate Formation

Now that molecular level characteristics contributing to the peculiar ν_3 absorption trends of coccoliths and a brief introduction to factors capable of disrupting IR absorption features have been considered, it is essential to address the consequences of authigenic carbonate formation that leads to overshadowing of the IR absorption signatures in sediments containing abundant coccoliths.

Coccoliths are widely distributed throughout the GoM, and are the primary carbonate source in the particle fraction < 6 μm of surficial sediments with taxonomic distributions variable at a regional scale.[1, 2, 4, 5, 7, 9, 14, 15] Throughout **Chapter 5** and previous sections within this chapter, the traceability of coccolith spectral signatures in MC118 sediments has been clearly demonstrated. Hence, at a particular location, such as the MC118 site, a characteristic ν_3 carbonate signature should be observed throughout the very fine sediment fractions reflecting a rather homogeneous taxonomic distribution of coccoliths unless disrupted from the appearance of 'non-coccolith' carbonate within the sediment matrix. In current studies, microbially driven authigenic carbonate precipitation of 'non-coccolith' carbonate has been demonstrated to degrade the peculiar spectral profile of sediments with abundant coccolith calcite at MC118.

Although authigenic carbonate formation at the MC118 hydrate site is biogeochemically driven by chemosynthetic communities associated with hydrocarbon seepage emanating from extensive fault conduits as discussed in **Chapter 5**, authigenic carbonate precipitation is a non-templated

abiotic process, which introduces a number of factors that can collectively attribute to spectral broadening of the ν_3 profiles characteristic to proliferate coccolith aggregations in seafloor sediments. The IR-ATR spectroscopic characterization of carbonate minerals from MC118 authigenic nodule formations revealed the presence of multiple carbonate minerals in each evaluated sample. Although sample grinding can potentially disrupt the spectral profile by damaging crystal lattices, the appearance of multiple carbonate species is interpreted to have the most significant impact upon ν_3 broadening due to spectral mixing of multiple modal contributions with slight variations in the fundamental absorption frequency respective of cationic substitution. Broadened ν_3 spectral characteristics from sediments with authigenic carbonate formation also exhibited clearly distinguishable carbonate species diversification with exception of sediments from the BC5 location, which contained several High Aragonite authigenic nodules and the only observed High Mg-calcite authigenic nodule sample.

Mg-calcite was observed in all nodule samples and sediments from the BC12 location. As discussed in **Section 5.1.3.3**, the occlusion of Mg^{2+} into calcite structures introduces positional disorder of CO_3^{2-} and unit-cell contraction of the calcite lattice. Disruption of the calcite lattice with Mg^{2+} substitution during formation of Mg-calcite leads to spectral broadening and blue shifting of characteristic calcite absorption bands with increasing Mg^{2+} substitution as described by Bottcher et al.[27] Hence, in addition to band broadening from spectral mixing with the appearance of Mg-calcite, seeded Mg-calcite growth on coccolith formations could diminish coccolith contributions to the ν_3 carbonate signature.

Spectral broadening from authigenic carbonate formation is also attributed to the spontaneous precipitation of non-templated crystals. In addition to the susceptibility of lattice defects, authigenic carbonate formation, morphology, and cementation can vary widely with temporal fluctuations in pore water chemistry, Mg^{2+} concentration, temperature, salinity, and pressure.[5, 36] This can result in the accumulation of diverse carbonate mineralogy and dissimilar crystal

formations comparable to mixed-crystals, which are known to contribute to spectral broadening.[24] Sensitivity of the ν_3 spectral profile between ground inorganic calcite and cultured calcite coccoliths (see **Figure 6-13**) illustrates the potential for significant broadening as a result of accumulated particulates with dissimilar and/or disrupted crystalline features.

In addition to the various molecular and crystallographic consequences authigenic carbonates can impart upon the broadening of the ν_3 profile for coccolith rich sediments, two additional factors associated with authigenic carbonates can also attribute to diminished coccolith spectral signatures in seafloor sediments. First, accumulation of authigenic carbonate dilutes the relative mass abundance and consequently the spectral contribution from coccoliths. Second, the potential seeded overgrowth of coccolith formations by authigenic carbonate, which can additionally reduce evanescent field interactions with coccoliths.

Although many factors from the appearance of authigenic carbonate can perturb the ν_3 profile characteristic to coccolith sediments, the diminished mass fraction of coccolith composition and concomitant diversification of carbonate minerals are considered to be the most influential factors impacting the IR spectrum. Overall, the peculiar coccolith absorption characteristics and the influences of authigenic carbonate formation on the IR spectrum enable the detection of authigenic precipitation within coccolith dominated sediments at MC118. Furthermore the presence of biodegraded crude oil, a foundational component for chemosynthetic communities driving authigenic carbonate formation, contributes spectral absorption features in the ν_3 carbonate region, which can influence detection capabilities (i.e., BC9 sediments exhibited depletion in ^{13}C from authigenic carbonate with no IR spectral indication of authigenic carbonate through species diversification or broadened ν^3 features).

6.5.3 Consideration of ν_2 Carbonate Signatures of Coccolith Laden Sediments and the Impact of Authigenic Carbonate Formation

It was previously mentioned in **Section 5.4.2.2** that, upon introduction of authigenic carbonates, the ν_2 carbonate absorption band exhibited similar characteristics and spectral changes observed in the ν_3 region. To aid visualization and facilitate discussion, **Figure 6-14** accentuates the ν_2 absorption region for inorganic calcite, coccoliths from culture, and sediments with and without ν_3 spectral broadening.

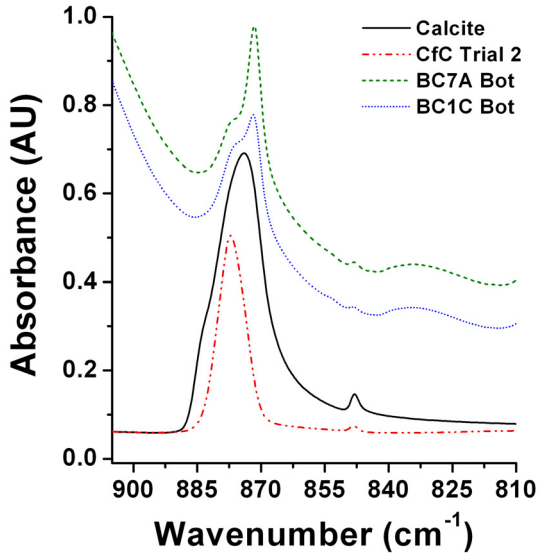

Figure 6-14: The ν_2 carbonate absorption region displaying the IR absorption of hand ground inorganic calcite (calcite), coccoliths from culture (CfC), BC7A Bot sediments without authigenic carbonate interference, and BC1C Bot sediments with authigenic carbonate interference.

Several key observations can be delineated from **Figure 6-14**. First, ν_2 absorption features from BC7A Bot sediments, representative of sediment signatures without authigenic carbonate interferences, contain a sharp absorption band at 871.6 cm^{-1} with a weak shoulder at 877 cm^{-1}. However, the prominence of the 871.6 cm^{-1} band is significantly decreased by the appearance of authigenic carbonate in BC1C Bot sediments; although, some resemblance to coccolith related features are still observed in both the ν_2 and ν_3 absorption profiles. The ν_2 absorption of cultured

coccoliths is observed at the same position as the weak shoulder in BC7A Bot sediments, and the inorganic calcite peak reflects the disrupted absorption trends from BC1C Bot sediments. The same contributing factors leading to similar spectral changes observed in the ν_3 absorption characteristics also influence the profile of ν_2 carbonate features. However, the origin of two clearly distinguishable ν_2 absorption bands from the coccolith rich BC7A Bot and similar sediments is unclear, as the ν_2 peak from cultured coccoliths only exhibits one peak matched with the weaker absorption feature from the sediment sample. This is currently attributed to inter-species variance of single-calcite crystal units contributing to the overall coccolith morphology; however, further investigations are necessary to elucidate the source of both absorption features observed in sediment samples without authigenic interferences.

6.6 Concluding Remarks from IR-ATR Spectral Analyses of Sediment Collections and Nodule Samples

The collective experiments performed throughout **Chapters 5** and **6** have demonstrated the ability to detect the impact of localized and patchy authigenic carbonate formation driven by chemosynthetic communities at the MC118 hydrate site from the background carbonate signature of widely distributed coccolith accumulations throughout the GoM. Carbon isotope data and the abundance of context clues supporting the potential for authigenic carbonate formation within sediments at sampling locations, including the recovery of authigenic nodules, shells from larger chemosynthetic organisms, and oily and/or gassy sediments, substantiate interpretations with the coincident appearance of spectroscopic perturbations to carbonate signatures. In addition, the capability to readily associate analytical results from each sampling location with respect to site geography and previous characterization of hydrate and carbonate formations further accentuate the value of context clues throughout this pioneering work with a limited number of sampling locations.

Sampling locations BC4, BC9, and BC12 exhibited signs for potential authigenic carbonate precipitation. However, IR evaluations revealed that only BC12 sediments were conclusively indicative to the presence of authigenic carbonates; thus, alluding to the localized effects and variability of pore water chemistry and perhaps biogeographic variance surrounding the fault conduits at the southwest vent. The patchy distribution of authigenic carbonates was further demonstrated from the analysis of spectral profiles in sediments from the BC5 location (NW ridge), which exhibited highly localized authigenic signatures. Sub-samples from the BC5A push-core did not indicate the presence of authigenic carbonate. However, the bottom sediments from push-core BC5B (approx. 8 – 13 cmbsf) were sampled and evaluated because of a diffuse streak of fine white particulates contrasting against sediments tainted black from abundant H_2S (i.e., smelly), a favorable biogeochemical component for promoting authigenic carbonate precipitation. Evaluation of this sample revealed characteristic spectral changes in the ν_3 carbonate region indicative of authigenic carbonate formation. The BC5B Bot sample was particularly interesting as the presence of additional carbonate minerals other than calcite were not detected in the ν_4 region. This could be the result of precipitated calcite and/or low Mg-calcite, low mass compositions of dolomite, or some combination with no detectable impact upon the ν_4 region. The recovery of shells, gassy mud, and spectral confirmation of authigenic carbonate in sediment samples from BC1 and BC5 locations and authigenic nodules recovered from BC5 strongly support further investigations to improve characterization of the region along the NW ridgeline at MC118.

Combined results from MC118 gravity core samples 21, 26, and 38 and the piston core samples from MD02-2570 provide a great deal of insight for additional applications of IR-ATR spectroscopy, including potential limitations for characterizing chemosynthetically driven authigenic carbonate formation surrounding oceanic hydrate locations throughout the GoM. Semi-quantitative analyses for estimating the relative mass % of dolomite to the total sediment

carbonate composition revealed considerably high dolomite compositions in core 21 and 26 samples and all samples evaluated from the MD02-2570 piston core. The high dolomite content could result from either pervasive and/or prolonged primary authigenic precipitation driven by chemosynthetic processes or diagenetic burial dolomitization processes, which are currently not well understood by the scientific community.[5, 37] Carbon isotope data confirms that carbonate from cores 21 and 26 and the 6 mbsf MD02-2570 sub-samples contain authigenic carbonate inherited from chemosynthetic processes; however, more extensive chemical and petrographic analyses are required to further characterize the origination of dolomite.

Although only a limited number of samples > 30 cmbsf have been evaluated, the strong occurrence of dolomite within the first meter of piston core sediment samples suggests potential depth limitations for definitive characterization of active authigenic carbonate precipitation driven by chemosynthetic processes. Additional IR-ATR studies evaluating the compositional changes of dolomite with higher resolution depth profiles coupled with classical isotopic, chemical, and petrographic analyses may facilitate advances towards understanding dolomite genesis/diagenesis at MC118, which is anticipated to be highly variable within these complex ecosystems. IR-ATR is particularly attractive for facilitating advances on this topic because it is amenable for *in situ* application and rapid on-ship/laboratory sediment screening. The rapid screening capability and simplicity of visual, qualitative sample diagnostics via broadened ν_3 carbonate absorption profiles should serve as an excellent procedure for quickly identifying the onset of dolomite transitional zones.[37] This should enable the focused analytical characterization (i.e., isotopic analysis, petrographic characterization, chemical composition, etc.) on samples collected within sediment zones demonstrating compositional changes in the IR-ATR spectra.

Spectroscopic evaluations of recovered authigenic carbonate nodules from MC118 revealed diverse carbonate mineral compositions. Initial qualitative characterization facilitated the identification of three general compositional classification groups. Although no substantial insight into the dynamics of the MC118 hydrate site can be gained from the limited number of

samples evaluated at this time, continued sample characterization and development of improved quantitative ternary (calcite + Mg-calcite, dolomite, and aragonite) or quaternary (calcite, Mg-calcite, dolomite, and aragonite) classification schemes may reveal intra-site trends and variability regarding the history and dynamics of carbonate formation at MC118. Additional characterization and dimensioning of such data sets with isotopic ratio analyses may also contextualize compositional changes with respect to the extent and variability of biological activity upon authigenic carbonate formations at this location.

The accuracy of semi-quantitative IR-ATR spectroscopic methods for characterizing calcite-dolomite compositions to the total sediment carbonate composition in this thesis was highly constrained. However, its application has facilitated an initial approximation as to the range of dolomite mass % composition in surficial sediments at MC118 and identified potential limitations for characterizing chemosynthetically influenced authigenic carbonate formation due to unknown processes leading to considerable dolomite fractions in deeper sediments. Furthermore, to facilitate broader application of this method for characterizing calcite-dolomite compositions in complex marine solid samples at MC118, as well as other locations, more careful considerations and correction for the spectral influences of quartz, clay, Mg-calcite, and aragonite are required.

Lastly, the most significant finding of this thesis was establishing the connection of peculiar ν_3 carbonate absorption features from surficial marine sediments to coccoliths. At MC118, the presence of authigenic carbonates driven by chemosynthetic organisms has been shown to occur in highly localized microenvironments through disruption in the spectral traceability of regionally distributed coccoliths. Hence, the capability to distinguish localized environmental changes to carbonate mineralogy among the background and context of regional coccolith carbonate cycles illustrates the potential for broader application and development of IR-ATR sensing strategies to further address additional aspects of complex marine carbonate cycles. During this initial work, coccoliths from *P. carterae* were found to exhibit similar IR absorption characteristics to the coccolith laden sediments at MC118, which primarily consisted of *E. huxleyi* morphologies.

However, slight spectral variations allude to potential inter-species variance of IR absorption characteristics. This is interesting as the coccolith signature observed at MC118 may exhibit geographic variations with respect to regional scale differences in the taxonomic distributions of coccoliths.

In conclusion, the capability to detect the presence of authigenic carbonates is attractive for assessing and characterizing the spatial distributions and mineralogical variance throughout the MC118 site. This is particularly important for evaluating the extent and significance of carbon cycling and sequestration mechanisms that act as buffers against the migration of greenhouse gasses from oceanic sources into the atmosphere. Furthermore, the appearance of strong dolomite interferences with increasing sediment depths reveal potential limitations for associating spectral drift to microbial influenced carbonate formation; however, IR-ATR should additionally facilitate depth profiling of the carbonate composition to identify critical interfaces where dolomite becomes a substantial carbonate constituent. Thus, enabling assessment of its own limitations and focusing additional studies that may facilitate the elucidation of dolomite formation processes and diagenetic zones of authigenic carbonates in the GoM as summarized in Botz et al.[37]

The use of IR-ATR spectroscopy for characterizing the carbonate composition in marine sediments within this thesis was highly focused on characterization of the MC118 gas hydrate ecosystem. Although only a limited number of samples were collected and analyzed from the MC118 site, the well-established contextual background for this particular location has facilitated the development of practical, qualitative and semi-quantitative applications for IR-ATR sensing strategies that are immediately applicable to on-ship and laboratory analysis. With regards to the GOMGHRC objectives, the most promising immediate applications include the spatial characterization of authigenic carbonate formation within surficial sediments and the variance of carbonate mineralogy. Information obtained from such studies should facilitate additional dimensional analyses of the MC118 site with a particular emphasis on coordination of the collective context to all consortium studies.

6.7 Outlook

Although the focus of carbonate work described in this thesis was centered on a single location within the GoM, the regional and global distributions of coccolithophores and isolated gas hydrate ecosystems associated with thriving chemosynthetic communities that drive accumulation of massive authigenic carbonate formations indicates a profound relevance for extending the application of IR-ATR sensing strategies to characterize oceanic gas hydrate ecosystems beyond the confines of the MC118 site.[2, 4, 5, 9, 14] For example, Milliman summarizes the global distributions of biogenic carbonate oozes to cover > 47% of the seafloor (typically between 45 ° N and 45 °S), and that deep-sea oozes account for > 89% of the total carbonate in surficial sediments of Earth's oceans.[5] In addition, the occurrence, distribution, variability, and complexity of carbonate mineralogy with respect to different marine environments provides ample opportunity for developing additional contextually relevant environmental applications for qualitative and quantitative IR-ATR spectroscopic carbonate analyses. In contrast, this technique should also provide an avenue for identifying the occurrence of biogeochemical and/or geophysical shifts in oceanic environments based upon the consequences that can be recorded through changes in carbonate signatures and mineralogy. Hence, the simplicity and capabilities of presented work is anticipated to stimulate broader application of this technique for on-ship screening of oceanic sediments. Furthermore, the current work establishes an immediate and significant *in situ* application for deep-sea MIR chemical sensing platforms, which substantiates the need to push forward development of instruments capable of performing in harsh oceanic environments.

The application for IR-ATR spectroscopy for assessing coccolith absorption characteristics opens the door for many research opportunities. Coccolithophores thrive throughout most photic waters of Earth's oceans and seas.[2, 4, 9] In the GoM, the abundance of *E. huxleyi* and the respective dominance of *E. huxleyi* coccoliths in marine sediments should impart the greatest influence over the spectroscopic signature of coccolith marine sediments off of the continental shelves.[1, 7]

However, the additional accumulations of coccoliths from other taxa have the capability for contributing to the overall carbonate spectral profile.[1] Hence, it will be of particular interest to assess and establish the spectral variance across coccolith species as well as mixed-species accumulations, with particular emphasis on the taxonomic distributions respective to primary oceanic zones and geographic regions (e.g., Tropical Atlantic, Transitional Atlantic, and the Mediterranean).[2, 4, 5] In addition, IR spectroscopic analysis may be useful for evaluating inter-species relationships based upon molecular consequences in the spectral features of coccolith formations. However, coccoliths are not the only significant source of biogenic carbonate with wide geographic distributions in deep-sea sediments. Planktonic foraminifera and pteropods are two additional primary sources of biogenic carbonates.[4, 5] Although the larger size of these carbonate formations compared to coccoliths limits their potential for generating traceable absorption features in the IR-ATR spectra of sediments, the fact that they are carbonate with a global prominence requires detailed considerations to fully assess their spectroscopic value.

It is additionally important to address the capabilities, limitations, and potential for quantitative and semi-quantitative applications for evaluating carbonate mineralogy within marine sediments with IR spectroscopy.

First, the semi-quantitative strategies utilized in this work limits highly accurate quantitative assessment of the relative calcite-dolomite compositions to the total sediment carbonate. However, despite the restricted accuracy, it has been demonstrated as a useful strategy for assessing large scale variability and general trends in shifting carbonate compositions. More careful considerations to sediment matrix compositions including quartz, clays, and carbonates are necessitated to improve quantitative capabilities for this evaluation strategy while adhering to established particle sizes of < 2 μm to ensure measurement accuracy and reproducibility.

Second, the quantification of total carbonate compositions in marine sediments with IR spectroscopy has been demonstrated previously in the published literature.[32, 38, 39] Although this application was not specifically addressed in this thesis, presented results are of particular

significance regarding the published work by Mecozzi et al.[32] They demonstrated the capability to quantify the total carbonate content in marine sediments through evaluation of the peak area respective to ν_3 carbonate absorption features. However, from this work there are perhaps two major oversights when projecting the potential capabilities for this evaluation strategy: (1) the developed analytical strategies would be widely applicable with exception to sediments with crude oil and (2) that the influence of additional carbonate species other than calcium carbonate would be negligible. In many marine environments, the influence of additional carbonate minerals or calcium carbonate polymorphs may be negligible. However, the variability and complexity of ν_3 absorption profiles with respect to calcium carbonate polymorphs and the origins of a single carbonate species, as demonstrated in the case of 'coccolith calcite', requires more careful considerations before generic implementation to ensure validity of proposed peak integration quantification methods. Chester and Elderfield displayed the capability to quantify total carbonate composition through peak height analysis with ratiometric correction for other major minerals in many types of marine sediments.[38] This strategy is advantageous to peak integration methods as peak height analysis is less susceptible to peculiar peak shapes. Overall, the few publications available limit a full assessment as to the capabilities of IR quantification strategies for characterizing all types of carbonates throughout the full range of in marine sediments in the Earth's oceans and seas. Until that has been fully demonstrated, specific considerations must be taken into account regarding local and regional processes that impact sediment matrix compositions (particularly carbonates) to ensure quantitative accuracy.

Lastly, despite the limited capability to fully address the adequacy and limitations for quantitative evaluation of carbonates in marine sediments with IR-ATR spectroscopy, the potential for developing robust quantitative methods applicable throughout diverse marine settings is not unrealistic. Through the development of chemometric algorithms, the full potential for IR spectroscopic strategies to quantify carbonate minerals in marine sediments may be realized.

Implementation of such data evaluation tools may enable direct quantification of carbonates in both dried sediments and native hydrated sediments, which is ideal for *in situ* applications. However, this will require rigorous data collection sets to realize this capability and correct for highly variable matrix compositions. Currently, the demonstration of simple, qualitative analysis for characterizing marine carbonates with IR-ATR spectroscopy in this work has significant potential to facilitate investigations for gaining new insight into globally significant phenomenon without necessitating highly accurate and precise quantitative capabilities. Ultimately, combining the utility of qualitative analysis with the development of accurate and precise quantitative characterization of carbonates throughout the diverse complexity of marine sediments should provide a powerful analytical tool for exploring the complexity of carbonate mineralogy within Earth's inner space.

6.8 References

1. R. W. Pierce and G. F. Hart, *Phytoplankton of the Gulf of Mexico: Taxonomy of Calcareous Nannoplankton*, (LSU Press, Baton Rouge, 1979).

2. A. Winter and W. G. Siesser, eds., *Coccolithophores*, (Cambridge Universtiy Press, Cambridge, 1994).

3. J. R. Young, M. Geisen, L. Cros, A. Kleijne, C. Sprengel, I. Probert, and J. Ostergaard, *A Guide to Extant Coccolithophore Taxonomy*, Journal of Nannoplankton Research **Special Issue**, 125 (2003).

4. H. R. Thierstein and J. R. Young, eds., *Coccolithophores - From Molecular Processes to Global Impact*, (Springer, Berlin, 2004).

5. J. D. Milliman, *Marine Carbonates*, (Springer, New York, 1974).

6. E. Paasche, *Biology and Physiology of Coccolithophorids*, Annual Review of Microbiology **22**, 71 (1968).

7. V. Pariente, *Coccolithophores of the Gulf of Mexico and Their Relationship to Water-column Properties*, Texas A & M University, p. 187, (1997).

8. P. M. Holligan, E. Fernandez, J. Aiken, W. M. Balch, P. Boyd, P. H. Burkill, M. Finch, S. B. Groom, G. Malin, and et al., *A Biogeochemical Study of the Coccolithophore, Emiliania huxleyi, in the North Atlantic*, Global Biogeochemical Cycles **7**, 879 (1993).

9. J. D. Milliman, *Production and Accumulation of Calcium Carbonate in the Ocean: Budget of a Nonsteady State*, Global Biogeochemical Cycles **7**, 927 (1993).

10. M. E. Marsh, *Regulation of CaCO3 Formation in Coccolithophores*, Comparative Biochemistry and Physiology, Part B: Biochemistry & Molecular Biology **136B**, 743 (2003).

11. C. W. Brown and J. A. Yoder, *Coccolithophorid Blooms in the Global Ocean*, Journal of Geophysical Research, [Oceans] **99**, 7467 (1994).

12. P. Ziveri, R. C. Thunell, and D. Rio, *Export Production of Coccolithophores in an Upwelling Region: Results from San Pedro Basin, Southern California Borderlands*, Marine Micropaleontology **24**, 335 (1995).

13. E. M. Hulburt and N. Corwin, *A Note on the Phytoplankton Distribution in the Offshore Water of the Eastern and Central Gulf of Mexico*, Caribbean Journal of Science **12**, 29 (1972).

14. W. L. Balsam and J. P. Beeson, *Sea-Floor Sediment Distribution in the Gulf of Mexico*, Deep-Sea Research, Part I: Oceanographic Research Papers **50**, 1421 (2003).

15. J. R. Young, J. M. Didymus, P. R. Bown, B. Prins, and S. Mann, *Crystal Assembly and Phylogenetic Evolution in Heterococcoliths* Nature **356**, 516 (1992).

16. M. Okazaki, T. Sato, N. Mutho, N. Wada, and T. Umegaki, *Calcified Scales (Coccoliths) of Pleurochrysis carterae (Haptophyta): Structure, Crystallography, and Acid Polysaccharides*, Journal of Marine Biotechnology **6**, 16 (1998).

17. B. L. Smith, G. T. Paloczi, P. K. Hansma, and R. P. Levine, *Discerning Nature's Mechanism for Making Complex Biocomposite Crystals*, Journal of Crystal Growth **211**, 116 (2000).

18. M. E. Marsh, A. L. Ridall, P. Azadi, and P. J. Duke, *Galacturonomannan and Golgi-derived Membrane Linked to Growth and Shaping of Biogenic Calcite*, Journal of Structural Biology **139**, 39 (2002).

19. K. Henriksen, S. L. S. Stipp, J. R. Young, and P. R. Bown, *Tailoring Calcite: Nanoscale AFM of Coccolith Biocrystals*, American Mineralogist **88**, 2040 (2003).

20. K. Henriksen, S. L. S. Stipp, J. R. Young, and M. E. Marsh, *Biological Control on Calcite Crystallization: AFM Investigation of Coccolith Polysaccharide Function*, American Mineralogist **89**, 1709 (2004).

21. R. Laguna, J. Romo, B. A. Read, and T. M. Wahlund, *Induction of Phase Variation Events in the Life Cycle of the Marine Coccolithophorid Emiliania huxleyi*, Applied and Environmental Microbiology **67**, 3824 (2001).

22. H. M. Stoll, Y. Rosenthal, and P. Falkowski, *Climate Proxies from Sr/Ca of Coccolith Calcite: Calibrations from Continuous Culture of Emiliania huxleyi*, Geochimica et Cosmochimica Acta **66**, 927 (2002).

23. L. V. Berlyand, N. V. Chukanov, and V. A. Dubovitskii, *Exactly Solvable Random Model and IR Spectroscopy of a Strained Defective Lattice*, Chemical Physics Letters **181**, 450 (1991).

24. G. Duyckaerts, *The Infrared Analysis of Solid Substances - A Review*, Analyst **84**, 201 (1959).

25. W. D. Bischoff, S. K. Sharma, and F. T. Mackenzie, *Carbonate Ion Disorder in Synthetic and Biogenic Magnesian Calcites: A Raman Spectral Study*, American Mineralogist **70**, 581 (1985).

26. J. Paquette and R. J. Reeder, *Single-crystal X-ray Structure Refinements of Two Biogenic Magnesian Calcite Crystals*, American Mineralogist **75**, 1151 (1990).

27. M. E. Bottcher, P.-L. Gehlken, and D. F. Steele, *Characterization of Inorganic and Biogenic Magnesian Calcites by Fourier Transform Infrared Spectroscopy*, Solid State Ionics **101-103**, 1379 (1997).

28. H. H. Adler and P. F. Kerr, *Infrared Spectra, Symmetry, and Structure Relations of Some Carbonate Minerals*, American Mineralogist **48**, 839 (1963).

29. R. Chester and H. Elderfield, *The Application of Infra-red Absorption Spectroscopy to Carbonate Mineralogy*, Sedimentology **9**, 5 (1967).

30. J. M. Hunt, M. P. Wisherd, and L. C. Bonham, *Infrared Absorption Spectra of Minerals and other Inorganic Compounds*, Analytical Chemistry **22**, 1478 (1950).

31. E. Loste, R. M. Wilson, R. Seshadri, and F. C. Meldrum, *The Role of Magnesium in Stabilising Amorphous Calcium Carbonate and Controlling Calcite Morphologies*, Journal of Crystal Growth **254**, 206 (2003).

32. M. Mecozzi, E. Pietrantonio, M. Amici, and G. Romanelli, *Determination of Carbonate in Marine Solid Samples by FTIR-ATR Spectroscopy*, Analyst (Cambridge, United Kingdom) **126**, 144 (2001).

33. F. B. Reig, J. V. G. Adelantado, and M. C. M. Moya Moreno, *FTIR Quantitative Analysis of Calcium Carbonate (Calcite) and Silica (Quartz) Mixtures using the Constant Ratio Method. Application to Geological Samples*, Talanta **58**, 811 (2002).

34. N. V. Vagenas, A. Gatsouli, and C. G. Kontoyannis, *Quantitative Analysis of Synthetic Calcium Carbonate Polymorphs using FT-IR Spectroscopy*, Talanta **59**, 831 (2003).

35. E. Gavish and G. M. Friedman, *Quantitative Analysis of Calcite and Mg-calcite by X-ray Diffraction. Effect of Grinding on Peak Height and Peak Area*, Sedimentology **20**, 437 (1973).

36. R. A. Berner, *Role of Magnesium in the Crystal Growth of Calcite and Aragonite from Sea Water*, Geochimica et Cosmochimica Acta **39**, 489 (1975).

37. R. Botz, E. Faber, M. J. Whiticar, and J. M. Brooks, *Authigenic Carbonates in Sediments from the Gulf of Mexico*, Earth and Planetary Science Letters **88**, 263 (1988).

38. R. Chester and H. Elderfield, *The Infra-red Determination of Total Carbonate in Marine Carbonate Sediments*, Chemical Geology **1**, 277 (1966).

39. T. D. Herbet, B. A. Tom, and C. Burnett, *Precise Major Component Determinations in Deep-Sea Sediments using Fourier Transform Infrared Spectroscopy*, Geochimica et Cosmochimica Acta **56**, 1759 (1992).

CHAPTER 7

TOWARDS A 2ND GENERATION OF SUBMERSIBLE MIR CHEMICAL SENSORS

This chapter presents design considerations and initial efforts towards the development of a 2nd generation submersible MIR chemical sensing platform for deep-sea exploration. The first part of this chapter focuses on a general overview of deep-sea spectrometers and progress towards a submersible FT-IR system with a spherical glass housing. Advantages and disadvantages of the proposed housing design are considered in addition to a general overview of common ATR sensor probe geometries. Following, experimental and ray tracing simulations are presented for characterization of ATR sensing surfaces. The described work demonstrates the utility of virtual test environments for assessing sensor probe design and fabrication, optical design, and integration into next-generation deep-sea MIR chemical sensors.

7.1 Spectrometers in the Deep-Sea

In recent years, mass, Raman, and FT-IR spectrometers have been introduced for a variety of deep-sea sensing applications. Mass spectrometers generally implement a membrane-based inlet system suited for the detection and monitoring of dissolved gases (i.e., O_2, CO_2, and CH_4) and a wide range of volatile organic compounds (VOCs).[1-10] Several Raman spectrometers have integrated different optical probes for exploring gas hydrate systems and hydrothermal vents, with particular interests in characterizing dissolved gases, gas hydrate structures and compositions, mineral components (i.e., SO_4^{2-}, NO_3^-, and CO_3^{2-}), and gas bubbles.[11-16] The only demonstrated submersible FT-IR spectrometer system used a U-shaped, polymer-coated AgX fiber-optic sensor head for investigating VOCs (i.e., tetrachloroethylene, 1,2-dichlorobenzene, and xylenes) with particular focus on coastal waters.[17-20]

Overall, submersible sensing platforms are suited for either mobile or stationary deployments. Mobile sensing objectives (primary application of current mass spectrometer systems) can range

from plume tracking to concentration profiling, and utilize state-of-the-art tracking and navigational systems for correlating analytical results with a precise time and sample location.[1, 2, 6, 9, 10] Navigational units are often integrated with the instrument carrier (i.e., AUV, remote operated vehicle (ROV), and/or main ship for tow-bodies).[6, 10] Short-term stationary sensing activities (primarily demonstrated by Raman-based platforms) have been facilitated with assisted deployment and interactive target acquisition with ROVs, which is a well-suited strategy for exploratory research.[12-16] Currently, deployments for described submersible sensing platforms have yet to be reported for durations extending beyond single dive sessions limited by carrier unit operational time.

Growing interest in the establishment of ocean observatories (i.e., the GOMGHRC's MC118 gas hydrate observatory and the ORION group's MARS and NEPTUNE observatory networks) has supported the development and integration of sensor technologies for long-term deployment. However, there are several factors collectively contributing to the lack of demonstrated long-term deployments of spectrometer systems in deep-sea environments: (1) systems testing, validation, and development, (2) need for recovering data from the instrument unit, (3) risk of losing one-of-a-kind, high-cost instruments, (4) operational costs (i.e., ship and submersible costs), and (5) power. Cost and power will likely remain enduring and limiting burdens; however, the underlying theme is the infancy of this field with only a limited number of instruments. The literature underscores that many of the developed instruments are capable of operating in extreme environments; yet, many are in still undergoing initial validation tests. With ever increasing numbers of deep-sea deployments and continuous system improvements to overcome the difficulties of sustained operation in deep-sea environments, it is only a matter of time until the described sensing platforms become a more common and vital asset for exploring the deep-ocean.

7.1.1 Submersible FT-IR Spectrometers

The history of deep-sea FT-IR spectrometers is rather brief with only one sensing platform described in the literature to date with a depth rating of approx. 500 m.[17, 18, 20] The described system implemented a Bruker Vector 22 FT-IR spectrometer encased in an aluminum cylindrical housing with a 38 cm active length of AgX fiber in a U-shaped geometry. The AgX fiber was coated with an ethylene-co-propylene membrane tailored to quantitative evaluation of VOCs. Overall, the complete system was approx. 1 m in length, 0.32 m in diameter, and a dry weight of approx. 95 kg.

7.1.1.1 Concept of 'Sphere-IR': A 2nd Generation Deep-Sea FT-IR Spectrometer

The design and construction of a smaller, lighter 2nd generation deep-sea FT-IR spectrometer, 'Sphere-IR', was initiated during this thesis; although, a completed system was not realized due to funding cutbacks. The instrument concept incorporates components from the commercially available, miniaturized Bruker IRcube FT-IR spectrometer (~17 kg with commercial housing) into a spherical glass housing (17" dia., 6,000 m depth rating with no penetrators (i.e., power and sensor probe) from Teledyne Benthos (North Falmouth, MA)). The instrument platform integrates a recently commercialized Stirling-cooled MCT detector (Model K508, Infrared Associates, Stuart, FL) with > 3,000 hrs of expected maintenance-free operation. **Figure 7-1** illustrates the overall design concept of 'Sphere-IR' with completed construction of the electronics sub-system and initial modeling of primary optics components.

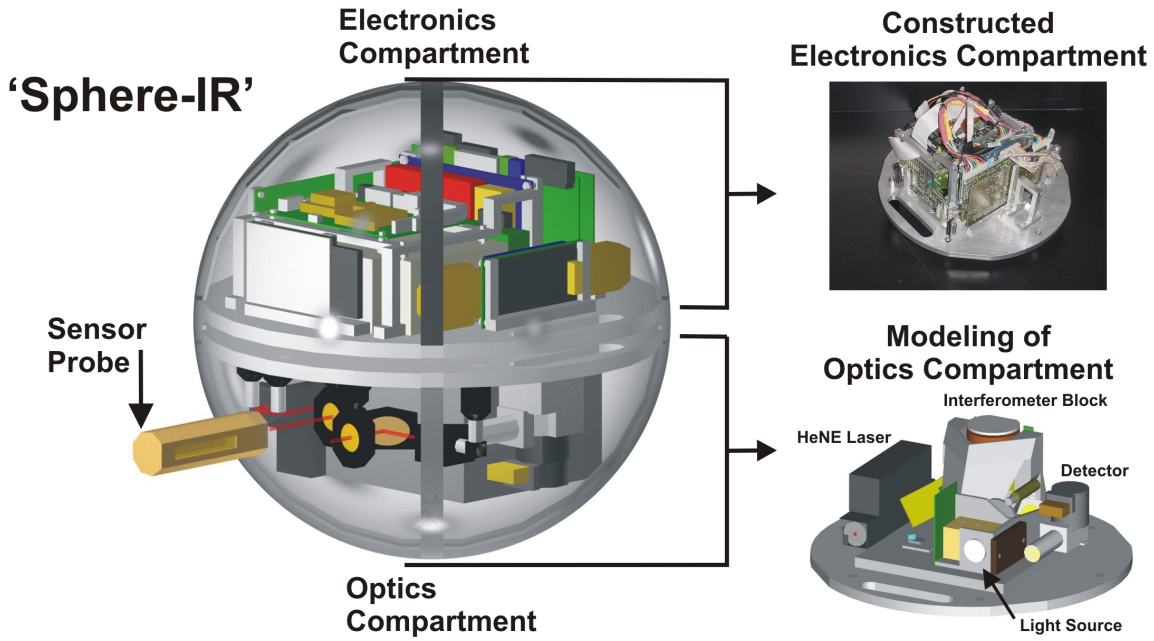

Figure 7-1: Conceptual scaled CAD rendering of the modeled 'Sphere-IR' unit indicating the design, construction, and incorporation of electronics sub-system components and initial modeling of primary optical components for the optics sub-system compartment.

In **Figure 7-1**, the design concept of 'Sphere-IR' includes two aluminum platforms for complementary optics and electronics compartments. The two platform system is designed to incorporate a compression system, which enables sealing and pressure compensation of the instrument housing by means of support struts for compressing and cinching the internal components in place without direct attachment to the glass unit. The submersible spectrometer was designed to include a single-board PC for operating spectrometer components, data collection, and on-board data evaluation strategies. Overall, 'Sphere-IR' is estimated to require between 140 – 175 Watts of power. To date, the electronics sub-system compartment has been constructed, and incorporates power distribution, signal processing, and computer control of instrument components to enable a low-powered "sleep" mode for intermittent measurement objectives. **Figure 7-2** displays a schematic for the electronics sub-system as designed by Dr. Frank Vogt.

Electronics Schematic

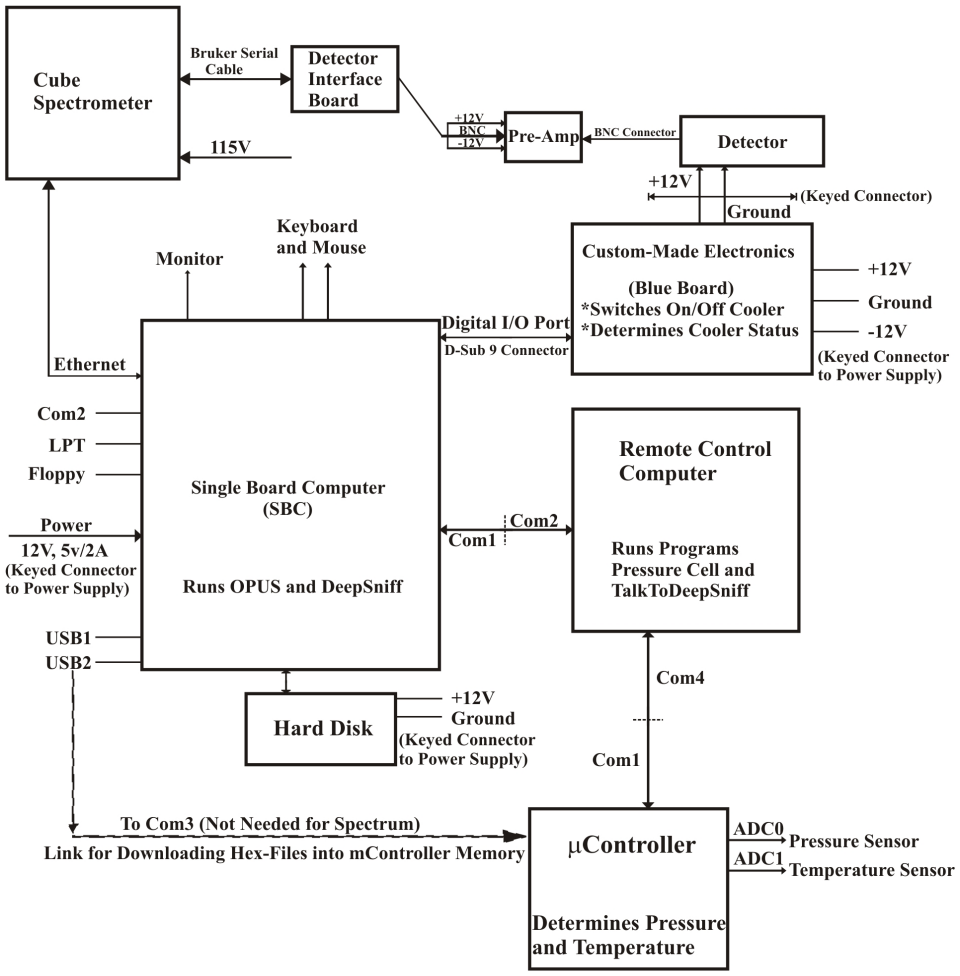

Figure 7-2: Schematic for the electronics sub-system designed by Dr. Frank Vogt. The IRcube spectrometer components are treated as a single entity in this diagram. (Drawing not to scale).

Following completed construction of the electronics compartment, the focus shifted towards design and construction of the optics compartment. CAD modeling of the primary optical components (**Figure 7-1**) was completed. However, fabrication of the optics compartment was not realized; limited by the design of an appropriate pressure-tested sensor head enabling selection of secondary optics components (i.e., mirrors, lens, etc.) and suitable configuration of all optical components. The indicated HATR sensor probe in **Figure 7-1** is only present for conceptual visualization with indication for the required penetration of the glass housing to spectroscopically access the external environment. **Sections 7.2** and **7.3** provide detailed

treatments considering various sensor probe configurations and an experimental and spectral ray tracing characterization of sensing regions on planar waveguide surfaces to facilitate development and incorporation of suitable sensor probes for 'Sphere-IR'.

7.1.1.2 Advantages and Disadvantages of 'Sphere-IR' Concept

Spherical instrument housings are attractive for minimizing the dry weight of a submersible instrument by enabling higher pressure ratings with thinner wall thicknesses than required to obtain the same pressure rating for a cylindrical housing.[21] In light of potential IR applications described in this thesis, the considerably large diameter of the current housing leads to anticipated difficulties for embedding a realized instrument into sediment matrices. Additionally, a sensor probe protruding from the glass housing, as illustrated in **Figure 7-1**, poses a substantial risk for shear forces to compromise system integrity. However, the housing material and reputation are of additional concern. Spherical glass housings have shown signs of degradation following multiple uses due to repeated pressurization and depressurization, causing splintering and ultimate peeling of glass sheets away from the housing.[22] Hence, this particular housing has a limited lifespan with continual degradation to structural stability and increased risk of failure after each use. An aluminum or titanium housing constructed to maintain the same form factor for incorporation of current design schemes can minimize long-term risk factors; however, glass spheres enable low-cost housing exchange when integrity is questionable or uncertain.

7.2 Sensor Head Design Considerations

The presence of Cl^- in solution continually diminishes the optical throughput of unprotected AgX fibers.[23, 24] U-shaped fiber degradation was eluded in measurement applications for the submersible FT-IR setup reported in literature from the use of a polymer enrichment membrane, which is necessary for signal enhancement of trace VOCs.[17] As demonstrated in this thesis, a variety of applications exist for IR-ATR sensing platforms whereby implementation of a polymer film would limit sensitivity by separating the evanescent field from interacting with sample

matrix components of interest. Hence, consideration of alternatives to polymer-coated AgX fibers is necessary to realize the full potential of MIR chemical sensors in oceanic environments.

An initial design goal of 'Sphere-IR' was to incorporate flexibility for the integration of replaceable sensor probes, which could implement various waveguiding materials (e.g., ZnSe, ZnS, etc.) and geometries (e.g., trapezoidal, conical, etc.). A variety of research applications have reported the use of commercially available ATR probes (Ocean Optics, StellarNet Inc., Remspec, Axiom Analytical, and Mettler Toledo)[25-29], and typically integrate fiber light guiding with diamond, ZnSe, or sapphire 2 – 6 bounce crystal elements.[30-38] Sapphire has a spectral cut-off at approx. 2000 cm^{-1}, which limits many practical applications for MIR sensors. Diamond crystals are expensive and can exhibit perturbations in the 2000 cm^{-1} regime with impurities.[39] ZnSe is a choice material for IR transparency; however, it is less rugged for high-pressure applications. Although a variety of ATR probes are commercially available, a custom high-pressure sensor probe incorporating a comparable trapezoidal ZnSe ATR element used in laboratory measurements was desired for to facilitate laboratory-like performance of 'Sphere-IR'. A prototype sensor probe was not constructed in this work; however, initial tests were performed to characterize signal generation along the measurement surface of a standard 72 × 10 × 6 mm trapezoidal crystal element to assist design and construction considerations.[40]

7.3 Characterizing 'Active' Sensing Regions along Trapezoidal ATR Waveguide Surfaces

Complementary experimental and spectral ray tracing analyses are described in this section for identifying and evaluating IR signal generation along the measurement surface of a standard trapezoidal HATR element. Ray tracing simulations provide a powerful tool for evaluating the design and performance of optical systems. The spectral ray tracing software used in this work, SPRAY (W. Theiss, Aachen, Germany), has been previously implemented for simulating IR absorption measurements of organic layers from complex three-dimensional optical environments modeling an FT-IR microscope.[41] In addition to computation of spectral absorption features, this

software enables the insertion of virtual detector elements anywhere within the simulated space for visualizing radiation distributions along optical paths. Hence, this aid provides a virtual environment suited for development and performance evaluation for a vast range of conceivable optical systems such as compact MIR sensing platforms.

Experimental collection of IR-ATR absorption spectra from a series of discrete poly(styrene-co-butadiene) (PSCB) deposits along the measurement surface of a standard 72 × 10 × 6 mm, 6-reflection ZnSe HATR crystal enabled the extraction of precise locations for individual sensing regions and the radiation path through the HATR crystal. This allowed formulation of spectral ray tracing procedures to accurately simulate experimental measurements. Through the comparison of normalized experimental and simulation data, accurate estimates of the experimental radiation parameters were derived. Consequently, a narrow range of two-dimensional representations for HATR experimental sensing regions were generated. The following sub-sections provide a detailed description of this work and demonstrate the utility for implementing virtual environments to assist the development and optimization of efficient IR-ATR sensing platforms for deep-sea environments.

7.3.1 Experimental

7.3.1.1 Instrumentation

All IR-ATR measurements were collected using a Bruker IFS 66/S FT-IR spectrometer (Bruker Optics Inc, Billerica, MA) fitted with a Specac Gateway in-compartment HATR unit (Specac Inc, Woodstock, GA). A standard 6-reflection, 72 × 10 × 6 mm ZnSe crystal with 45° coupling facets and 1 mm 90° chamfers at each end of the 72 mm-axis was mounted in a custom horizontal flow cell. The top plate of the flow cell was removed for sample droplet deposition onto the measurement surface. The spectrometer was equipped with a KBr beamsplitter, ZnSe windows (dia. 40 mm) at the radiation inlet/outlet of the sample compartment, and an Infrared Associates D316/6 LN_2 cooled MCT detector (Infrared Associates, Stuart, FL) with a 1 × 1 mm detection

element. The distance from the radiation inlet (ZnSe window) to the focal point in the sample chamber of the spectrometer is 128 mm. An Olympus BX41 optical microscope (Olympus America Inc., Melville, NY) with a x2.5 objective was used to evaluate the dimensions and repeatability of polymer droplet deposition at the ZnSe sensing surface.

7.3.1.2 Materials

A 10% (w/v) solution of PSCB in toluene was prepared by dissolving 1.0063 g of polymer (Aldrich Chemical Company, Milwaukee, WI) in 10 mL of toluene (Certified ACS grade, Fisher Scientific, Fair Lawn, NJ) at room temperature with brisk mixing for 1 hr. The polymer solution was stored in a refrigerator at 2 °C. Polymer residues were formed following deposition of 0.75 μL aliquots of solution at the crystal surface with a calibrated 0.50 – 10 μL Eppendorf pipet (Eppendorf North America Inc., New York, NY).

7.3.1.3 Ray Tracing Simulation Environment

A 5-component model was devised to represent the experimental configuration in real dimensions for spectral ray tracing simulations with a constant environmental refractive index of 1.0003 using SPRAY software (W. Theiss, Aachen, Germany). The simulated set-up modeled in-coupled radiation as a circular light source such that the internal reflection angle ($\theta_{int,}$) equaled the beveled HATR element coupling facet angles (45°). The circular light source was positioned at the 45º in-coupling facet, and was off-set from the central axis of the modeled 72 × 10 × 6 mm HATR element; closely emulating experimental conditions. The HATR element was assigned a constant refractive index of 2.44 corresponding to that of ZnSe at λ = 2.75 μm. A 72 × 10 mm rectangular screen was implemented for imaging the radiation distribution along the measurement surface of the HATR element. In addition, a 40 × 42.4 mm rectangular detector element was modeled in parallel to the beveled radiation exit facet of the crystal. Hence, all photons transmitted through the HATR waveguide during simulation measurements were collected by this detector for generating IR absorption spectra of simulated polymer deposits.

To simulate the spectral response of deposited PSCB residues, a 2.5 mm dia., closed cylinder was assigned a constant refractive index of 1.4 using a harmonic oscillator to simulate an arbitrary IR absorption band at 1443 cm^{-1} (oscillator strength: 30, damping constant: 1). For simulations, the deposit was defined as an absorbing cylindrical thin-film (20 μm thickness) virtually placed 'inside' the HATR element near the measurement surface (30 μm). As the radiation distribution at each reflection region inside an HATR element provides a very close approximation of the resulting 2-dimensional evanescent field profile generated at the interface between the optically dense and the optically rare media, this model enables the direct comparison of normalized measurement data between experimental IR-ATR measurements and simulated IR transmission-absorption measurements. Additional simulation parameters are provided in **Appendix A-6**.

Integration of the large detector element for measurement simulations enabled the capability to evaluate signal generation for virtually any combination transmitted radiation parameters, including the in-coupled light source radius, radiation cone angle, and in-coupling position, without requiring precise dimensional modeling or configuration of optical components for a particular experimental setup. Furthermore, this simple model represents an ideal experimental situation of precise imaging optics with the focal plane of radiation on the order of detector element size. Tradeoffs and consequences of this modeling approach are addressed with discussion of two-dimensional approximations of sensing regions and error considerations in **Section 7.3.3.2** and **Section 7.3.3.3**, respectively.

7.3.2 Measurement and Simulation Procedures

7.3.2.1 Experimental Data Acquisition

20 polymer deposition locations were marked along the measurement surface of a ZnSe crystal with an ultra fine point black permanent marker (Sharpie) at 3 mm intervals, excluding the first 8 mm from the in-coupling facet and the last 7 mm prior to the exit facet, before polymer

deposition and collection of the respective IR-ATR spectra. The first and last 4 mm of crystal surface were inaccessible from waveguide mounting in the modified flow cell. Hence, the first and sixth internal reflection regions were not fully resolved with experimental measurements. IR absorption features from the permanent marker were negligible and effectively eliminated after collection of an initial background (reference) measurement following marker application and prior to the first polymer spot deposition. All PSCB/toluene aliquots were deposited without disrupting or removing the crystal mounting unit. Reference spectra were collected prior to the deposition of each 0.75 μL PSCB/toluene droplet. After each sample deposition, 15 spectra were recorded at 2 min intervals, allowing evaporation of toluene and providing a robust signal for the remaining PSCB residue. IR-ATR spectra were the average of 100 sample scans at 2 cm^{-1} resolution from 4000 – 400 cm^{-1} while the instrument was purged with dry air. The light source aperture was set at 4 mm.

Additional experiments were performed utilizing a continuously variable iris diaphragm (maximum opening of 2.5 cm) for approximating the solid cone angle of radiation propagated to the MCT detector element with and without the in-compartment HATR accessory. The iris diaphragm was centrally positioned in the spectrometer sampling compartment respective to the radiation inlet with a 6 mm space between the inlet and iris diaphragm. Radiation impingent upon the detector element was recorded as arbitrary energy units (ADC counts) displayed by the Bruker OPUS software package for the same eight aperture diameters in each scenario. Aperture diameters were set by closing the iris diaphragm to values between 0.3 cm and 2.0 cm with aid of a vernier caliper. Instrument source apertures during measurements with and without the in-compartment ATR accessory were 4 mm and 2 mm, respectively.

7.3.2.2 Simulated Data Acquisition

Simulated IR absorption measurements were collected from 1900 – 900 cm^{-1}. A spectral resolution of approx. 8 cm^{-1} was defined for all simulations with 120 sample points spanning 1000 cm^{-1}. The light source was set to emit 125 photons per spectral point. Simulation series were

performed for various combinations of light source radii and radiation cone angles. All simulation cone angle values represent the cone angle of radiation as it is transmitted through the simulated ZnSe HATR crystal. For each simulation measurement series, a reference spectrum was generated with the cylindrical thin-film placed in a non-reflection (no absorption) region of the HATR element. After collecting a reference spectrum, simulated transmission-absorption measurements were performed consecutively as the cylindrical thin-film was positioned along the crystal surface corresponding to deposition locations in experimental studies. All simulated data were exported from SPRAY as percent transmission with respect to wavenumber for further data analysis. For all simulations, a single run was performed for each set of optical parameters and deposition location.

7.3.2.3 Experimental Data Analysis

Eight spectral regions corresponding to IR absorption features of PSCB were evaluated by integrating respective peak areas. An IR-ATR spectrum of a PSCB residue with highlighted and numbered spectral regions used for data analysis is provided in **Figure 7-3** with detailed peak integration regions listed in **Table 7-1**. **Figure 7-3** also contains peak area evaluations for PSCB residues deposited at representative internal reflection and non-reflection regions, where the peak areas from 15 consecutive measurements are plotted versus time following aliquot deposition. A generally stable IR signal was observed during the last five measurements; therefore, peak areas for these five measurements with respect to each spectral region were averaged and used for further calculations. For simplification, the five averaged peak areas for a given spectral feature will be indicated as a singular peak area (PA) from here on.

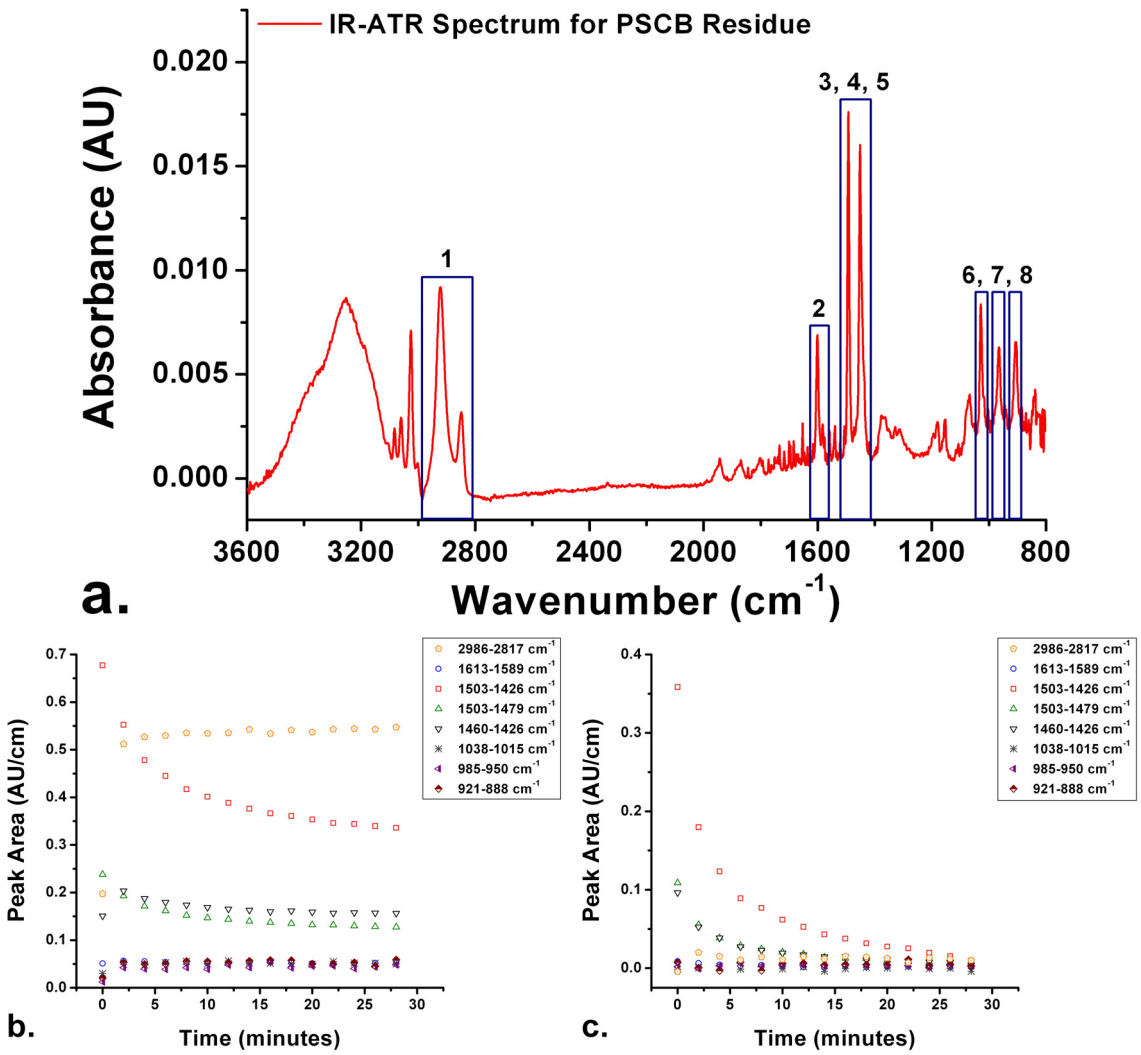

Figure 7-3: (a.) Representative IR-ATR absorbance spectrum of PSCB with highlighted spectral features utilized for peak area evaluation. Spectral regions are provided in **Table 7-1**. Peak area values obtained for PSCB absorption features for (b.) internal reflection and (c.) non-reflection regions along the ZnSe waveguide surface.

Table 7-1: Spectral regions used for evaluation of IR-ATR absorbance spectra of PSCB residues.

Highlighted PSCB Spectral Features in Figure 7-3	**Region (cm^{-1})**
1	2936 – 2817
2	1613 – 1589
3	1503 – 1426
4	1503 – 1479
5	1460 – 1426
6	1038 – 1015
7	985 – 950
8	921 – 888

The central location for individual internal reflection elements along the waveguide surface were determined utilizing normalized PAs from 5 consecutive residues at 3 mm intervals in the spatial region for each reflection. PAs were plotted versus the respective distances from the in-coupling facet and fit with the Gaussian function:

$$y = y_0 + \frac{A}{w\sqrt{\pi/2}} e^{-2\frac{(x-x_c)^2}{w^2}}$$

Equation 7.1

From **Equation 7.1**, x_c provides the Gaussian peak center, corresponding to distance from the in-coupling facet for the reflection center. The described fitting procedure assumes an axially symmetric radiation profile; however, this does not imply that the true radiation distribution and resulting signal generation profile is Gaussian. Other symmetric functions such as a Lorentzian curve can be used in lieu. In this work, a Gaussian bandshape provided consistently superior fitting results reflected by larger R^2 values in contrast to Lorentzian curve fits.

Normalized PAs for each spectral region and spot location were used to extrapolate the center of individual reflection elements. All data were normalized to the highest observed PSCB absorption for the respective spectral regions. From all residue positions, the highest PAs, regardless of spectral region evaluated, were observed at the deposition site corresponding to 17 mm from the in-coupling facet. Averages of all normalized PAs for the eight spectral regions for each deposition location were also calculated and fit with a Gaussian profile. In addition, the average of all PAs from the eight spectral regions for each deposition location were calculated and then normalized for fitting with the Gaussian function. Reflection center values for experimental measurements are presented as the average and standard deviation for these three fit procedures.

To facilitate determination of the solid cone angles of radiation transmitted to the instrument detector with and without the in-compartment HATR accessory, iris diaphragm diameters and a

constant focal point distance of 122 mm inside the sample compartment (accounting for the 6 mm diaphragm offset) were used to calculate the radiation cone angle allowed to propagate with respect to each iris setting. ADC counts contributing to the overall signal throughput (total ADC counts measured with largest diaphragm opening) for each diaphragm setting were calculated by $R_2 = C_2 - C_1$, where C_1 and C_2 are the total ADC counts from successive diaphragm settings, R_2 is the contributed ADC counts for the larger diaphragm opening, C_1 is the total measured ADC counts for the smaller diaphragm setting, and C_2 is the total ADC counts measured for the larger diaphragm setting. The percent of total radiation coupled through to the detector was calculated by $P = R_2/C_T)*100$, where P is the percentage of total signal throughput for the larger diaphragm setting used in calculating R_2, and C_T is the total ADC counts for the largest diaphragm setting. The average radiation density for the exposed area between two successive diaphragm settings was calculated by $D = (C_2 - C_1)/(A_2 - A_1)$, where D is the radiation density represented as ADC counts per cm^2, C_1 and C_2 follow the description above, and A_1 and A_2 are the respective open diaphragm areas for the corresponding settings at C_1 and C_2. Values for the described measurements and calculations are given in **Table 7-2**.

7.3.2.4 Spectral Ray Tracing Data Analysis

Exported transmission (*T*) data were converted into absorption (*A*) spectra following the transformation $A = -\log T$. A background correction was applied to all data for each simulation series by subtracting the respective transformed transmission reference spectrum from the absorption spectra. Infrared absorption spectra were then evaluated by integrating peak areas across the entire simulated spectral region of 1900 – 900 cm^{-1}. Representative absorption spectra for simulated reflection and non-reflection regions are provided in **Figure 7-4**.

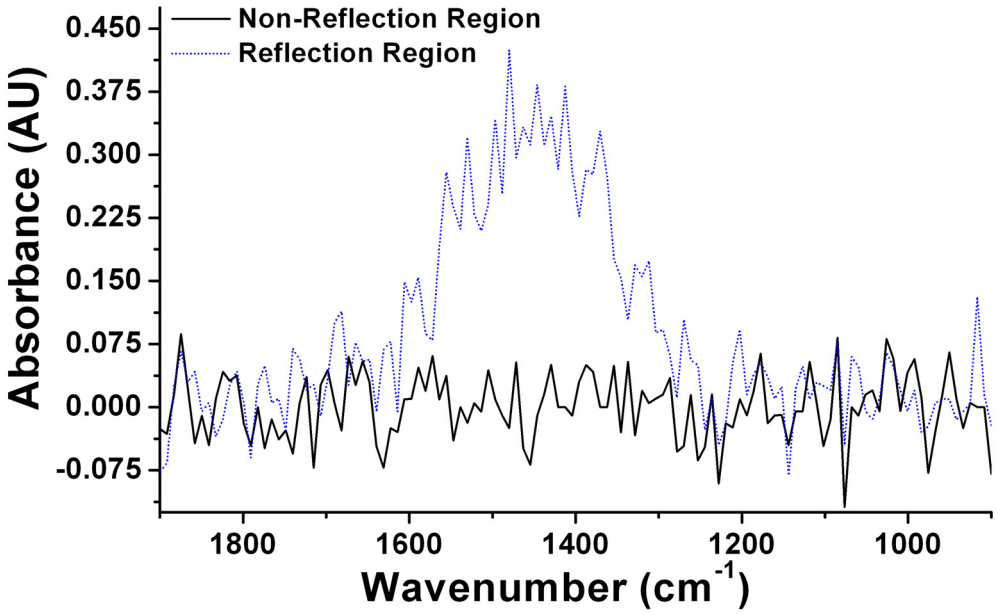

Figure 7-4: Representative absorbance spectra from a simulated HATR reflection and non-reflection region.

The center of each internal reflection region along the HATR measurement surface was calculated for each simulation series from normalized PAs and the same Gaussian fit procedure described for experimental data evaluation. Peak areas for each simulation series were normalized to the highest observed absorption value, which always corresponded to a distance of 17 mm from the in-coupling facet. Calculated peak centers for simulation measurements are presented as the average and standard deviation of values obtained for all presented simulation series with combinations of cone angles from 1° – 16° and light source radii from 0.00215 cm – 0.1697 cm.

The quality of match between normalized experimental and simulation data was evaluated as total residual error (TRE) based on the sum-of-squares of the residuals with respect to experimental data for all deposition locations from 11 mm to 59 mm. TRE was calculated for each combination of cone angle and light source radius. In addition, TRE values for the averages of normalized PAs for the three best matched combinations of cone angles with a constant light source radius of 0.1278 cm (CLSR), the three best matched combinations of light source radii with a constant

cone angle of 2° (CCA), and the averages of normalized PAs for the three best overall matching combinations were calculated.

7.3.3 Results and Discussion

7.3.3.1 Experimental Results

The described experimental procedure enables visualization and evaluation of spatially resolved sensing regions along a HATR element from the investigation of evanescent field interactions with an IR active species (**Figure 7-5**). **Figure 7-5 (a.)** depicts PSCB residues deposited along the central axis for the 72 × 10 mm measurement surface of a ZnSe HATR crystal. PSCB absorption values (displayed as PAs) for each residue and the eight evaluated spectral regions are plotted versus distance from the in-coupling facet of the HATR crystal in **Figure 7-5 (b)**. From this plot, four distinct sensing regions are evident with onset of a fifth region near the exit facet. Sensing regions are indicated by larger PAs relative to regions with little or no evanescent field interaction with PSCB residues resulting in near zero PAs. **Figure 7-5 (c.)** contains a surface map displaying an approximated signal generation profile for PSCB deposits along the crystal measurement surface generated by data extrapolation of Gaussian fits utilized for calculating peak centers. The two-dimensional representation in **Figure 7-5 (c.)** does not reflect the actual 'active' width per individual sensing region, as measurements were only taken along one transect of the measurement plane. Additionally, the Gaussian function only provides an approximation of the actual signal profile for each reflection region. A thorough treatment of two-dimensional approximations is contained in the ensuing discussion.

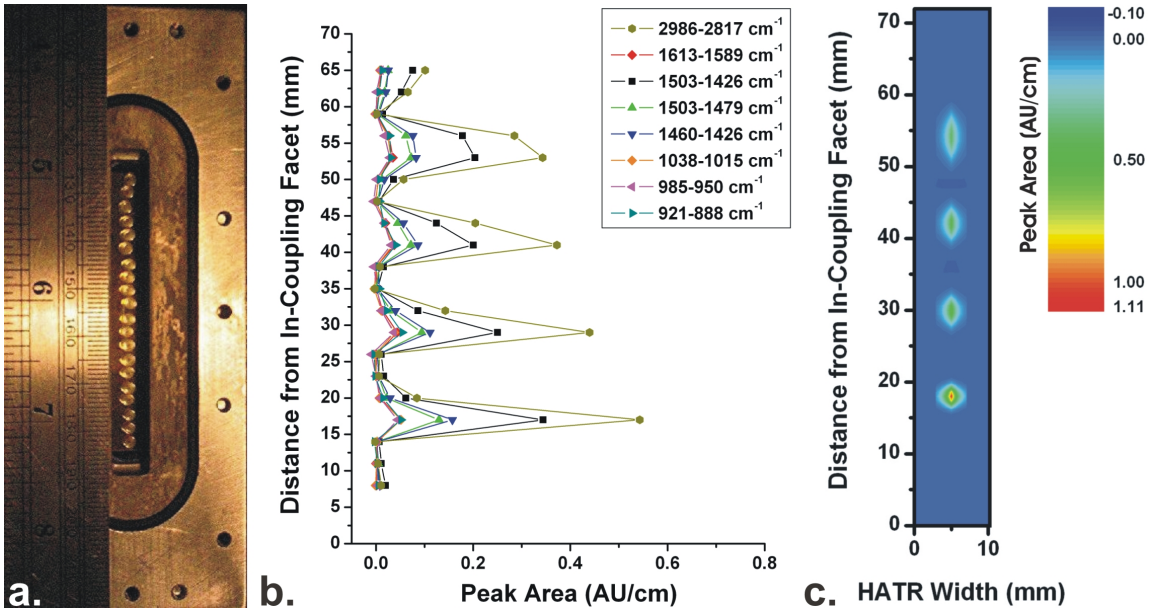

Figure 7-5: (a.) Optical image of PSCB deposits along the HATR crystal surface mounted in a topless flow cell. (b.) Absorption intensity (as PAs) of PSCB vs. distance from the in-coupling facet along the measurement surface.* (c.) Surface map projecting the absorbance intensity of PSCB residues along the measurement surface of a HATR crystal and displaying discrete 'active' sensing regions along the crystal surface.** (* Lines are for assisting visual inspection. ** Plot generated from PAs for PSCB absorbance in the spectral region from 2986 – 2817 cm^{-1}).

For spatially resolving individual internal reflection regions, the experimental procedure was designed by adapting the Nyquist theorem from a temporal consideration to a one-dimensional spatial treatment. According to the Nyquist theorem, it is necessary to sample at least 2x the signals highest frequency component to extract all available information. The Nyquist theorem is generally presented in the form $f < 1/(2\,\Delta t)$, where f is the signals highest frequency component and Δt is the time interval between samples. In this work, the equation was adapted to $f < 1/(2\,\Delta x)$, where f represents the highest spatial frequency component and Δx is the distance between PSCB deposits. For a 6 mm thick ATR crystal with light coupled at 45°, the internal reflection frequency is 1 reflection per 12 mm along the measurement surface ($f = 0.083$). Thus, a sampling frequency of 4 deposition spots per 12 mm ($1/(2\,\Delta x) = 0.17$) adequately fulfills sampling requirements for the adapted version of the Nyquist theorem.

Experimentally, this was achieved by depositing 2.5 mm dia., PSCB residues at discrete 3 mm intervals along the HATR surface. An improved spatial resolution could potentially be achieved by depositing smaller residues at shorter intervals. However, smaller residues could result in a systematic bias for characterizing smaller 'active' sensing regions towards the exit facet due to reduced signal strength from less spatial interaction with the evanescent field and decreased evanescent field intensity at each successive sensing region from radiation divergence.

A well-defined decay profile in the PSCB absorption behavior with respect to each successive sensing region was observed with increasing distance from the in-coupling facet. This is a result of the spatial dependence from both the overlap of PSCB residues with the evanescent field and the evanescent field intensity probing the PSCB deposits. In these experiments, the PSCB spot diameter was held constant; therefore, precise knowledge regarding three experimental descriptors is required to accurately account for the observed decay behavior: (1) the radiation path through the HATR crystal, (2) the through-coupled solid radiation cone angle, and (3) the diameter of the radiation cone coupled into the HATR crystal.

Radiation Path through the HATR Crystal:

The path of radiation propagated through the HATR crystal, as determined by the position of radiation incident at the in-coupling facet and θ_{int}, dictates the precise location of each reflection region along the measurement surface. Hence, by precisely determining the location of each reflection region, the path of radiation can be defined and the position of in-coupled radiation at the entrance facet and θ_{int} can be extrapolated.

For a 72 mm long and 6 mm thick trapezoidal crystal with radiation coupled orthogonally into the 45° in-coupling facet, θ_{int} is 45°, and a simple ray optic calculation reveals 6 reflections spaced 12 mm apart along the sensing surface. Hence, the central location for each internal reflection element along the 72 mm axis is only dependent upon the position of in-coupled radiation at the entrance facet. If incident radiation is assumed to be centered at the midpoint of the 45° beveled

section, the central locations for internal reflections along the 72 mm axis are calculated as 6 mm, 18 mm, 30 mm, 42 mm, 54 mm, and 66 mm from the in-coupling facet.

The average centers of reflection from experimental data for the 2nd through 5th internal reflections were determined to be 17.97 mm ± 0.11 mm, 30.17 mm ± 0.09 mm, 42.14 mm ± 0.06 mm, and 54.22 mm ± 0.01 mm, respectively, with standard deviations reflecting the relative variance. Calculated reflection centers for each identified sensing region are in excellent agreement with values predicted by ray optic calculations for a radiation path with $\theta_{int} = 45°$ and orthogonally incident radiation on the midpoint of the beveled section at the in-coupling facet.

Based on this excellent agreement, the 1st and 6th internal reflection centers were extrapolated by subtracting and adding the average difference of distances between each consecutive identified reflection center (12.06 mm ± 0.15 mm) to the 2nd and 5th reflection center values, respectively. The extrapolated positions were calculated to be 5.90 mm ± 0.15 mm and 66.28 mm ± 0.15 mm for the 1st and 6th reflections, respectively. The extrapolated values are again in excellent agreement with values predicted for the defined radiation path obtained from ray optic calculations. Finally, the experimental radiation path through the ATR crystal was verified utilizing the calculated reflection centers to extrapolate θ_{int} and the position of light coupled into the beveled facet. The experimental internal reflection angle was calculated as 45° ± 1°, and the calculated position of radiation at the in-coupling facet deviated only 0.07 mm ± 0.14 mm towards the measurement surface from the midpoint of the 45° beveled section.

Through-Coupled Solid Radiation Cone Angle:

To evaluate the through-coupled solid cone angle of radiation incident upon the detector element, measurements were performed to assess detector signal (in ADC counts; saturation at 32,676) with respect to a range of iris diaphragm diameters (values provided in **Table 7-2**). Approximately 99% of the total through-coupled radiation was detected with an open diaphragm

diameter of 2 cm; corresponding to a radiation cone angle of 9.4° in air (3.8° in ZnSe). However, the average radiation density across the exposed region between the 2 cm and 1.5 cm settings reveal a relatively low signal of approx. 655 ADC counts per cm^2. Radiation density successively increases toward the radiation center with a maximum of approx. 31,120 counts per cm^2 for a 0.3 cm iris aperture. From the estimated radiation density values in **Table 7-2**, the potential for signal generation relative to the highest radiation density diminished to approx. 5% after an aperture of 1.2 cm with a 5.6° radiation cone angle in air (2.3° in ZnSe).

Table 7-2: Experimental characterization of through-coupled radiation with and w/out the HATR accessory present in the instrument sample compartment. (* R_2 values are the ADC counts contributed to the overall signal throughput for the respective diaphragm settings. ** P is the percentage of total radiation throughput with respect to values of R_2. *** D is the calculated average radiation density as ADC counts per cm^2 for the area exposed between successive diaphragm settings).

Through-Coupled Radiation with In-Compartment ATR Accessory and 4 mm Source Aperture						
Diaphragm Opening (cm)	**Cone Angle (Air)**	**Cone Angle (ZnSe)**	**Total Signal (ADC Counts)**	**R_2***	**P****	**D*****
2.5	11.7°	4.8°	14900	200	1.3	113
2	9.4°	3.8°	14700	900	6.0	655
1.5	7.0°	2.9°	13800	1000	6.7	1572
1.2	5.6°	2.3°	12800	1300	8.7	3761
1	4.7°	1.9°	11500	2100	14.1	7426
.8	3.8°	1.6°	9400	3400	22.8	11099
.5	2.3°	0.94°	6000	3800	25.5	30236
.3	1.4°	0.57°	2200	2200	14.8	31120
Through-Coupled Radiation w/out In-Compartment ATR Accessory and 2 mm Source Aperture						
Diaphragm Opening (cm)	**Cone Angle (Air)**	**Cone Angle (ZnSe)**	**Total Signal (ADC Counts)**	**R_2**	**P**	**D**
2.5	11.7°	4.8°	Saturated	NA	NA	NA
2	9.4°	3.8°	31800	8300	26.1	6038
1.5	7.0°	2.9°	23500	6300	19.8	9902
1.2	5.6°	2.3°	17200	3500	11.0	10127
1	4.7°	1.9°	13700	1900	6.0	6719
.8	3.8°	1.6°	11800	6200	19.5	20239
.5	2.3°	0.94°	5600	3500	11.0	27849
.3	1.4°	0.57°	2100	2100	6.6	29705

Assuming an axial-symmetric radiation distribution, a two-dimensional approximation of the radiation density profile for internal reflection elements can be generated by plotting each value of D with respect to the aperture center (represented as 0) at ± the radius of the larger diaphragm

setting used for calculations (**Figure 7-6**). Fitting of this plot with a Gaussian profile from **Equation 7.1** provides a close functional resemblance, and yields an R^2 value of approx. 0.97. Radiation densities listed in **Table 7-2** do not indicate the absolute radiation density for each reflection region. These values will be larger as a result of focusing onto the in-coupling facet with a successive decrease at each reflection region from divergence. However, the proportionality of these values should be conserved.

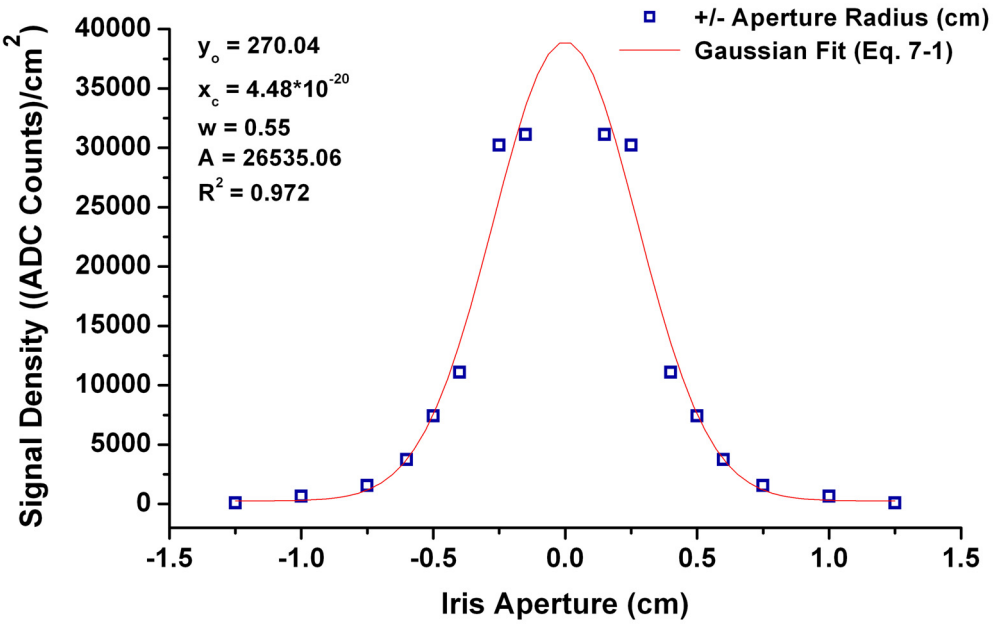

Figure 7-6: Calculated signal densities across each incremental area exposed with stepped iris aperture diaphragm settings and the ATR bench placed in the sample chamber. Signal densities are plotted ± the aperture radius in cm with 0 representing the aperture center positioned on the central axis of radiation propagation. The Gaussian fit provides a close functional resemblance to the data plot assuming an axial-symmetric radiation profile.

The instrument source aperture for iris diaphragm measurements without the HATR accessory required a decrease from 4 mm to 2 mm to avoid detector saturation. This indicates that radiation has been vignetted from the detector element in addition to reflection losses occurring at the in-coupling facet. From **Table 7-2**, it is evident that through-coupled radiation at diaphragm settings > 1 cm without the HATR accessory is almost entirely vignetted following addition of the HATR accessory. Thus, the largest through-coupled radiation cone angle contributing to the majority of

detected signal was determined to be between 4.7° and 7° in air (1.9° and 2.9° in ZnSe). Vignetted radiation, regardless of source (e.g., instrument focusing optics, detector element size, and/or presence of the HATR accessory optics), restricts efficiency of the total optical throughput (signal intensity) by filtering radiation that may actually propagate through the ATR element. In addition, the two-dimensional image of 'active' sensing regions along the HATR surface can be influenced due to vignetting with partial filtering of instrument radiation through-coupled to the detection element.

Diameter of In-Coupled Radiation Cone into the HATR Crystal:

To approximate the actual dimensions of 'active' sensing regions along the measurement surface, precise knowledge of the radiation path, through-coupled cone angle, and diameter of the through-coupled radiation cone at the HATR in-coupling facet is required. The radiation path and through-coupled cone angle, described previously, govern the relative dimensions of successive 'active' sensing regions with respect to beam divergence and location of each reflection region in the radiation path. However, without knowing the diameter of in-coupled radiation cone into the HATR crystal, accurate dimensions cannot be defined. With an estimated range of through-coupled cone angles and a defined radiation path respective to fixed instrument optical components, the relative position of the HATR element in the optical path will dictate the diameter of the through-coupled radiation cone incident upon the in-coupling facet and resultant dimensions of each measurement region. A direct and accurate determination of the in-coupled diameter of radiation is not readily available without exact knowledge of the instrument focal point diameter and the influence of HATR accessory optical components. Thus, complementary spectral ray tracing simulations were used to assist in approximation of this value in addition to confirming experimental estimates of the through-coupled cone angles for the defined radiation path. Once a complete set of experimental values are obtained, two-dimensional representations for 'active' sensing regions can be approximated.

7.3.3.2 Ray Tracing Results

In this study, approx. 50 simulation series were performed with various combinations of light source radii and cone angles ranging from 0.00215 cm – 0.25 cm and 1° – 16°, respectively. From all series, model data obtained with the following combinations most closely emulated experimental results in this study: (1) 0.1278 cm ± 0.042 cm light source radii with a constant cone angle of 2° (CCA), and (2) a constant light source radius of 0.1278 cm with cone angles of 2° ± 1° (CLSR). To compare simulation and experimental results, an average of normalized PAs for each of these simulation sets were calculated. **Figure 7-7** exhibits simulation values plotted with respect to deposit locations along the HATR element alongside experimental results representing the average of normalized PAs from all investigated PSCB spectral regions. Error bars for simulation data represent ±1 standard deviation from the average of normalized PAs for each deposit location for CCA and CLSR simulation sets, respectively. Error bars for experimental data represent the relative variance (±1 standard deviation) of normalized PAs from all evaluated PSCB features. In **Figure 7-7**, the net decrease in IR absorption behavior for each successive sensing region in both simulation (CCA and CLSR) and experimental data resemble each other exceptionally well with a TRE of 0.119 for the CCA set and 0.123 for the CLSR set.

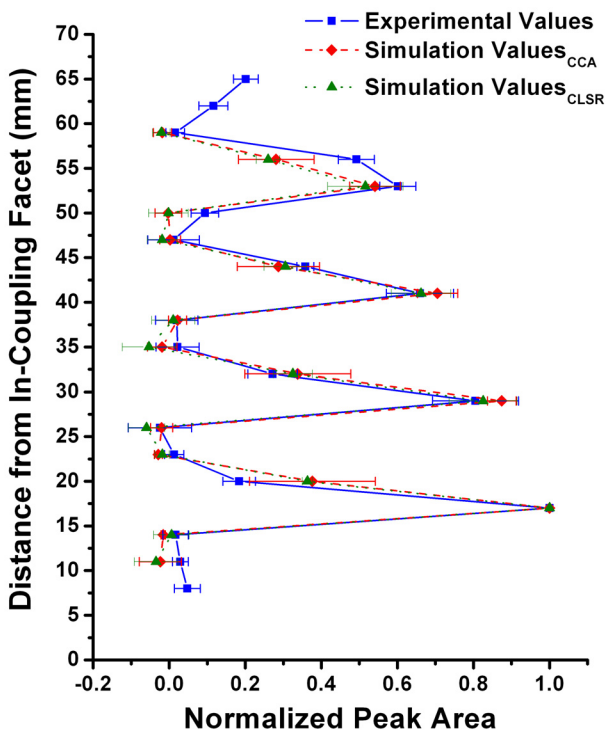

Figure 7-7: Averages of normalized PAs for experimental and simulation data*,** with respect to the measurement location plotted versus distance from the in-coupling facet of the HATR crystal (error bars are ± 1 standard deviation).*** (* Simulation Values$_{CCA}$ represent normalized and averaged PAs for data obtained with combinations of a 0.1278 cm ± 0.042 cm light source radii with a constant cone angle (CCA) of 2°. ** Simulation Values$_{CLSR}$ represent normalized and averaged PAs for data obtained with combinations of a constant light source radius (CLSR) of 0.1278 cm with cone angles of 2° ± 1°. *** Lines are present for assisting visual inspection).

In addition, ray tracing simulations were performed to aid visualization of the influence different cone angles (2°, 4°, 8°, and 16°) have on the spatial distribution of radiation at sensing regions along the measurement surface of the simulated HATR element. **Figure 7-8** provides simulated surface maps of the radiation distributions obtained for increasing cone angles (designated as 2°, 4°, 8°, and 16°) with a constant light source radius of 0.1278 cm. Qualitative visual inspection of experimentally generated and simulated surface maps (displaying all 6 internal reflection regions) yield excellent comparisons for both 2º and 4º simulation plots. However, upon inspection of normalized quantitative data, it was determined that simulated measurements generated with cone angles ≥ 4º reveal enhanced deviations from the experimental data. Thus, a cone angle of 2° was determined to provide a more appropriate representation of the experimental setup.

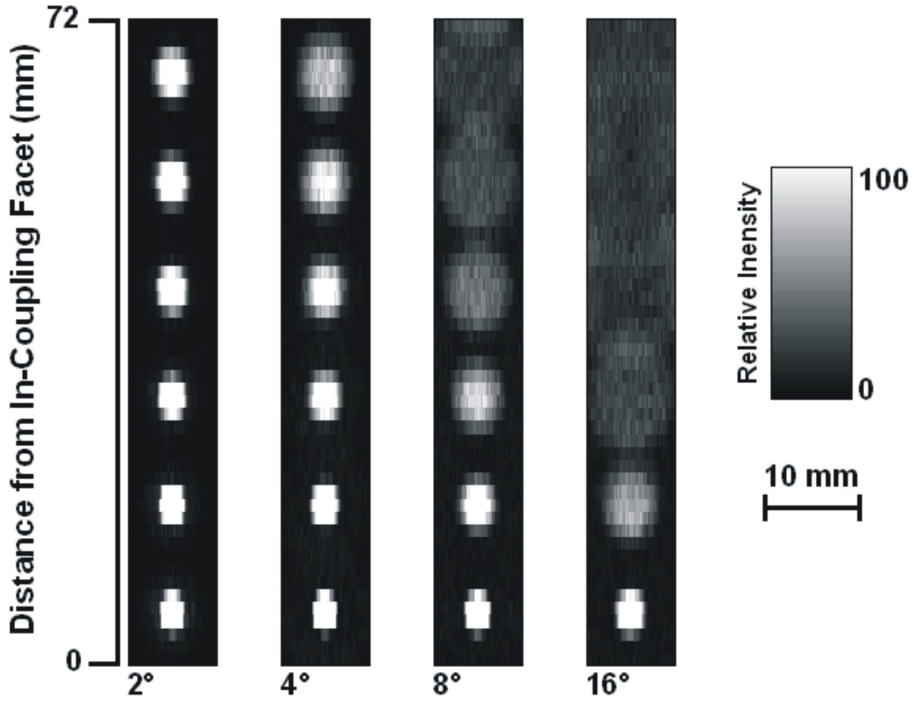

Figure 7-8: Simulated radiation density maps for visualizing internal reflection regions and the influence of increasing radiation cone angles from left to right (2º, 4°, 8°, and 16°). Simulations were generated with a source radius of 0.1278 cm.

Simulated Radiation Path through HATR Crystal:

The circular light source was positioned at the mid-point of the beveled 45º in-coupling facet to generate the radiation path determined from experimental measurements. Average central locations for individual reflection regions (2^{nd} through 5^{th} reflection) from simulated spectral data were calculated as 17.98 mm ± 0.23 mm, 30.11 mm ± 0.22 mm, 41.88 mm ± 0.14 mm, and 54.04 mm ± 0.28 mm. These values are in close agreement with both experimental and ray optic values. Therefore, the radiation paths in experimental and simulation measurements are quantitatively equivalent and confirm that the proposed fitting procedure enables an accurate assessment of central locations for reflection regions.

Simulated Through-Coupled Solid Radiation Cone Angles:

To enable direct comparison between experimental and simulation data for estimating the experimentally through-coupled radiation cone angle, normalized PAs for simulation series with

increasing cone angles (2°, 4°, 8°, and 16°) and CLSR of 0.1278 cm were calculated. **Figure 7-9 (a.)** displays the normalized profile of IR absorption intensities for simulated deposits along the sensing surface versus distance from the HATR in-coupling facet. Evaluation of the TRE for each cone angle revealed that simulated measurements with a cone angle $\geq 4^{\circ}$ (TREs 0.271 for 4°, 0.935 for 8°, and 2.423 for 16°) result in a considerable mismatch with experimental data. Increasing TRE values reflect a heightened decay in signal generation from enhanced radiation divergence with successively larger radiation cone angles being transmitted in the simulation environment relative to the actual through-coupled radiation in experimental measurements.

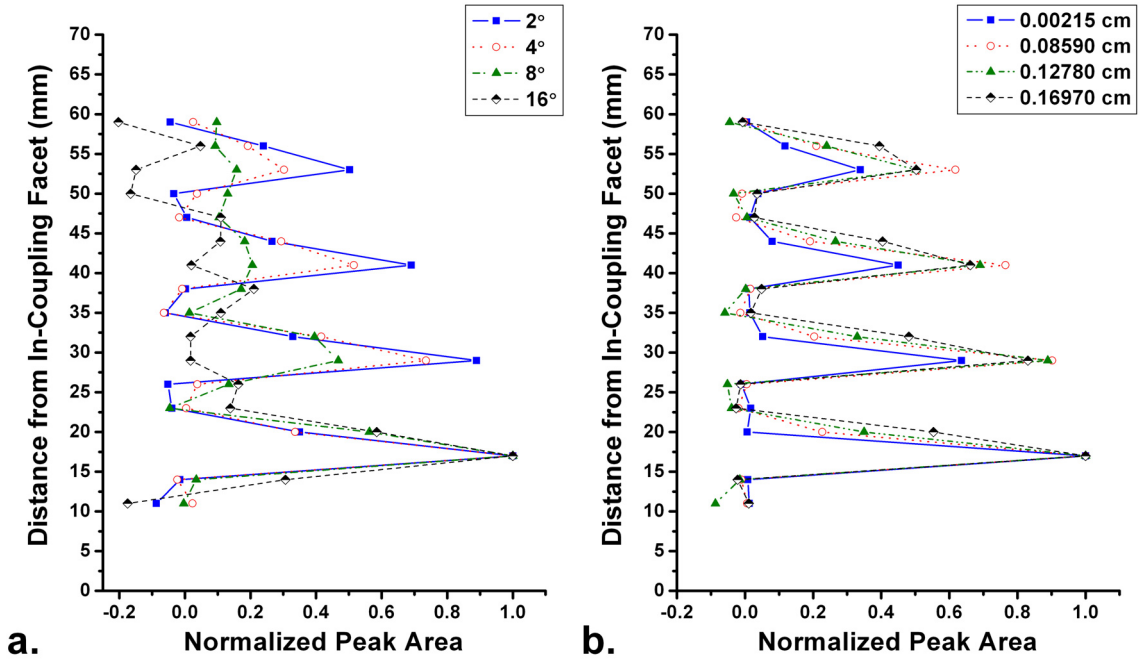

Figure 7-9: (a.) Normalized peak areas for simulated deposits plotted versus distance from the HATR in-coupling facet with increasing cone angles and a source radius of 0.1278 cm.* (b.) Normalized peak areas for simulated deposits plotted versus distance from the HATR in-coupling facet with increasing source radii and a cone angle of 2°.* (* Lines are for assisting visual inspection).

Additional simulation series with a constant light source radius of 0.1278 cm were performed to estimate a narrow range of cone angles that could produce similar results to experimental measurements. Simulated absorption measurements with cone angles of 1º, 2º, and 3º resulted in

comparable TRE values of 0.101, 0.166, and 0.205, respectively. With consideration of experimental error, the estimated range of experimentally through-coupled radiation cone angles based on simulation results was 2° ± 1°. This estimation was consistent with iris diaphragm studies (radiation cone angle between 1.9° and 2.9° in ZnSe). A TRE of 0.110 was obtained from averaged normalized simulation PAs for this range of cone angles and light source radius of 0.1278 cm (CLSR data set).

Simulation of the Diameter of In-Coupled Radiation Cone into the HATR Crystal:

To estimate the experimental diameter of in-coupled radiation into the HATR crystal, four simulation series were performed with different source radii (0.00215 cm, 0.0859 cm, 0.1278 cm, and 0.1697 cm) while maintaining a constant cone angle of 2°. Normalized PAs were calculated for comparison with experimental data. Results plotted in **Figure 7-9 (b)** illustrate the relative signal contributions for simulated deposits with respect to the highest observed absorption value at 17 mm from the in-coupling facet. The simulation series with a source radius of 0.00215 cm was eliminated as a candidate due to a significant mismatch with experimental values (TRE = 0.443). Low normalized PAs were observed at essentially all locations due to minimal spatial overlap between residues and transmitted radiation. For the remaining simulations, normalized PAs closely tracked the experimental values with TREs of 0.152, 0.166, and 0.211 for source radii of 0.0859 cm, 0.1278 cm, and 0.1697 cm, respectively. Thus, an estimated range of experimentally in-coupled radiation radii was 0.1278 cm ± 0.042 cm based on simulation results. The TRE for averaged normalized PAs for these simulation series was 0.123 (CCA data set).

Two-dimensional Approximations of 'Active' Sensing Regions:

Two-dimensional approximations of the shape and size for 'active' sensing regions can now be projected with the culmination of previously defined radiation parameters. For ideal imaging optics and a focal plane on the order of the detector element size, the shape of experimental sensing regions can be closely approximated as an ellipse with the minor axis (width) approx. 41% of the major axis (length). The elliptical shape results from differences in the radiation

pathlength at the reflection surface due to internal reflection at an angle of 45°. Thus, the ellipse major axis is projected along the 72 mm axis of the HATR measurement surface. In this approximation, the minor axis of the ellipse (projected on the 10 mm crystal axis) is the calculated radiation cone diameter with respect to distance from the ATR crystal in-coupling facet to the central location of each sensing region, the radius of in-coupled radiation, and the through-coupled cone angle.

Figure 7-10 assists visualization of calculated projections for 'active' sensing regions with estimated radiation parameters determined for the experimental set-up. Minimum (min.) and maximum (max.) combinations of the through-coupled cone angles and radii of in-coupled radiation from simulation measurements were used to calculate a range of dimensions for experimentally 'active' sensing regions. The range of possible dimensions for each sensing region is depicted as the area (shaded green) between calculated projections for the respective min. and max. combinations. An area circumscribed by the smallest projected measurement region (shaded orange) represents 'active' sensing areas for all estimated through-coupled radiation parameters. The most probable size range for sensing regions was determined as the area (shaded red) between projected ellipses from the three simulation series best matched with experimental data (lowest TREs). The probability of actual sensing region dimensions decrease as the distance from this shaded region (red) increases; either toward the 'inactive' areas (shaded blue) or the center of 'active' regions (shaded orange). **Table 7-3** provides minor axis dimensions used in calculating elliptical projections for each sensing region depicted in **Figure 7-10**.

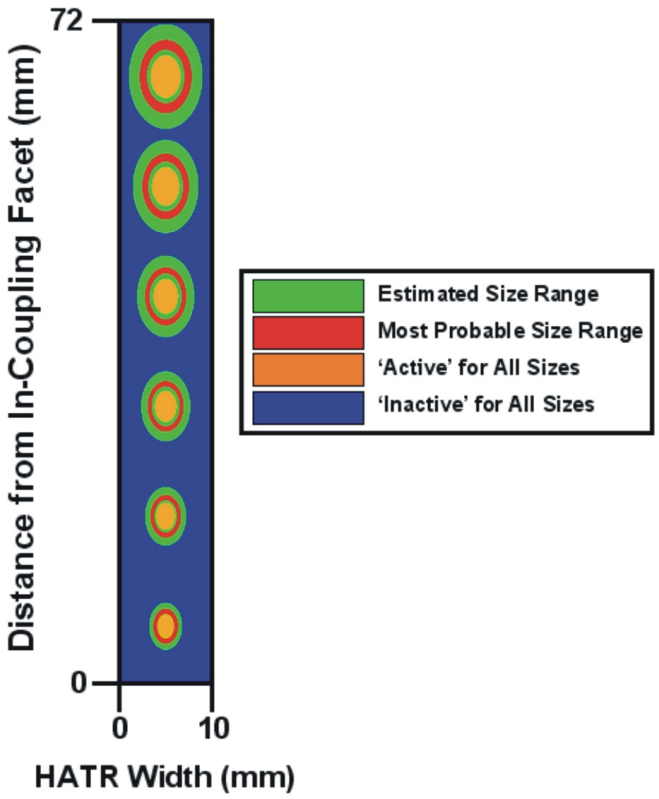

Figure 7-10: Elliptical surface projections of (i) the estimated range of dimensions for 'active' sensing regions shaded green, (ii) the most probable range of dimensions for 'active' sensing regions shaded in red, (iii) always 'active' sensing regions shaded in orange, and (iv) always 'inactive' measurement regions shaded blue. The ellipse minor axis diameters used for calculating these projections are provided in **Table 7-3** where the minor axis diameter is approx. 41% of the major axis diameter.

Table 7-3. Ellipse minor axis diameters used for calculating the projected 'active' sensing regions depicted in **Figure 7-10**. (* CA represents cone angle. ** LSR represents the light source radius in cm).

	Estimated Range				**Most Probable Range**					
	CA*	**LSR****	**CA**	**LSR**	**CA**	**LSR**	**CA**	**LSR**	**CA**	**LSR**
	1°	**0.0859**	**3°**	**0.1697**	**1°**	**0.1278**	**2°**	**0.0859**	**2°**	**0.1278**
Location (mm)	**Minor Axis (mm)**		**Minor Axis (mm)**		**Minor Axis (mm)**		**Minor Axis (mm)**		**Minor Axis (mm)**	
6	1.80		3.65		2.64		1.89		2.73	
18	2.10		4.54		2.94		2.48		3.32	
30	2.40		5.43		3.23		3.08		3.91	
42	2.69		6.32		3.53		3.67		4.51	
54	2.99		7.21		3.83		4.26		5.10	
66	3.29		8.10		4.12		4.85		5.69	

The projected two-dimensional sensing regions represent an ideal experimental scenario, and the accuracy is inherently constrained by the one-dimensional experimental analysis. Improved two-dimensional architectures of the 'active' sensing regions may be achieved in future experiments by incorporating imaging effects of instrument and ATR accessory optics as well as accounting for all radiation components projected onto and vignetted from the detector element. In addition, more complex simulation environments that precisely model the overall optical system (including the radiation profile) can facilitate highly accurate two-dimensional modeling of sensing regions for specific systems and aid efficient instrument design for dedicated IR-ATR applications.

7.3.3.3 Error Considerations

Experimental PSCB deposits were comparatively reproducible with an average diameter of 2.49 mm ± 0.098 mm. Therefore, minimal experimental error is expected from variance in residue dimensions. The most significant source of experimental error was the accuracy of PSCB/toluene aliquot deposition at the center of marked locations. The estimated error for physically depositing spots at their designated location was approx. 1 mm. The accuracy and precision of depositing concentric PSCB spots at desired location is of substantial importance as the IR absorption is dependent upon the spatial overlap of the PSCB deposit with the evanescent field. In addition, integration of PSCB spectral features can lead to a variance of approx. 10% for the experimental PAs. Considering potential sources and magnitudes of experimental error, calculated peak centers, the extrapolated internal reflection angle, and the position of in-coupled radiation were in very close agreement with expected values from ray optic considerations for the defined radiation path.

For a combination of light source radius (0.1278 cm) and cone angle (2°), entire simulation series were repeated five times to confirm the quality of information determined from single trials was not compromised considering the potential gain in signal-to-noise ratio via averaging of multiple trials. The average standard deviation for 120 spectral data points from five consecutively executed trials was < 4 %. There are a few nominal deviations from the direct comparison of

simulation results (either CCA or CLSR from **Figure 7-7**) with the experimental results. The most apparent deviations occur at locations of 20 mm and 56 mm from the in-coupling facet. These deviations have been primarily attributed to artifacts from deposition of polymer droplets exactly at their intended locations.

Additional variations from the direct comparison of experimental results with data generated using a simulation environment resembling an ideal optical system are expected. Inherent differences between the experimental setup and simulated apparatus are apparent in the capability of extracting exact through-coupled radiation parameters from the simulations. Considering such limitations, a relatively small range of through-coupled cone angles ($2^{o} \pm 1^{o}$) extrapolated from the comparative analysis are quantitatively consistent with values obtained from the experimental iris diaphragm measurements. Furthermore, small TRE values obtained from the direct comparison of experimental and simulation data indicate an overall consistency between the two systems. Therefore, the simulation apparatus provides a viable approximation of the real-world measurement situation in this study.

7.4 Conclusions

A brief summary of progress towards the development of a 2^{nd} generation of deep-sea FT-IR sensor, 'Sphere-IR', was included in this chapter. To date, the general design concept for incorporating a Bruker IRcube spectrometer into a spherical glass instrument housing has been established. CAD modeling and design facilitated the completion of the electronics sub-system. Although a fully functional system was not realized in this work due to an incomplete optics compartment, all primary optical components have been modeled to scale to assist final alignments for construction of an optics baseplate. Additional discussion was provided regarding the advantages and disadvantages of the current 'Sphere-IR' concept. A variety of issues surround the use of spherical glass housings; however, realization of the proposed instrument should facilitate further demonstration as to the value of deep-sea MIR chemical sensing platforms.

For ‘Sphere-IR’, a high-pressure sensor probe incorporating a trapezoidal ZnSe waveguide is desirable for performance; however, this material and geometry present an engineering challenge. Hence, complementary experimental and simulation procedures were explored to identify and evaluate localized IR-ATR signal generation for common trapezoidal HATR elements through the identification of ‘active’ measurement regions via evanescent field interactions with discrete deposits of IR active residues. The presented methods enabled direct insight into the two-dimensional architectures of individual sensing regions along a multi-reflection ATR element. Accurate emulation of the experimental setup was demonstrated by the consistent comparison of normalized experimental and simulated spectral data. Hence, the experimentally validated simulation apparatus and methods provide a powerful analytical approach for characterizing signal generation from individual ‘active’ sensing regions expandable to a vast array of IR-ATR configurations. In context of this thesis, a virtual environment has been established to facilitate development of robust high-pressure sensor probes by enabling optically efficient design of crystal dimensions, crystal mounting, and selection and alignment of secondary optical components to manipulate radiation beam geometry and propagation.

7.5 Outlook

A variety of deep-sea spectrometers have been reported in the literature. Currently, the application of submersible chemical sensors is still in a state of infancy, which is anticipated to continuously improve in great strides with broader recognition and demonstration of their value in long-term monitoring and expeditionary oceanic research. The development and application of FT-IR spectrometers for deep-sea research currently lags behind that of Raman and mass spectrometers; however, the collective works presented in **Chapters 4**, **5**, and **6** of this thesis have established the analytics and application feasibility for investigating gas hydrates and carbonate mineralogy ideally suited for *in situ* investigation with MIR chemical sensors. However, the

development of a deep-sea FT-IR spectrometer capable of operating at depths ≥ 1000 m is required to facilitate extensive investigations on such topics.

With consideration of experimental works described in this thesis, the greatest factor currently limiting realized deployment and application of submersible MIR chemical sensing platforms is system engineering. With two well-defined measurement objectives described in this thesis, the engineering of MIR sensors can be focused and tailored to facilitate operation for a specific application in a particular type of environment (i.e., sediment characterization or water column monitoring). The presented ray tracing simulation environment enabled accurate mimicking of signal generation for IR-ATR experiments; hence, virtual optimization of sensor probes and optical configurations for deep-sea FT-IR systems should assist platform engineering through the rational design and fabrication of viable submersible MIR sensors for monitoring applications in harsh, deep-sea environments.

7.6 References

1. R. Camilli and H. F. Hemond, *NEREUS/Kemonaut, A Mobile Autonomous Underwater Mass Spectrometer*, TrAC, Trends in Analytical Chemistry **23**, 307 (2004).

2. D. P. Fries, R. T. Short, L. L. Langebrake, J. T. Patten, M. L. Kerr, G. Kibelka, D. C. Burwell, and J. C. Jalbert, *In-water Field Analytical Technology: Underwater Mass Spectrometry, Mobile Robots, and Remote Intelligence for Wide and Local Area Chemical Profiling*, Field Analytical Chemistry and Technology **5**, 121 (2001).

3. H. Hemond and R. Camilli, *NEREUS: Engineering Concept for an Underwater Mass Spectrometer*, TrAC, Trends in Analytical Chemistry **21**, 526 (2002).

4. C. Janfelt, F. R. Lauritsen, S. K. Toler, R. J. Bell, and R. T. Short, *Method for Quantification of Chemicals in a Pollution Plume Using a Moving Membrane-based Sensor Exemplified by Mass Spectrometry*, Analytical Chemistry (Washington, DC, United States) **79**, 5336 (2007).

5. R. A. Ketola, T. Kotiaho, M. E. Cisper, and T. M. Allen, *Environmental Applications of Membrane Introduction Mass Spectrometry*, Journal of Mass Spectrometry **37**, 457 (2002).

6. G. P. G. Kibelka, R. Timothy Short, S. K. Toler, J. E. Edkins, and R. H. Byrne, *Field-deployed Underwater Mass Spectrometers for Investigations of Transient Chemical Systems*, Talanta **64**, 961 (2004).

7. R. T. Short, D. P. Fries, M. L. Kerr, C. E. Lembke, S. K. Toler, P. G. Wenner, and R. H. Byrne, *Underwater Mass Spectrometers for In Situ Chemical Analysis of the Hydrosphere*, Journal of the American Society for Mass Spectrometry **12**, 676 (2001).

8. R. T. Short, D. P. Fries, S. K. Toler, C. E. Lembke, and R. H. Byrne, *Development of an Underwater Mass-spectrometry System for In Situ Chemical Analysis*, Measurement Science and Technology **10**, 1195 (1999).

9. R. T. Short, S. K. Toler, G. P. G. Kibelka, D. T. Rueda Roa, R. J. Bell, and R. H. Byrne, *Detection and Quantification of Chemical Plumes using a Portable Underwater Membrane Introduction Mass Spectrometer*, TrAC, Trends in Analytical Chemistry **25**, 637 (2006).

10. P. G. Wenner, R. J. Bell, F. H. W. Van Amerom, S. K. Toler, J. E. Edkins, M. L. Hall, K. Koehn, R. T. Short, and R. H. Byrne, *Environmental Chemical Mapping using an Underwater Mass Spectrometer*, TrAC, Trends in Analytical Chemistry **23**, 288 (2004).

11. T. M. Battaglia, E. E. Dunn, M. D. Lilley, J. Holloway, B. K. Dable, B. J. Marquardt, and K. S. Booksh, *Development of an In Situ Fiber Optic Raman System to Monitor Hydrothermal Vents*, Analyst (Cambridge, United Kingdom) **129**, 602 (2004).

12. P. G. Brewer, G. Malby, J. D. Pasteris, S. N. White, E. T. Peltzer, B. Wopenka, J. Freeman, and M. O. Brown, *Development of a Laser Raman Spectrometer for Deep-ocean Science*, Deep-Sea Research, Part I: Oceanographic Research Papers **51**, 739 (2004).

13. K. C. Hester, R. M. Dunk, S. N. White, P. G. Brewer, E. T. Peltzer, and E. D. Sloan, *Gas Hydrate Measurements at Hydrate Ridge using Raman Spectroscopy*, Geochimica et Cosmochimica Acta **71**, 2947 (2007).

14. K. C. Hester, S. N. White, E. T. Peltzer, P. G. Brewer, and E. D. Sloan, *Raman Spectroscopic Measurements of Synthetic Gas Hydrates in the Ocean*, Marine Chemistry **98**, 304 (2006).

15. J. D. Pasteris, B. Wopenka, J. J. Freeman, P. G. Brewer, S. N. White, E. T. Peltzer, and G. E. Malby, *Raman Spectroscopy in the Deep Ocean: Successes and Challenges*, Applied Spectroscopy **58**, 195A (2004).

16. S. N. White, R. M. Dunk, E. T. Peltzer, J. J. Freeman, and P. G. Brewer, *In Situ Raman Analyses of Deep-sea Hydrothermal and Cold Seep Systems (Gorda Ridge and Hydrate Ridge)*, Geochemistry, Geophysics, Geosystems **7**, No pp given (2006).

17. M. Kraft, M. Jakusch, M. Karlowatz, A. Katzir, and B. Mizaikoff, *New Frontiers for Mid-infrared Sensors: Towards Deep Sea Monitoring with a Submarine FT-IR Sensor System*, Applied Spectroscopy **57**, 591 (2003).

18. M. Kraft, M. Jakusch, and B. Mizaikoff, *A Miniaturised Fourier-Transform Infrared Spectrometer for Seawater Monitoring*, IEEE1701 (1998).

19. M. Kraft, M. Karlowatz, B. Mizaikoff, R. Stuck, M. Steden, M. Ulex, and H. Amann, *Sensor Head Development for Mid-infrared Fiber-optic Underwater Sensors*, Measurement Science and Technology **13**, 1294 (2002).

20. M. Kraft and B. Mizaikoff, *A Mid-infrared Sensor for Monitoring of Chlorinated Hydrocarbons in the Marine Environment*, International Journal of Environmental Analytical Chemistry **78**, 367 (2000).

21. W. C. Young and R. G. Budynas, *Roark's Formulas for Stress and Strain*, (McGraw-Hill, New York, 2002).

22. R. Camilli, *Personal Communication*, (2005).

23. R. Goebel, R. Krska, R. Kellner, and A. Katzir, *Development of Protective Polymer Coatings for Silver Halide Fibers and Their Application as Threshold Level Sensors for Chlorinated Hydrocarbons in Seawater*, Fresenius' Journal of Analytical Chemistry **348**, 780 (1994).

24. M. Kraft, *Mid-Infrared Spectrosocpy using Optical Waveguides in the Marine Environment*, Technische Universitat Wien, (2000).

25. *Ocean Optics, Inc.*, http://www.oceanoptics.com/ (July 2007).

26. *StellarNet, Inc.*, http://www.stellarnet-inc.com/ (July 2007).

27. *Mettler Toledo*, http://us.mt.com/home (July 2007).

28. *Axiom Analytical, Inc.*, http://www.goaxiom.com/index.html (July 2007).

29. *Remspec Corporation*, http://www.remspec.com/ (July 2007).

30. A. Brooks, N. I. Afanasyeva, V. Makhine, R. F. Bruch, S. F. Kolyakov, S. Artjushenko, and L. N. Butvina, *New Method for Investigations of Normal Human Skin Surfaces In Vivo Using Fiber-optic Evanescent Wave Fourier Transform Infrared Spectroscopy (FEW-FTIR)*, Surface and Interface Analysis **27**, 221 (1999).

31. C. S. Creaser, W. E. Hutchinson, and G. R. Stephenson, *An Attenuated Total Reflectance Optrode Sensor Incorporating Infrared-active Carbonylmetal Probe Groups*, Sensors and Actuators, B: Chemical **B82**, 150 (2002).

32. D. L. Doak and J. A. Phillips, *In Situ Monitoring of an Escherichia coli Fermentation Using a Diamond Composition ATR Probe and Mid-infrared Spectroscopy*, Biotechnology Progress **15**, 529 (1999).

33. D. D. Dunuwila and K. A. Berglund, *ATR FTIR Spectroscopy for In Situ Measurement of Supersaturation*, Journal of Crystal Growth **179**, 185 (1997).

34. H. M. Heise, L. Kupper, W. Pittermann, and M. Stucker, *Epidermal In Vivo and In Vitro Studies by Attenuated Total Reflection Mid-infrared Spectroscopy Using Flexible Silver Halide Fiber-probes*, Journal of Molecular Structure **651-653**, 127 (2003).

35. R. Howley, B. D. MacCraith, K. O'Dwyer, P. Kirwan, and P. McLoughlin, *A Study of the Factors Affecting the Diffusion of Chlorinated Hydrocarbons into Polyisobutylene and Polyethylene-co-propylene for Evanescent Wave Sensing*, Vibrational Spectroscopy **31**, 271 (2003).

36. P. J. Melling and M. Thomson, in Handbook of Vibrational Spectroscopy (J. M. Chalmers and P. R. Griffiths, eds.), John Wiley & Sons Ltd, Chichester, 2002.

37. J. Pastre, A. Zogg, U. Fischer, and K. Hungerbuehler, *Determination of Reaction Parameters Using a Small Calorimeter with an Integrated FT-IR Probe and Parameter Fitting*, Organic Process Research & Development **5**, 158 (2001).

38. R. F. Storey, A. B. Donnalley, and T. L. Maggio, *Real-time Monitoring of Carbocationic Polymerization of Isobutylene Using In Situ FTIR-ATR Spectroscopy with Conduit and Diamond-composite Sensor Technology*, Macromolecules **31**, 1523 (1998).

39. *Harrick Scientific Products, Inc.*, http://www.harricksci.com/ (July 2007).

40. G. T. Dobbs and B. Mizaikoff, *Shining New Light on Old Principles: Localization of Evanescent Field Interactions at Infrared-Attenuated Total Reflection Sensing Interfaces*, Applied Spectroscopy **60**, 573 (2006).

41. M. Hiller, B. Mizaikoff, R. Kellner, W. Theiss, and P. Grosse, *Numerical Simulation of IR-spectroscopic Experiments*, Mikrochimica Acta, Supplement **14**, 283 (1997).

CHAPTER 8

CONCLUSIONS AND OUTLOOK

The main objective for this thesis was the development of IR spectroscopic measurement and data evaluation strategies for monitoring and evaluating chemical signals encountered within oceanic gas hydrate ecosystems. This thesis has demonstrated the application of fiber-optic evanescent field spectroscopy for monitoring gas hydrate growth dynamics in solution, including the establishment of initial quantification strategies and efficacy for real-world application. The potential of MIR chemical sensors for ocean exploration was further exemplified with the elucidation of spectral signatures corresponding to the detection of localized formation of authigenic carbonates in fine marine sediment fractions inundated with coccolith calcite.

8.1 IR Spectroscopic Monitoring of Gas Hydrates

Fiber-optic evanescent field spectroscopy was utilized to monitor the formation and dissociation of simple gas hydrates grown in solution with methane, ethane, and propane gases. This was achieved by tracking spectral changes in the IR absorption of water during the liquid-to-hydrate and hydrate-to-liquid phase transitions. Data evaluation strategies included peak area analyses for the O-H stretch, H-O-H bend, and the libration modes, and the assessment of peak shifts in the 3rd libration overtone. Utilizing the Beer-Lambert law, a first approximation based on the peak position of the 3rd libration overtone was derived for quantifying the percent of gas hydrate in the total water volume interacting with the evanescent field.

In addition to establishing the first principles for IR spectroscopic monitoring and quantification of gas hydrate growth dynamics, the developed strategies were utilized to monitor methane hydrate growth in solution for approx. 23 days at simulated hydrostatic pressures corresponding to ocean depths approaching 500 m. IR monitoring of gas hydrate formation and dissociation was also achieved for time periods extending upwards of 29 days, illustrating the potential for long-

term spectroscopic monitoring objectives in isolated oceanic gas hydrate ecosystems. Efficacy for real-world deep-sea monitoring applications was verified by the determination of minimal spectral interferences with the IR absorption features of water from sediment matrix constituents in samples collected at the MC118 gas hydrate site in the GoM.

Furthermore, anticipated power restrictions that would limit long-term, uninterrupted operation of MIR chemical sensing platforms in isolated oceanic gas hydrate ecosystems was considered. With an artificially imposed reduction in the temporal resolution of spectroscopic data generated during a 29 day hydrate measurement campaign by a factor of 100 (i.e., 5450 spectra reduced to 55 spectra), the major formation and dissociation events of that trial were still captured. This was attained by the collection of approx. 1.8 IR spectra per day with an estimated instrument operation time of approx. 18.3 hrs required to facilitate comparable data generation with a 29 day deployment of a deep-sea MIR chemical sensing platform. Hence, the studies described in this thesis demonstrate the initial practical feasibility for utilizing IR spectroscopy to monitor the dynamics gas hydrate within hydrate-bearing sediments in oceanic environments.

8.2 Characterizing Deep-Sea Carbonates with IR Spectroscopy

An IR-ATR spectral database was generated for 10 of the most common anhydrous carbonate minerals in this thesis to facilitate the characterization of carbonate minerals in marine sediments and authigenic carbonate nodules collected from two gas hydrate systems in the Mississippi Canyon region of the GoM. Calcite was found to be the most prevalent carbonate species in marine sediments evaluated in this thesis. In addition, an unexpected and peculiar IR spectral profile for the ν_3 carbonate vibration was observed in most surficial sediment samples surrounding the MC118 site. This IR signature was traced to the regional sedimentation of coccolith calcite produced in the photic zone by thriving, single-celled photosynthetic coccolithophores throughout the GoM.

Spectroscopic analysis revealed a diverse array of carbonate mineral compositions for authigenic carbonate nodules recovered from the MC118 site. The broad ν_3 carbonate absorption features characteristic to recovered authigenic nodule samples were additionally observed in the IR spectra of several sediment samples, which were frequently coincident with nodule accumulations. Hence, spectral broadening of the ν_3 carbonate profile in sediments with abundant and regionally distributed coccolith calcite was linked to the occurrence of localized authigenic carbonate formation driven by chemosynthetic communities associated with cold hydrocarbon seepage at the MC118 site. This link was further confirmed with carbon isotope analysis of carbonates within select sediment and nodule samples that exhibited strong depletions in ^{13}C from the inheritance of carbon from the chemosynthetic oxidation of seeping hydrocarbons.

Semi-quantitative evaluation of the relative mass percentages of calcite and dolomite in the total carbonate composition of sediment samples collected in the GoM were additionally performed. A wide range of dolomite mass fractions were observed in the various sediment amples. Although inhomogeneous particle sizes and spectral interferences from quartz, clay, and Mg-calcite limited precise quantitative characterization, the semi-quantitative analysis facilitated an initial spectroscopic assessment to the composition and variability of dolomite presence in sediments encountered within gas hydrate ecosystems in the GoM. In addition, this particular evaluation provided insight into specific issues that must be considered to further improve the application of IR-ATR spectroscopy for quantitative assessment of carbonate minerals in complex marine sediment matrices.

Within the scope of this thesis, the assessment of non-manipulated sediment samples in their native hydrated state was of particular interest. The strong ν_3 carbonate absorption was accessible in all examined hydrated sediment samples, which enabled rapid characterization (i.e., several minutes) to the presence of authigenic carbonate in sediment samples. This demonstrates the feasibility for *in situ* IR spectroscopic detection of authigenic carbonate formation, which is

anticipated to facilitate improved characterization and assessment of the significance and spatial distribution of authigenic carbonates throughout the fine sediment fractions surrounding oceanic gas hydrate ecosystems. Furthermore, the presented qualitative and semi-quantitative characterization strategies are well-suited for rapid on-ship sediment analyses (hydrated and dried sediments and nodules).

8.3 Outlook for Improving the Application of IR Spectroscopy for Hydrate Monitoring and Carbonate Analysis

With exception to the realization of a capable MIR sensing platform, improved characterization of the influences from pressure, salinity, pH, and perhaps alkalinity on the IR absorption features of water over environmentally relevant values should facilitate more precise extraction of hydrate composition information within the analytical volume probed via the evanescent field for oceanic monitoring of gas hydrates. To improve the IR spectroscopic quantification of carbonate minerals (i.e., calcite and dolomite) in dried marine sediments, improved assessment and compensation for spectral interferences from quartz, clay, and Mg-calcite with multivariate data evaluation routines should facilitate more robust quantification strategies. In addition, the adherence to strict measurement protocols (i.e., grinding and particle size uniformity) is essential to ensure reproducible and accurate mineral quantification. However, an initial qualitative/semi-quantitative analysis of non-manipulated sediment samples should be implemented, as this rapid evaluation strategy can provide valuable composition information prior to more laborious sample preparation treatments and costly analysis (i.e., XRD and carbon isotopes).

8.4 Can IR Spectroscopy Currently Contribute to Deep-Sea Research and the Scientific Goals of the GOMGHRC?

The studies described in this thesis demonstrated a variety of applications for IR spectroscopy to contribute to both short and long-term goals of the GOMGHRC and deep-sea research in general.

At current status, the most significant application of IR spectroscopy for supporting the GOMGHRC is the qualitative and semi-quantitative evaluation and characterization of carbonate minerals in sediment and nodule formations in the laboratory and on-ship. IR spectroscopy is anticipated to facilitate guided and collective studies for assessing potential correlations in the variability and diversity of microbiological, biogeochemical, and geologic processes surrounding the MC118 site. This is expected to be achieved most readily by implementing IR analysis as a first analytical characterization tool, on-ship, and immediately following the recovery of sediments during coring operations.

In addition to qualitative and semi-quantitative sediment analyses, the characterization of carbonate mineral diversity in nodule samples may reveal trends in the spatial and/or temporal dynamics at the MC118 site (i.e., pore water conditions and chemosynthetic activities). Initial nodule characterization revealed three general composition classifications; however, a continuum of diverse carbonate mineral compositions of authigenic nodules surrounding hydrate ecosystems is anticipated. Thus, improved tertiary (calcites, dolomite, and aragonite) and/or quaternary (calcite, dolomite, aragonite, and Mg-calcite) compositional analyses with IR-ATR spectroscopy may facilitate more insightful characterization of the carbonate diversity and potential trends at the MC118 site, as well as inter-site variability within the GoM and other gas hydrate systems.

Although the initial principles for gas hydrate monitoring have been established, a submersible MIR sensing platform capable of operating at the MC118 site has yet to be realized. With conclusion of this thesis, the greatest limiting factor for the application of IR spectroscopy to fulfill long-term *in situ* monitoring goals of the GOMGHRC is the lack of a robust MIR sensing platform. From the work performed in this thesis, two primary applications are readily accessible upon realization of such an instrument. First, *in situ* characterization of the spatial distribution of authigenic carbonates is anticipated to improve assessments in the variability and significance of authigenic carbonate within the fine sediment fractions surrounding the MC118 hydrate system. Second, *in situ* spectroscopic monitoring of gas hydrates at MC118 is anticipated to provide

direct insight into the dynamics of hydrate formation and dissociation. This is of particular interest to assess the influence of warm-water eddies from the Gulf Loop current and other environmental factors (i.e., pressure changes with tidal cycles and seismic activity) that could stimulate wide-spread dissociation events by disrupting the stability of gas hydrates within hydrate-bearing sediments.

In general, the application of IR spectroscopy for monitoring and evaluating hydrates and carbonates should be widely applicable for assisting the characterization of other oceanic gas hydrate ecosystems. However, it is prudent to acknowledge that the application of IR spectroscopy as a tool by itself can only provide a fraction of the information required to fully characterize the complexity of such ecosystems. The establishment of seafloor observatories, such as that envisioned by the GOMGHRC, for long-term, *in situ* monitoring by integrated sensor networks with multiple sensor technologies, including optical sensors (IR-ATR and Raman), mass spectrometers, temperature, salinity, oxygen, pH, accelerometers, and acoustics, should provide a wealth of complementary information that will facilitate significant advances in current knowledge regarding the spatiotemporal dynamics of complex oceanic gas hydrate ecosystems. Furthermore, the IR spectroscopic characterization of carbonate minerals is anticipated to have more universal application for investigating carbonate minerals and carbonate cycles in oceanic environments resulting from the diversity, complexity, and wide-spread global distributions, whereas the occurrence of gas hydrate is spatially restricted to the presence of appropriate hydrocarbon guests at thermodynamically suitable conditions. Ultimately, the development of appropriate MIR chemical sensing platforms for both on-ship and *in situ* measurements has significant potential for supporting deep-sea oceanic research following the demonstrated applications in this thesis.

APPENDIX A

A-1 Carbon Isotope Analysis of Sediment and Nodule Samples

Carbon isotope analysis of carbonates from selected sediment and nodule samples were performed to verify the direct connection of IR spectroscopic detection of chemosynthetically driven carbonate precipitation. Initial sample preparations were performed at Georgia Tech, and sample analyses were conducted under contract by the Stable Isotope Lab, INSTAAR, University of Colorado, Boulder (Lab Manager, Bruce Vaughn).

A-1.1 Sample Preparation and Sample Analysis

Ample portions (~300 mg) of sediment samples selected for isotope analysis were isolated and dried at room temperature for at least 7 days. Nodule samples were rinsed with DI water and allowed to dry for at least 48 hours. After drying, individual samples were hand ground with a ceramic mortar and pestle into a fine powder. Following, samples were placed in labeled glass centrifuge tubes and treated with a 6% hypochlorite solution for approx. 24 hrs to remove organic carbon. Samples were then mixed and centrifuged for approx. 30 mins before removing the hypochlorite solution. Ground specimens were then rinsed 3 times with a KOH solution (pH ~9.5) by: (1) filling centrifuge tube with approx. 12 mL and mixing with vial contents, (2) centrifuging vials for approx. 30 mins, and (3) removing and discarding KOH supernatant. After performing this 3 times (no scent of hypochlorite), ground samples were transferred to polystyrene weigh boats and dried at 60 °C for approx. 14 hrs. Once dried, samples were re-ground with a ceramic mortar and pestle and stored in labeled, plastic storage vials until isotopic characterization.

Carbon isotope analysis of carbonates within the selected sediment and nodule samples were performed by reacting 2 to 4 mg of sample with 100% phosphoric acid in an acid bath carousel system. CO_2 released during the reaction of acid and carbonate was then analyzed a Micromass

SIRA Series II Dual Inlet mass spectrometer. All results are presented on the Vienna-Pee Dee Belemnite (V-PDB) scale.

A-1.2 Results

Table A-1.1: Carbon isotope data for carbonate analysis of selected sediment and nodule samples from gas hydrate ecosystems in the GoM. Additional considerations to this data are provided in **Chapter 5** and **Chapter 6**.

Sample	Type	$\delta^{13}C$	SD $\delta^{13}C$
BC1C Bot	Sediment	-5.8	0.285
BC5B Bot	Sediment	-18.7	0.562
BC7A Bot	Sediment	0.4	0.029
BC9A Bot	Sediment	-2.3	0.367
BC11A Top	Sediment	0.6	0.031
BC12A Bot	Sediment	-22.6	0.300
Core 21	Sediment	-1.0	0.144
Core 26	Sediment	-11.1	0.690
6m MD02-2570	Sediment	-4.0	0.268
BC3 Nod	Nodule	-26.6	0.057
BC5 Nod	Nodule	-24.0	0.096
Core 21 Nod	Nodule	-34.0	0.105
Core 26 Nod	Nodule	-31.3	0.506
BC9 Mollusk Shell	Shell	2.8	0.268

A-2 IR-ATR Spectral Database for Anhydrous Normal Carbonate Minerals

Each of the following carbonate mineral IR-ATR spectra were collected on a Bruker 55 FT-IR spectrometer with measurement procedures and specimens described in **Section 5.2**. All spectra were the average of 100 sample scans collected from 4000 – 400 cm^{-1} at a spectral resolution of 1 cm^{-1}. Only the spectral region from 1650 – 600 cm^{-1} has been selected for graphical display.

Quick Figure Reference:

Figure A-2.1: Calcite

Figure A-2.2: Magnesite

Figure A-2.3: Siderite

Figure A-2.4: Rhodochrosite

Figure A-2.5: Smithsonite

Figure A-2.6: Aragonite

Figure A-2.7: Witherite

Figure A-2.8: Strontianite

Figure A-2.9: Cerussite

Figure A-2.10: Dolomite

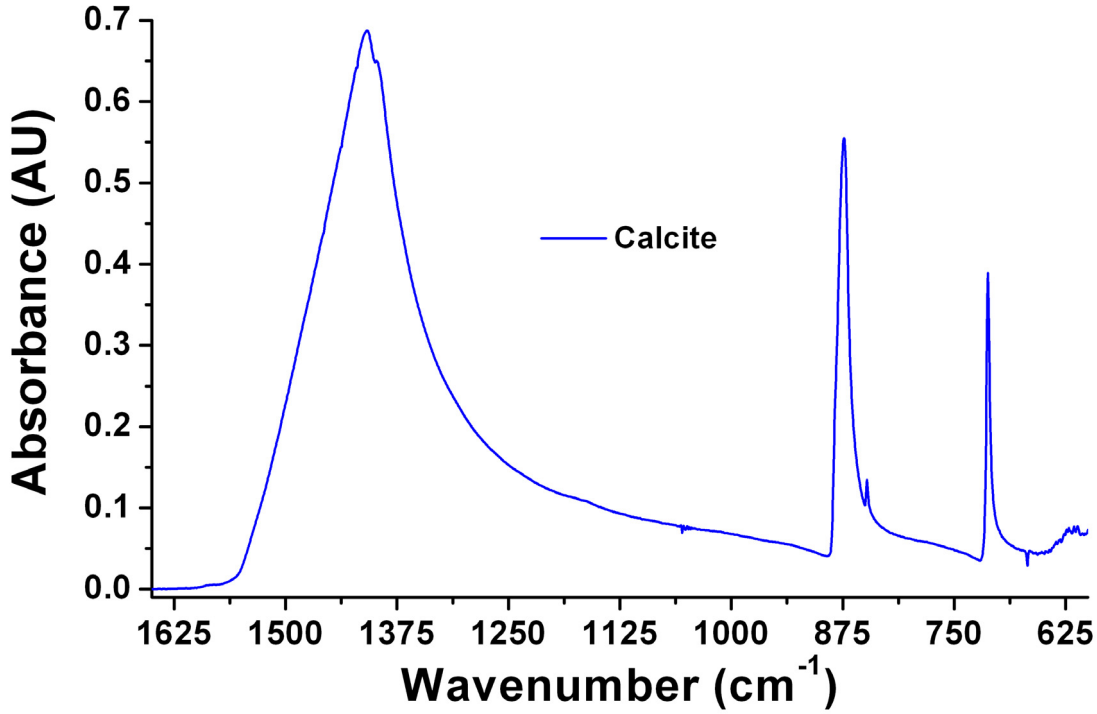

Figure A-2.1: IR-ATR spectrum of calcite, $CaCO_3$.

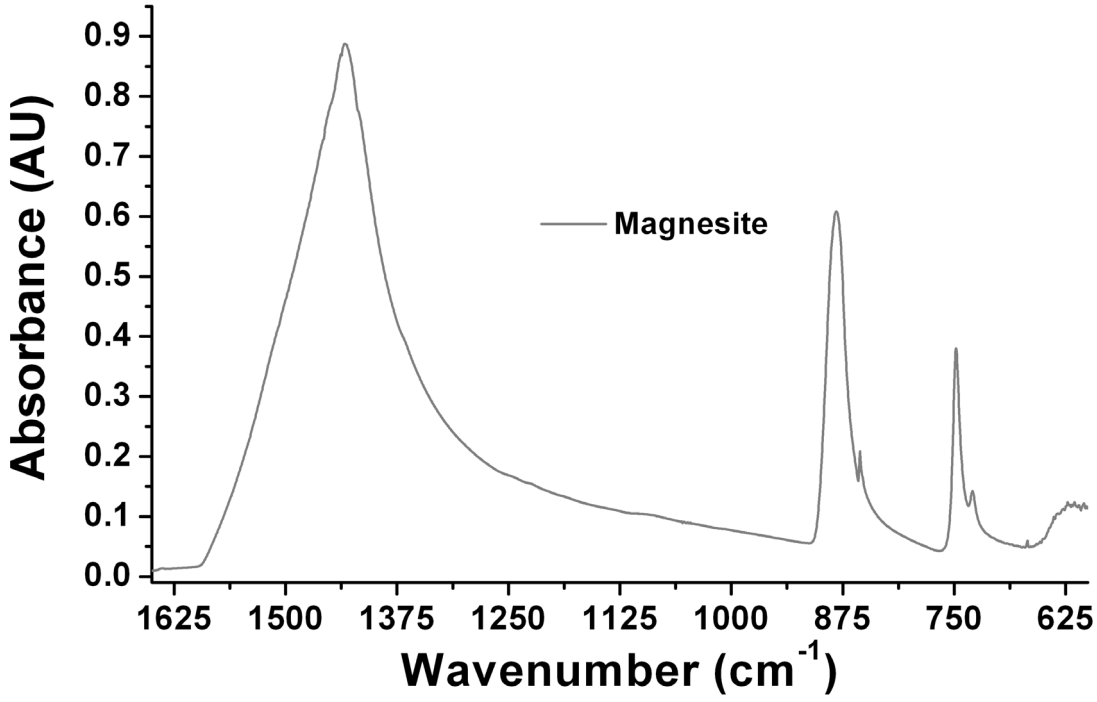

Figure A-2.2: IR-ATR spectrum of magnesite*, $MgCO_3$ (* very minor dolomite contamination).

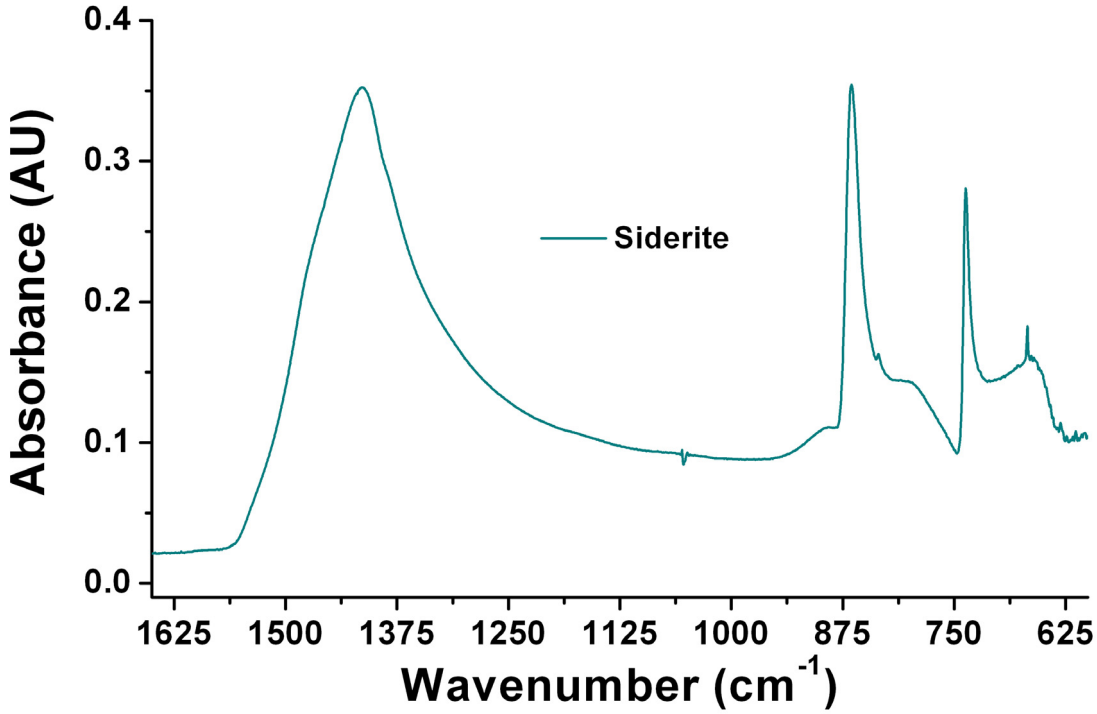

Figure A-2.3: IR-ATR spectrum of siderite, $FeCO_3$.

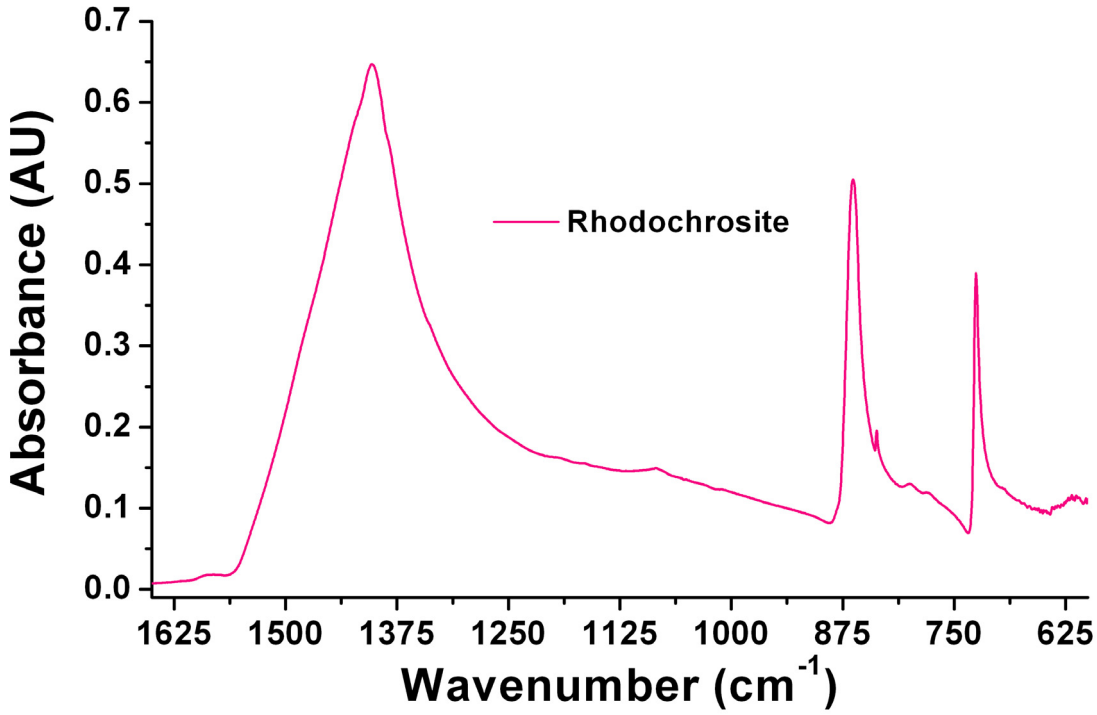

Figure A-2.4: IR-ATR spectrum of rhodochrosite, $MnCO_3$.

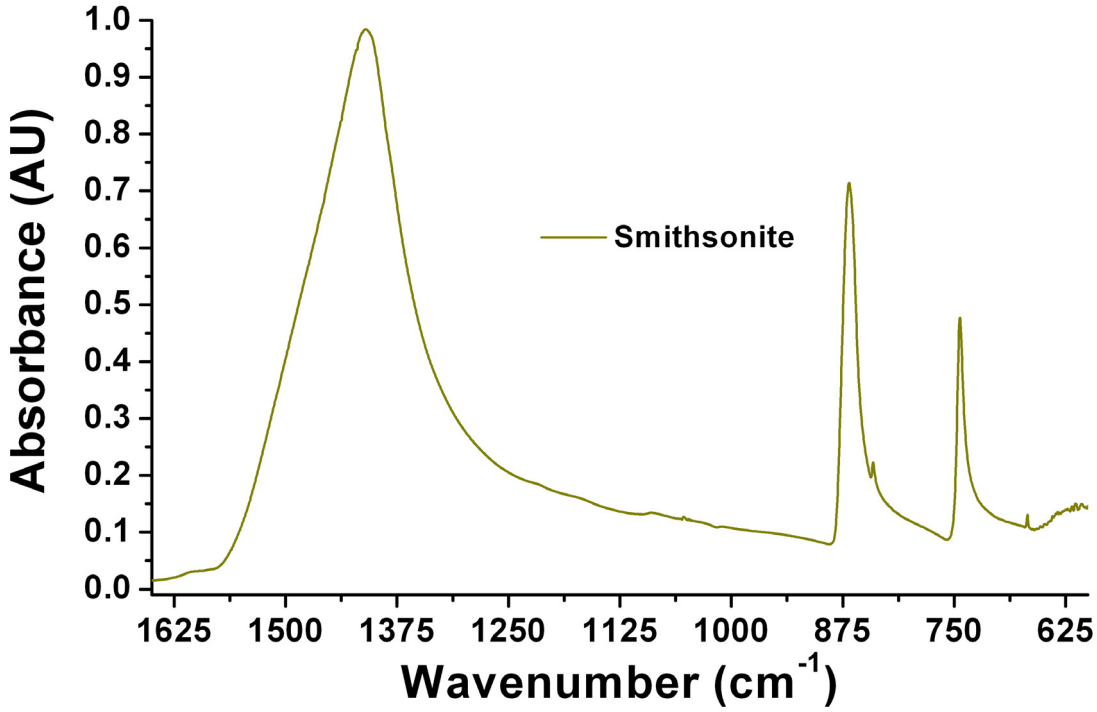

Figure A-2.5: IR-ATR spectrum of smithsonite: $ZnCO_3$.

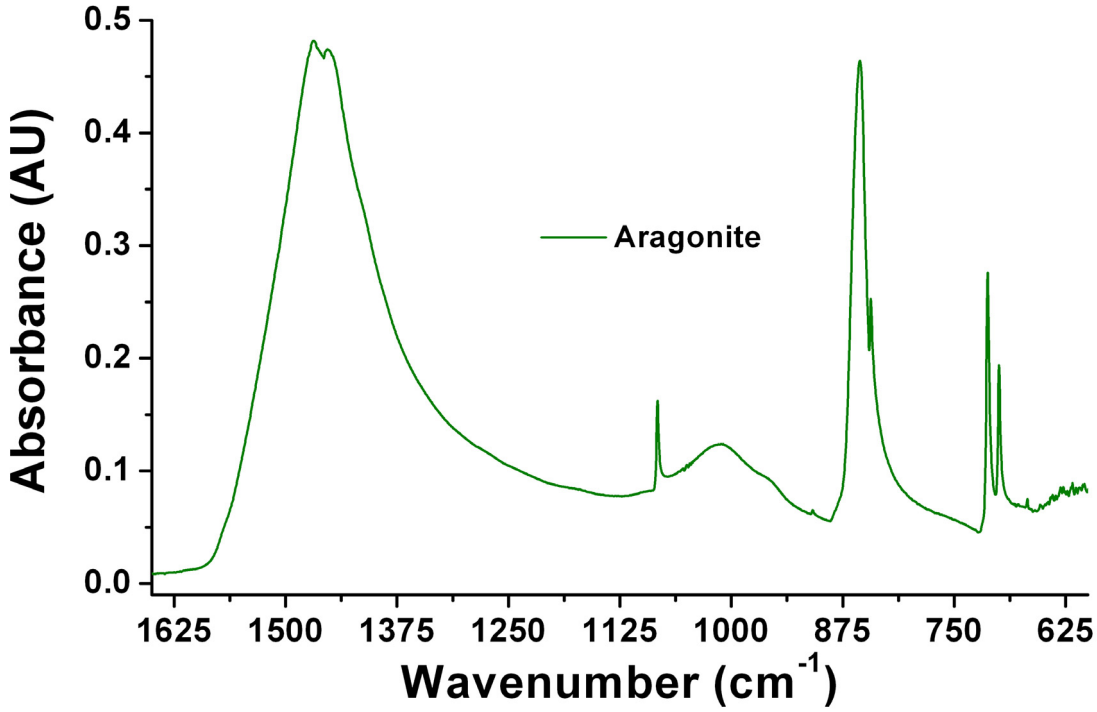

Figure A-2.6: IR-ATR spectrum of aragonite: $CaCO_3$.

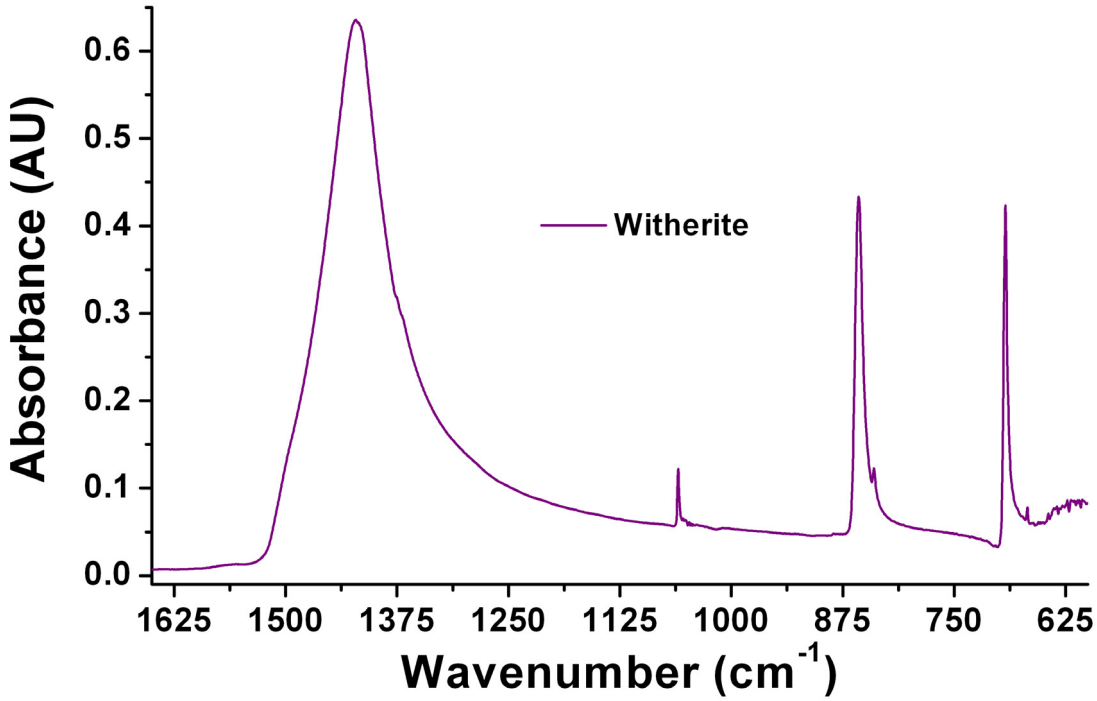

Figure A-2.7: IR-ATR spectrum of witherite, $BaCO_3$.

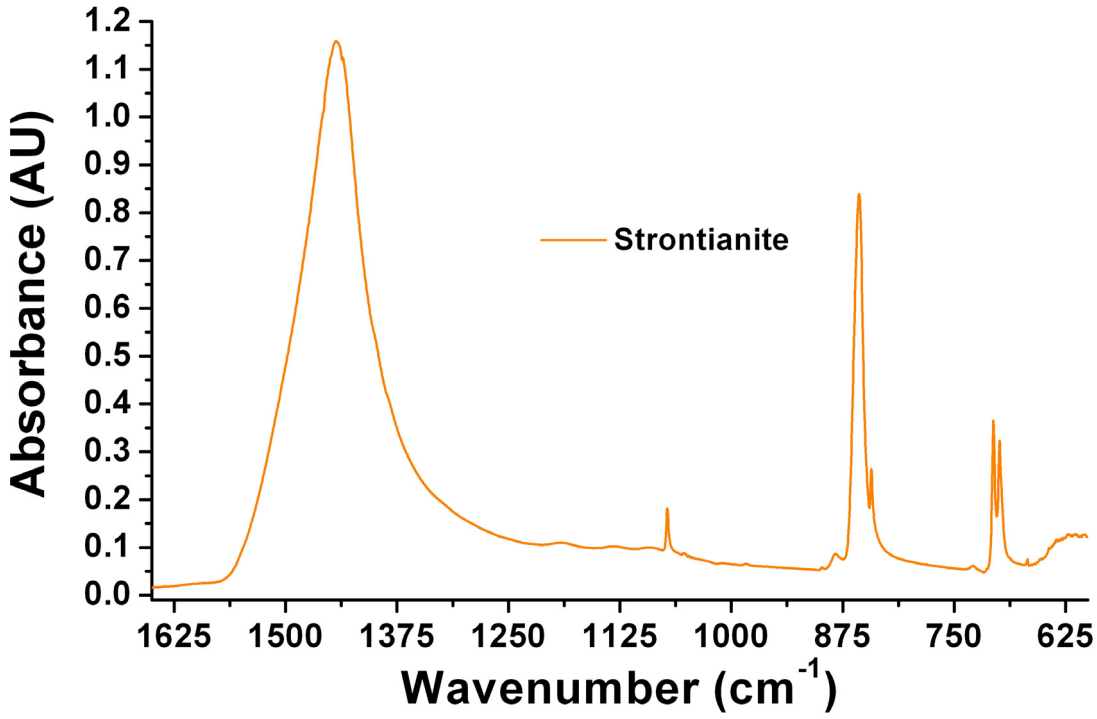

Figure A-2.8: IR-ATR spectrum of strontianite*, $SrCO_3$ (* very minor dolomite contamination).

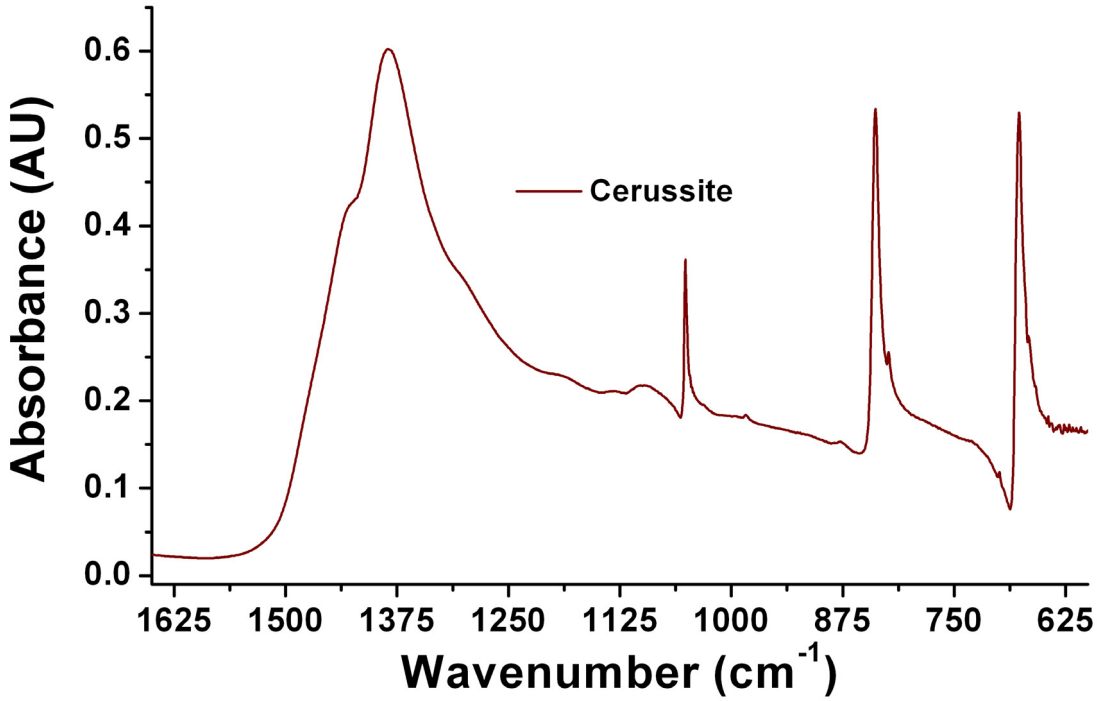

Figure A-2.9: IR-ATR spectrum of cerussite, $PbCO_3$.

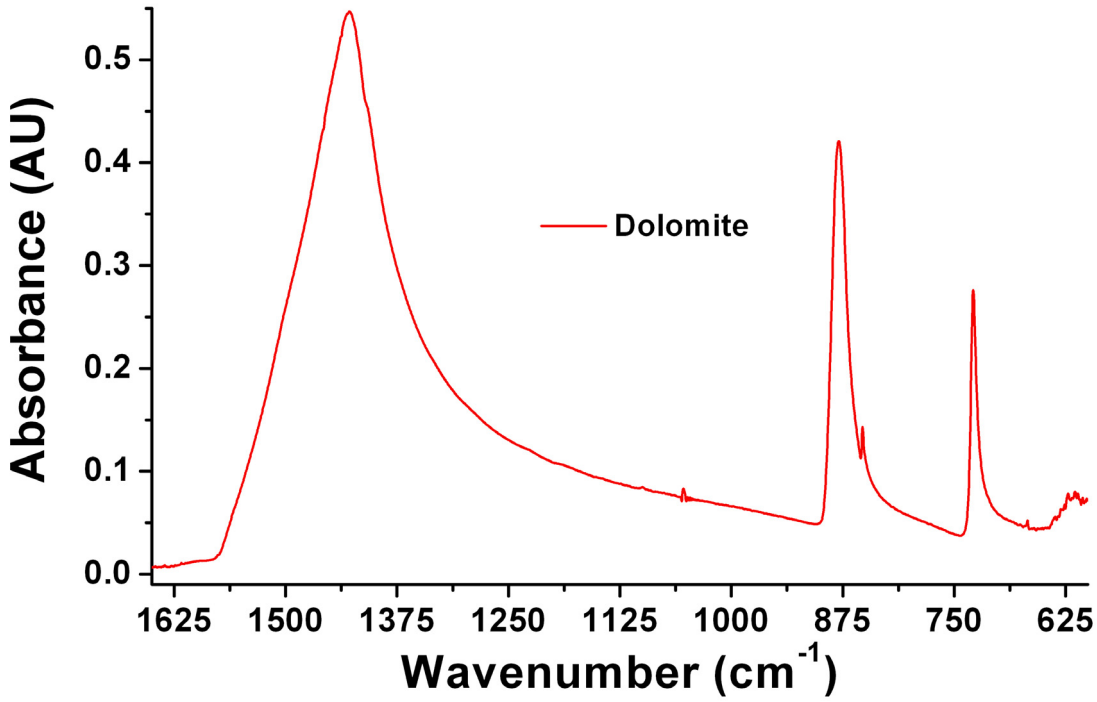

Figure A-2.10: IR-ATR spectrum of dolomite, $CaMg(CO_3)_2$.

A-3 Sediment Collections from GOMGHRC Cruise to MC118 during June 2006

Table A-3.1 provides a summary of sediments collected from MC118 box cores obtained during the GOMGHRC cruise in June 2006. Push-core designations (A, B, C) refer to duplicate/triplicate samples collected from the same box core. Sub-samples (S-S) were stored in plastic bags with designations T = Top, M = Middle, and B = Bottom where depth below seafloor follows the order T < M1 < M2 <B. See **Section 5.1.3** for additional sample collection details.

Table A-3.1: List of sediments collected from the MC118 gas hydrate site during a GOMGHRC cruise in June 2006.

Location	Push-Core	Sub-Samples	S-S Designations	P-C Length (cm)
BC1	BC1A	1 bag	T	NA
	BC1B	3 bags	T, M, B	NA
	BC1C	3 bags	T, M, B	NA
BC2	BC2A	3 bags	T, M, B	NA
	BC2B	3 bags	T, M, B	NA
BC3	BC3	No PCs, Mud Spilled, Nodules were Collected for Dr. Rogeer Sassen		
BC4	BC4A	3 bags	T, M, B	NA
	BC4B	2 bags	T, B	NA
BC5	BC5A	2 bags	T, B	16
	BC5B	2 bags	T, B	13
BC6	BC6A	2 bags	T, B	22
	BC6B	2 bags	T, B	27
BC7	BC7A	2 bags	T, B	14
	BC7B	2 bags	T, B	16
BC8	BC8A	4 bags	T, M1, M2, B	24
	BC8B	4 bags	T, M1, M2, B	25
BC9	BC9A	2 bags	T, B	25
	BC9B	2 bags	T, B	24
BC10	BC10	Did Not Collect From this Core		
BC11	BC11A	3 bags	T, M, B	29
	BC11B	3 bags	T, M, B	26
BC12	BC12A	2 bags	T, B	18
	BC12B	2 bags	T, B	20
BC13	BC13	BC Did Not Trip		

A-4 IR-ATR Analysis of Calcite-Dolomite Standard and Blind Samples

See **Section 5.5** for more additional sample preparation and evaluation information.

Table A-4.1: IR-ATR analytical results from the evaluation of carbonate standards with 90% dolomite and 10% calcite.

90D:10C Standard		**D**	**C**			
	Target	90	10			
	Mass (g)	1.6068	0.1796			
	Mass %	89.95	10.05			
	D PA	**D Stdev**	**C PA**	**C Stdev**	**D/(D+C)**	**C/(D+C)**
Trial 1	0.9959	0.0028	0.0944	0.0020	0.9134	0.0866
Trial 2	0.9287	0.0026	0.0819	0.0019	0.9189	0.0811
Trial 3	0.9277	0.0034	0.0839	0.0030	0.9171	0.0829
	0.9508	**Average**	0.0867	**Average**	0.9165	0.0835
	0.0391	**StDev**	0.0067	**Stdev**	0.0028	0.0028
	4.12	**% RelStDev**	7.75	**% RelStDev**	0.31	3.36

Table A-4.2: IR-ATR analytical results from the evaluation of carbonate standards with 70% dolomite and 30% calcite.

70D:30C Standard		**D**	**C**			
	Target	70	30			
	Mass (g)	1.2611	0.5504			
	Mass %	69.62	30.38			
	D PA	**D Stdev**	**C PA**	**C Stdev**	**D/(D+C)**	**C/(D+C)**
Trial 1	0.8475	0.0025	0.3391	0.0021	0.7142	0.2858
Trial 2	0.7427	0.0023	0.3009	0.0021	0.7116	0.2884
Trial 3	0.7833	0.0029	0.3111	0.0020	0.7157	0.2843
	0.7912	**Average**	0.3171	**Average**	0.7139	0.2861
	0.0529	**StDev**	0.0198	**Stdev**	0.0021	0.0021
	6.68	**% RelStDev**	6.23	**% RelStDev**	0.29	0.72

Table A-4.3: IR-ATR analytical results from the evaluation of carbonate standards with 50% dolomite and 50% calcite.

50D:50C Standard		**D**	**C**			
	Target	50	50			
	Mass (g)	0.9003	0.9001			
	Mass %	50.01	49.99			
	D PA	**D Stdev**	**C PA**	**C Stdev**	**D/(D+C)**	**C/(D+C)**
Trial 1	0.5346	0.0025	0.5288	0.0025	0.5027	0.4973
Trial 2	0.5298	0.0031	0.5392	0.0022	0.4956	0.5044
Trial 3	0.4579	0.0023	0.4754	0.0020	0.4906	0.5094
	0.5074	**Average**	0.5145	**Average**	0.4963	0.5037
	0.0429	**StDev**	0.0342	**Stdev**	0.0061	0.0061
	8.46	**% RelStDev**	6.65	**% RelStDev**	1.22	1.20

Table A-4.4: IR-ATR analytical results from the evaluation of carbonate standards with 30% dolomite and 70% calcite.

30D:70C Standard		**D**	**C**			
	Target	30	70			
	Mass (g)	0.5433	1.2603			
	Mass %	30.12	69.88			
	D PA	**D Stdev**	**C PA**	**C Stdev**	**D/(D+C)**	**C/(D+C)**
Trial 1	0.3461	0.0026	0.7945	0.0018	0.3034	0.6966
Trial 2	0.3188	0.0028	0.7441	0.0021	0.3000	0.7000
Trial 3	0.2863	0.0030	0.6753	0.0019	0.2978	0.7022
	0.3171	**Average**	0.7379	**Average**	0.3004	0.6996
	0.0299	**StDev**	0.0598	**Stdev**	0.0029	0.0029
	9.43	**% RelStDev**	8.11	**% RelStDev**	0.95	0.41

Table A-4.5: IR-ATR analytical results from the evaluation of carbonate standards with 10% dolomite and 90% calcite.

10D:90C Standard		**D**	**C**			
	Target	10	90			
	Mass (g)	0.1805	1.6135			
	Mass %	10.06	89.94			
	D PA	**D Stdev**	**C PA**	**C Stdev**	**D/(D+C)**	**C/(D+C)**
Trial 1	0.1239	0.0021	1.0642	0.0021	0.1043	0.8957
Trial 2	0.1059	0.0023	0.9315	0.0021	0.1021	0.8979
Trial 3	0.1072	0.0019	0.9411	0.0027	0.1023	0.8977
	0.1123	**Average**	0.9789	**Average**	0.1029	0.8971
	0.0100	**StDev**	0.0740	**Stdev**	0.0012	0.0012
	8.91	**% RelStDev**	7.56	**% RelStDev**	1.17	0.13

Table A-4.6: IR-ATR analytical results from the evaluation of blind carbonate samples.

	Blind Sample Analysis: Sum(C+D) = 100% Sample Mass											
	Mass (g)		Mass (%)		PA	StDev	D/(C+D)	Pred % (C or D)		Actual % (C or D)		Abs. % Error
ID	D	C	D	C	D	D	D	D	C	D	C	(C or D)
BS1	0.5786	1.2246	32.09	67.91	0.3375	0.0023	0.3370	33.47	66.53	32.09	67.91	1.38
BS2*	0.8298	0.9738	46.01	53.99	0.5402	0.0023	0.4750	46.94	53.06	46.01	53.99	0.93
BS3	0.1163	1.6821	6.47	93.53	0.0809	0.0019	0.0690	7.30	92.70	6.47	93.53	0.83
BS4	1.4033	0.3937	78.09	21.91	0.9469	0.0030	0.7822	76.94	23.06	78.09	21.91	1.15

	PA	StDev	C/(C+D)
ID	C	C	C
BS1	0.6640	0.0025	0.6630
BS2*	0.5971	0.0022	0.5250
BS3	1.0907	0.0019	0.9310
BS4	0.2636	0.0020	0.2178

A-5 IR-ATR Analysis of Calcite-Dolomite Composition Relative to the Total Carbonate Mass in Marine Sediment Samples from the GoM

See **Section 5.5** for full experimental details and discussion.

Table A-5.1: IR-ATR analysis of calcite and dolomite in BC1 sediments.

BC1										
Sample	**Sub**	**D PA**	**D SD**	**C PA**	**C SD**	**D/(D+C)**	**C/(D+C)**	**% D**	**% C**	**D Vis. ID**
BC1C	Top	0.0012	0.0026	0.1643	0.0026	0.0070	0.9930	1.25	98.75	Low
BC1C	Top	0.0014	0.0023	0.1549	0.0020	0.0087	0.9913	1.41	98.59	Low
BC1C	Top	0.0006	0.0017	0.1392	0.0020	0.0043	0.9957	0.99	99.01	Low
BC1B	Top	0.0021	0.0025	0.1766	0.0030	0.0119	0.9881	1.72	98.28	Low
BC1B	Top	-0.0003	0.0014	0.1142	0.0017	-0.0023	1.0023	0.34	99.66	V Low
BC1B	Top	0.0020	0.0015	0.1241	0.0018	0.0158	0.9842	2.11	97.89	Low
BC1B	Top	-0.0004	0.0013	0.1119	0.0011	-0.0033	1.0033	0.24	99.76	V Low
BC1C	Mid	0.0116	0.0031	0.2238	0.0039	0.0491	0.9509	5.36	94.64	Clear
BC1C	Mid	0.0066	0.0021	0.2124	0.0015	0.0302	0.9698	3.51	96.49	Clear
BC1C	Mid	0.0021	0.0019	0.1822	0.0020	0.0112	0.9888	1.66	98.34	Low
BC1B	Mid	0.0041	0.0021	0.1389	0.0029	0.0286	0.9714	3.36	96.64	Low
BC1B	Mid	-0.0048	0.0015	0.0898	0.0013	-0.0564	1.0564	-4.94	104.94	ND
BC1B	Mid	-0.0044	0.0015	0.1327	0.0022	-0.0345	1.0345	-2.80	102.80	ND
BC1C	Bot	0.0121	0.0023	0.1236	0.0028	0.0889	0.9111	9.24	90.76	Clear
BC1C	Bot	0.0078	0.0019	0.1182	0.0018	0.0621	0.9379	6.63	93.37	Clear
BC1C	Bot	0.0187	0.0020	0.1672	0.0020	0.1005	0.8995	10.38	89.62	Clear
BC1B	Bot	0.0093	0.0022	0.1978	0.0040	0.0450	0.9550	4.96	95.04	Low
BC1B	Bot	0.0029	0.0020	0.1764	0.0024	0.0162	0.9838	2.15	97.85	Low
BC1B	Bot	0.0027	0.0024	0.1930	0.0036	0.0138	0.9862	1.92	98.08	Low

Table A-5.2: IR-ATR analysis of calcite and dolomite in BC2 sediments.

BC2										
Sample	**Sub**	**D PA**	**D SD**	**C PA**	**C SD**	**D/(D+C)**	**C/(D+C)**	**% D**	**% C**	**D Vis. ID**
BC2A	Top	-0.0065	0.0029	0.2504	0.0030	-0.0268	1.0268	-2.05	102.05	ND
BC2A	Top	-0.0016	0.0010	0.0637	0.0011	-0.0256	1.0256	-1.94	101.94	ND
BC2A	Mid	-0.0032	0.0037	0.2395	0.0038	-0.0135	1.0135	-0.75	100.75	ND
BC2A	Bot	-0.0045	0.0021	0.3411	0.0036	-0.0134	1.0134	-0.75	100.75	ND

Table A-5.3: IR-ATR analysis of calcite and dolomite in BC4 sediments.

BC4										
Sample	**Sub**	**D PA**	**D SD**	**C PA**	**C SD**	**D/(D+C)**	**C/(D+C)**	**% D**	**% C**	**D Vis. ID**
BC4A	Top	-0.0031	0.0028	0.1990	0.0035	-0.0156	1.0156	-0.96	100.96	ND
BC4A	Mid	-0.0027	0.0025	0.1869	0.0025	-0.0147	1.0147	-0.87	100.87	ND
BC4A	Bot	-0.0011	0.0027	0.1919	0.0028	-0.0057	1.0057	0.01	99.99	ND
BC4A	Bot	-0.0048	0.0043	0.1987	0.0029	-0.0246	1.0246	-1.84	101.84	ND

Table A-5.4: IR-ATR analysis of calcite and dolomite in BC5 sediments.

BC5										
Sample	**Sub**	**D PA**	**D SD**	**C PA**	**C SD**	**D/(D+C)**	**C/(D+C)**	**% D**	**% C**	**D Vis. ID**
BC5A	Top	-0.0067	0.0025	0.0481	0.0033	-0.1609	1.1609	-15.15	115.15	ND
BC5A	Top	-0.0059	0.0012	0.0577	0.0015	-0.1141	1.1141	-10.58	110.58	ND
BC5A	Top	-0.0064	0.0010	0.0633	0.0008	-0.1117	1.1117	-10.34	110.34	ND
BC5A	Bot	-0.0133	0.0027	0.1446	0.0039	-0.1011	1.1011	-9.31	109.31	ND
BC5A	Bot	-0.0101	0.0018	0.0579	0.0012	-0.2104	1.2104	-19.98	119.98	ND
BC5A	Bot	-0.0116	0.0018	0.0735	0.0028	-0.1883	1.1883	-17.82	117.82	ND
BC5A	Bot	-0.0026	0.0012	0.0206	0.0010	-0.1451	1.1451	-13.61	113.61	ND
BC5B	Bot	-0.0207	0.0037	0.0936	0.0039	-0.2834	1.2834	-27.10	127.10	ND
BC5B	Bot	-0.0203	0.0025	0.0686	0.0031	-0.4205	1.4205	-40.49	140.49	ND
BC5B	Bot	-0.0292	0.0020	0.0919	0.0015	-0.4660	1.4660	-44.93	144.93	ND
BC5B	Bot	-0.0333	0.0023	0.0992	0.0024	-0.5055	1.5055	-48.79	148.79	ND

Table A-5.5: IR-ATR analysis of calcite and dolomite in BC6 sediments.

BC6										
Sample	**Sub**	**D PA**	**D SD**	**C PA**	**C SD**	**D/(D+C)**	**C/(D+C)**	**% D**	**% C**	**D Vis. ID**
BC6A	Top	-0.0059	0.0033	0.2328	0.0046	-0.0260	1.0260	-1.97	101.97	ND
BC6A	Top	-0.0065	0.0038	0.2977	0.0034	-0.0225	1.0225	-1.63	101.63	ND
BC6A	Bot	-0.0063	0.0025	0.3653	0.0041	-0.0176	1.0176	-1.15	101.15	ND

Table A-5.6: IR-ATR analysis of calcite and dolomite in BC7 sediments.

BC7										
Sample	**Sub**	**D PA**	**D SD**	**C PA**	**C SD**	**D/(D+C)**	**C/(D+C)**	**% D**	**% C**	**D Vis. ID**
BC7A	Top	-0.0057	0.0027	0.1082	0.0021	-0.0560	1.0560	-4.90	104.90	ND
BC7A	Top	-0.0080	0.0014	0.1707	0.0017	-0.0491	1.0491	-4.23	104.23	ND
BC7A	Top	-0.0064	0.0017	0.1616	0.0015	-0.0413	1.0413	-3.46	103.46	ND
BC7A	Bot	-0.0048	0.0022	0.2737	0.0039	-0.0179	1.0179	-1.18	101.18	ND
BC7A	Bot	-0.0083	0.0019	0.2409	0.0020	-0.0355	1.0355	-2.90	102.90	ND
BC7A	Bot	-0.0100	0.0020	0.2497	0.0019	-0.0417	1.0417	-3.51	103.51	ND

Table A-5.7: IR-ATR analysis of calcite and dolomite in BC8 sediments.

BC8										
Sample	**Sub**	**D PA**	**D SD**	**C PA**	**C SD**	**D/(D+C)**	**C/(D+C)**	**% D**	**% C**	**D Vis. ID**
BC8A	Top	-0.0032	0.0029	0.1139	0.0027	-0.0287	1.0287	-2.24	102.24	ND
BC8A	Mid1	-0.0055	0.0026	0.1441	0.0027	-0.0400	1.0400	-3.34	103.34	ND
BC8A	Mid2	-0.0021	0.0030	0.1049	0.0034	-0.0203	1.0203	-1.42	101.42	ND
BC8A	Bot	-0.0041	0.0035	0.1988	0.0041	-0.0212	1.0212	-1.50	101.50	ND

Table A-5.8: IR-ATR analysis of calcite and dolomite in BC9 sediments.

BC9										
Sample	**Sub**	**D PA**	**D SD**	**C PA**	**C SD**	**D/(D+C)**	**C/(D+C)**	**% D**	**% C**	**D Vis. ID**
BC9A	Top	-0.0045	0.0018	0.0276	0.0016	-0.1949	1.1949	-18.47	118.47	ND, Oil
BC9A	Bot	0.0008	0.0018	0.0090	0.0018	0.0784	0.9216	8.22	91.78	ND, Oil
BC9A	Bot	0.0006	0.0007	0.0016	0.0007	0.2603	0.7397	25.98	74.02	ND, Oil
BC9A	Bot	0.0008	0.0007	0.0022	0.0009	0.2591	0.7409	25.86	74.14	ND, Oil

Table A-5.9: IR-ATR analysis of calcite and dolomite in BC11 sediments.

BC11										
Sample	**Sub**	**D PA**	**D SD**	**C PA**	**C SD**	**D/(D+C)**	**C/(D+C)**	**% D**	**% C**	**D Vis. ID**
BC11A	Top	-0.0032	0.0022	0.0616	0.0018	-0.0552	1.0552	-4.82	104.82	ND
BC11A	Mid	-0.0044	0.0033	0.3063	0.0030	-0.0145	1.0145	-0.85	100.85	ND
BC11A	Bot	-0.0072	0.0036	0.4985	0.0056	-0.0147	1.0147	-0.87	100.87	ND

Table A-5.10: IR-ATR analysis of calcite and dolomite in BC12 sediments.

BC12										
Sample	**Sub**	**D PA**	**D SD**	**C PA**	**C SD**	**D/(D+C)**	**C/(D+C)**	**% D**	**% C**	**D Vis. ID**
BC12A	Top	0.0052	0.0025	0.0120	0.0014	0.3032	0.6968	30.17	69.83	Yes, Oil
BC12A	Top	0.0017	0.0018	0.0156	0.0016	0.0973	0.9027	10.06	89.94	Yes, Oil
BC12A	Top	0.0040	0.0008	0.0119	0.0007	0.2529	0.7471	25.25	74.75	Yes, Oil
BC12A	Top	0.0150	0.0012	0.0359	0.0010	0.2943	0.7057	29.30	70.70	Yes, Oil
BC12A	Bot	0.0096	0.0023	0.0196	0.0017	0.3276	0.6724	32.55	67.45	Yes, Oil
BC12A	Bot	0.0028	0.0021	0.0111	0.0016	0.2031	0.7969	20.40	79.60	Yes, Oil
BC12A	Bot	0.0058	0.0008	0.0414	0.0012	0.1224	0.8776	12.51	87.49	Yes, Oil
BC12A	Bot	0.0057	0.0007	0.0296	0.0010	0.1615	0.8385	16.34	83.66	Yes, Oil

Table A-5.11: IR-ATR analysis of calcite and dolomite in MC118 gravity core 21 sediments.

MC118 Core 21										
Sample	**Trial**	**D PA**	**D SD**	**C PA**	**C SD**	**D/(D+C)**	**C/(D+C)**	**% D**	**% C**	**D Vis. ID**
21	1	0.1588	0.0020	0.1486	0.0022	0.5166	0.4834	51.01	48.99	High
21	2	0.1544	0.0033	0.1487	0.0023	0.5094	0.4906	50.30	49.70	High
21	3	0.1342	0.0016	0.1285	0.0024	0.5108	0.4892	50.44	49.56	High

Table A-5.12: IR-ATR analysis of calcite and dolomite in MC118 gravity core 26 sediments.

MC118 Core 26										
Sample	**Trial**	**D PA**	**D SD**	**C PA**	**C SD**	**D/(D+C)**	**C/(D+C)**	**% D**	**% C**	**D Vis. ID**
26	1	0.0586	0.0017	0.0823	0.0016	0.4156	0.5844	41.15	58.85	High
26	2	0.1084	0.0017	0.0983	0.0018	0.5244	0.4756	51.77	48.23	High
26	3	0.0596	0.0019	0.0499	0.0026	0.5442	0.4558	53.70	46.30	High

Table A-5.13: IR-ATR analysis of calcite and dolomite in MC118 gravity core 38 sediments.

MC118 Core 38										
Sample	**Trial**	**D PA**	**D SD**	**C PA**	**C SD**	**D/(D+C)**	**C/(D+C)**	**% D**	**% C**	**D Vis. ID**
38	1	-0.0153	0.0014	0.1698	0.0014	-0.0992	1.0992	-9.12	109.12	V Low (?)
38	2	-0.0125	0.0019	0.2083	0.0026	-0.0637	1.0637	-5.66	105.66	V Low (?)

Table A-5.14: IR-ATR analysis of calcite and dolomite in MD02-2570 piston core sediments.

MD02-2570										
Sample	**Trial**	**D PA**	**D SD**	**C PA**	**C SD**	**D/(D+C)**	**C/(D+C)**	**% D**	**% C**	**D Vis. ID**
1 m	1	0.0341	0.0019	0.0144	0.0014	0.7035	0.2965	69.26	30.74	High
6 m	1	0.0532	0.0034	0.0113	0.0025	0.8246	0.1754	81.08	18.92	High
6 m	2	0.0665	0.0024	0.0082	0.0022	0.8896	0.1104	87.43	12.57	High
6 m	3	0.0406	0.0011	0.0022	0.0013	0.9481	0.0519	93.14	6.86	High
9 m	1	0.0563	0.0025	0.0441	0.0035	0.5608	0.4392	55.32	44.68	High
12 m	1	0.0540	0.0028	0.1066	0.0035	0.3362	0.6638	33.39	66.61	High
15 m	1	0.0616	0.0046	0.0521	0.0042	0.5417	0.4583	53.45	46.55	High
18 m	1	0.0453	0.0047	0.0277	0.0030	0.6212	0.3788	61.21	38.79	High
18 m	2	0.0760	0.0078	0.0536	0.0050	0.5866	0.4134	57.84	42.16	High
18 m	3	0.0541	0.0026	0.0346	0.0022	0.6096	0.3904	60.09	39.91	High
21 m	1	0.0754	0.0030	0.0550	0.0024	0.5784	0.4216	57.04	42.96	High
21 m	2	0.2014	0.0051	0.1001	0.0055	0.6681	0.3319	65.79	34.21	High
21 m	3	0.1021	0.0026	0.0660	0.0024	0.6074	0.3926	59.87	40.13	High
24 m	1	0.0366	0.0018	0.0541	0.0019	0.4040	0.5960	40.01	59.99	High
27 m	1	0.0690	0.0031	0.0576	0.0030	0.5447	0.4553	53.75	46.25	High
27+ m	1	0.2477	0.0102	0.0946	0.0084	0.7236	0.2764	71.21	28.79	High

A-6 Spectral Ray Tracing Simulation Settings for SPRAY Software

Additional information for spectral ray tracing simulations can be found in **Section 7-3**.

Table A-6.1: SPRAY values for dielectric function models for optical materials.

Dielectric Function (DF) Models for Optical Materials				
Material	DF Model	Points	Range (cm^{-1})	Value
Air	Constant Refractive Index	20	4000-400	1.0003
ZnSe	Constant Refractive Index	20	4000-400	2.44

Table A-6.2: SPRAY values for dielectric properties of simulated absorbers.

Simulated Absorber Dielectric Function Properties			
DF Model	Value	Oscillator Strength	Damping Constant
Dielectric Background	1.4		
Harmonic Oscillator	1443 cm^{-1}	30	1

Table A-6.3: SPRAY values for simulated object interfaces.

Simulated Object Interfaces			
Interface	Type	Material	Thickness
Simulated Absorber Interface	Thinfilm	Absorber	10 nm
	Halfspace	ZnSe	
	Halfspace	ZnSe	
ATR Crystal Interfaces	Halfspace	Air	
	Halfspace	ZnSe	

Table A-6.4: SPRAY parameters for simulated objects.

Simulated Object Parameters					
ATR Crystal	Location (x,y,z)	Vector 1 (x,y,z)	Vector 2 (x,y,z)	Vector 3 (x,y,z)	Angle
	0, 0, 0	3.4, 0, 0	0, 0.5, 0	0, 0, 0.3	45
Circular Light Source	Location (x,y,z)	Surface Normal (x,y,z)	Cone Angle	Radius	
	-3.4, 0, 0.1	1, 0, -1	1.0° – 16.0°	0.00215 – 0.25 cm	
Absorbing Cylinder	Location (x,y,z)	Radius Vector	Axis Vector		
	-2.5 – 2.3, 0, -0.297	0.125, 0, 0	0, 0, 0.001		
Surface Imaging Screen	Location (x,y,z)	Vector 1 (x,y,z)	Vector 2 (x,y,z)		
	0, 0, -0.29995	3.6, 0, 0	0, 0.5, 0		
Rectangular Detector	Location (x,y,z)	Vector 1 (x,y,z)	Vector 2 (x,y,z)		
	5, 0, 2	0, -2, 0	-1.5, 0, 1.5